EFFECT OF COOLING FLOW ON THE OPERATION OF A HOT ROTOR-GAS FOIL BEARING SYSTEM

A Dissertation

by

KEUN RYU

Submitted to the Office of Graduate Studies of
Texas A&M University
in partial fulfillment of the requirements for the degree of

DOCTOR OF PHILOSOPHY

December 2011

Major Subject: Mechanical Engineering

Effect of Cooling Flow on the Operation of a Hot Rotor-Gas Foil Bearing System

EFFECT OF COOLING FLOW ON THE OPERATION OF A HOT ROTOR-GAS FOIL BEARING SYSTEM

A Dissertation

by

KEUN RYU

Submitted to the Office of Graduate Studies of
Texas A&M University
in partial fulfillment of the requirements for the degree of

DOCTOR OF PHILOSOPHY

Approved by:

Chair of Committee,	Luis San Andrés
Committee Members,	Alan Palazzolo
	Yong-Joe Kim
	Javier Jo
Head of Department,	Jerald A. Caton

December 2011

Major Subject: Mechanical Engineering

ABSTRACT

Effect of Cooling Flow on the Operation of a Hot Rotor-Gas Foil Bearing System.

(December 2011)

Keun Ryu, B.S., Hanyang University, Seoul, Korea;

M.S., Hanyang University, Seoul, Korea;

M.S., Texas A&M University

Chair of Advisory Committee: Dr. Luis San Andrés

Gas foil bearings (GFBs) operating at high temperature rely on thermal management procedures that supply needed cooling flow streams to keep the bearing and rotor from overheating. Poor thermal management not only makes systems inefficient and costly to operate but could also cause bearing seizure and premature system destruction. To date, most of thermal management strategies rely on empirically based "make-and-break" techniques which are often inefficient.

This dissertation presents comprehensive measurements of bearing temperatures and shaft dynamics conducted on a hollow rotor supported on two first generation GFBs. The hollow rotor (1.36 kg, 36.51 mm OD and 17.9 mm ID) is heated from inside to reach an outer surface temperature of 120ºC. Experiments are conducted with rotor speeds to 30 krpm and with forced streams of air cooling the bearings and rotor. Air pressurization in an enclosure at the rotor mid span forces cooling air through the test GFBs. The cooling effect of the forced external flows is most distinct when the rotor is

hottest and operating at the highest speed. The temperature drop per unit cooling flow rate significantly decreases as the cooling flow rate increases. Further measurements at thermal steady state conditions and at constant rotor speeds show that the cooling flows do not affect the amplitude and frequency contents of the rotor motions. Other tests while the rotor decelerates from 30 krpm to rest show that the test system (rigid-mode) critical speeds and modal damping ratio remain nearly invariant for operation with increasing rotor temperatures and with increasing cooling flow rates. Computational model predictions reproduce with accuracy the test data. The work adds to the body of knowledge on GFB performance and operation and provides empirically derived guidance for successful integration of rotor-GFB systems.

DEDICATION

This dissertation is dedicated

To my Lord and Savior Jesus Christ, who is rich in mercy and love

To my wife, Dong Yun Lee, for her love and prayers

To my daughters, Arin and (Faith)

To my father and mother, for their love, guidance, and support

To my brother, Hoon, for his love and encouragement

To my home country, Korea

ACKNOWLEDGEMENTS

First and foremost, I would like to thank my Lord and Savior Jesus Christ through whom all things are sustained and held together. May He receive all the honor, all glory be His.

I do express my gratitude to my wife, Dong Yun Lee, who has been my advisor and helpmate, giving me two beautiful and lovely daughters.

I am forever indebted to a great many people – too many to mention – many have been mentors and many I have collaborated with.

I thank my advisor, Dr. Luis San Andrés, for giving me the opportunity to join the Tribology group and pursue a doctorate degree at the TAMU Turbomachinery Laboratory and for providing the environment which made all of this work possible. His encouragement, advice, and guidance are gratefully appreciated. He treated me as his peer and valued my opinions, characteristics that made him invaluable as a mentor.

I thank my committee members, Dr. Alan Palazzolo, Dr. Yong-Joe Kim and Dr. Javier Jo, for their time and effort in offering advice.

The support of NASA NRA on Subsonic Rotary Wing, SSRW2-1.3 Oil-Free Engine Technology (Foil Gas Bearing Modeling). Grant Cooperative Agreement NNX07P98A and the TAMU Turbomachinery Research Consortium are acknowledged. Thanks to the Korea Institute of Science and Technology (KIST) for donating the test foil bearings and rotor.

I also acknowledge the many contributions of Dr. Tae Ho Kim (currently at KIST) to the success of the TAMU foil bearing project. He was invaluable throughout my time as a graduate student at KIST and TAMU as both my colleague and my mentor.

Thanks to my former fellow lab-mates and colleagues at TAMU Turbolab: Dr. Adolfo Delgado, Thomas Chirathadam, Ash Maruyama, Anthony Breedlove, Sanjeev Seshagiri, Paola Mahecha, Zach Ashton, Arian Vistamehr, Yaying Niu, Jose Baker, Chad Jarrett, Jared Goldsmith, Katherine Janica, Chris Kulhanek, Manish Thorat, and Jason Wilkes, for their friendship and support over the last few years. I also would like to thank Mr. Eddie Denk for his assistance.

I also thank Dr. Yong-Bok Lee and Dr. Chang-Ho Kim, former advisors at KIST, and Prof. Gunhee Jang, former advisor at Hanyang University, for their continuous mentorship and encouragement.

I thank Pastor Young-Sik An for his love and prayers.

Thanks also go to TAMU Judo team members, in particular, Coach Bob Perez, Daniel Gomez, and Dr. Jean-Francois Chamberland.

Finally, I thank my parents and brother, Hoon, for their continuous and unconditional support and love throughout my entire life.

NOMENCLATURE

C_r	Bearing radial clearance [m]
$C_{\alpha\beta}$	Bearing damping coefficients; $\alpha\beta=X,Y$ [Ns/m]
c_+	Operating bearing radial clearance [m]
D_i	Rotor inner diameter [m]
D_I	Bearing cartridge inner diameter [m]
D_o	Rotor outer diameter [m]
D_O	Bearing cartridge outer diameter [m]
D_T	Top foil inner diameter [m]
$f_{z_{inner}}$, $f_{z_{outer}}$	Friction factors for inner and outer gaps [-]
h_B	Bump height [m]
$k_{z_{inner}}, k_{z_{outer}}$	Shear flow parameter for inner and outer gaps [-]
$K_{\alpha\beta}$	Bearing stiffness coefficients; $\alpha\beta=X,Y$ [N/m]
L	Top foil axial length [m]
L_O	Bearing cartridge axial length [m]
l_B	Bump length [m]
$\dot{m}_{inner}, \dot{m}_{outer}$	Mass flow rates through inner and outer gaps [kg/s]
$\dot{m}_{overall}$	Overall mass flow rates, $\dot{m}_{overall} = \dot{m}_{outer} + \dot{m}_{inner}$ [kg/s]
$\dot{M}_{inner}, \dot{M}_{outer}$	Mass flow rates per circumferential length through inner and outer gaps [kg/s-m]

N_B	Number of Bumps [-]
P	Gas film pressure [N/m^2]
P_a	Ambient pressure [N/m^2]
P_{Co}	Outer cooling gas stream entrance pressure [N/m^2]
P_{ent}	Entrance gas pressure [N/m^2]
P_{exit}	Exit gas pressure [N/m^2]
P_S	Supply gas pressure [N/m^2]
Q	Volume flow rate [m^3/s]
r_B	Bump arc radius [m]
R_c	Ideal gas constant [J/kg-K]
$\mathrm{Re}_{a_{inner}}, \mathrm{Re}_{a_{inner}}$	Axial flow Reynolds numbers for inner and outer gaps [-]
$\mathrm{Re}_{c_{ent}}, \mathrm{Re}_{c_{exit}}$	Circumferential flow Reynolds number at entrance and exit planes [-]
R_I	Rotor inner diameter [m]
R_O	Rotor outer diameter [m]
s_0	Bump pitch [degree]
t	Time [s]
T	Gas temperature [K]
$T_1 - T_4$	Free end GFB cartridge outboard temperature [ºC]
T_5	Free end bearing support housing surface temperature [ºC]
$T_6 - T_9$	Drive end GFB cartridge outboard temperature [ºC]
T_{10}	Drive end bearing support housing surface temperature [ºC]

T_{amb}	Test rig ambient temperature [ºC]
t_B	Bump foil thickness [m]
t_{BC}	Bearing cartridge wall thickness [m]
T_{Co}	Outer cooling gas stream entrance temperature [ºC]
T_e	Air temperature inside housing enclosure [ºC]
T_{Fo}	Top foil back surface temperature [ºC]
T_h	Cartridge heater temperature [ºC]
T_{hs}	Heater reference temperature [ºC]
T_{out}	Exhaust air temperature released into ambient air from FE bearing [ºC]
Tr_{DE}	Drive end rotor surface temperature [ºC]
Tr_{FE}	Free end rotor surface temperature [ºC]
t_T	Top foil thickness [m]
U	Circumferential bulk flow velocity in inner gap [m/s]
u_c	Mean circumferential flow velocity [m/s]
U_{ent}	Entrance circumferential bulk flow velocity in inner gap [m/s]
W_{inner}	Axial bulk flow velocity in inner gap [m/s]
W_{outer}	Axial bulk flow velocity in outer gap [m/s]
X,Y,Z	Inertial Cartesian coordinate system [m]
Z_c	Compressibility factor [-]
α	Inlet flow pre-swirl factor [-]
α_B	Bump arc angle [degree]

ζ	Damping ratio
λ	Thermal inlet mixing coefficients
μ	Gas viscosity [Ns/m^2]
ρ	Gas density [kg/m^3]
τ_{xy}	Circumferential wall shear stress function [N/m^2]
τ_{zy}	Axial wall shear stress function [N/m^2]
Θ	Circumferential coordinate [rad]
Ω	Rotor angular velocity [/s]

Acronyms

DE	Drive end bearing
DH	Drive end, horizontal direction
DV	Drive end, vertical direction
FE	Free end bearing
FH	Free end, horizontal direction
FV	Free end, vertical direction
GFB	Gas foil bearing
N.F.	Natural frequency
TEHD	Thermohydrodynamic

TABLE OF CONTENTS

CHAPTER Page

Page

LIST OF FIGURES

FIGURE Page

FIGURE Page

FIGURE Page

FIGURE Page

FIGURE Page

FIGURE Page

FIGURE Page

FIGURE Page

LIST OF TABLES

CHAPTER I

INTRODUCTION

Micro gas turbine engines (<400 kW) are light-weight compact units operating at extreme temperatures and at high rotor speeds to achieve the desired power with reduced emissions [1]. Employing gas foil bearings (GFBs) in micro gas turbines increases system efficiency and operating life while reducing system complexity [2]. GFBs also enable low drag power losses and maintenance-free system [3].

GFBs are compliant, self-acting, hydrodynamic bearings using ambient air or any other process gas as a lubricant. GFBs have been commercialized since the 1970's in air cycle machines in aircrafts. Recent advances in bearing structural components and solid lubricant coatings accompanied by accurate computational design tools anchored to reliable test data have widen the application range of GFBs [4−6]. Current commercial applications include micro gas turbines, compressors, turbo expanders, and turbochargers, for example.

Figure 1 shows photographs of a 1st generation bump-type GFB, consisting of a rigid cartridge where corrugated bumps, as a compliant foundation, are assembled with a smooth arcuate top foil. The trailing edge of the top foil is affixed to the bearing cartridge and the bump foil strips support the rest of the top foil. The bump strip layers provide the bearing structural stiffness [7]. Coulomb-type damping arises due to material hysteresis and dry-friction between the bump strips and the top foil, as well as between

---

This dissertation follows the style of Journal of Engineering for Gas Turbines and Power.

the bump strips and the bearing inner surface [8].

The static and dynamic forced performance of GFBs relies on the geometry of the bump structure and its material properties [9,10]. Engineered coatings (solid lubricants) are typically applied on the surface of the top foil and/or the rotor to avoid excessive power losses and to minimize wear during frequent start and stop cycles [11].

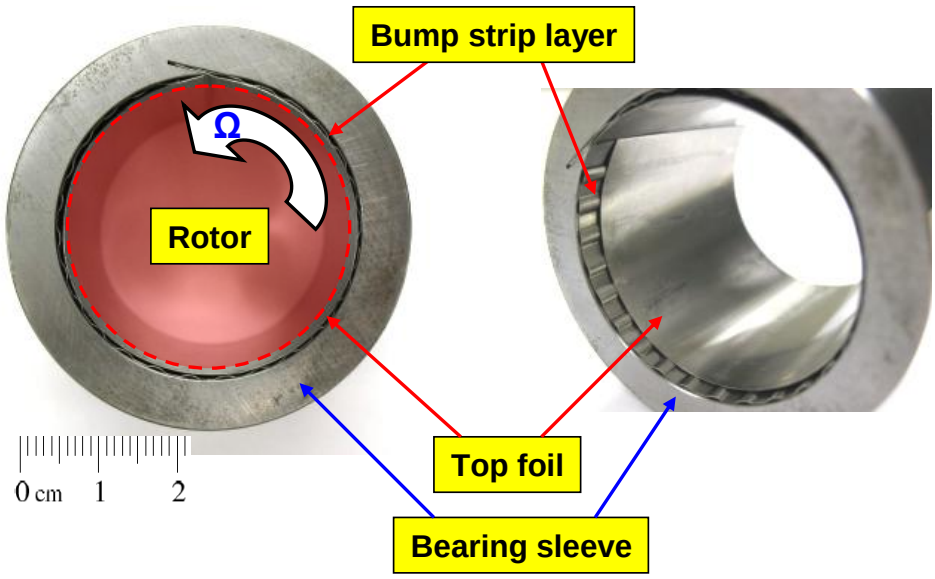

Fig. 1 Photographs of bump-type 1st generation gas foil bearing for oil-free turbomachinery. Manufacturer: Korea Institute of Science and Technology (KIST).

An engineered thermal management is a necessity for the successful implementation of GFBs in high temperature applications. The most widespread approach for thermal control in a GFB system is to supply adequate amounts of air, flowing axially underneath the top foil and through the bump foils. A cooling gas flow assists to carry away heat and prevents GFBs from encountering thermal seizure, thus

maintaining an adequate load capacity and thermal stability [12]. Since gases have a very low density, large mass flow rates are typically required to carry away (convect) thermal energy. At high speed and extreme temperature operating conditions, localized *hotspots*[1] in foil bearings can result in excessive thermal gradients and, likely, bearing seizures [12,13].

Reliable testing of GFBs and the development of experimentally benchmarked predictive tools reinforce the path for reliable commercial implementations. An independent experimental database is a welcome addition must to gauge the accuracy of predictive computational tools. This data base must detail in full the test rotor and bearing system configuration with bump dimensions, and materials' mechanical properties, and the test conditions (i.e., system component temperatures, operating clearance and assembly preload, etc).

The present work, extending prior art [14], shows more measurements of bearings' and rotor temperatures and rotor motions in a laboratory rotor bearing system that operates at high temperature. An electric cartridge heater warms a hollow rotor and its supporting foil bearings. A further focus of the study is the investigation of adequate thermal management strategies using forced cooling flow into the GFBs. Most importantly, the measurements serve to benchmark a predictive analysis for the static and dynamic forced performance of GFBs [14]. The experimentally validated tool will significantly reduce time and expenses in further developments of micro-turbomachinery (MTM).

[1] A hot spot denotes the place where there is *light* rubbing of a rotor on the top foil surface that quickly generates heating and that is not conducted adequately into other parts of the bearing.

CHAPTER II

LITERATURE REVIEW

In 1953, Block and van Rossum introduced compliant foil bearings [15]. Over the first four decades of FB development, GFBs were successfully deployed in several types of small turbomachinery, such as aircraft air cycle machines and microturbines. This is because GFBs fulfill most of the requirements of efficient oil-free turbomachinery by increasing the bearing load capacity and its reliability [16]. In 2006, Klaass and DellaCorte [17] provide a comprehensive review on the development of gas foil bearings for oil-free gas turbines over the previous 45 years. References [18,19] report the efforts to demonstrate oil-free gas turbines employing multi-leaf type foil bearings during the 1970s and the 1980s.

Thermal considerations are mandatory when incorporating GFBs into high temperature applications. The most common method for thermal management in GFB-rotor systems is to supply pressurized air at one end of the bearing to remove *hot spots* in the bearings.

Ruscitto *et al.* [20] conduct comprehensive experiments to determine the requirement of bearing cooling flow with a test foil bearing operates at 315°C ambient temperature. The test rig consists of an air turbine driven overhung shaft and a foil bearing. A furnace comprised of eight 500W quartz tubes houses a test journal and foil bearing. The shaft is supported on two ceramic hybrid ball bearings. The test foil bearing (1^{st} generation with 37.1 mm in diameter and length) is mounted outboard of the support

ball bearings and is free to float on the air film generated in the bearing during shaft rotation. Two J-Type thermocouples are affixed on the backside of the bump foil. A forced cooling air flow, 210°C in inlet temperature and at 50−110 L/min flow, is supplied to the test bearing to maintain a constant temperature (at 315°C) while increasing rotor speed and static load to 45 krpm and 111 N, respectively. In the tests, the cooling air enters the test FB at the radial gap in the top foil, between the welded and the free ends. As the ambient temperature increases from room temperature to 315ºC, the load capacity of the test bearing increases by 8% (from 1.61 bar to 1.75 bar). The bearing temperature, nearly invariant to increases in the static load applied to the bearing, decreases as the strength of the cooling flow rate increases.

Without cooling flow into the bearing, DellaCorte [21] provides measurements of FB load capacity and torque during start-up and shut-down events up to 70 krpm and operating at 700ºC. The overall layout and configuration of the test rig is similar with the test apparatus in Ref. [20]. Even though the operating temperature of the test GFB is extreme, no thermal management is attempted. The test bearing has an ID (inner diameter) of 35 mm and length of 25mm. The bearing cartridge and journal are made of Inconel 718. The load capacity and start-up/shut-down torque of the test bearing decrease with increasing in operating temperature. This is because the test bearing ID expands as the ambient temperature increases. A decrease in the bearing preload due to

bearing cartridge expansion leads a decrease in bearing load capacity and torque. Note that a decrease in bearing preload eliminates the possibility of thermal runaway[2].

Using the same test rig in [21], Radil *et al.* [23] perform experiments to evaluate the effectiveness of three different cooling methods (axial cooling, direct and indirect shaft cooling) for thermal management in a GFB. The authors claim that the axial cooling method, forcing air through the test bearing by pressurizing one side of the bearing cartridge slightly above ambient pressure, is the most effective to decrease bearing internal temperatures. The measured bearing temperatures during cooling air delivery determine the effectiveness of the cooling method. Three type-K thermocouples are embedded at the top foil spot weld location in the test foil bearing (3rd generation, 50 mm in diameter D and 48 mm in length L), with one in the middle and one at each edge, see Fig. 2. The experiments are conducted at 60 krpm with a 222 N (W_s) static load (specific load W_s/LD=0.93 bar) on the test bearing. Note that, during the experiments, the furnace surrounds and heats the test bearing and rotating journal. For direct and indirect shaft cooling methods, see Figs. 3 (a) and (b), a 9.5 mm ID steel tube delivers hot air (150−200ºC, warmed by an electric tube heater) through the rotor ID.

In the direct cooling method (Fig. 3(a)), the air jet impinges on the rotor inner surface underneath the test bearing; while in the indirect cooling (Fig. 3 (b)), the air is forced on the drive end of the rotor. For the axial cooling method, see Fig. 3 (c), the test foil bearing and journal are enclosed inside a "can". Then, compressed air is supplied to the "can", thereby traveling axially through the test bearing and journal. For the axial

[2] Thermal runaway is a consequence of the thermal growth mismatch between the shaft and bearing and manifests as a continual increase in bearing preload [22].

cooling method, the cooling air is supplied at ambient temperature, i.e., the cooling air is not heated by the electric tube heater. It is important to note that, for the axial cooling method, the cooling air temperature decreases from 400ºC to 150ºC as the air flow rate increases from 40 to 170 L/min. On the other hand, the cooling air temperature for the direct and indirect cooling methods is kept at 150−200ºC. Furthermore, while heating both the bearing and rotating journal (held inside the furnace), the authors identify the effectiveness of each cooling method based on the bearing temperature. Note that only the axial cooling method "directly" cools the test bearing while the others (direct and indirect cooling methods) do not.

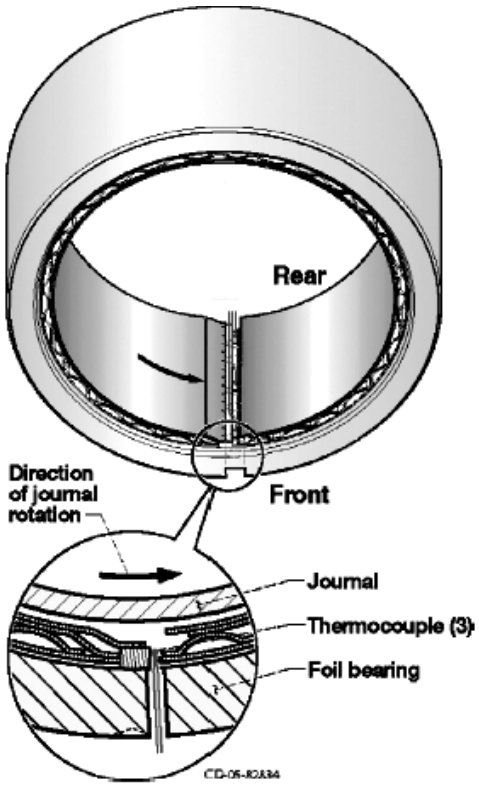

Fig. 2 Schematic view of thermocouple locations in a test foil bearing. Reproduced from [23].

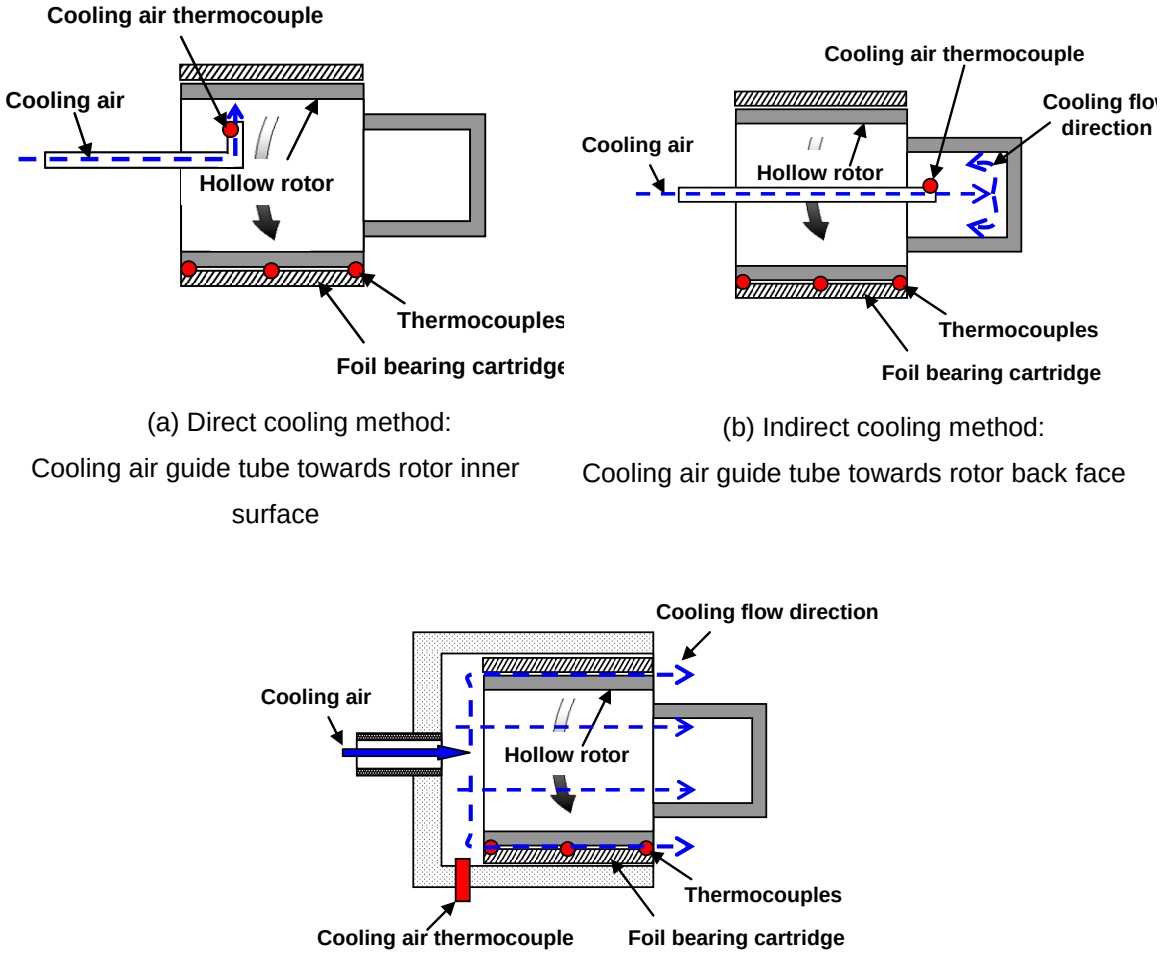

(a) Direct cooling method:
Cooling air guide tube towards rotor inner surface

(b) Indirect cooling method:
Cooling air guide tube towards rotor back face

(c) Axial cooling method: Bearing enclosed with can.
Cooling air supply tube connected to can's closed end.

Fig. 3 Schematic views for three methods of foil bearing thermal management using forced cooling air. Taken from Ref. [23].

Lee and Kim [24] present temperature measurements on a three-pad FB for increasing cooling flow rates (up to ~25 L/min) with static loads applied on the test bearing (to ~100N) and for rotor speeds ranging from 30 krpm to 40 krpm. The tests are conducted at room temperature without a heat source. The FB, 50.1 mm in (top foil)

diameter and 37.5 mm in axial length, floats atop a (Inconel 718) shaft that is driven by a 3kW electric motor. Static vertical loads are applied on the bearing by pulling a flexible string connected to the bearing housing. Cooling air is fed axially into one side of the test bearing while the other side is exposed to ambient air. The cooling scheme is similar to the axial cooling method in Ref. [23]. Temperatures are recorded at both the loaded and unloaded top foils, as well as the bearing housing ODs. At 35 krpm with 76 N of static load, 8 L/min of cooling air makes the top foil temperature 11% lower than that without cooling air (i.e, 75ºC without cooling flow→67ºC with 8 L/min cooling flow). On the other hand, at the same operating condition, the top foils' temperatures with cooling streams over 16 L/min are just a few degrees lower than those at 16 L/min cooling flow (i.e., 61ºC at 16 L/min cooling flow→59ºC at 25 L/min cooling flow). Note that, as the cooling flow rate increases, the cooling air temperature into the bearing decreases (i.e., the air temperature in the plenum decreases from 40ºC with 8L/min cooling air to 31ºC with 25 L/min cooling air). The same authors also present a thermohydrodynamic model to predict the transient thermal behavior of the rotor-FB system and compare predictions with the measurements. See Refs. [24,25] for more details on the authors' thermal analyses for the foil structure and rotor.

Dykas [12] investigates the effect of thermal management on the performance of foil thrust bearings. The test rig consists of a turbine-driven rotating shaft, supported on two foil journal bearings, a magnetic thrust bearing at one end maintaining axial position, and a foil thrust bearing at the other end. The maximum rotor speed is 80 krpm while the test thrust bearing is heated to 540ºC. The test bearing comprises 8-pads, 43

mm in ID (inner diameter) and 90 mm in OD (outer diameter), arranged in an annulus around a backing plate. Thermocouples, three per each pad, are attached to the backside of the bump foils using a thermally conductive epoxy. Forced cooling air enters the inner diameter of the bearing and exhausts to its outer diameter through the bump foil structure. Cooling flow rates, varying from 0 to 450 L/min, set to enhance the test bearing load capacity at high rotor speeds (~50 krpm); albeit the effect is small at low rotor speeds (~25 krpm). When testing at a fixed cooling flow rate, the bearing load capacity decreases with rotor speed. Inadequate thermal management renders thermo-elastic distortions of the shaft and top foil surfaces, thereby reducing the load capacity of the test bearing.

The references above [12,20,21,23,24] show bearing component-level tests. The following literature [26−28] presents system-level experimental work. Kirschmann and Agrawal [26] demonstrate a 2.2 kN thrust class turbojet engine which implements a 2nd generation FB (40 mm in diameter and length). The test FB replaces a roller bearing located between the compressor and turbine. During the operation at 55 krpm, 280ºC cooling air from an upstream supply is forced into the test bearing. A ceramic based solid film, offering performance superior to that of a silver alloy coating, coats the top foil. Lower preload FBs are preferable since they make the rotor start at a lower torque yielding less wear during start and shutdown cycles.

Walton *et al.* [27] perform exhaustive rotordynamic tests on a (290N thrust) miniature turbojet engine rotor, max. 150 krpm, mounted on 3rd generation FBs. The light weight rotor (400 g) is supported on two, 15 mm diameter, radial foil bearings and

a multi-pad, 25 mm diameter, double acting thrust foil bearing. A series of rapid acceleration/deceleration tests from 75 krpm to 15 krpm are conducted while 345ºC hot air is supplied to the test rig. The hot air warms the whole test rotor-bearing system, the test FB temperature reaching up to 290ºC during the experiments. In the tests, *cooling* air at 290ºC is directed through the foil thrust bearings; then it is pressurized into the inboard of the journal bearing while the outboard of the journal bearing is exposed to ambient pressure. The bearing temperature increases with rotor speed.

In Ref. [28], the same authors further demonstrate a turbojet engine integrating a hybrid support bearing system that uses a ball bearing and a foil bearing. The maximum rotor speed and bearing temperature are 60 krpm and 650ºC, respectively. The hot section rolling element bearing and the entire existing lubrication system are replaced with a FB. The rotor is accelerated from rest to 60 krpm while the bearing is cooled with an airflow rate of 566 L/min. When the cooling flow rate is below 140 L/min, the bearing temperatures continue to increase without indication of stabilizing, i.e., reaching thermal equilibrium. Higher rotor speeds and cooling flow rates render larger axial thermal gradients (13ºC/cm). A large axial thermal gradient may result in uneven bearing and shaft growths, thereby altering the local bearing clearance. To verify the ability of the foil bearings to accommodate the centrifugal and thermal growths in the bearings and rotor, comprehensive transient performance tests (rapid start/stop cycle operations) are conducted at a bearing temperature of 650ºC. In an actual application, lower cooling flows are preferable so as not to compromise severely the engine compressor performance.

Engineered thermal management strategies for high temperature GFB systems are customarily known in industry. LaRue *et al.* [29] develop a bearing support housing and cooling system for adequate thermal management of a GFB system in turbochargers (TCs) for diesel or gasoline engines. Note that the reference is the first production patent for an oil-free turbocharger. An effective thermal management is achieved by cooling the TC rotor and FBs (journal and thrust), as well as the TC center housing. The TC rotor is supported on two journal GFBs. Two double acting thrust bearings, positioned between the journal bearings, maintain the rotor axial position. Cooling air extracted from the engine intake duct downstream of the compressor is supplied to the center housing. The center housing includes a cooling air supply passage into the center housing bore. Cooling air is supplied into the thrust bearings first; then flowing into the journal bearings, to later return to the compressor inlet. The FB configuration with a double bump strip layer, as shown in Fig. 4, renders larger cooling flow paths than in a single-layer bump type FB, thereby increasing the air flow rate between the top foil and bearing housing. Several slots, see Fig. 4, in the center housing ID allow cooling air to pass underneath the bump strip layers.

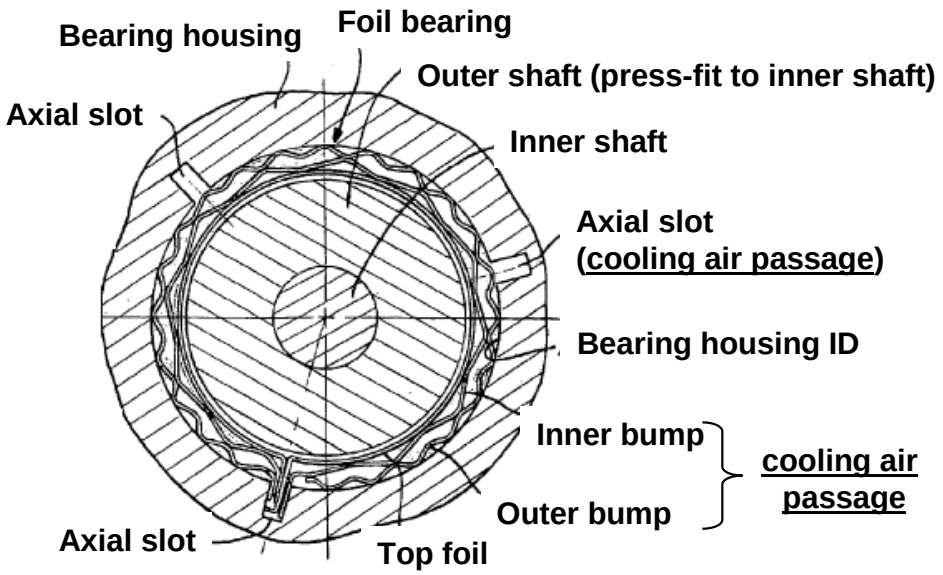

Fig. 4 Schematic view of radial foil bearing and its housing in an oil-free turbocharger. Reproduced from [29].

Lubell and Weissert [30] patent a rotor-bearing system integrating a sound thermal management strategy for oil-free gas turbines. A single gas foil bearing, named as first bearing, is located between a turbine and a compressor. The area between the compressor and the turbine generally experiences a higher temperature and larger load and stress as compared to the other portions of the rotor since it is close to the combustion chamber. Another gas foil bearing marked as the second bearing, is positioned far away from this area, opposite to the rotor turbine end. This configuration minimizes the cooling requirement for the second FB. A reduced rotor span between the compressor and turbine increases the gas flow from the compressor into the “first” GFB, thereby significantly decreasing the bearing operating temperature. Air bled from the

compressor flows through the gap underneath the top foil, as well as inside the hollow rotor. This later flow remarkably decreases rotor temperature. A combination of carefully managed rotor and bearing bleed flows ensures adequate thermal management in the high temperature rotor-GFB system. Note that this rotor-bearing layout and cooling scheme is successfully applied in a commercial oil-free microturbine [31].

Except recent efforts at the author's laboratory [14], there is no open literature which fully details the geometry and materials of test foil bearings, and test conditions including cooling air flow rates and temperatures. San Andrés *et al.* [14] present measurements of bearing temperatures and rotor dynamic motions obtained in a hollow rotor supported on 2nd generation GFBs. The test rotor surface is heated up to 157ºC using an electric cartridge heater that is inserted loosely in a hollow rotor. The rotor weighs 1.065 kg and has 38.07 mm OD at the bearing locations. The extensive test results show that forced cooling flow has a limited effectiveness for operation at low shaft temperature conditions.

CHAPTER III

DESCRIPTION OF TEST ROTOR-BEARING SYSTEM AND INSTRUMENTATION

3.1 Test Rig

Figure 5 depicts photographs of the high temperature GFB rotordynamic test rig and its components. A solid AISI 4140 steel holds two test foil bearings and contains an enclosure to supply air with feed pressures for cooling the bearings when needed.

The hollow rotor (Inconel 718[3]) weighs 1.360 kg (13.33 N) and is 200.66 mm long; its outer (D_o) and inner diameter (D_i) equaling 36.51 mm and 17.9 mm, respectively (D_i/D_o) = 0.49 (at ambient temperature). At each rotor end face, eight equally spaced threaded holes, 13 mm deep, at a radius of 15.5 mm serve to add known (im)balance masses.

The rotor OD (outer diameter) surface is coated with a proprietary solid lubricant designed for high temperature operation (up to 400ºC) [32]. The axial length of the coated portion is 50 mm. The rotor OD has a 0.25 mm deep undercut at the locations of bearing placement to allow for deposition of the solid lubricant. The rotor pre-test surface root mean square roughness (R_{RMS}) at the bearing locations is 0.22 μm (manufacture provided)[4].

[3] Appendix A lists the material properties of Inconel 718.

[4] This roughness is much finer than the typical surface roughness of PS304 coating [33], a NASA-developed high temperature composite coating. Plasma-sprayed PS304 coatings are generally limited to $R_{RMS} > 0.25$ μm, with $R_{RMS} = 0.8$ μm typical after grinding and polishing [34].

The center of mass of the rotor is 105.8 mm away from the rotor free end. The fractions of rotor weight acting on the drive end (DE) bearing and free end (FE) bearing equal 7.39 N and 5.94 N, respectively. Two pairs of eddy current sensors facing the rotor ends record the dynamic displacements of the rotor along the vertical and horizontal axes.

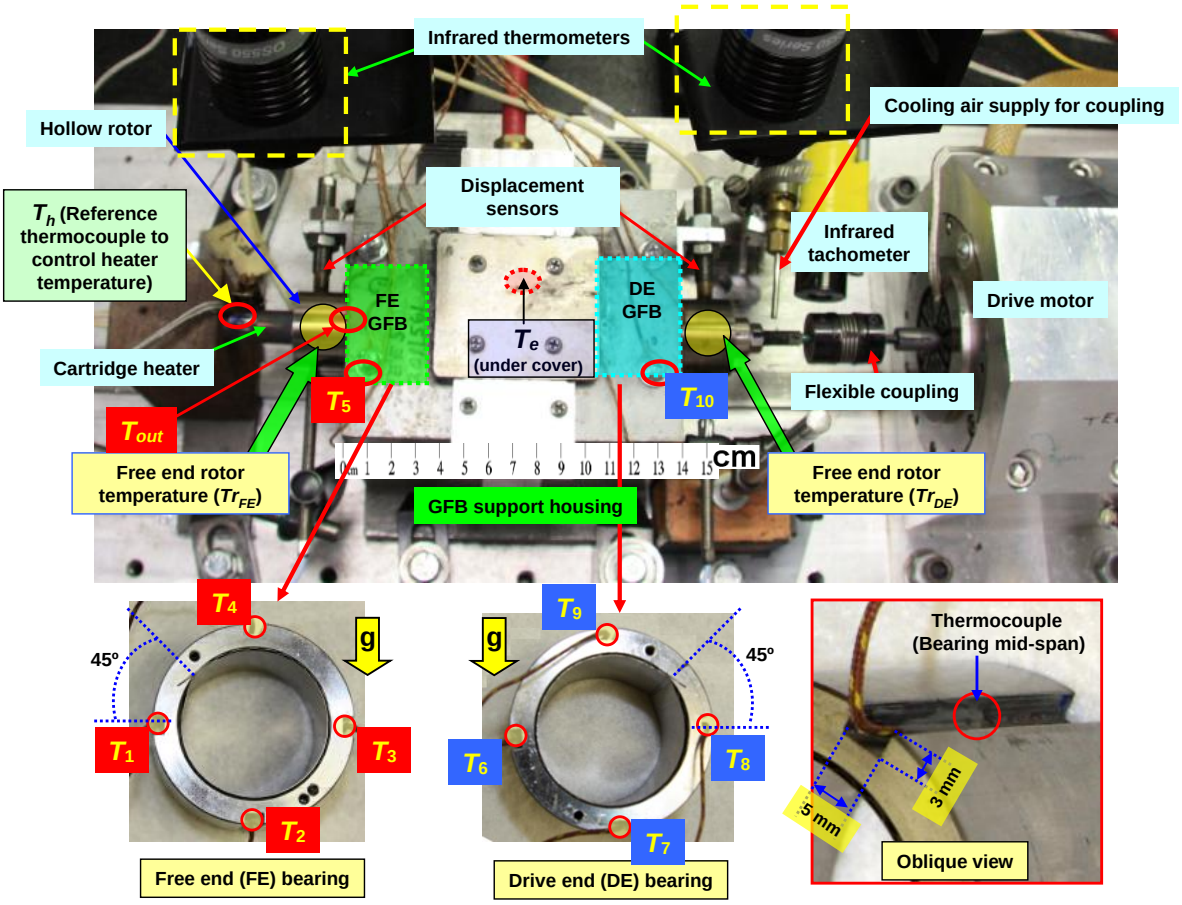

Fig. 5 Photographs of high temperature GFB rotordynamic test rig. T_1 – T_{10}, T_h, T_{out}, and T_e represent locations of temperature measurement. A bearing sleeve with an axial slot to route a thermocouple installed at the bearing mid-span also shown (oblique view).

An electric cartridge heater, 15.875 mm in diameter, fits loosely inside the hollow rotor, see Fig. 6. The heater is rated at 1.6 kW when supplied with 240 VAC. Symbols T_1−T_{10}, T_h, T_e, T_{out}, Tr_{DE}, and Tr_{FE} denote the locations for temperature measurements.

Four axial slots, depth=3 mm and 90º apart, are machined on the outer surface of the bearings. These grooves serve to route type-K thermocouples, each affixed with cold-weld compound onto the bearing OD at its middle axial plane; see Fig. 5. T_1−T_4 denote thermocouples on the FE bearing. Similarly, T_6−T_9 denote thermocouples affixed to the OD of the DE FB sleeve.

Figure 6 illustrates a schematic view (not to scale) for the dimensions of the test rotor, the cartridge heater, the housing and its air feed enclosure. Figures 5 and 6 depict the location of the thermocouple T_h serving as a reference to control the electric heater circuit. Prior work, see Ref. [14], demonstrated that the heater warms unevenly the test rotor, with distinct axial and circumferential temperature gradients [14]. Clearly, the rotor (drive) end on the other side of the cartridge heater and next to the coupling is coldest.

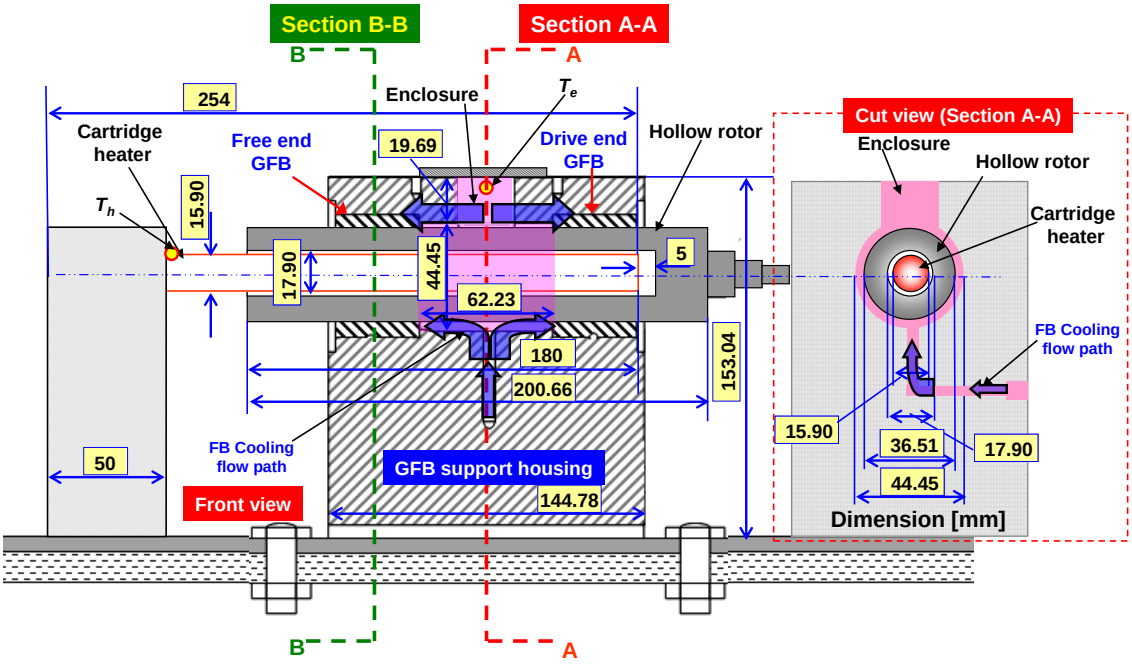

Fig. 6 Schematic view (not to scale) for dimensions (mm) of test rotor, cartridge heater, bearing support housing air feed enclosure. Noted locations of thermocouples for feed enclosure air temperature (T_e) and reference to control heater set temperature (T_{hs}).

Figure 7 shows the bearing support housing with dimensions of thickness around the test bearings. The bearing housing is 16.51 mm and 85.73 mm thick at its thinnest and thickest locations, respectively.

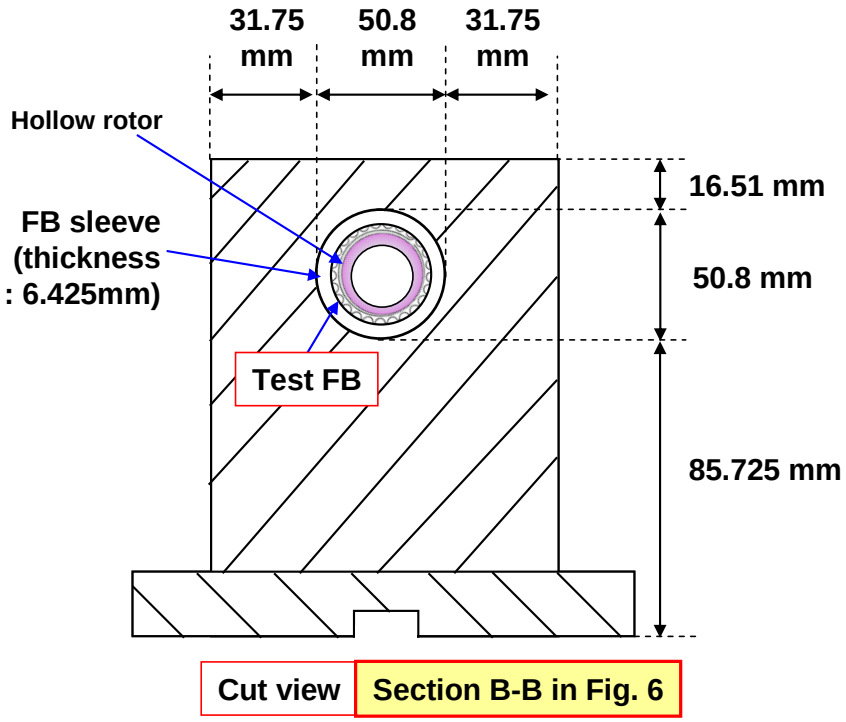

Fig. 7 Cut view (not to scale) of section B-B in Fig. 6 of bearing support housing with dimensions of wall thickness around test bearing. Material of bearing support housing and bearing sleeve: AISI 4140.

The drive motor (induction type with two electromagnetic poles), 9.5 kW at its maximum operating speed of 65 krpm, is rated with a 85 N-cm torque at 6 krpm. A flexible coupling (35 mm in length, 25 mm in outer diameter, and 5.08 mm inner diameter) connects the rotor to a drive motor through an Inconel 718 slender rod (14.2 mm in length and 5.1 mm in diameter). The coupling rated (maximum service) torque and torsional stiffness are 2.0 N-m and 1200 N-m/rad, respectively. The maximum operating temperature of the inexpensive coupling is 120°C. Hence, during the tests, a stream of shop air (1.36 bar gauge and 21ºC) cools the flexible coupling.

Two infrared thermometers record the rotor OD surface temperatures at the drive and free ends, hereby denoted as Tr_{DE} and Tr_{FE}. The sensor has an adjustable emissivity setting. The distance-to-spot ratio (the ratio of the distance to the object and the diameter of the temperature measurement area) is 68:1 [35]. Presently, the sensor head locates 150 mm above the rotor surface. Hence, the displayed temperature averages the temperature over a 17 mm diameter area, refer to Fig. 8. A laser sighting device, installed in front of the sensor head, aids to focus the infrared spot from the sensor head on the rotor surface to be measured.

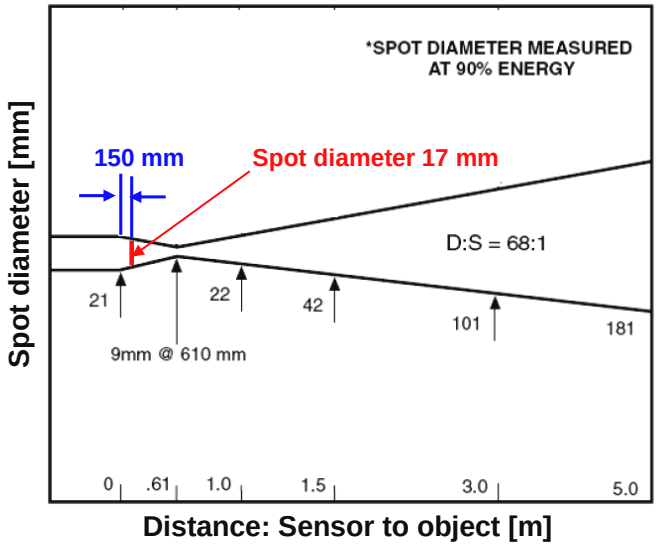

Fig. 8 Distance-to-spot ratio of infrared thermometer [35].

Figure 9 shows a photograph of the air feed enclosure at the mid plane of the bearings' housing (cover removed) with thermocouple T_e that measures the gas temperature inside the enclosure, and thermocouples T_5 and T_{10} recording temperatures

on the outer surface of the thick housing. A thermocouple T_{out}, 1.5 mm (±0.25mm) above the rotor FE surface, measures the exhaust air temperature released into the ambient air from the FE test bearing, see Fig. 10.

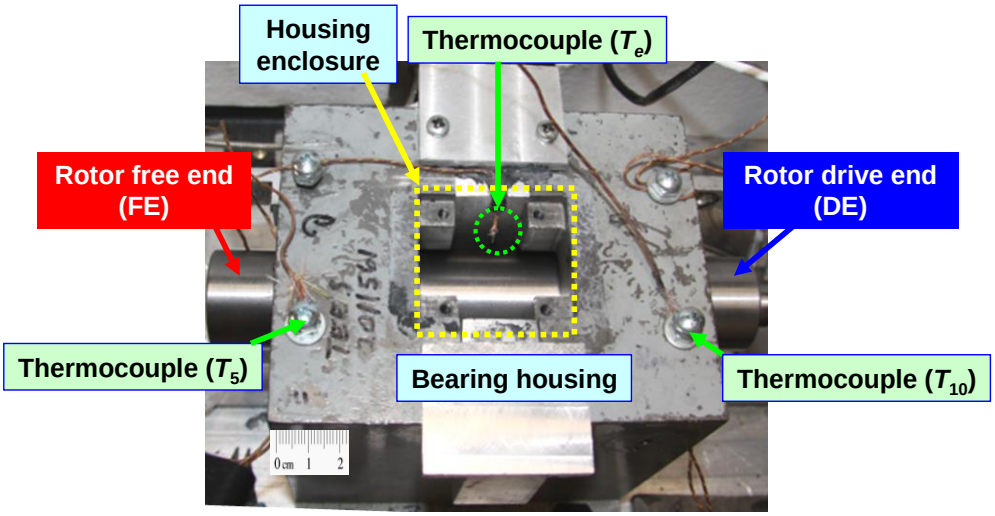

Fig. 9 Air feed enclosure at mid plane of bearing housing (cover removed for photograph) and locations of thermocouples (T_e, T_5 and T_{10}).

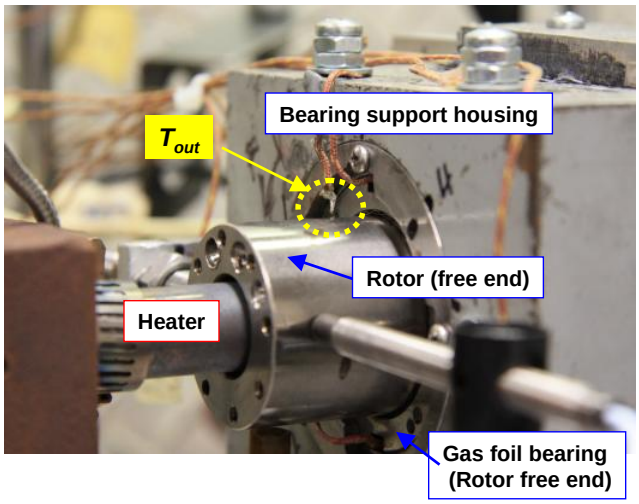

Fig. 10 Location of thermocouple T_{out} to record bearing exhaust air temperature.

Figure 11 depicts a layout of the supply air system into the test rig, the instrumentations, and the data acquisition system. Pressure gauge monitors the air supply pressure into the test bearings. A manually operated pressure regulator in the main shop air line serves to adjust the supply pressure (flow rate) into the bearings. The supplied air enters at one axial end of each test bearing, flows through the gas film region and underneath of the top foil, and exits through the other bearing end at ambient pressure, see the blue color arrows in Fig. 10. A gas flow meter[5], max. 500 L/min, records cooling airflow rates into both foil bearings. A thermocouple T_{in} records the supply air temperature well upstream to the test rig.

The instruments displaying temperature digitally have uncertainties of 0.6ºC and 1.7ºC for the thermocouples and infrared sensor, respectively. Temperatures are read visually and recorded manually while commercial DAQ systems (*Bentley Nevada ADRE® for Windows* and *LabVIEW®*) record and save the rotor vibration test data while the rotor spins. An infrared tachometer serves as a keyphasor signal for data acquisition. Rotor displacement voltage signals from the displacement sensors are routed through a signal conditioner to bias their DC offset levels. Two analog oscilloscopes display the unfiltered real time rotor orbits recorded at the free and drive ends of the rotor. A two-channel dynamic signal analyzer displays the frequency content of selected motion signals.

[5] The flowmeter is calibrated by the manufacturer at 1 atmosphere and 21ºC. The uncertainty in the measured flow is ±1.5% of the full scale range (500 L/min).

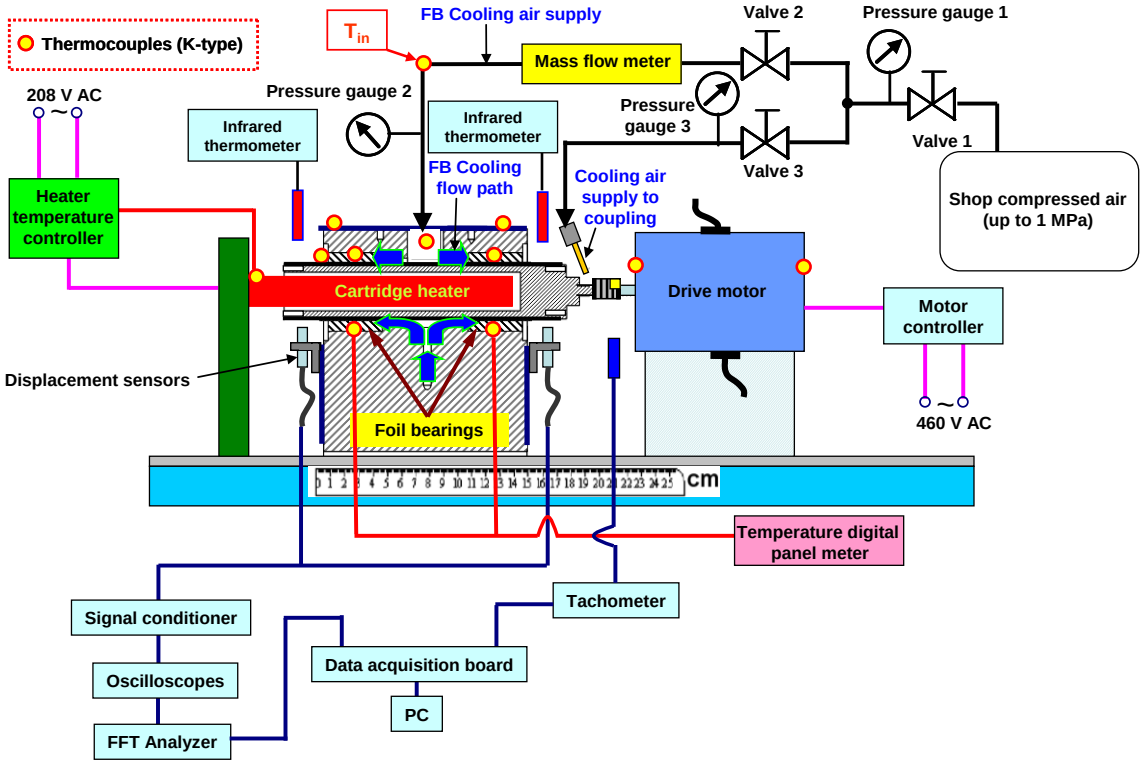

Fig. 11 Schematic view (not to scale) of cooling air supply system, instrumentation, and data acquisition system of high temperature gas foil bearing test rig. Flow path of force cooling air also shown.

During rotor speed up and down conditions, *ADRE*® and *LabVIEW*® collect rotor displacements at Δrpm = 50 rpm and 1,000 rpm intervals, respectively. When the rotor operates at a constant speed (10, 20, and 30 krpm), *ADRE*® stores data at Δ_{time}=10 s intervals. The sampling size and rate for *ADRE*® are 512 (2^9) and 64 (2^6) samples/revolution, respectively. The (user-defined) sampling size and rate for *LabVIEW*® are 2,048 (2^{11}) and 10,000 samples/s, respectively.

Appendix B lists technical specifications of the equipment and instrumentation for the high temperature rotor-GFB test rig.

3.2 Dimensions of Test Bearings and Estimation of Bearing Clearances

Table 1 lists measured dimensions of both test foil bearings and the rotor[6]. The bump pitch, length, height, arch radius, and arch angle are estimated from the zoomed photograph in Fig. 12. A foil bearing, 1st generation type, has a single arcuate Inconel X-750[7] top foil and a single bump strip layer (no axial splits). The top foils are bare, i.e., without any coating. The ends of the bump strip and top foil are inserted into a thin slot in the bearing cartridge, while the other ends are free [36]. Upon installation of both bearings, the orientation of the top foil trailing edge with respect to the vertical (gravity) plane is 45º.

[6] KIST designed and constructed the test foil bearings and rotor. KIST donated the components for the current research.
[7] Appendix A shows the material properties of Inconel X-750.

Table 1. Geometry of test hollow rotor and gas foil bearings (Unit: mm)

Rotor	
Outer diameter, $2R_O$	$36.51^{(1)*}$
Inner diameter, $2R_I$	$17.9^{(1)*}$
Material	Inconel 718 (KIST proprietary solid lubricant coated)
Bearings	
Sleeve outer diameter, D_O	$50.8^{(1)*}$
Sleeve wall thickness, t_B	$6.425^{(1)*}$
Sleeve inner diameter, $D_I = D_O - 2\ t_B$	37.95^{**}
Sleeve axial length, L_O	$38.1^{(1)*}$
Sleeve material	AISI 4140
Top foil axial length, L	$38.1^{(1)*}$
Top foil thickness, t_T	$0.12^{(1)*}$ (bare surface)
Bump foil thickness, t_B	$0.12^{(1)*}$
Number of Bumps, N_B	26 × 1 axial
Bump pitch, s_0	$4.4^{(2)***}$
Bump length, l_B	$2.5^{(2)***}$
Bump height, h_B	$0.50^{(2)***}$
Bump arc radius, r_B	$2.25^{(2)***}$
Bump arc angle, α_B (deg)	$67^{(3)***}$
Top foil inner diameter, $D_T = D_I - 2(t_T + h_B)$	36.71^{**}
Foil material	Inconel X-750
Radial (assembly) clearance, $C_r = ½\ (D_T - D_S)$	0.10^{**}

Bearing mass (sleeve + bump foil + top foil): 0.25 kg

Uncertainty: (1) ±0.005 mm, (2) ±0.013 mm, (3) ± 5º

* Measured value using digital vernier caliper

** Calculated from other measured or estimated dimensions

*** Estimated from zoomed photograph in Fig. 12

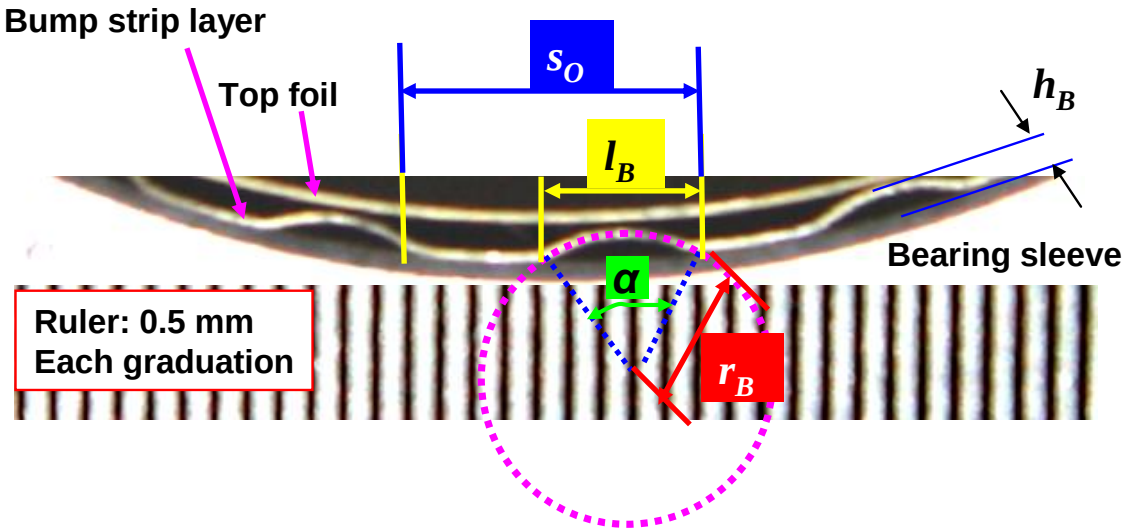

Fig. 12 Zoomed photograph of test bearing to estimate its geometry.

A series of static load versus FB deflection measurements serves to estimate the bearing radial clearance (at room temperature). Figure 13 shows the schematic view of the simple test setup and procedure to apply static loads into the test bearings resting on its rotor. During the static load tests, the test bearing is tightly fitted into a thick steel (AISI4140) bearing housing[8]. The thickness and mass of the bearing housing are 11.57 and 0.670 kg, respectively. The orientation of the top foil trailing edge with respect to the vertical (gravity) plane is 45º.

To minimize the shaft elastic deflection under static loads, both ends of the shaft are secured to the lathe. A lathe tool holder displaces manually to deliver a static load on the bearing. A strain gauge load cell (uncertainty 0.45 N) is affixed to the lathe tool

[8] The *thick* bearing housing aids to avoid undesirable deformation of the *thin* bearing sleeve due to the imposed static loads.

holder and connected to the test bearing outer housing. Moving the lathe tool holder forward and backward provides push and pull forces onto the test bearing, respectively. An eddy current displacement sensor (uncertainty: 0.104 V/mm) facing the bearing OD measures the displacements of the test bearing. Measured shaft displacements are subtracted from the corresponding bearing displacements to obtain the actual bearing bump deflection.

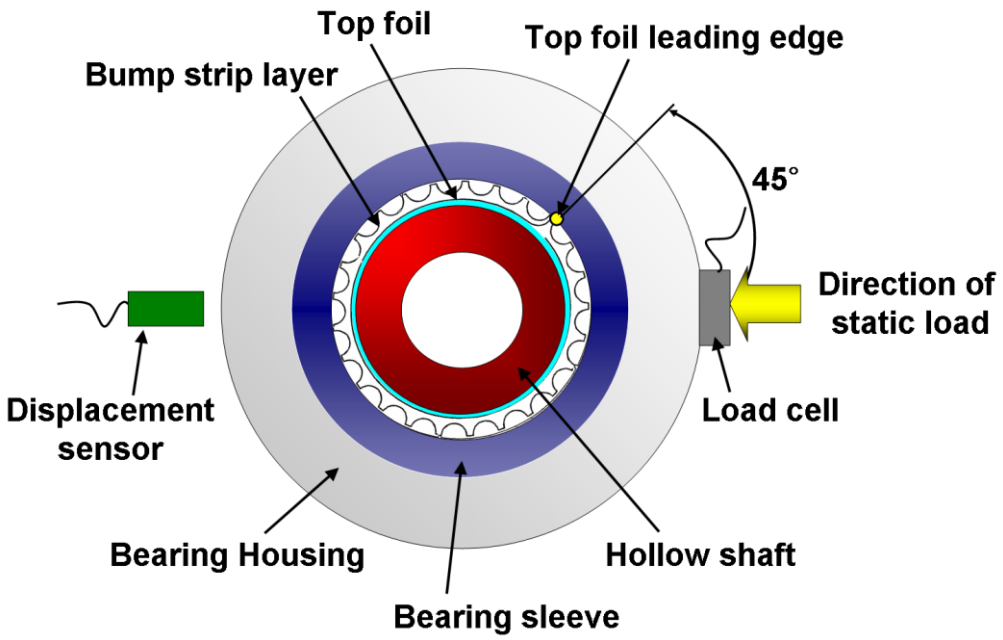

Fig. 13 Schematic view (not to scale) of test setup for static load and FB structural deflection test. Static load 45° away from top foil trailing edge.

Figure 14 depicts the measured FB deflection versus applied static load for the free end (FE) and drive end (DE) bearings. The bearing forced deflection is highly nonlinear during consecutive loading-unloading cycle with a distinctive hysteresis loop

showing dissipated mechanical energy. Note that once the bumps are active due to the applied static loads, the increase in bearing displacements for the FE bearing is more significant than the DE bearing[9]. The "ad-hoc" radial clearance (i.e., *radial play* or *sway space*), defined as in Ref. [20], for both bearings is ~100 μm. The agreement of "ad-hoc" clearance to the clearance derived from the bearing geometry is remarkable, see Table 1.

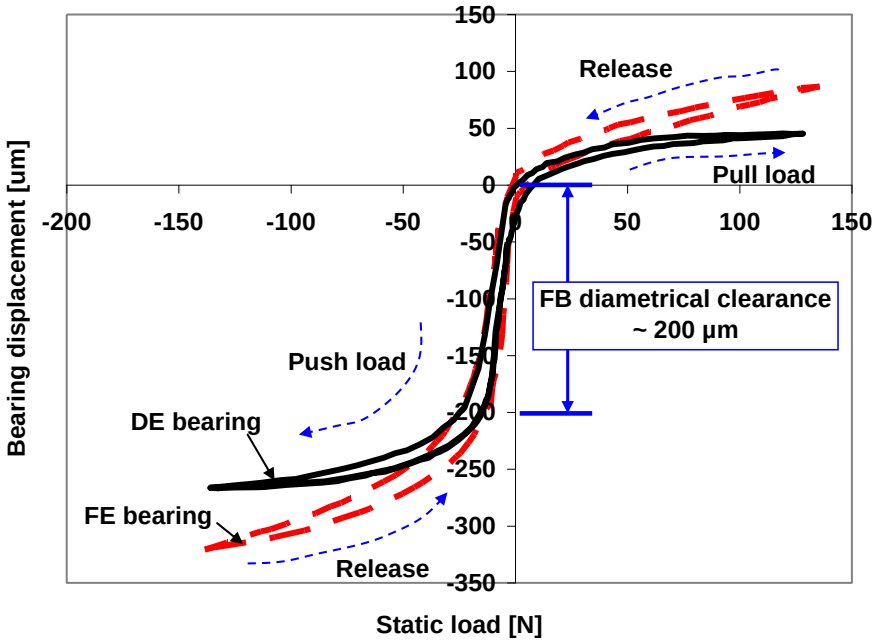

Fig. 14 Recorded foil bearing deflections (drive and free ends) versus static load for estimation of diametrical clearance.

A polynomial curve fit over the span of applied loads establishes an analytical relation between the static load (F_{FB_s}) and the FB deflection *(r)*; i.e.,

[9] Inaccurate manufacturing of support structure, i.e., bump foils, may result in different structural stiffnesses between two test bearings.

$F_{FB_s} = F_0 + K_1 r + K_2 r^2 + K_3 r^3 + K_4 r^4 + K_5 r^5$ [37]. Therefore, the FB structural stiffness is the first spatial derivative of the curve fit, i.e., $K_s = \partial F_{FB_s} / \partial r$ $= K_1 + 2K_2 r + 3K_3 r^2 + 4K_4 r^3 + 5K_5 r^4$.

Figure 15 depicts the identified FB static structural stiffness. The FB stiffness shows a typical hardening effect as the bearing deflection increases. The structural stiffness of the DE bearing increases more rapidly than the FE bearing as the FB deflection increases. Figure 16 depicting the FB stiffness (K_s) versus applied static load shows a strong load dependency.

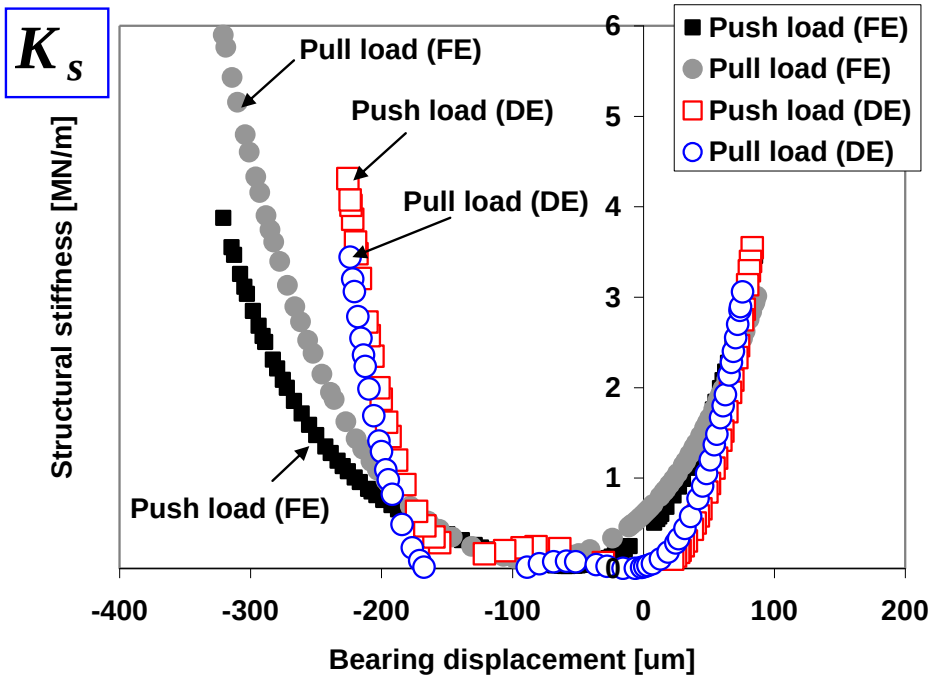

Fig. 15 Identified FB structural stiffness versus bearing displacement. DE: Drive end bearing, FE: Free end bearing.

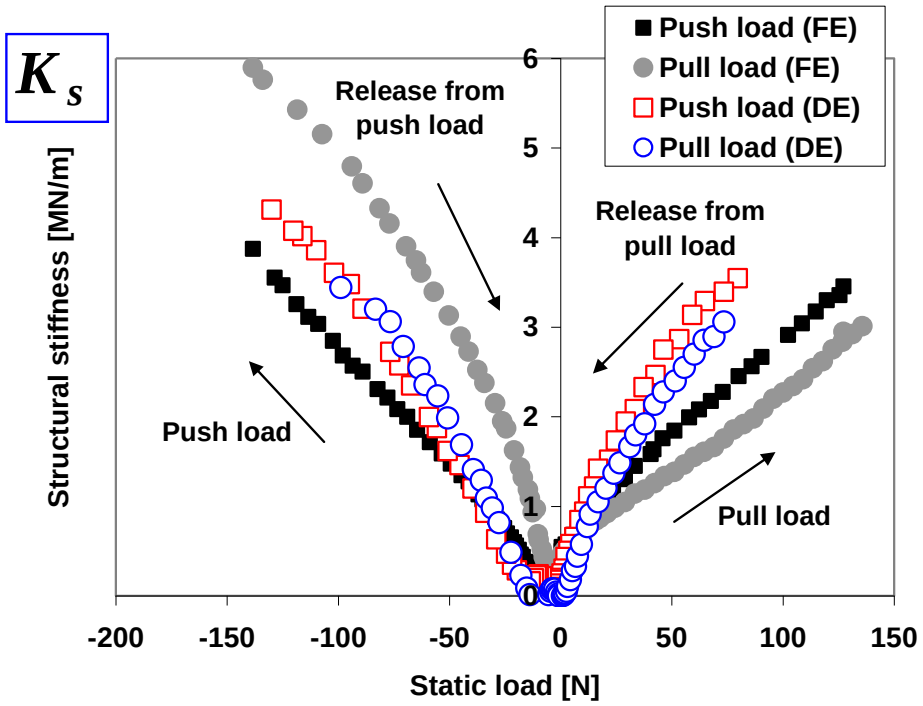

Fig. 16 Identified FB structural stiffness versus static load. DE: Drive end bearing, FE: Free end bearing.

From the mechanical hysteresis loop in Fig. 14, the FB structural loss factor estimated from $\gamma = \frac{1}{\pi K_s r^2} \oint F_{FB_s} dr$, where K_s is a local (average) stiffness coefficient[10], is ~0.20 for the test bearings [38]. Recall that the static load-FB deflection measurements substantially decrease the time and cost in evaluating the mechanical energy dissipation characteristic of bump-type foil bearings [39].

[10] The stiffness of the FB structure (K_s) derived from positive displacements in the hysteresis loop in Fig. 14 is approximately 2.2 MN/m, see Figs. 15 and 16.

CHAPTER IV

EXPERIMENTAL PROCEDURE

Table 2 presents the matrix of operating conditions for tests with increasing rotor speeds (no rotor spinning, 10 krpm, 20 krpm, and 30 krpm) and heater set temperatures (T_{hs}= 65 ºC, 100 ºC, and 150 ºC). Test cases #1−#3 and #4−#6 represent conditions without and with rotor spinning, respectively. In the non-rotating shaft experiments (test cases #1−#3), a forced axial cooling flow rate into the test bearings decreases from ~420 L/min to 0 L/min. While the rotor is spinning (test cases #4−#10), the weakest forced gas stream into the bearings is ~50 L/min. This is because even small quantities of air are effective to promote the evacuation of hot air from the bearing[11]. In each test case, the heater set (reference) temperature T_{hs} is kept constant as listed in the Table.

For test cases #1−#3, while the rotor is not spinning, at T_{hs}= 65 ºC, 100 ºC, and 150 ºC, the cooling flow rate into the bearings is decreased after 20−30 minute intervals once a thermal steady state is achieved. In test cases #4−#6, the test system component temperatures are recorded while the rotor speed is set at 10, 20 and finally 30 krpm. The cooling flow rate into the test bearings is decreased in a similar fashion as in test cases #1−#3. The flow rates quoted distribute into both test bearings.

During each experiment, the ambient temperature T_{amb}, recorded away from the test rig, increases little, from 22ºC at the beginning of the tests (heater off) to a

[11] The qualitative assessment for GFB system thermal management requires considerable experience; thermal runaway could occur when very low or no cooling flow is supplied.

maximum of 28ºC when the heater set temperature T_{hs}=150 ºC. This is because the safety cover of the test rig was not in place during the measurements.

Table 2. Test cases for three heater set temperatures (T_{hs}) and four cooling flow rate conditions

Test case #	Heater set temperature [ºC]	Rotor speed [krpm]	Set cooling flow rate[12] (into two bearings) [L/min]	Time [min]
1	65	0	350 → 250 → 150 → 50 → 0	87
2	100	0	350 → 250 → 150 → 50 → 0	84
3	150	0	350 → 250 → 150 → 50 → 0	108
4	65	10→ 20 → 30	350 → 250 → 150 → 50	248
5	100	10→ 20 → 30	350 → 250 → 150 → 50	266
6	150	10	350 → 250 → 150 → 50	136
7	Off	30	350	30
8	65	30	350	30
9	100	30	350	30
10	100	30	50	30
				Overall 1049 min

[12] In the experiments, the operator sets the cooling flow rate at 350 L/min, 250 L/min, 150 L/min, and 50 L/min. However, as shown in Figs. 18 and 19 later, the cooling flow rate into the test bearings is not constant, i.e., it varies with time elapsed. Due to the limited compressed air reservoir (tank) capacity, cooling gas flow from the shop compressed air line provides fluctuating air flow rates.

Table 2 also shows the time elapsed for each test case. The temperatures are carefully recorded until reaching a thermal equilibrium state. Recall that the sides of the safety cover remain open to reduce the operating time for thermal equilibrium condition of the test system and to minimize thermal damage of the instrumentation[13] and drive motor.

The procedure for the current experiments is to

1) Affix the motor support housing on the rig base plate.

2) Install the drive motor.

3) Clean the bearing support housing inner surfaces in contact with the bearing sleeve OD.

4) Insert the test bearings into the rig housing. The bearings must be installed into the rig housing without any perceptible play or looseness. For each bearing, a stainless steel shim, ~350º in circumferential extent with 25.4 μm thickness, is inserted between the bearing sleeve OD and rig housing ID. Light pressure, manually applied, is required to assemble mating parts. This interference fit corresponds with *FN*1 *light drive fit* defined in AISI Standard B4.1 [40]. The side caps pushing on the bearing sides assure the tight assembly of the bearings into the rig housing.

5) Insert the rotor into its bearings.

6) Align the rotor with respect to the motor shaft by inserting metal shims underneath the bearing support housing.

[13] Maximum operating temperature of the infrared thermometer sensor head is 50ºC.

7) Affix the bearing support housing on the rig base plate.

8) Connect the rotor and the drive motor through a flexible coupling.

9) Install the eddy-current displacement sensors to measure shaft displacements.

10) Check the clearance of each bearing through an oscilloscope by manually rotating the test rotor. The clearances between the free end (FE) and drive end (DE) bearings must be similar.

11) Insert the cartridge heater into the hollow test rotor and affix it to the rig base plate.

12) Affix the steel tube, for cooling of the flexible coupling, on the rig base plate.

13) Install infrared thermometers to measure the shaft surface temperature. Focus the infrared spot of the sensor head on the shaft surfaces using a laser sighting device.

14) Install a tachometer and focus its infrared spot on a reflective tape affixed at the coupling surface.

15) Verify proper connections, conditioning, and gains from displacement sensors keyphasor input to the data acquisition systems.

16) Open air valve (1) fully to supply forced cooling air into the test bearings and the coupling. Regulate air supply valve (3) at pressure of 1.36 bar (20 psig) for cooling of the flexible coupling. Then, regulate air valve (2) to set the cooling mass flow rate into the bearings. See Fig. 10 for locations of air valves (1) through (3).

17) Turn the heater controller on and set the heater reference temperature.

18) Prepare the configuration of data acquisition system, and start recording the rotor response.

19) Turn motor controller power on and operate the motor. Presently, the motor pre-set ramp rate (both acceleration and deceleration) is 16.7 Hz/s.

20) Record manually temperatures of the test system components at 3−4 minute intervals.

During the experiments with test case #6, the rotor speed was increased to 20 krpm after 136 minutes of elapsed operation time. Then, the operator heard a noise, akin to that of rubbing of parts. Thus, the operator immediately turned off the drive motor as well the cartridge heater to avoid permanent damage of the test bearings[14]. The operator removed the rotor from its bearings and inspected both rotor and bearings. There was no evidence of damage of the test bearings. Then, the rotor was reinserted into the bearings for further rotordynamic experiments.

After completion of the extensive experiments with test cases #1 through #6, rotor speed-down tests were conducted. Recall that the drive motor is controlled to speed down the rotor with a constant ramp rate of 16.7 Hz/s; therefore, the rotor is not coasting down. The power to the cartridge heater is turned off after the rotor has fully rested on its bearings. In all tests, only baseline rotor motions are measured (no added imbalance masses).

[14] Note that the maximum test temperature is not limited by the heater capability.

CHAPTER V

EXPERIMENTAL RESULTS: TEMPERATURE MEASUREMENTS

5.1 Temperature Rise of System Components versus Elapsed Time

Measurements without rotor spinning

While the heater set (reference) temperature T_{hs} is fixed at 150 ºC with a stationary (non-rotating) shaft, Fig. 17 depicts temperature rises (T_i -T_{amb}) where $_{i=}r_{FE,}$ $r_{DE,\ 1-10,\ in,\ e,\ out}$) of the test system components versus elapsed time. The measurements correspond to test case #3. See Figs. 5, 6, 9 and 10 for the thermocouples designation and location.

As seen in Fig.17, the temperature of each test component increases steadily with elapsed test time. Recall that the cartridge heat does not flow uniformly along the heater axial length; and hence a distinctive thermal gradient is evident[15]. The tests reproduce similar conditions as in a bearing supporting the hot end of a micro gas turbine, for example [41]. As expected, the temperatures at the rotor OD are much higher than those for the other system components. Note that T_{in}, the supply air temperature, is constant (T_{in}=T_{amb}+~2ºC). T_{out}[16], the exhaust air temperature released into the ambient air from the free end bearing (see Fig. 10), follows a similar trend as the enclosure temperature (T_e) but with a smaller magnitude, i.e., (T_{out}-T_{amb})=1ºC→9ºC and (T_e-T_{amb})=1ºC→23ºC for cooling rates ranging from 350 L/min to 50 L/min. Note $T_e > T_{out} > T_{in}$.

---

[15] Recall that the heater temperature controller sets the heater surface temperature at one location (Fig. 5).

[16] Thermocouple T_{out} locates at 1.5 mm (±0.25mm) above the rotor FE surface and 8mm (±0.5mm) away from the outboard plane of the FE bearing top foil. Therefore, the recorded temperature does not fully represent the exhaust air temperature leaving the free end bearing.

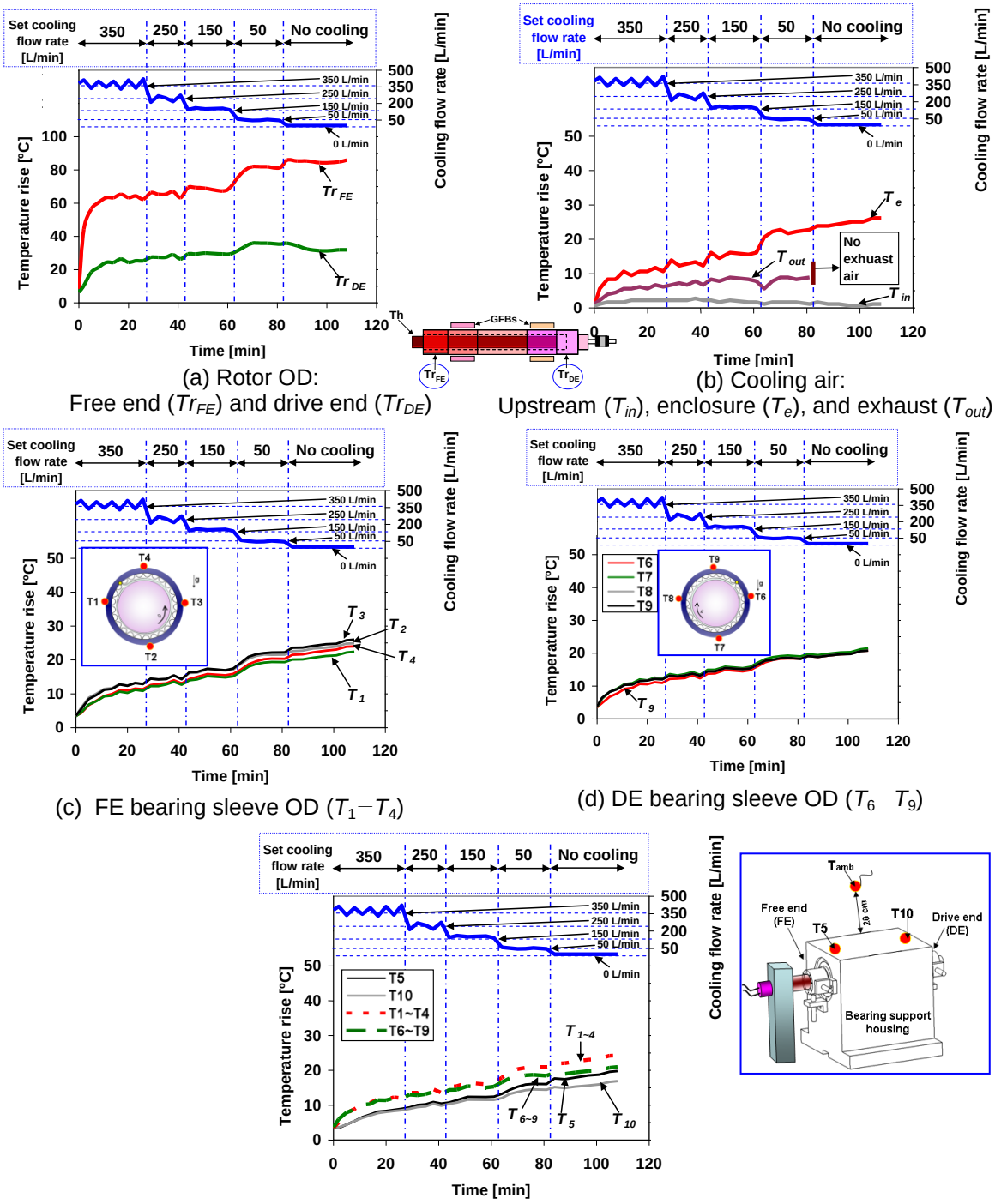

(a) Rotor OD: Free end (Tr_{FE}) and drive end (Tr_{DE})

(b) Cooling air: Upstream (T_{in}), enclosure (T_e), and exhaust (T_{out})

(c) FE bearing sleeve OD (T_1−T_4)

(d) DE bearing sleeve OD (T_6−T_9)

(e) Bearing housing surface (T_5 and T_{10}) and bearing mean temperature (FE: T_{1-4}, DE: T_{6-9})

Fig. 17 Test case #3. Heater set temperature at 150ºC. No rotor spinning: Recorded test system component temperature rises (T_i-T_{amb}; where $_{i\ =\ r_{FE},\ r_{DE},\ 1-10,\ in,\ e,\ out}$) versus elapsed time. Axial cooling flow into bearings decreases from 420 to 0 L/min. Note different vertical scales.

Recall that T_1-T_4 and T_6-T_9 are the temperatures measured at the OD of the bearing sleeve mid-plane[17], see Fig. 5. As shown in Fig. 17 (c), the temperature rises are different depending on the bearing OD circumferential location ($T_3>T_2>T_4>T_1$), even without rotor spinning. The small differences in these four temperatures in the bearings are attributed to the differences in the rotor surface temperature along its circumference, see Ref. [14]. On the other hand, $T_6 \approx T_7 \approx T_8 \approx T_9$ for the (rotor) drive end bearing, see Fig. 17 (d).

In Fig. 17 (e), T_{1-4} and T_{6-9} represent the arithmetic mean from the four measurements around the bearing circumference. Details on the standard deviation for the four measurements follow later (Section 5.4).

T_5 and T_{10}, the bearing support housing surface temperatures, are lower (up to 5ºC) than the bearing sleeve temperatures, T_{1-4} and T_{6-9}. Recall that the heat input into the test rig is disposed into the ambient condition of the laboratory room.

To evaluate repeatability of the test method, three additional temperature measurement tests were conducted. As an example, Appendix C shows the recorded temperature rise of T_1, T_e, Tr_{FE} and Tr_{DE} versus the air cooling flow rate. The results demonstrate acceptable repeatability, with an average variability less than 5°C.

Appendix D presents the electric power measurements on the cartridge heater at T_{hs}=150°C with a non-rotating shaft. While the cooling flow rate decreases from ~400 L/min to ~150 L/min, the electric power to maintain T_{hs} decreases slightly with cooling

[17] The recorded bearing sleeve temperatures (T_1-T_4) and (T_6-T_9) are representative of the bearing ID temperatures. Chapter VII shows the details on predicted radial temperature profiles in the test FB.

flow rate, i.e., ~1,160 W (at ~400 L/min) → ~1,140 W (at ~150 L/min). However, when the cooling flow rate further decreases from 150 L/min to 0 L/min, the power increases from ~1,140 W to ~1,160 W.

Measurements with rotor spinning at 10 krpm

For test case #6 (T_{hs}=150ºC), Fig. 18 depicts temperature rises ($T_i - T_{amb}$) where $_i = r_{FE,}\, r_{DE,\,1-10,\,in,\,e,\,out}$) of the test system components versus elapsed test time. The cooling flow rate into the bearings decreases from ~420 L/min to ~50 L/min at ~100 L/min decrements. In Fig. 18, the trend of the temperatures' increase with time elapsed for each system component is similar as those in Fig. 17 (non-rotating shaft condition)[18]. The maximum rotor OD and bearing sleeve OD temperature rises are as high as 93ºC and 31ºC, respectively.

Figures 17 and 18 also demonstrate that the tests took enough time to reach steady state thermal conditions. Further discussion on the effects of cooling flow rate into the bearings, rotor speed, and rotor OD temperature follow later. For test cases #1, #2, #4, and #5, Appendix E shows the complete temperature data of each system component versus elapsed time. In addition, Appendix F contains the complete raw data of the recorded temperatures presented in this chapter. Appendix G presents the recorded cooling flow rate versus supply pressure for test cases #1—#6.

[18] Figure 18 (d) shows $T_7 > T_6 > T_8 > T_9$. However, the differences among four measurements are less than 2°C.

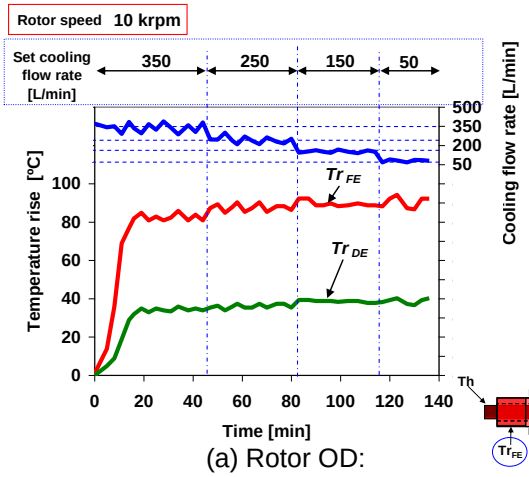

(a) Rotor OD: Free end (Tr_{FE}) and drive end (Tr_{DE})

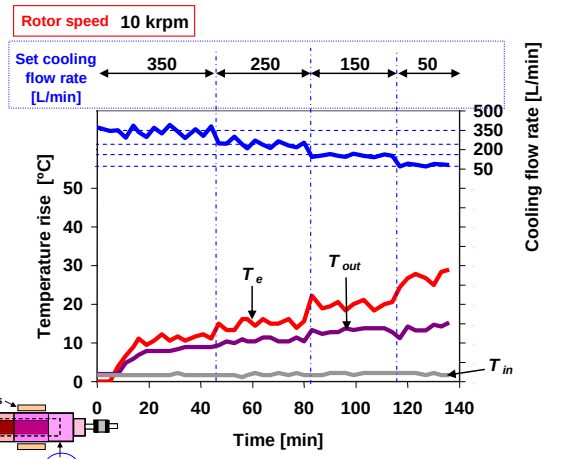

(b) Cooling air: upstream (T_{in}), enclosure (T_e), and exhaust (T_{out})

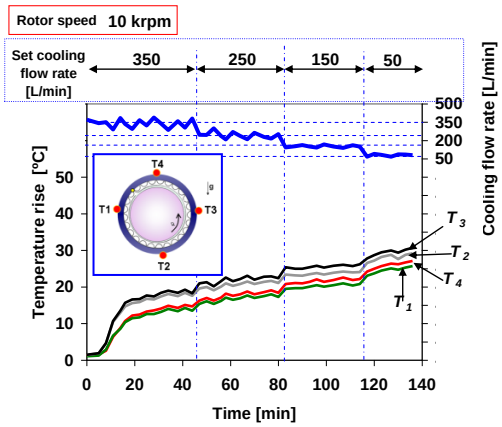

(c) FE bearing sleeve OD (T_1–T_4)

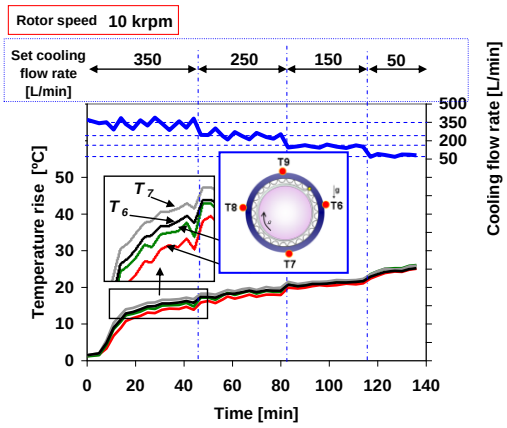

(d) DE bearing sleeve OD (T_6–T_9)

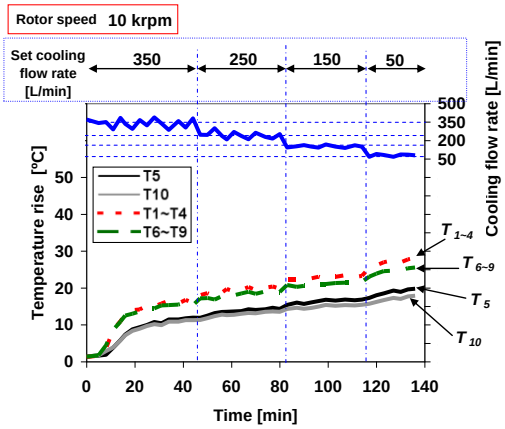

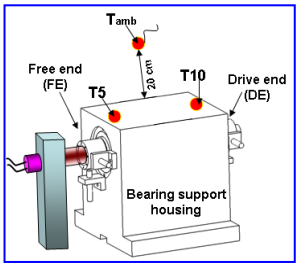

(e) Bearing housing surface (T_5 and T_{10}) and bearing mean temperature (FE: T_{1-4}, DE: T_{6-9})

Fig. 18 Test case #6, Heater set temperature at 150°C. Rotor speed of 10 krpm: Recorded test system component temperature rises (T_i-T_{amb}; where $_i$ = r_{FE}, r_{DE}, 1–10, *in*, *e*, *out*) versus elapsed time. Axial cooling flow into bearings decreases from 420 to 0 L/min. Note different vertical scales.

5.2 Rotor Surface and Bearing Sleeve Temperatures versus Cooling Flow Rate

For test case #2 (T_{hs}=100ºC and no rotor spinning), Fig. 19 depicts surface plots of temperature rises at the rotor free end ($Tr_{FE}-T_{amb}$), the free end bearing sleeve ($T_{1-4}-T_{amb}$) (arithmetic mean), the housing enclosure ($T_e - T_{amb}$), the drive end bearing sleeve ($T_{6-9}-T_{amb}$) (arithmetic mean), and the rotor drive end ($Tr_{DE}-T_{amb}$) versus shaft axial location and versus cooling air flow rate. The inset graph displays the location of the thermocouples. The figure clearly shows a pronounced temperature drop along the shaft axial length from the rotor free end (FE) toward the drive end (DE), $Tr_{FE} >> Tr_{DE}$[19]. Recall the test rotor is a heat source with its OD surface at a higher temperature than the gas film[20].

The temperatures along the rotor axial length drop quickly due to the convection of thermal energy by the forced cooling gas stream. Recall the air feeding enclosure is located at the mid-plane of the test rotor. Incidentally, recall that the rotor OD temperatures Tr_{FE} and Tr_{DE} are recorded on the outer boards of each bearing cartridge.

The mean temperatures of the FE and DE bearing sleeves are almost identical. Recall that the bearing mean temperatures T_{1-4} and T_{6-9}, derived from four measurements taken around the bearing sleeve circumference, do not have a significant standard deviation, see figures on pages 53 and 54. For each rotor speed, the system component temperatures hardly change for cooling flow rates larger than ~300 L/min.

---

[19] Presently, as shown in Appendix E, the maximum axial thermal gradient reaches up to ~55°C from the rotor FE toward its DE.

[20] When the rotor is at a lower temperature due to an inner cooling flow (i.e., the cooling stream flows through the hollow rotor to cool directly the rotor ID), thermal energy flows from the gas film to the rotor surface. For this case, a hollow rotor becomes a sink of thermal energy.

With cooling flow rates from 420 L/min to 150 L/min, the rotor and bearing temperatures steadily decrease. On the other hand, the system components temperatures suddenly increase when the cooling flow decreases from ~150 L/min to ~50 L/min. For example, Tr_{FE} increases by 20% (50ºC → 60 ºC) with cooling flow decreasing from 150 L/min to 50 L/min. The air temperature in the enclosure T_e increases linearly with rotor temperature while the air cooling flow rate decreases.

Note that the bearing temperatures follow a similar trend as the enclosure air temperature (T_e), see Figs. 20 and 21 and Appendix H. In general, T_e increases as the cooling flow rate decreases due to the longer residence of air particles inside the enclosure.

Details on the bearing housing surface temperatures T_5 and T_{10} are omitted for brevity. In general, T_5 and T_{10} show similar trends as $T_{1–4}$ and $T_{6–9}$ depicted in Fig. 19, albeit with lower magnitudes. The decrease in temperature from a bearing sleeve OD to the support housing surface is due to heat conduction and convection to ambient air surrounding the test rig.

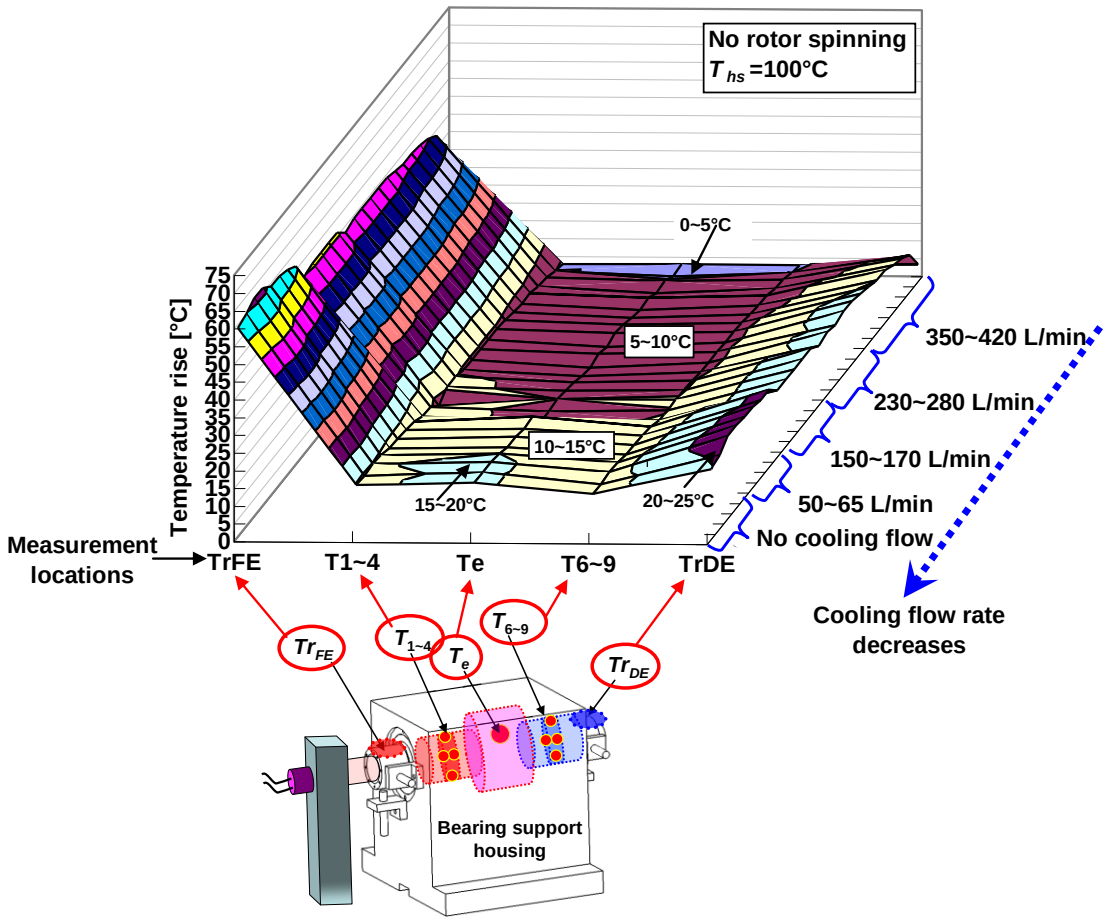

Fig. 19 Test case #2. T_{hs}=100ºC. No rotor spinning: Surface plot of temperature rises at the rotor free end (Tr_{FE} –T_{amb}), the free end bearing sleeve (T_{1-4}–T_{amb}) (arithmetic mean), the housing enclosure (T_e – T_{amb}), the drive end bearing sleeve (T_{6-9}–T_{amb}) (arithmetic mean), and the rotor drive end (Tr_{DE} –T_{amb}) versus shaft axial location and versus cooling air flow rate.

Figures 20 and 21 depict the arithmetic mean temperatures on the bearing sleeves, (T_{1-4}–T_{amb}) (FE) and (T_{6-9}–T_{amb}) (DE), versus air temperature in the enclosure (T_e – T_{amb}), respectively. The measurements correspond to test cases #2 through #5.

Appendix H shows more test data at T_{hs}=65ºC and 150ºC. In the figures, the dash line denotes a condition where the bearing temperature is identical to the enclosure air temperature. The bearing temperature linearly increases with the enclosure air temperature as the cooling flow rate into the bearings decreases. When the rotor is stationary (i.e., no rotor spinning), $(T_{1-4}\text{-}T_{amb}) \approx (T_e\text{-}T_{amb})$ and $(T_{6-9}\text{-}T_{amb}) \approx (T_e\text{-}T_{amb})$ for cooling flow rate > 100 L/min.

In general, the air temperature inside the enclosure is lower than that in the bearings sleeve OD. However, while operating at 0 and 10 krpm and with cooling flow rate less than 100 L/min, air temperatures in the enclosure are slightly higher than the bearing temperatures. For example, see Figs. 20 (a) and (b) and Figs. 21 (a) and (b). This is because, when no (or small) cooling flow is forced into the bearings, the air in the enclosure acts as a *thermal sink* since the enclosure is not open to ambient (i.e., closed, see Fig. 5). While no cooling flow is supplied into the bearings, T_e increases because of natural convection and radiation from the rotor OD. Recall that the air temperature (T_e) in the enclosure also increases as the rotor temperature rises (see Figs. 17 and 18, and Appendix E). In addition, T_e increases with rotor speed due to windage effects (added drag or fluid resistance to rotation)[21] [42,43]. It is important to note that the air temperature (T_e) in the enclosure can be also regarded as the inlet cooling stream temperature into the bearing.

[21] Windage effect occurs between two surfaces moving in relation to each other. This effect strongly depends on the rotor surface speed, rotor-stator clearance and "wetted" area, surface roughness, and fluid properties, in particular the gas pressure [44]. Presently, the windage effect inside the enclosure is not quantified.

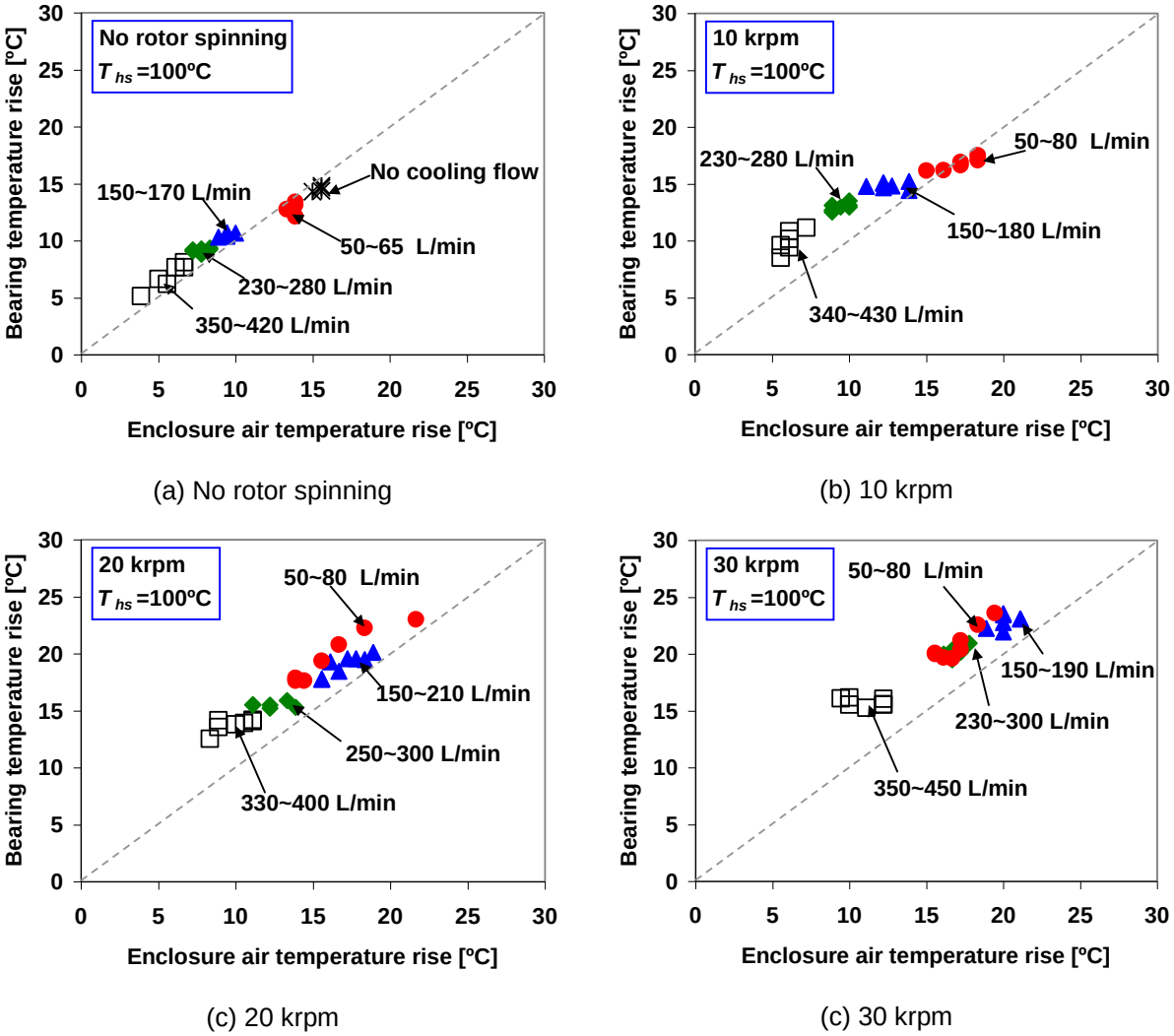

(a) No rotor spinning

(b) 10 krpm

(c) 20 krpm

(c) 30 krpm

Fig. 20 Test cases #2 and #5. T_{hs}=100ºC: Free end bearing temperature rise (T_{1-4}-T_{amb}) versus air temperature rise in the enclosure (T_e-T_{amb}). Arithmetic mean of (T_1, T_2, T_3, and T_4) shown.

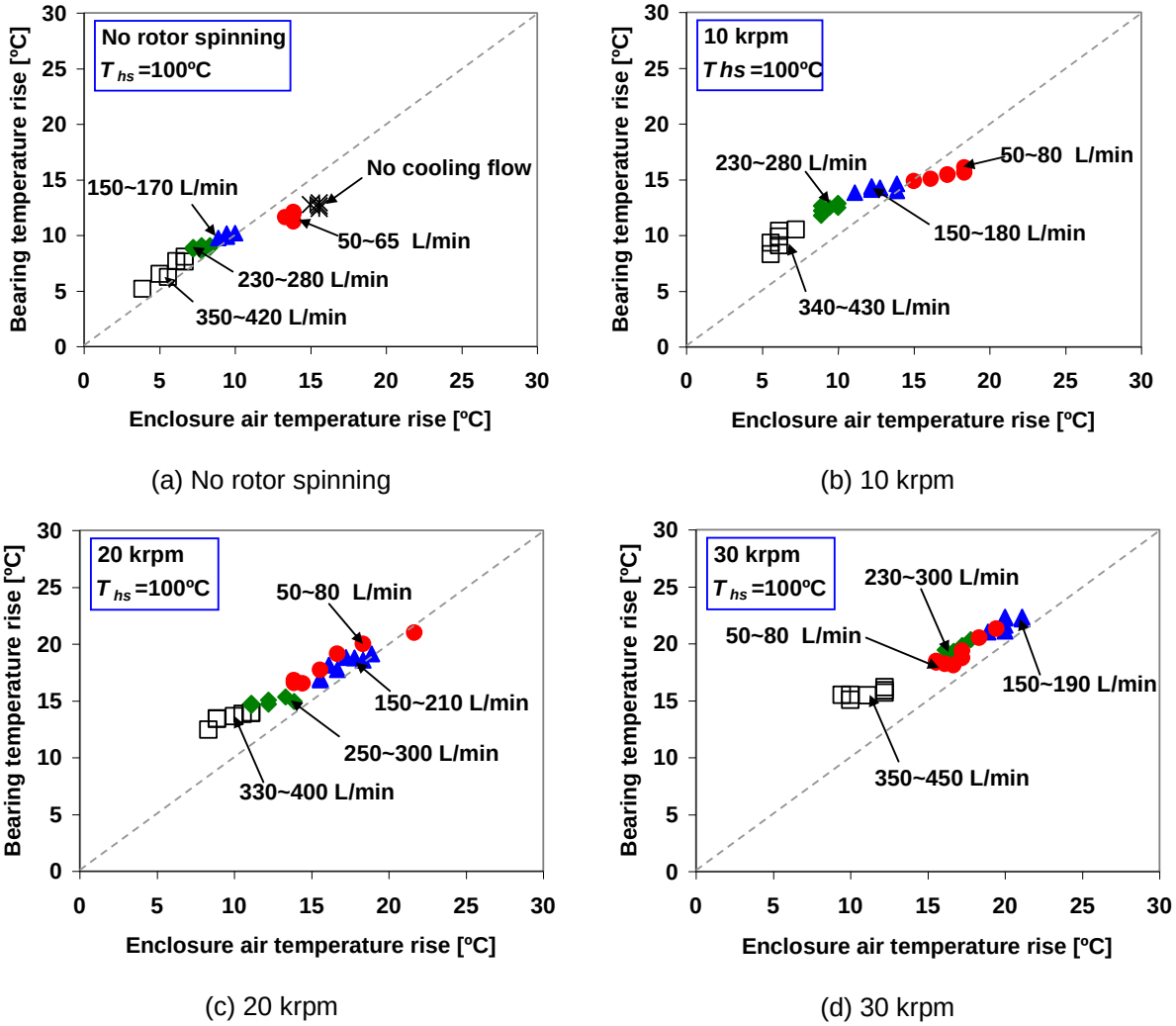

Fig. 21 Test cases #2 and #5. T_{hs}=100ºC: <u>Drive end bearing</u> temperature rise (T_{6-9}-T_{amb}) versus air temperature rise in the enclosure (T_e-T_{amb}). Arithmetic mean of (T_6, T_7, T_8, and T_9) shown.

The temperature difference ($T_i - T_e$) where $_{i\ =\ 1-4\ \text{and}\ 6-9}$ of the bearings above the air temperature in the enclosure (T_e) shows the temperature rise relative to the forced

inlet cooling stream temperature. Therefore, ($T_i - T_e$) leads to determine the effect of cooling flow rate and rotor speed on the bearing temperatures.

Figure 22 depicts the arithmetic mean temperatures of the bearing sleeve ODs above the inlet cooling air temperature (T_{1-4}–T_e) for the FE bearing and (T_{6-9}–T_e) for the DE bearing versus cooling flow rate for increasing heater set temperatures (T_{hs}=65ºC, 100ºC, and 150ºC) and three rotor speeds (10, 20 and 30 krpm). Data shown in Figs. 17−18 and Appendix E are combined to make Fig. 22. Recall Figs. 5, 6, 9 and 10 for the location of the thermocouples.

Temperature differences between the bearing sleeve OD and the air inside the enclosure are nearly invariant while increasing the cooling flow rate. That is ($T_i - T_e$) at 10−30 krpm are a few degrees (< 10ºC) higher than those for the no rotor spinning condition due to the increase in shear drag power within the gas film in the bearing while the shaft rotates. Recall that ($T_i - T_e$) < 0ºC[22] for cooling flow rates lesser than 100 L/min is due to a bearing housing feed enclosure at its center that is not open to ambient. The supply air temperature well upstream of the test rig is shown in Figs. 17 and 18 and Appendix E.

[22] This condition represents the air inside the enclosure is hotter than the bearing ODs.

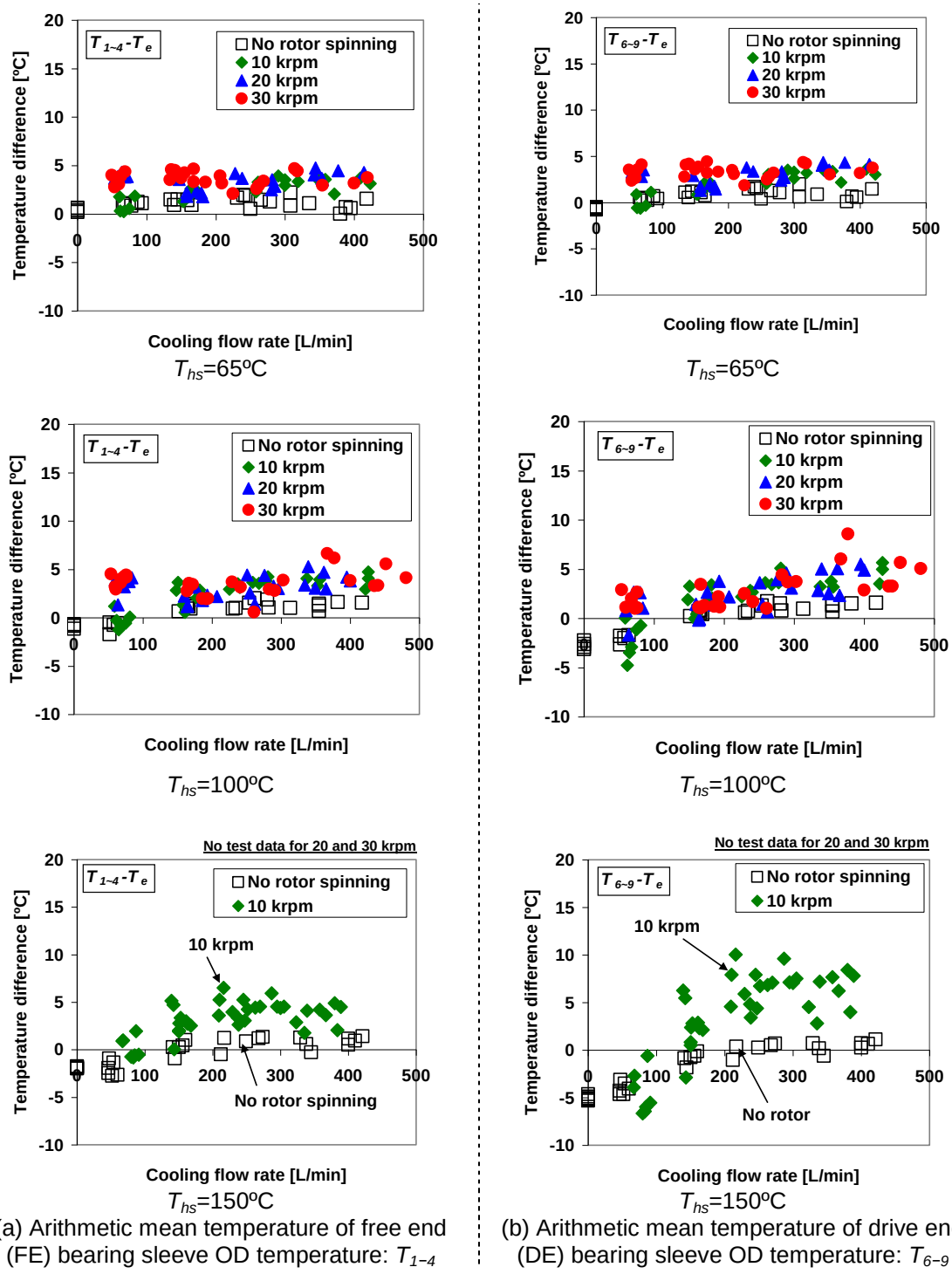

(a) Arithmetic mean temperature of free end (FE) bearing sleeve OD temperature: T_{1-4}

(b) Arithmetic mean temperature of drive end (DE) bearing sleeve OD temperature: T_{6-9}

Fig. 22 Test cases #1−#6, Heater set temperature=65, 100, and 150ºC. No rotor spinning and rotor speed of 10, 20, and 30 krpm: Recorded temperature difference of bearing sleeve OD above inlet cooling air temperature (T_{1-4}-T_e) and (T_{6-9}-T_e) versus cooling flow rate.

5.3 Rotor and Bearing Sleeve Temperature Rises per Unit Cooling Flow Rate: Cooling Capability of Forced Axial Flow

The temperature rise per unit cooling flow rate gives more insight to realize its effects on the thermal performance of the test rotor-bearings system. Figures 23 and 24 show the recorded temperature rise $(T_i - T_{amb})_{i\,=\,r_{FE},\, r_{DE},\, 1-4,\, \text{and}\, 6-9}$ divided by the cooling flow rate (L/min) versus increasing cooling flow rate for various heater temperatures (T_{hs}) from 65 ºC to 150 ºC.

The cooling capability of the forced axial flow on the bearing and rotor temperatures shows a nearly exponential decay. In particular, with cooling flow rates over 300 L/min, the cooling capability of the forced axial flow for the test bearing is less than 0.05°C/L/min, hardly changing with flow rate. The cooling effectiveness of the forced cooling stream is most distinct at the free end rotor OD and at 30 krpm. It is important to note that the cooling stream takes away most of the heat from the back of the top foil, with little heat conduction into the bearing sleeve.

For cooling flow rates of increasing strength, Appendix I shows predictions for the axial and circumferential flow Reynolds numbers that identify the flow characteristics of the inner and outer cooling streams. Laminar flow prevails through the inner film gap (i.e., thin film gas region); while for the outer cooling flow, a transition from laminar flow to turbulent flow occurs when the cooling flow is larger than ~115 L/min (per bearing).

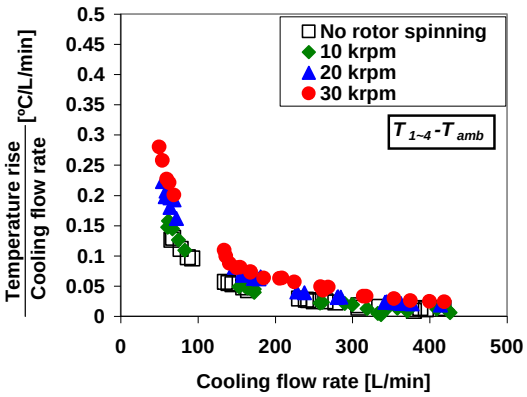

T_{hs}=65ºC

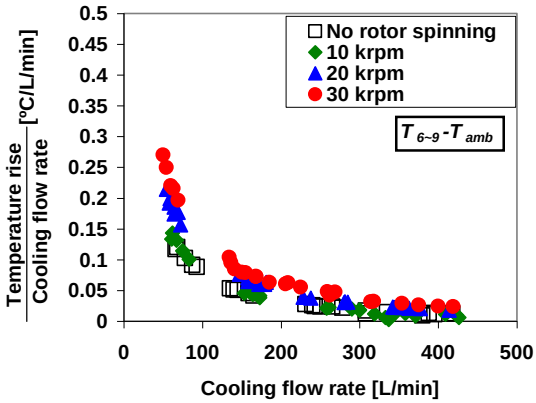

T_{hs}=65ºC

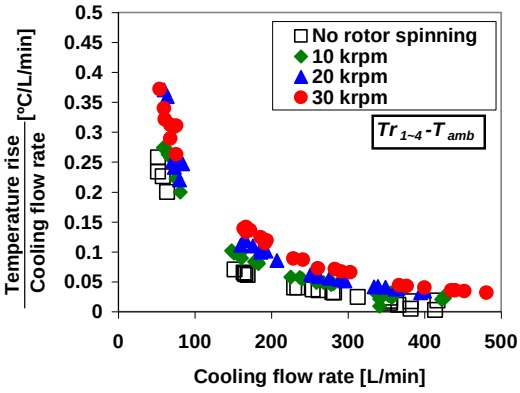

T_{hs}=100ºC

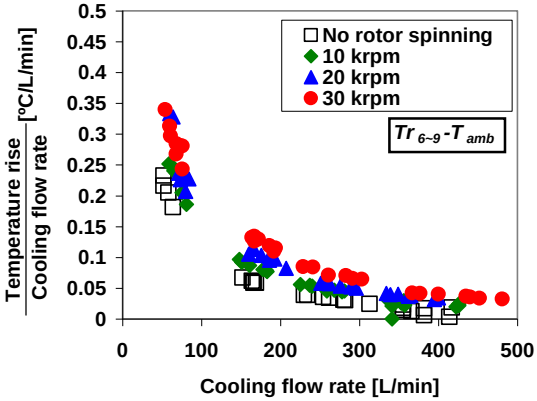

T_{hs}=100ºC

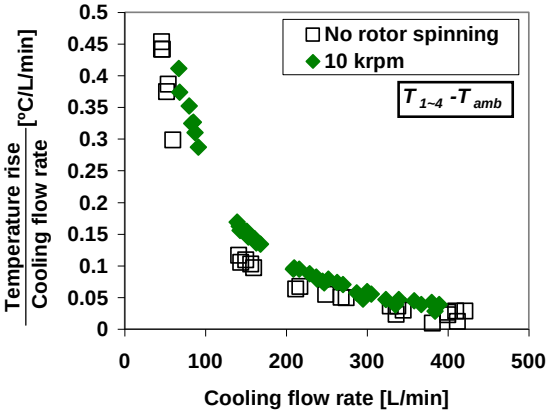

T_{hs}=150ºC: No test data for 20 and 30 krpm

(a) Arithmetic mean temperature of free end (FE) bearing sleeve OD temperature: T_{1-4}

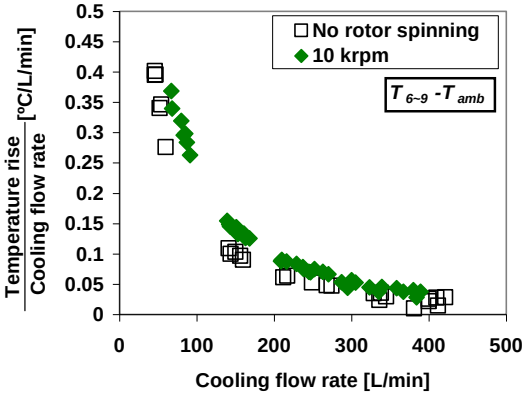

T_{hs}=150ºC: No test data for 20 and 30 krpm

(b) Arithmetic mean temperature of drive end (DE) bearing sleeve OD temperature: T_{6-9}

Fig. 23 Test cases #1−#6. Heater set temperature=65, 100, and 150ºC. No rotor spinning and rotor speed of 10, 20, and 30 krpm: Recorded temperature rise on bearing sleeve ODs, (T_{1-4}-T_{amb}) and (T_{6-9}-T_{amb}) per unit cooling flow rate (L/min) versus cooling flow rate.

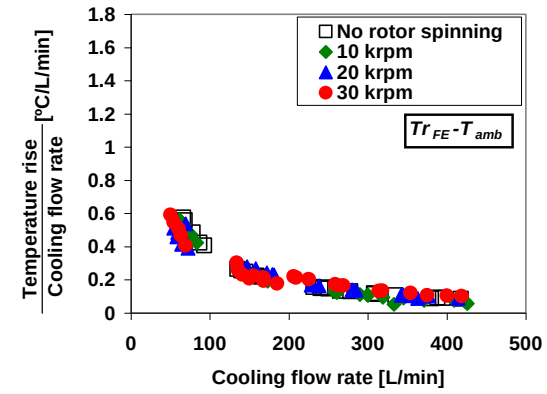

T_{hs}=65ºC

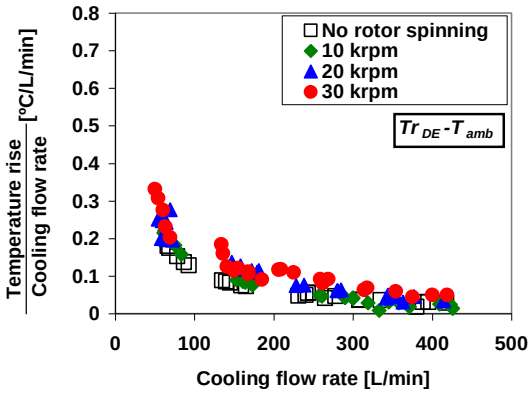

T_{hs}=65ºC

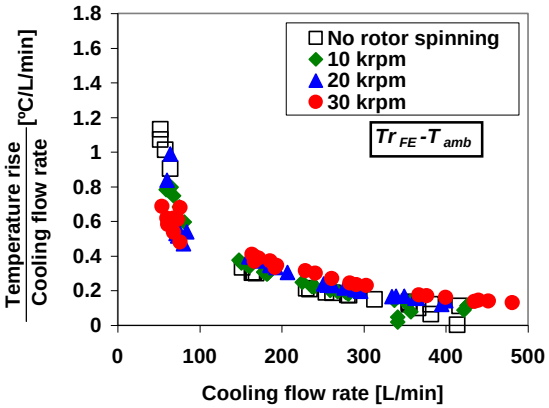

T_{hs}=100ºC

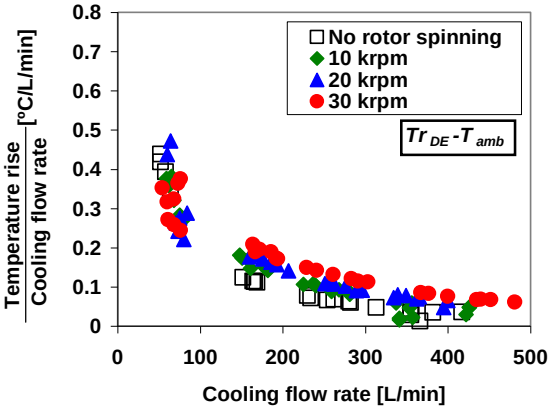

T_{hs}=100ºC

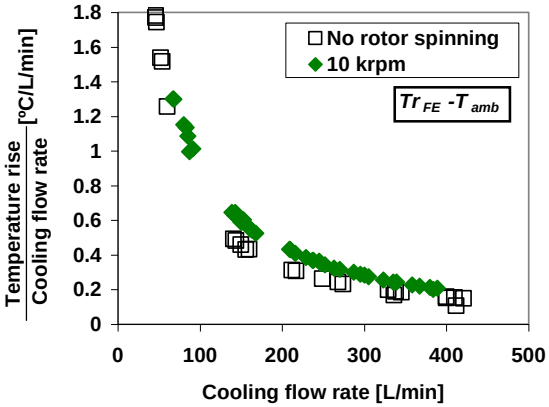

T_{hs}=150ºC: No test data for 20 and 30 krpm

(a) Rotor free end OD (Tr_{FE})

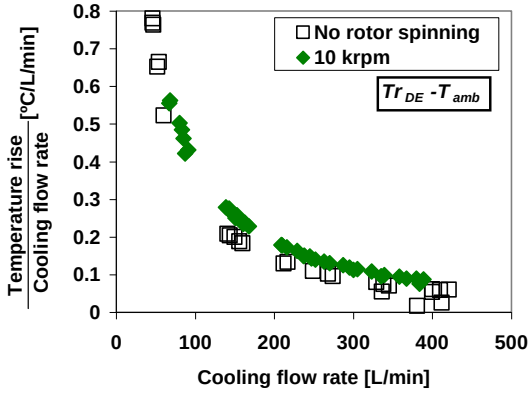

T_{hs}=150ºC: No test data for 20 and 30 krpm

(b) Rotor drive end OD (Tr_{DE})

Fig. 24 Test cases #1−#6. Heater set temperature=65, 100, and 150ºC. No rotor spinning and rotor speed of 10, 20, and 30 krpm: Rotor OD temperature rise, (Tr_{FE}-T_{amb}) and (Tr_{DE}-T_{amb}) per unit cooling flow rate (L/min) versus cooling flow rate. Note different scales of vertical axes.

5.4 Temperatures on Bearing Sleeves

While the shaft is non-rotating and while rotating at 10 krpm, Figs. 25 and 26 show the standard deviation of the four temperatures recorded on the OD circumference of the FE and DE bearing sleeves versus elapsed time. The standard deviation is a measure of the temperatures dispersion from the average value (an arithmetic mean). Recall Figs. 17−18 and Appendix E for two bearings temperatures. Note that, even without rotor spinning, the temperature rises are different around the bearing circumference location due to the unevenness of the heater temperature along its circumference. As the rotor spins, the temperatures at the bearing circumferential locations increase. The FE bearing OD sleeve temperatures (T_1 through T_4) show more variation around the bearing circumference than on the drive end bearing (T_6 through T_9). A small temperature difference among the four thermocouples on each bearing leads to a uniform circumferential thermal growth of the bearing sleeve. In general, the standard deviation of the four bearing temperatures slightly increases with the cooling flow rate, i.e., higher cooling flow rate results in a more pronounced circumferential temperature gradient.

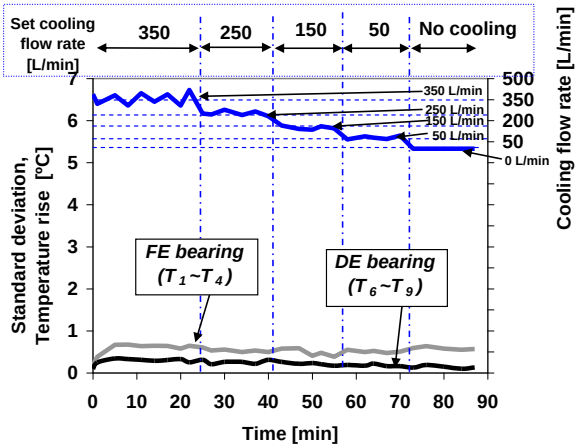

(a) Test case #1: T_{hs}=65ºC

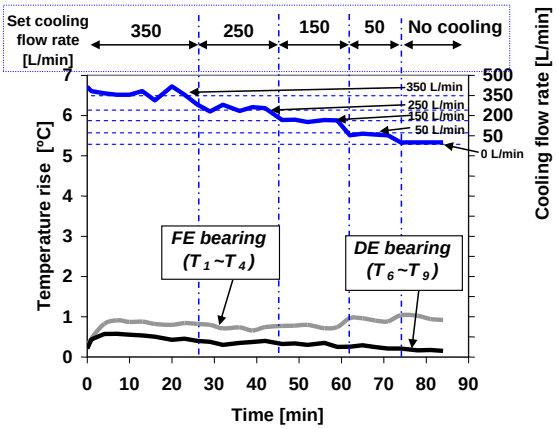

(b) Test case #2: T_{hs}=100ºC

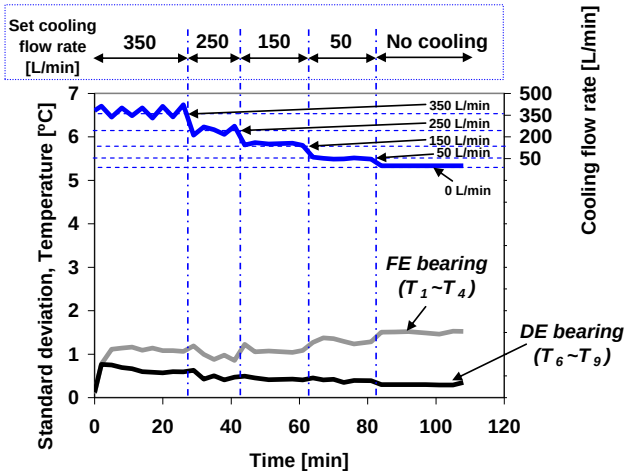

(c) Test case #3: T_{hs}=150ºC

Fig. 25 Test cases #1−#3. No rotor spinning: Standard deviation of FE and DE bearing temperature rise versus elapsed time. T_1~T_4: Standard deviation of FE bearing temperatures, T_6~T_9: Standard deviation of DE bearing temperatures.

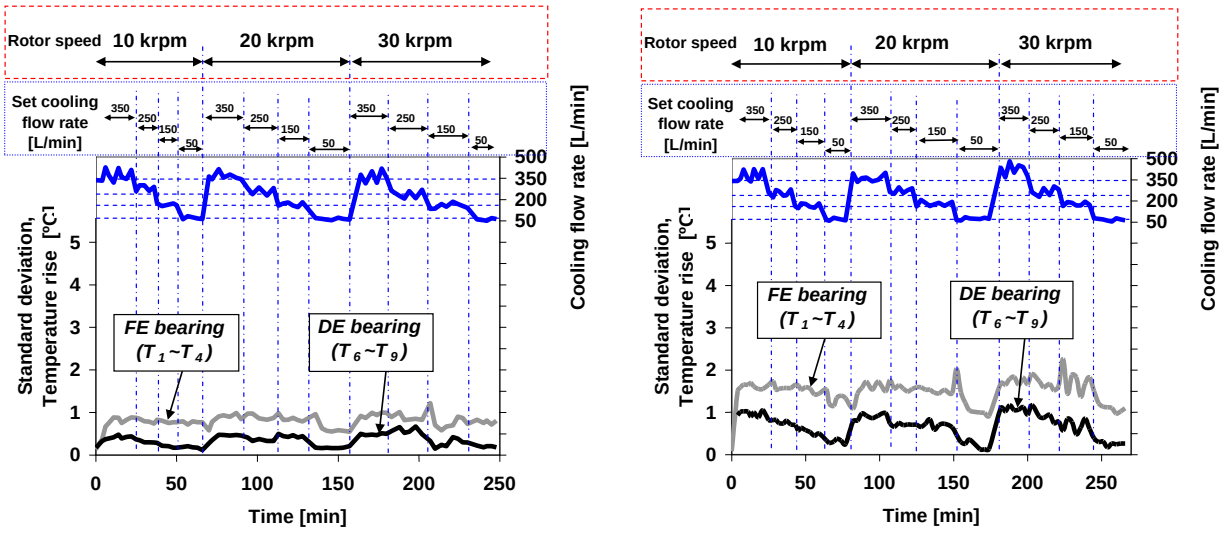

(a) Test case #1: T_{hs}=65ºC

(b) Test case #2: T_{hs}=100ºC

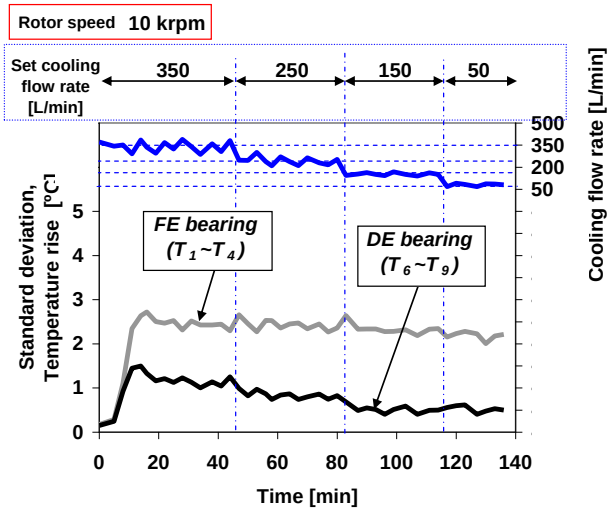

(c) Test case #3: T_{hs}=150ºC

Fig. 26 Test cases #4−#6. Rotor speed of 10, 20, and 30 krpm: Standard deviation of FE and DE bearing temperature rise versus elapsed time. T_1~T_4: Standard deviation of FE bearing temperatures, T_6~T_9: Standard deviation of DE bearing temperatures.

CHAPTER VI

EXPERIMENTAL RESULTS: ROTORDYNAMIC RESPONSE MEASUREMENTS

6.1 Fixed Rotor Speed Operation

For test case #4, Fig. 27 depicts waterfall plots of rotor vertical and horizontal motions recorded at the rotor free and drive ends and while the rotor speed equals 10, 20 and 30 krpm. In the following, the designations FV and FH corresponds to the rotor responses at the free end rotor side, vertical and horizontal planes, respectively. A similar notation follows for the rotor drive sides, DV and DH. The measurement corresponds to operation with the heater set temperature (T_{hs}) at 65 ºC. Each graph on the figure labels the rotor speed and the overall test time.

The data shows that the cooling flow rate does not affect the amplitude and frequency contents of rotordynamic displacements. Recall Fig. E.3 for details on cooling flow rate changes versus elapsed time. Along the drive end (DE) bearing, the rotor displacements are mainly synchronous, while at the free end (FE) plane the 2X (twice synchronous) whirl motions are distinct with large amplitude at the highest speed of 30 krpm. For FV plane, the 2X rotor response amplitude is 3−4 times larger than that of the 1X rotor response over the entire rotor speed range. The 2X rotor motions may be due to the misalignment between the rotor and drive motor. Note that, for the three rotor speeds and during the elapsed times of testing, no subsynchronous whirl motions ever appeared.

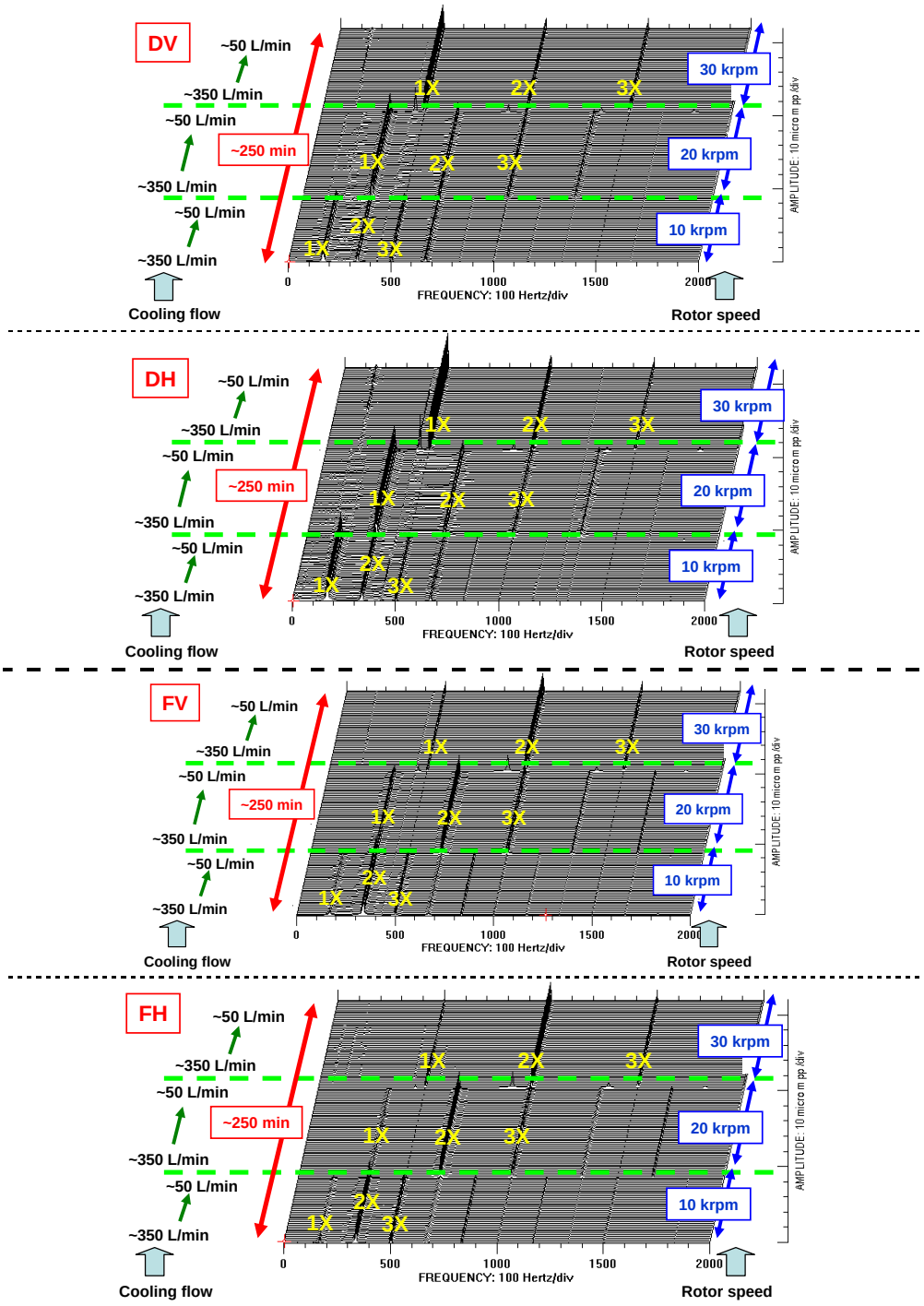

Fig. 27 Test case #4: FFTs of rotor responses at rotor drive end, vertical (DV) and horizontal (DH) planes, and rotor free end, vertical (FV) and horizontal (FH) planes. Rotor speed = 10, 20 and 30 krpm. Cooling flow into bearings from ~350 L/min to ~50 L/min for each set rotor speed. Heater set temperature T_{hs} = 65 ºC.

Figures 28 and 29 depict the rotor whirl orbits, (a) unfiltered, (b) synchronous, and (c) 2X at the rotor drive and free ends, respectively, for rotor speeds equal to 10, 20, and 30 krpm. In the figures, the rotor orbit combines the time based waveform data from a pair of orthogonally mounted displacement sensors (*X*: transducer along the horizontal direction, *Y*: transducer along the vertical direction) to show the dynamic motion of the shaft centerline. The center of the orbit plot is defined by the average values of the *X* and *Y* time based waveforms. In addition, a keyphasor mark (the blank/dot sequence in the figures) represents the location of the shaft centerline at the instant when the once-per-revolution mark passes a tachometer (keyphasor transducer). The blank/dot sequence also shows the direction of rotor motion with time.

Recall that for rotor response along the rotor drive end, the synchronous (1X) whirl motion is dominant while the amplitude of 2X (twice synchronous) rotor response are larger than the 1X rotor response recorded near the rotor free end. In Fig. 28 (b) (DE rotor orbits), rotor synchronous speed motion amplitude along the horizontal plane remain similar with increasing rotor speed; while the vertical motion amplitude increases with rotor speed. The 2X rotor orbit shapes (amplitude and phase angle) do not change with rotor speed.

The rotor synchronous speed rotor orbits measured at the rotor FE, shown in Fig. 29 (b), are highly elliptical, thereby showing the anisotropic character of the bearing stiffnesses. The stiffnesses of the FE bearing along horizontal plane are higher than those along vertical direction. Note the distinctive backward whirl motions in the 2X rotor orbits. Note the scale difference of Fig. 29 (b) to Figs.29 (a) and (c).

The keyphasor mark shows that the synchronous (1X) orbits at each rotor end are out of phase, representing a conical mode shape of the *(rigid)* rotor. The angle of the major axis of the elliptical 2X orbit is ~45º from the horizontal plane. This coincides with the direction of the top foil trailing edge.

For test case #6, Fig. 30 depicts the waterfall plots of rotor vertical and horizontal motions recorded at the rotor drive and free ends. The measurement corresponds to a rotor speed of 10 krpm, and bearing supplied with cooling flow rates varying from ~350 L/min to ~50 L/min. Similar as in Fig. 27, there is no noticeable difference in rotor displacement amplitudes and frequency content while increasing the cooling flow rate into the bearings.

Note that the rotor OD temperature does not affect the amplitude and frequency contents of the rotor dynamic displacements, compare Figs. 27 (T_{hs}=65ºC) and 30 (T_{hs} =150ºC). The rotor whirl orbits (unfiltered, synchronous, and 2X) at 10 krpm depicted in Fig. 31 also display nearly identical amplitudes and shapes with Figs. 28 and 29 (see the leftmost figures for 10 krpm), thereby rendering no changes in rotor response amplitude and phase angle due to increases in the rotor OD temperature.

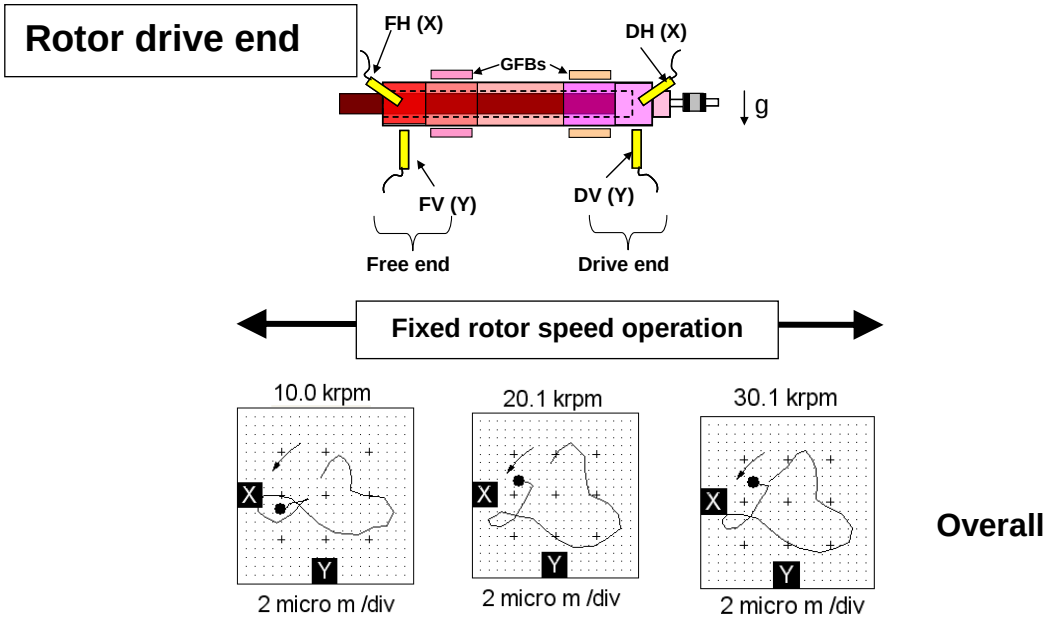

(a) Rotor unfiltered orbits

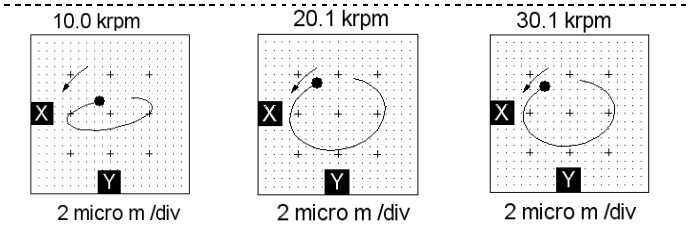

(b) Synchronous speed rotor orbits

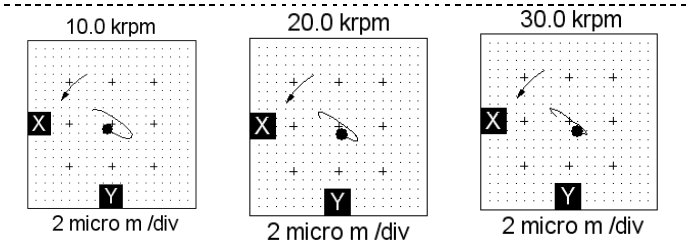

(c) 2X rotor orbits

Fig. 28 Test case #4. Rotor orbits at drive end. Heater set temperature T_{hs} = 65 ºC. Cooling flow into bearings ~350 L/min. Rotor speed set at 10, 20, and 30 krpm. No slow roll compensation.

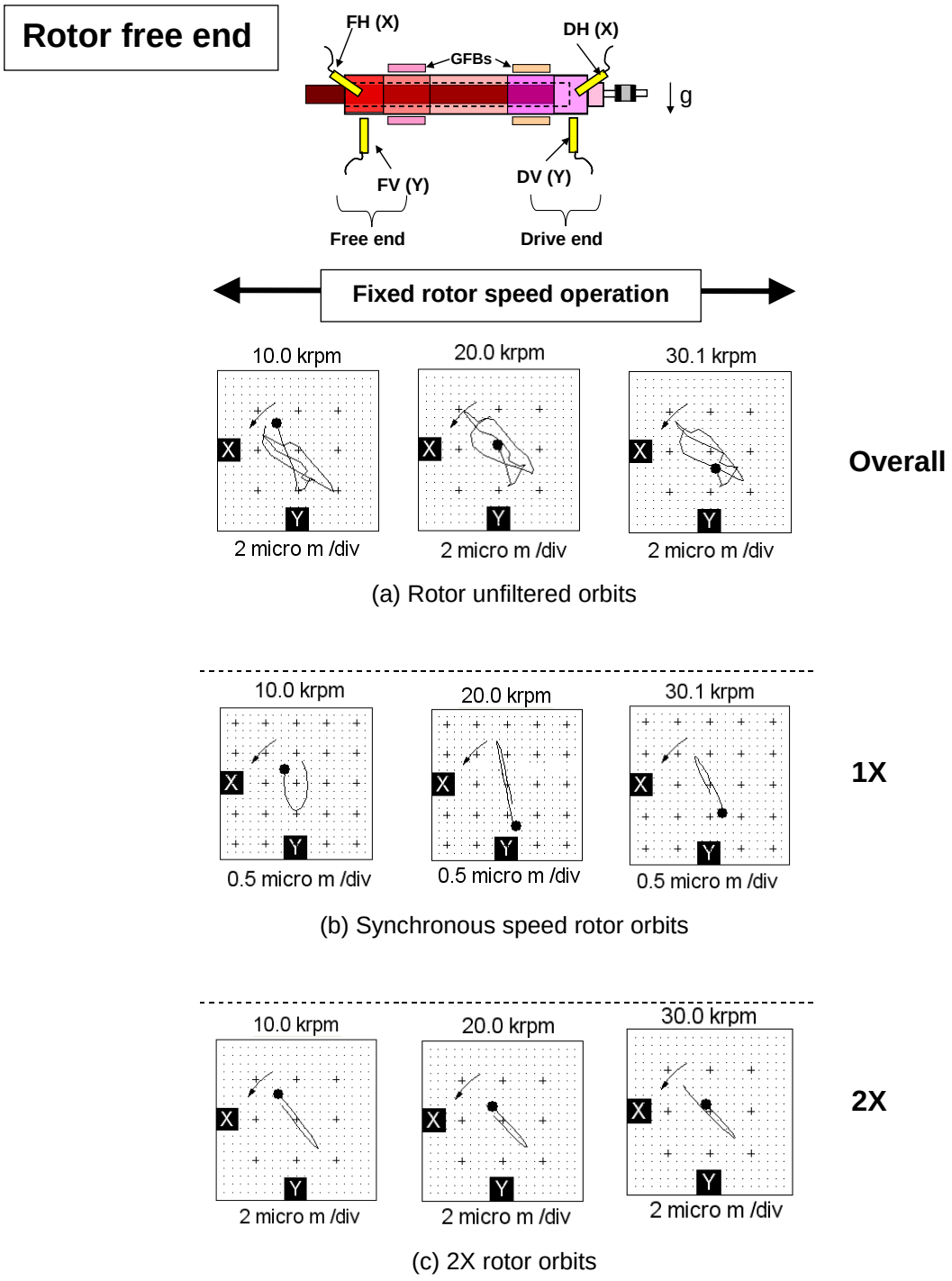

(a) Rotor unfiltered orbits

(b) Synchronous speed rotor orbits

(c) 2X rotor orbits

Fig. 29 Test case #4. Rotor orbits at free end. Heater set temperature T_{hs}=65ºC. Cooling flow into bearings ~350 L/min. Rotor speed set at 10, 20, and 30 krpm. Note different scale between (a) and (b). No slow roll compensation. Note different scale for (b).

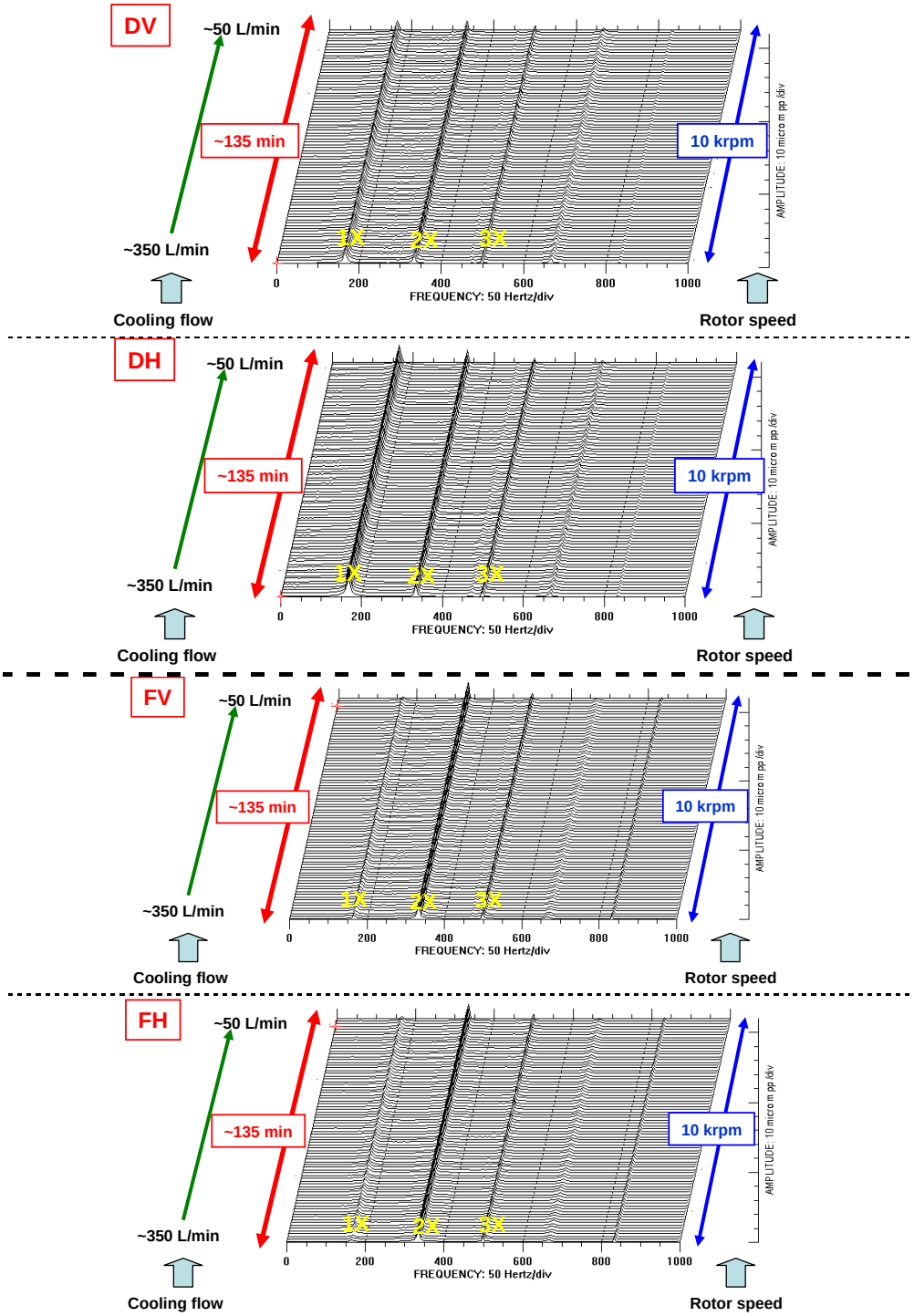

Fig. 30 Test case #6: FFTs of rotor responses at rotor drive end vertical (DV) and horizontal (DH) planes, and rotor free end vertical (FV) and horizontal (FH) planes. Rotor speed = 10 krpm. Cooling flow into bearings from ~350 L/min to ~50 L/min. Heater set temperature T_{hs} = 150 ºC.

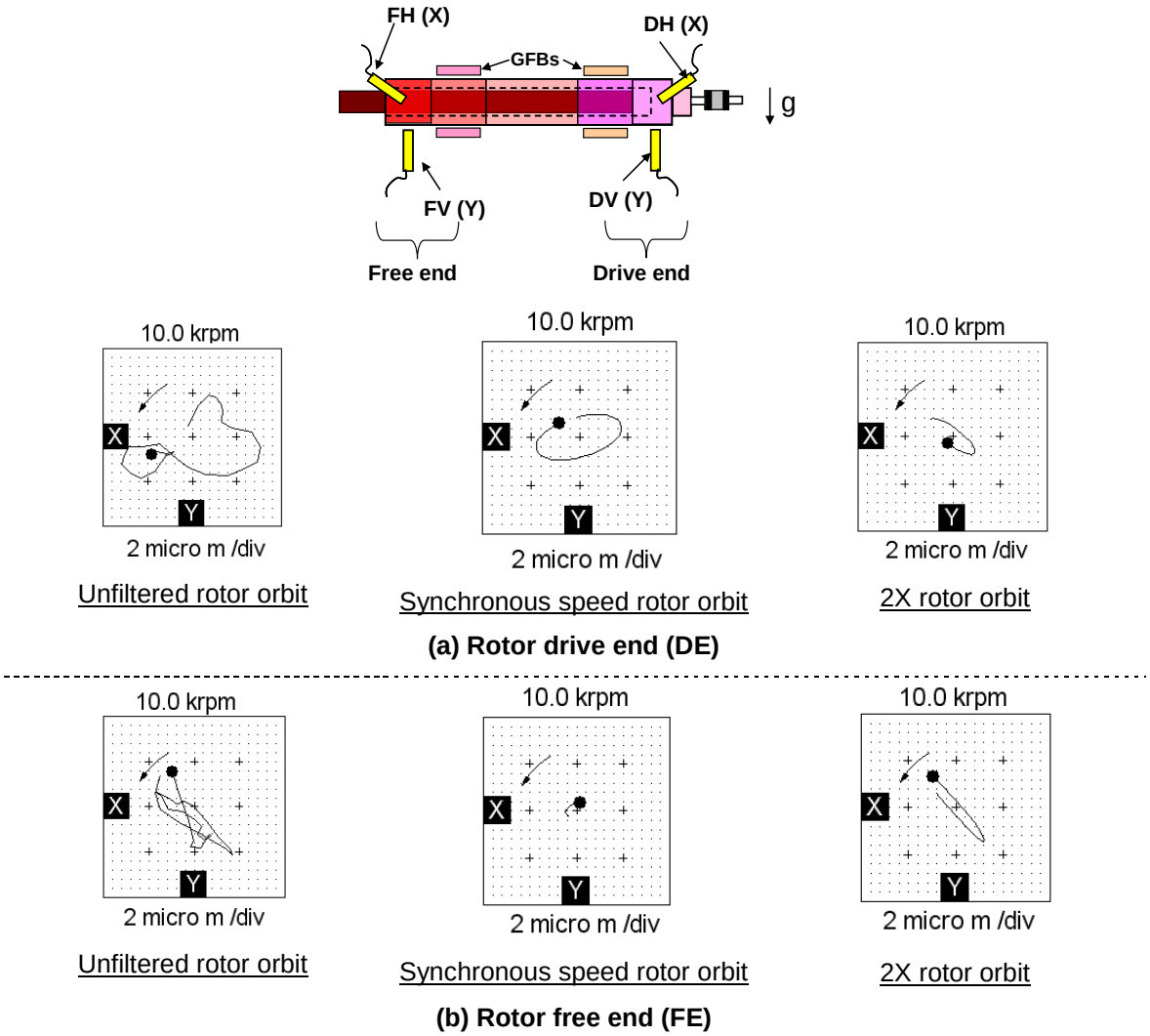

Fig. 31 Test case #6. Rotor orbits at free end. Heater set temperature T_{hs}=150ºC. Cooling flow into bearings ~350 L/min. rotor speed set at 10 krpm. No slow roll compensation.

6.2 Rotor Deceleration with Constant Speed Ramp Rate

While decelerating from 30 krpm to rest, Figs. 32 and 33 show waterfall plots of the rotor motions depicting the amplitude and frequency content of the rotor dynamic displacements for test cases # 7 and #9, respectively. Recall that the set speed ramp rate of the drive motor is 16.7 Hz/s. There are no major differences between the rotor responses for operation with either the heater off and with the heater on at temperature T_{hs}=100 ºC. For the rotor free end, the 2X whirl motions dominate rotor response above ~12 krpm. See Figs. 34 and 35 later for rotor response amplitude of each frequency component (1X and 2X).

Appendix J depicts the recorded amplitudes of synchronous rotor response during a rotor speed-up from rest to 30 krpm. The rotor dynamic responses during rotor acceleration are quite different with those during rotor deceleration although the speed ramp rate is identical |16.7 Hz/s|. The flexible coupling has a lateral stiffness coefficient of 4.4×10^3 N/m[23]. The stiff coupling and short connecting rod (length 4.4 mm and diameter 5.08 mm) may not fully isolate the rotor-GFB system from the drive motor system.

[23] This is an experimentally determined value. Reference [14] details the test method.

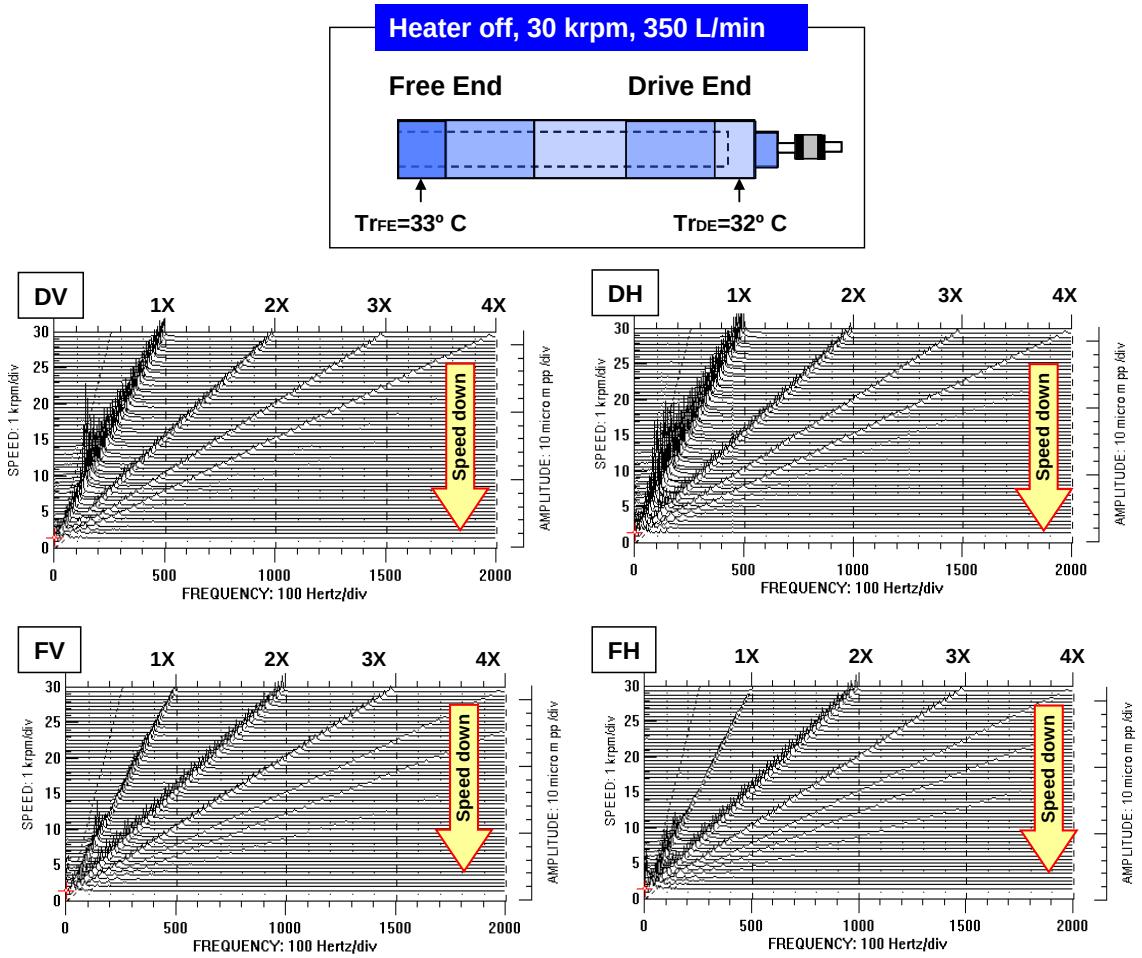

Fig. 32 Test case #7: Waterfalls of rotor motion during decelerating from 30 krpm to rest Heater off, cooling flow rate ~350 L/min, deceleration= 16.7 Hz/s. Rotor drive end, vertical (DV) and horizontal (DH) planes and rotor free end, vertical (FV) and horizontal (FH) planes.

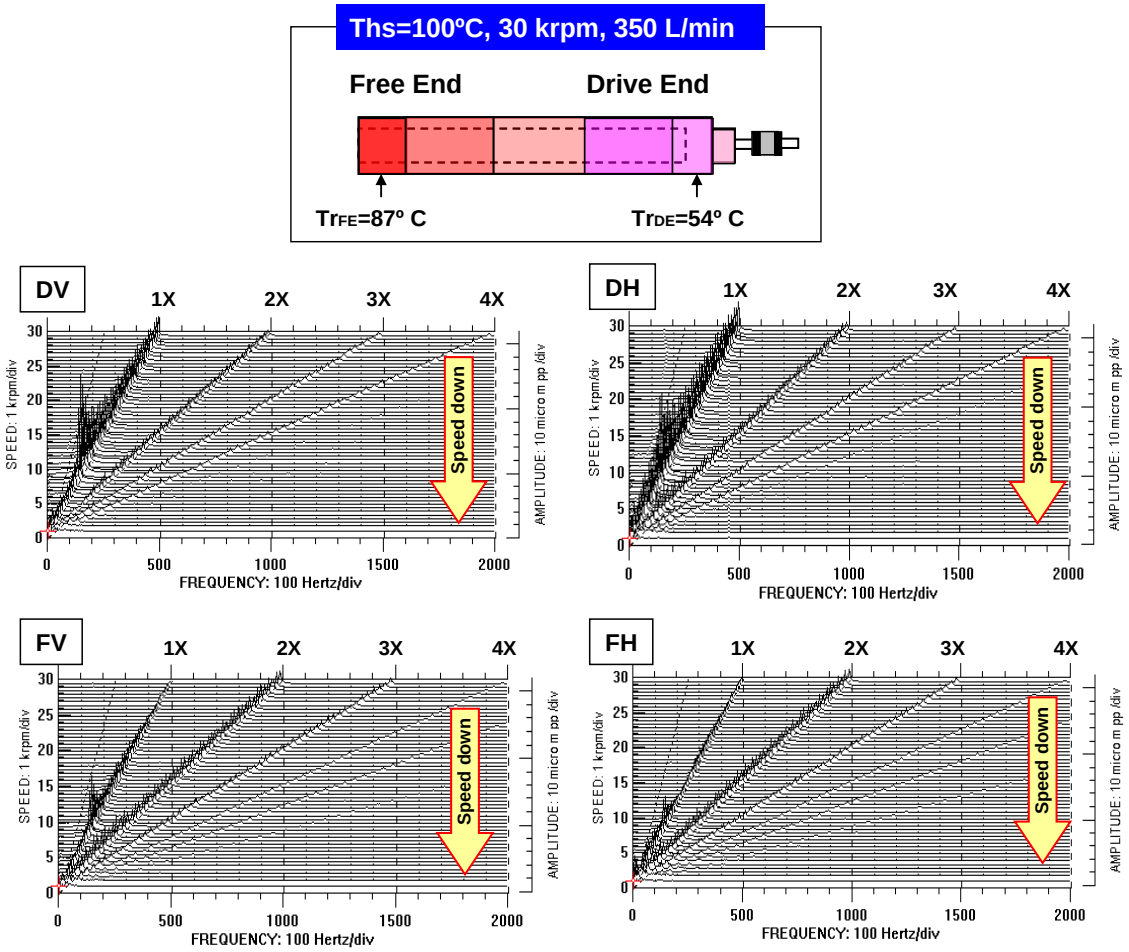

Fig. 33 Test case #9. T_{hs}=100ºC: Waterfalls of rotor motion during decelerating from 30 krpm to rest Heater off, cooling flow rate ~350 L/min, deceleration= 16.7 Hz/s. Rotor drive end, vertical (DV) and horizontal (DH) planes and rotor free end, vertical (FV) and horizontal (FH) planes.

For operation at two heater set temperatures (T_{hs}= 65 ºC and 100 ºC) and also while at ambient temperature (i.e., heater off), Fig. 34 depicts rotor amplitudes of synchronous response recorded during rotor speed-down (deceleration) tests from 30 krpm with a cooling flow rate ~350 L/min. Slow roll compensation at 2 krpm excludes rotor run-out amplitudes. Recall that Δ rpm = 50 in the DAQ system (ADRE®). The measurements are taken at the rotor drive and free ends, vertical and horizontal planes without imbalance masses.

The synchronous rotor responses along the vertical plane, for both drive and free ends, show a distinctive peak at 8−9 krpm. On the other hand, along the rotor horizontal planes for the drive and free ends, two critical speeds (corresponding to rigid body modes, cylindrical conical and conical, see figures on pages 86 and 87) are evident due to the bearing stiffness asymmetry in the vertical and horizontal directions.

Rotor operation beyond the system critical speed shows a significant decrease in amplitudes of rotor motion. For example, $|DV|_{\text{at critical speed}} \approx 7 \times |DV|_{\text{at 30 krpm}}$, where |DV| denotes rotor motion amplitudes recorded at the drive end of the rotor along the vertical plane. In general, rotor motion amplitudes at the drive end are larger than that at free end.

Overall, no prominent differences are apparent in synchronous rotor response for operation at ambient temperature and at the hottest shaft temperature (T_{hs}=100ºC). The inset figures depict the measured rotor temperature corresponding to the respective heater set temperature.

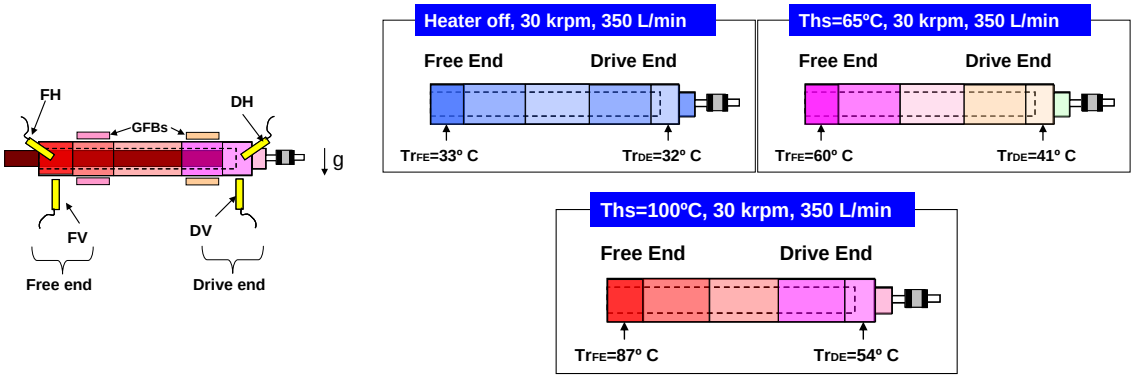

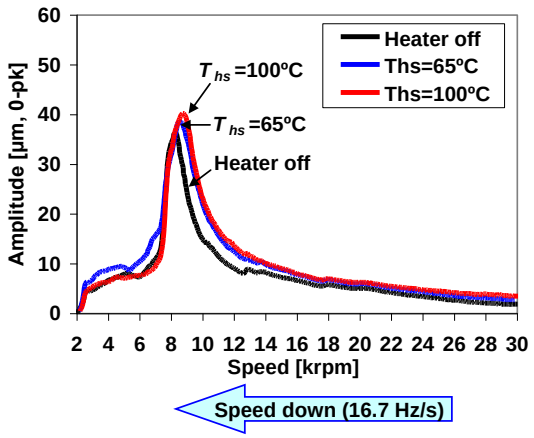

(a) Rotor drive end vertical plane (DV)

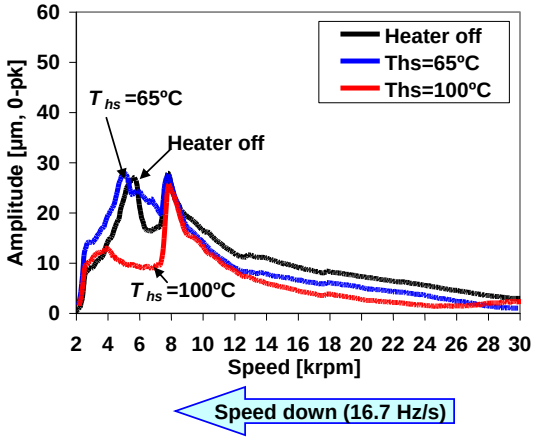

(b) Rotor drive end horizontal plane (DH)

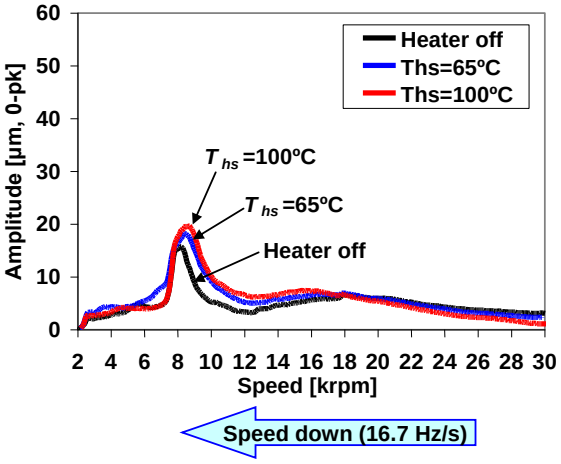

(c) Rotor free end vertical plane (FV)

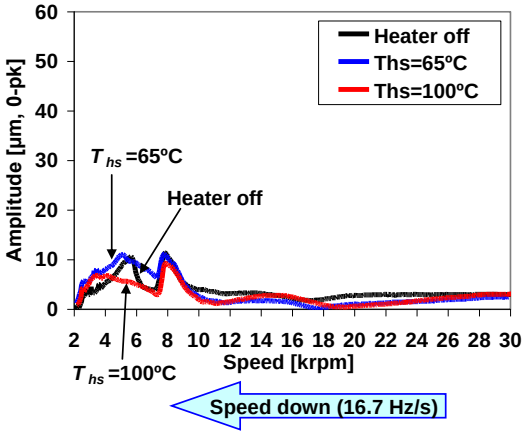

(d) Rotor free end horizontal plane (FH)

Fig. 34 Test cases #7−#9: Rotor amplitudes of synchronous response. Slow roll compensation at 2 krpm. Cooling flow rate ~350 L/min.

Figure 35 depicts the 2X (twice synchronous) rotor response amplitudes for test cases #7−#9. The 2X rotor response amplitudes do not vary with rotor OD temperature, i.e., the rotor response are almost identical while increasing T_{hs} up to 100ºC. Beyond the system critical speed (~8 krpm), the 2X rotor motion amplitudes along the rotor FE increase with rotor speed. On the other hand, the 2X rotor motions along the rotor DE remain similar amplitude above 10 krpm.

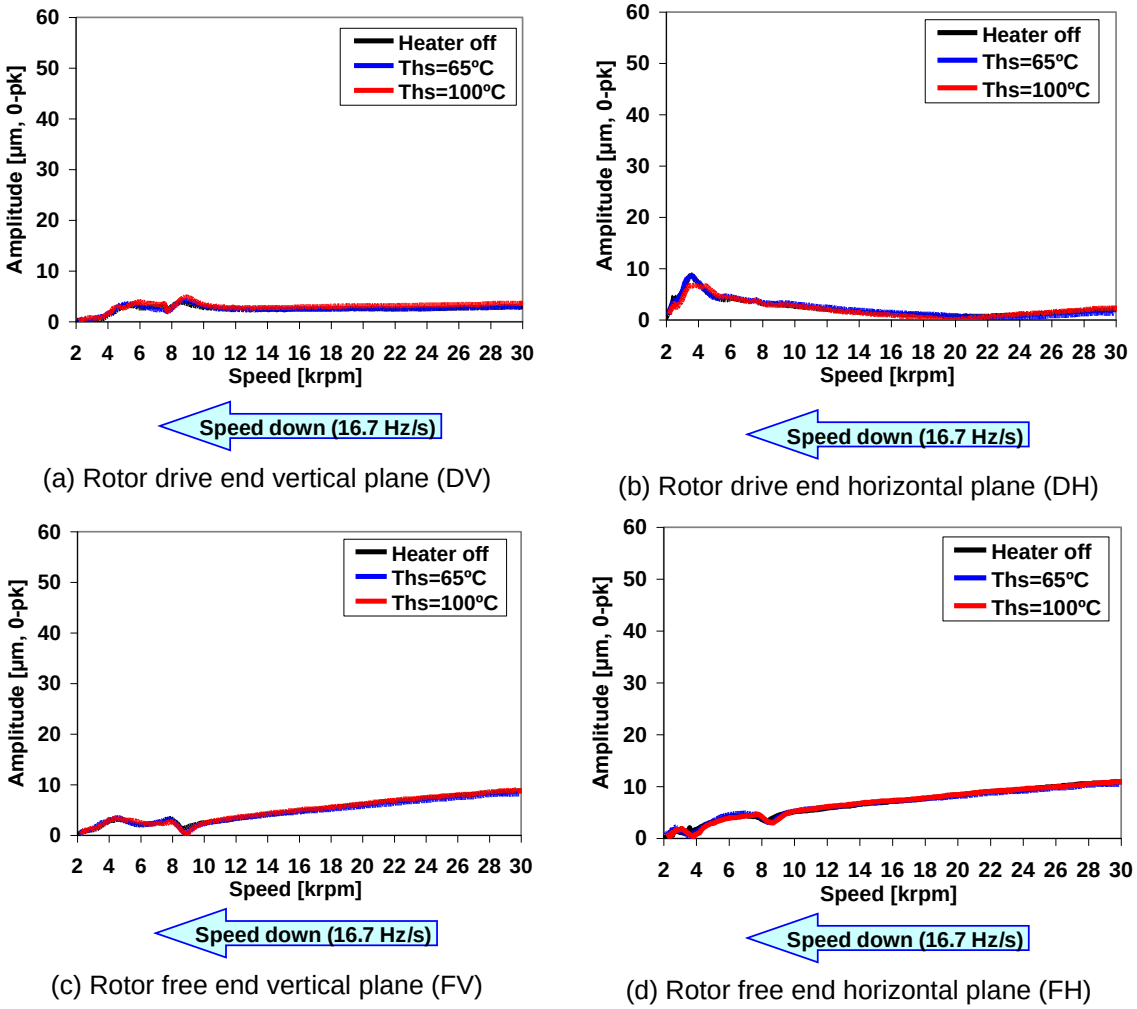

(a) Rotor drive end vertical plane (DV)

(b) Rotor drive end horizontal plane (DH)

(c) Rotor free end vertical plane (FV)

(d) Rotor free end horizontal plane (FH)

Fig. 35 Test cases #7−#9: Rotor amplitude of 2X (twice synchronous) response. Slow roll compensation at 2 krpm. Cooling flow rate ~350 L/min.

Impact load tests on the rotor show a distinctive flexural mode due to the soft connecting rod and coupling at 1.5 kHz (90 krpm), see Appendix K. Therefore, the test rotor is regarded as a rigid body within the rotor speed range to 30 krpm. The shape of the synchronous responses can be readily determined by subtracting the phase angles of the measured displacements at each end of the rotor[24].

For test cases # 7 and #9, Fig. 36 depicts a phase difference of 180 deg while traversing the speeds with largest response amplitudes. Therefore, a conical mode is prevalent while traversing the critical speeds of the rotor bearing system. For increasing rotor OD temperature, the phase differences ($\angle$FH-$\angle$DH) have similar trends, but are less consistent in the shift amount than ($\angle$FV-$\angle$DV) because the response amplitudes along the horizontal plans are considerably small (< 3 μm above 10 krpm).

Figure 37 displays the ratio of amplitudes recorded at the rotor drive and free ends along the vertical and horizontal planes. This ratio aids to determine the relative size of the end displacements. In general, the rotor response at the drive end renders higher amplitude than the free end. At the system critical speed (~8 krpm), the rotor motions at DE are ~ twice larger than those at FE. As the rotor speed decreases from 30 krpm, the node in the conical mode moves from the rotor center (because of nearly identical amplitudes of motion at each end) toward the drive end of the rotor. For both test cases, the ratios of amplitudes (DE over FE) are largest at rotor speeds of ~11 krpm and ~19 krpm. Appendix L fully presents rotor whirl orbits for test cases #7 and #9.

[24] Operation with near 0 deg phase difference indicates a cylindrical mode, while a phase difference of 180 deg denotes a conical mode.

More experimental data for test cases #8−#10 is omitted for brevity. Overall, there is no noticeable difference in rotor response for test cases #7−#10.

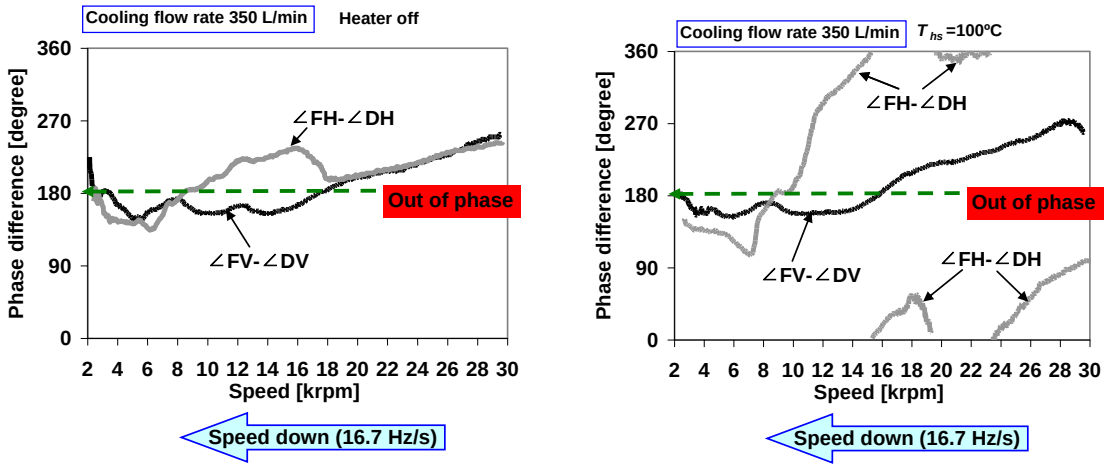

(a) Test case #7: Heater off

(b) Test case #9: T_{hs}=100 ºC

Fig. 36 Test cases #7 and #9: Speed down from 30 krpm to rest with ramp rate of 16.7 Hz/s. Phase differences of recorded imbalance response versus rotor speed. Cooling flow rate ~350 L/min.

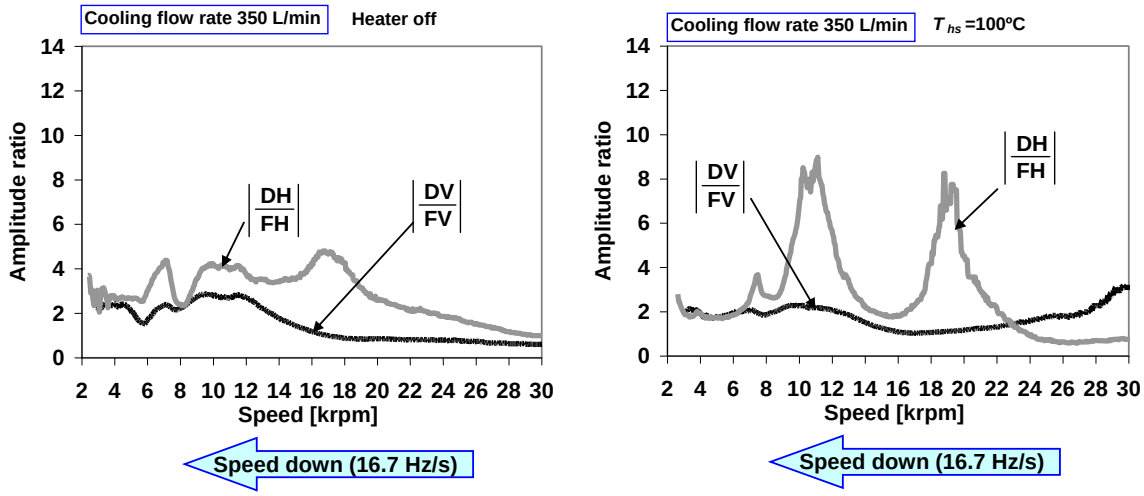

(a) Test case #7: Heater off

(b) Test case #9: T_{hs}=100 ºC

Fig. 37 Test cases #7 and #9: Speed down from 30 krpm to rest with ramp rate of 16.7 Hz/s. Amplitude ratio of recorded imbalance response versus rotor speed. Cooling flow rate ~350 L/min.

CHAPTER VII

PREDICTIONS OF BEARING TEMPERATURES AND ROTORDYNAMIC RESPONSE AND COMPARISONS TO EXPERIMENTAL DATA

San Andrés and Kim [14] develop a model for thermal energy transport in a hot-rotor-GFB system with cooling flow paths to predict the bearing temperature and pressure fields, static load capacity and power loss, and dynamic force coefficients. The analysis couples the gas film pressure equation to the thermal energy transport equation with appropriate boundary conditions. The model accounts for forced cooling conditions and an actual operating clearance determined from thermal changes in material properties and the mechanical components thermal and centrifugal growths.

Figure 38 depicts a schematic view of a GFB with a hollow shaft with uniform heat source and a cooling air flow supplied on one side of the bearing and flowing through the gap underneath the top foil. In the model, the inner and outer cooling gas streams are regarded as sinks of thermal energy. In addition, the cooling stream is large enough to remain at a uniform temperature (T_{Co}) while advecting (removing) heat from the top foil back surface at temperature (T_{Fo}). Figure 39 shows the complex heat flow paths in a GFB. The nomenclature for temperatures is also noted. References [14,45,46] fully detail the TEHD model for prediction of GFBs static and dynamic forced performance.

Presently, thermal expansion of the whole test rig casing is not considered in the predictions. In the model, an empirically derived thermal mixing coefficient λ=0.65

represents best the gas flow and thermal energy balance at the conjunction of the top foil leading and trailing edges [14,46][25].

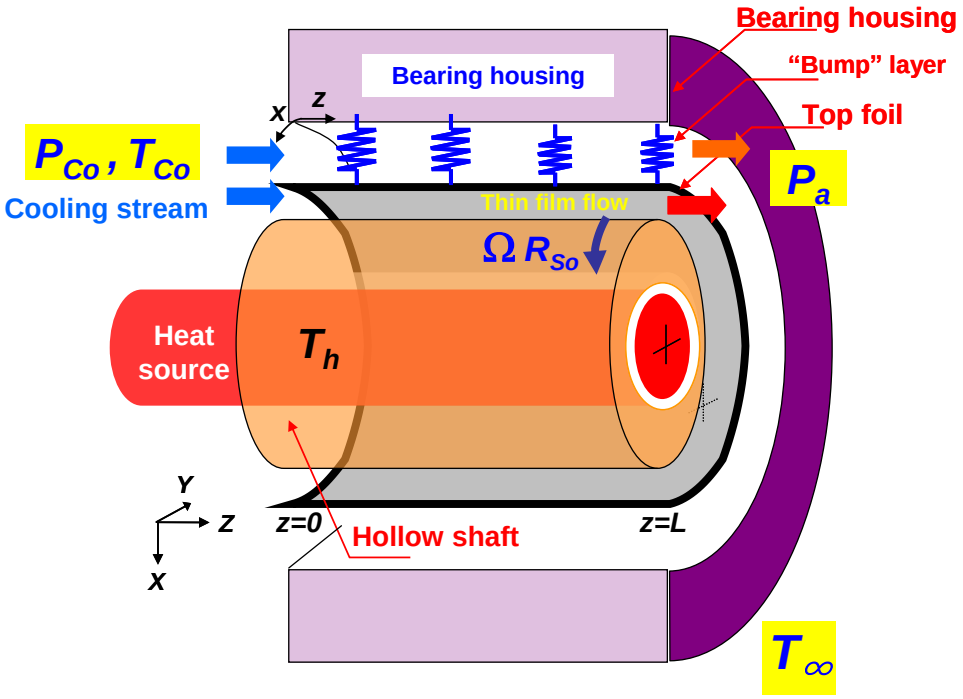

Fig. 38 Schematic side view of foil bearing with heat source warming hollow rotor and outer cooling stream (T_{Co}, P_{Co}) flowing through thin film region and underneath top foil. Outer cooling flow exits to ambient pressure (P_a). Taken from [46].

[25] The thermal mixing coefficient λ denotes the fraction of upstream gas flow (top foil trailing edge) re-entering the thin film of the GFB at the leading edge of the top foil. λ is an empirical parameter depending on the foil bearing arrangement and the cooling method. Reference [47] discusses thoroughly the mixing flow and inlet temperature at the leading edge of top foil. References [24,25] derive a similar mixing model and add CFD prediction validations.

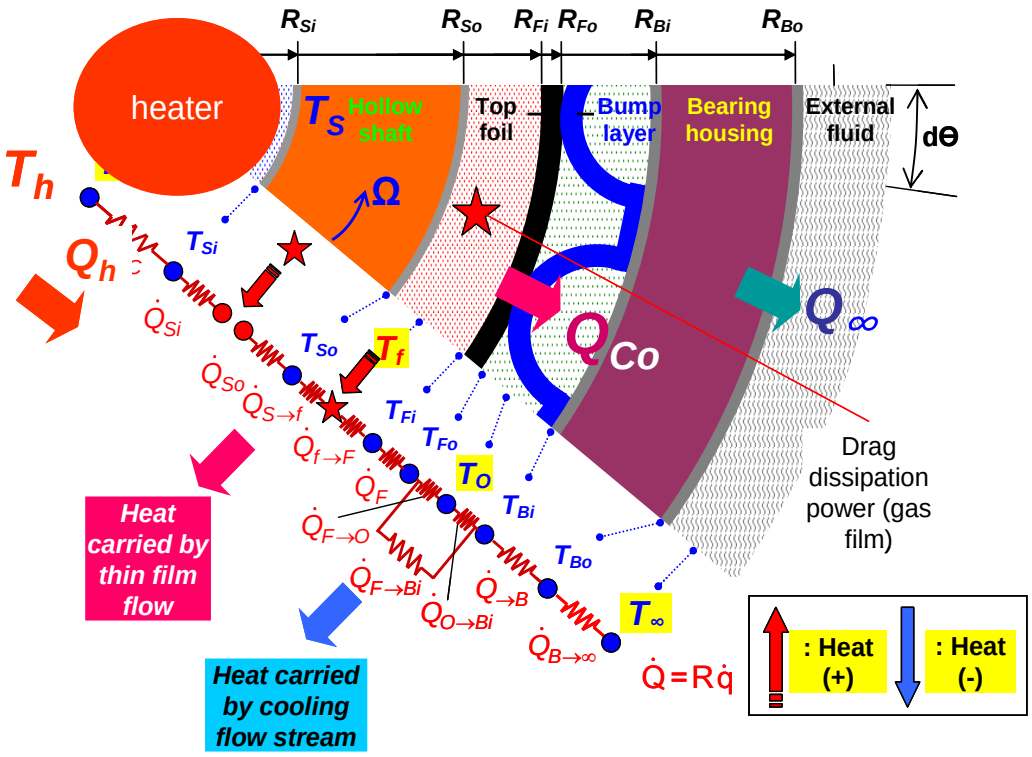

Fig. 39 Nomenclature for temperatures in a foil bearing operating with a hot rotor and an outer cooling gas stream. Schematic representation of heat flows shown. Taken from [46].

7.1 Prediction of Bearing Temperatures and Comparison to Test Data

Model predictions are compared to the temperature measurements while the test rig operates without and with a forced cooling gas flow (0−350 L/min). Appendix M shows complete input data for the bearing predictive model including the bearings and rotor dimensions and structural properties, operating clearances, and cooling flows. The appendix also lists the predicted (peak and average) film temperatures, (peak and average) bearing cartridge ID temperatures, and static load parameters (journal

eccentricity, attitude angle, minimum film thickness and drag torque). Discussions on the predicted static load parameters follow in Section 7.2.

For test cases #4−#6, Fig. 40 depicts the predicted and measured temperatures of the bearing sleeve mid-span OD versus cooling flow rate for rotor speed at 10, 20, and 30 krpm. Symbols and continuous lines represent the test data and the THD model predictions, respectively. Presently, predicted GFB housing ID temperatures are compared to the measure temperatures at the bearing sleeve OD. In the analysis, cooling flow rates into each test bearing are 175 L/min, 125 L/min, 75 L/min, and 25 L/min, half of the total supply cooling stream of 350, 250, 150, and 50 L/min[26]. Recall (see Section 3.1) that the applied static loads on the drive and free end bearings are 7.39 N and 5.94 N, respectively. In the prediction, for each rotor speed and cooling flow rate, the inlet cooling stream temperature $T_{Co} = T_e$ (enclosure air temperature) and the rotor OD temperature is uniform and equal to either Tr_{FE} or Tr_{DE}. Note that the rotor temperatures at the bearing locations are estimated from a constant temperature gradient (linear temperature drop) from the recorded rotor FE and DE temperatures (Tr_{FE} and Tr_{DE})[27].

Figure 40 depicts the arithmetic mean value from four recorded temperatures T_1 to T_4 for the FE bearing cartridge OD, and T_6 to T_9 for the DE bearing OD[28]. Recall that the computational model accounts for material property changes and the bearing

[26] It is assumed that the flow rates distribute evenly into the two test bearings.
[27] As shown in Figs. 19 through 22, the actual temperatures of the rotor OD at the bearing locations are slightly lower than the estimated temperatures used for the predictions.
[28] The bearing temperatures are measured along the bearing sleeve OD mid-plane shown in Fig. 5. Typically, the gas film peak temperature is at the bearing mid-plane and along the loading direction [23].

components' expansion and shaft centrifugal growth due to temperature increases and rotational speed, respectively.

In general, predicted temperatures are in good agreement with measurements. The trends also appear quite similar. Note that the difference between prediction and measurement decreases as the rotor speed increases. However, predictions for the FE bearings at the hottest rotor temperature and lowest cooling flow rate condition are 22% higher than the recorded temperatures. The discrepancies are due to the large temperature gradient along the heater axial length (particularly) on the rotor free end, the side facing the hottest section of the heater cartridge. Reference [14] also reports similar findings.

At rotor speed of 30 krpm and for test case #5 (T_{hs}=100ºC), Figs. 41 and 42 depict the predicted GFB film mean temperature fields for operation with 175 L/min and 25 L/min forced cooling stream, respectively. The figure caption shows cooling air inlet temperature, rotor surface temperature, and ambient temperature for each case. Note that the bearing OD and rotor ID are exposed to ambient temperature T_{amb}. See Tables 3 and 4 later for details on the predicted journal eccentricity, journal attitude angle, and minimum film thickness. Recall that the top foil leading edge locates at Θ=45º where fresh gas enters into the film. The gas film temperature increases from 45º <Θ<200 º where the bulk of the shear mechanical energy is generated. The predicted gas film temperature at the bearing mid-plane grows as the rotor surface temperature increases. For operation at 10 krpm in test case #5, Appendix N shows the predicted GFB film temperature fields for operating with 175 L/min and 25 L/min forced cooling stream.

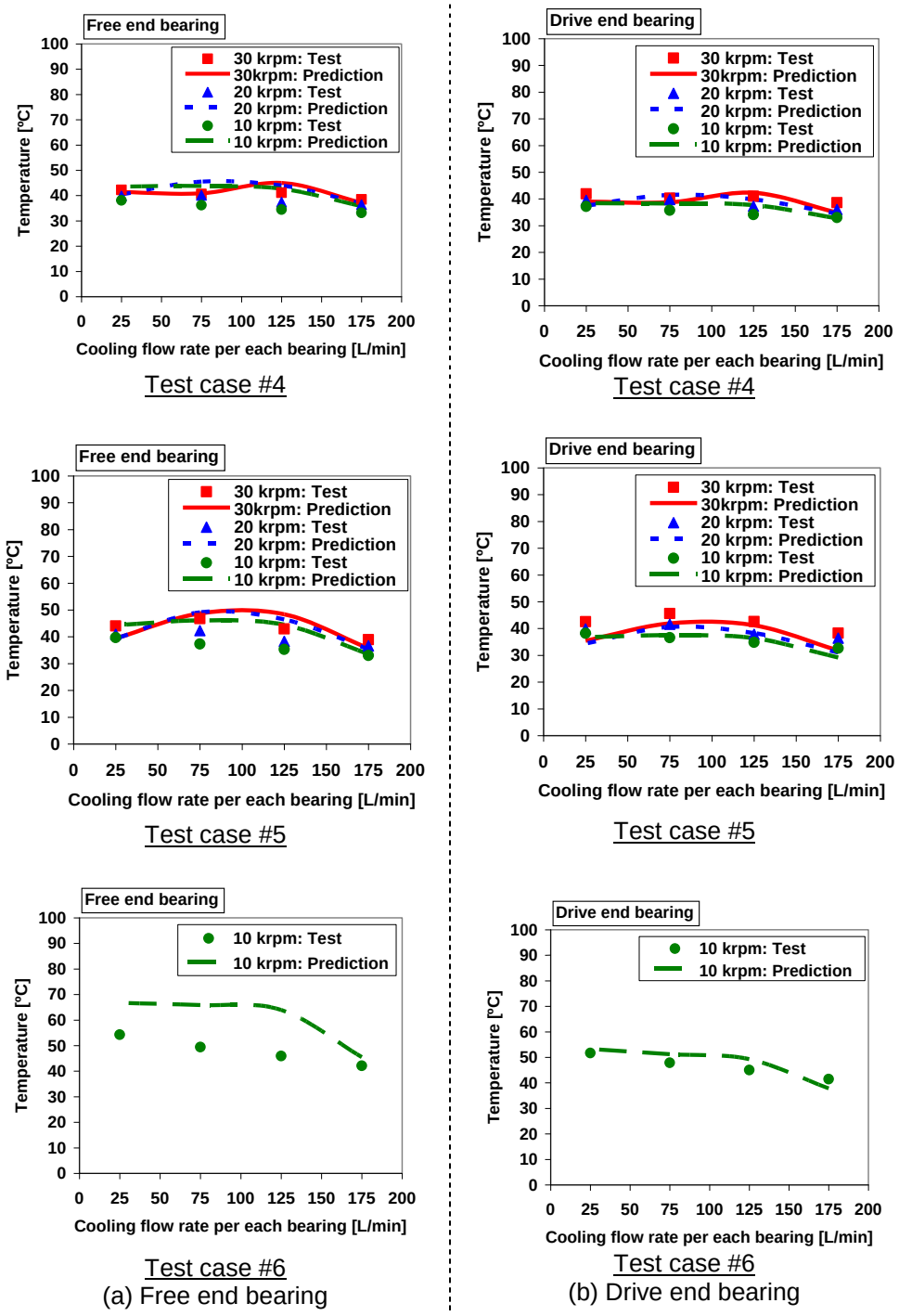

Fig. 40 Prediction versus test data: Temperatures of bearing sleeves (free and drive ends) versus cooling flow rate. See Appendix M for complete inputs for prediction.

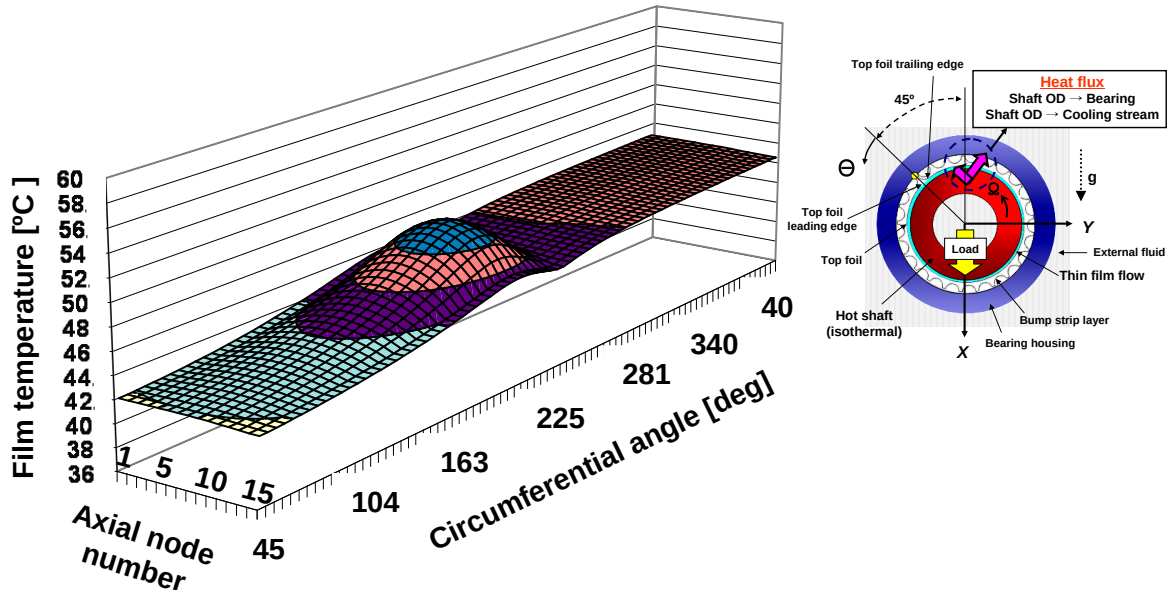

(a) Drive end bearing

(Cooling stream inlet temperature= 33ºC, uniform rotor OD temperature= 61ºC, T_a= 23ºC)

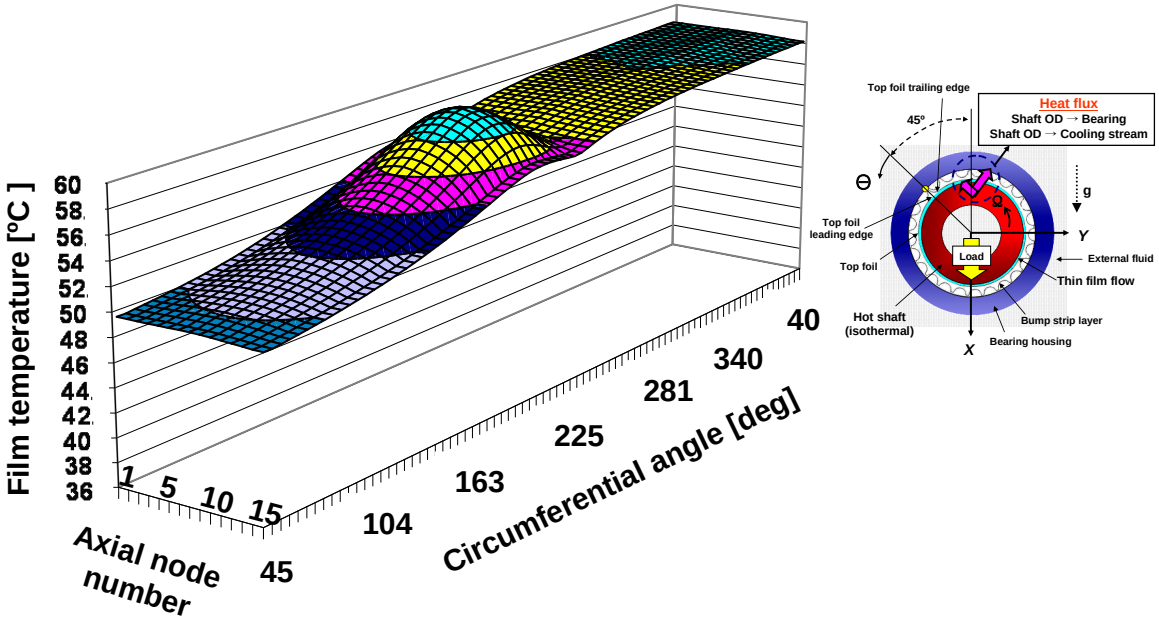

(b) Free end bearing

(Cooling stream inlet temperature=33ºC, uniform rotor OD temperature= 80ºC, T_a= 23ºC)

Fig. 41 Prediction: Test case #5. Thin film temperature fields in GFBs. T_{hs}=100ºC, rotor speed at 30 krpm. Cooling flow rate per each bearing 175 L/min. Thermal mixing coefficient λ=0.65.

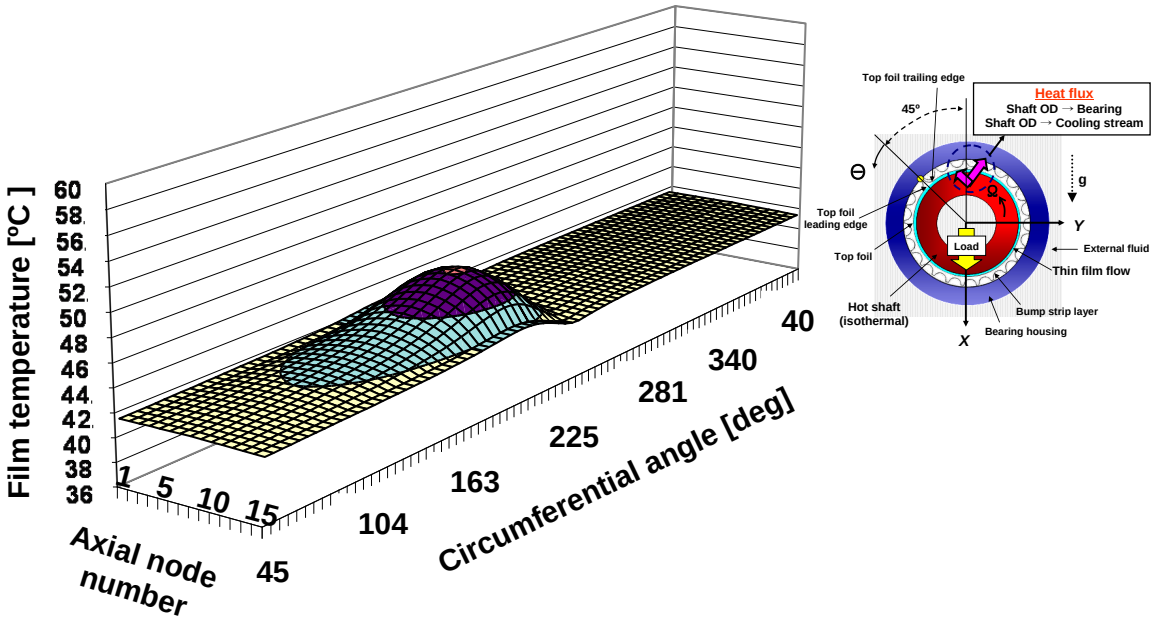

(a) Drive end bearing

(Cooling stream inlet temperature= 41ºC, uniform rotor OD temperature= 45ºC, T_a= 24ºC)

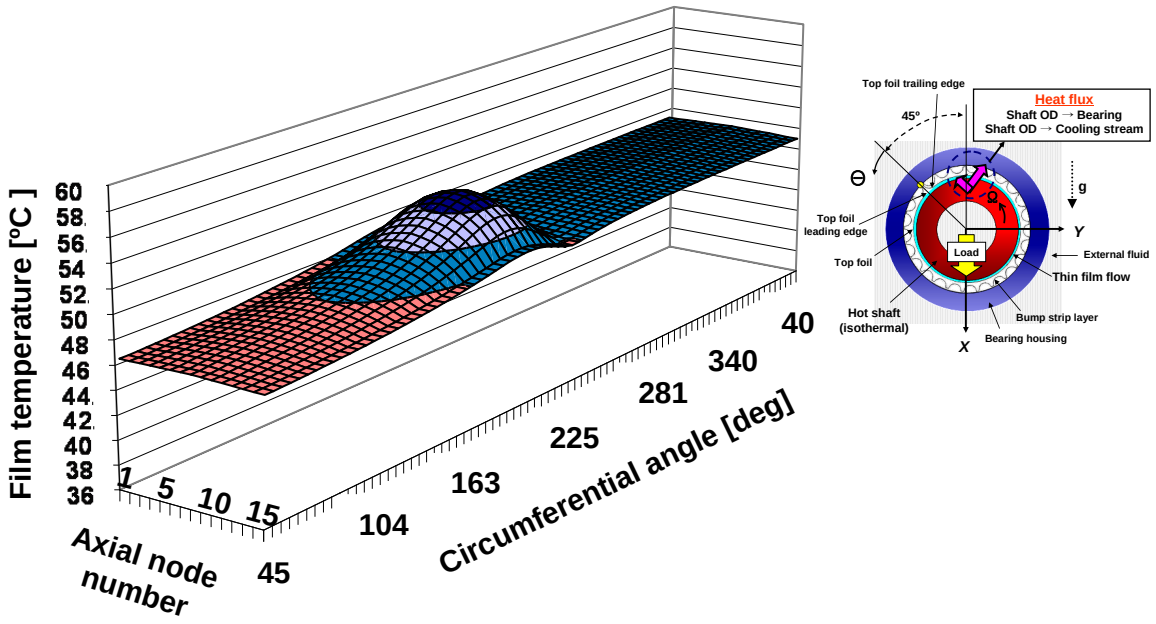

(b) Free end bearing

(Cooling stream inlet temperature= 41ºC, uniform rotor OD temperature= 56ºC, T_a= 24ºC)

Fig. 42 Prediction: Test case #5. Thin film temperature fields in GFBs. T_{hs}=100ºC, rotor speed at 30 krpm. Cooling flow rate per each bearing 25 L/min. Thermal mixing coefficient λ=0.65.

7.2 Prediction of Rotor Imbalance Responses and Comparison to Test Data

The rotordynamic analysis consists of modeling of the test rotor structure using XLTRC^2® and predicting the force coefficients of GFBs using XLGFBTH©. Tables 3 and 4 list the predicted GFB dynamic force coefficients at a frequency synchronous with rotor speed.

Appendix M shows the predicted GFB journal eccentricity, attitude angle, minimum film thickness, and drag torque. The cooling flow rate into each bearing decreases from 175 L/min to 25 L/min with a 50 L/min interval. The static load on each bearing equals a fraction of the rotor weight, 7.39 N and 5.94 N on the drive end and free end bearings, respectively. As the rotor speed increases, the journal eccentricity decreases while the journal attitude angle, the minimum film thickness and the bearing drag torque increase. In general, the journal eccentricity decreases with rotor OD temperature. The GFB operating at T_{hs}=150°C with low cooling stream (25 L/min per bearing) shows the largest journal eccentricities. Note that the minimum film thickness largely relies on gas viscosity and the bearing operating clearance. The attitude angle, minimum film thickness, and drag torque do not change noticeably with rotor temperature. When the rotor speed increases from 10 krpm to 30 krpm, the predicted bearing drag torque increases nearly twice.

For test case #5, Figs. 43 and 44 depict the GFB force coefficients calculated at a whirl frequency synchronous with rotor speed. Note that direction *X* is along the static load direction, i.e., vertical. In each figure, graphs (a) and (b) depict the stiffness and damping coefficients for the drive end bearing; graphs (c) and (d) display those for the

free end bearing. Note the different vertical scale between the direct and cross-coupled force coefficients. The inset figure shows the coordinate system.

High rotor speed renders lower stiffness and damping coefficients, both direct and cross-coupled. The force coefficients along the static load direction (X) are larger than those along the Y direction (horizontal), i.e., $K_{xx} > K_{yy}$ and $C_{xx} > C_{yy}$ denoting stiffness and damping asymmetry. Note that the GFB rotordynamic force coefficients do not change significantly with the strength of the cooling flow rate. The cross-coupled stiffnesses decrease with rotor speed due to high eccentricities (71 μm − 121 μm, see Appendix M). Recall that for the non-rotating shaft at room temperature, the estimated radial clearance for each bearing is ~100 μm (Fig. 14). Appendix O displays the predicted GFB force coefficients for test cases #4 and #6. In general, the stiffness and damping coefficients of the drive end bearing are slightly higher than those of the free end bearing due to its larger static load mainly.

Table 3 Complete drive end bearing predicted dynamic force coefficients (whirl frequency synchronous with rotor speed)

Test Case #	T_{hs} [ºC]	Rotor speed [krpm]	Cooling flow rate (per bearing) [L/min]	$T_{Co}=T_e$ [ºC] (1)	T_{amb} [ºC] (1)	Rotor OD [ºC] (1)(2)	K_{xx} [MN/m]	K_{xy} [MN/m]	K_{yx} [MN/m]	K_{yy} [MN/m]	C_{xx} [Ns/m]	C_{xy} [Ns/m]	C_{yx} [Ns/m]	C_{yy} [Ns/m]
7	Off	10	175	25	23	33	0.83	0.55	0.09	0.29	896	235	416	250
7	Off	20	175	25	23	33	0.50	0.43	0.03	0.29	332	99	189	163
7	Off	30	175	25	23	33	0.39	0.37	-0.01	0.29	188	51	114	123
4,8	65	10	175	30	29	43	0.78	0.52	0.08	0.28	841	225	396	250
4,8	65	20	175	32	29	50	0.46	0.40	0.01	0.28	307	93	177	164
4,8	65	30	175	36	28	53	0.36	0.35	-0.02	0.28	174	47	106	125
5,9	100	10	175	28	22	49	0.79	0.50	0.08	0.26	828	219	376	228
5,9	100	20	175	33	23	55	0.47	0.38	0.02	0.25	302	92	168	147
5,9	100	30	175	33	23	61	0.36	0.33	-0.01	0.26	169	49	102	113
6	150	10	175	37	26	70	0.74	0.46	0.07	0.23	749	206	340	211
4	65	10	125	31	29	45	0.77	0.51	0.08	0.27	822	223	387	244
4	65	20	125	34	29	50	0.46	0.39	0.01	0.27	301	92	173	159
4	65	30	125	38	28	57	0.36	0.33	-0.02	0.27	168	46	102	120
5	100	10	125	31	22	51	0.84	0.49	0.09	0.23	853	218	367	206
5	100	20	125	35	23	56	0.47	0.36	0.03	0.23	290	90	157	129
5	100	30	125	40	23	64	0.36	0.31	-0.03	0.22	159	49	94	96
6	150	10	125	42	27	72	0.81	0.44	0.09	0.20	759	199	321	180
4	65	10	75	34	28	46	0.77	0.51	0.08	0.27	818	223	385	244
4	65	20	75	38	28	53	0.45	0.38	0.01	0.27	296	91	170	158
4	65	30	75	36	28	49	0.36	0.34	-0.02	0.28	173	48	105	122
5	100	10	75	34	22	54	0.81	0.48	0.09	0.23	782	205	343	200
5	100	20	75	40	23	60	0.47	0.35	0.03	0.22	284	88	153	125
5	100	30	75	43	23	64	0.36	0.31	-0.02	0.22	159	50	94	96
6	150	10	75	48	27	75	0.77	0.42	0.08	0.20	694	185	297	170
4	65	10	25	38	28	46	0.77	0.51	0.08	0.27	818	224	386	245
4	65	20	25	37	29	44	0.47	0.40	0.02	0.28	309	94	178	161
4	65	30	25	39	29	47	0.37	0.35	-0.02	0.28	173	48	106	122
5,10	100	10	25	40	23	50	0.82	0.49	0.09	0.24	796	209	351	202
5,10	100	20	25	38	23	45	0.48	0.39	0.03	0.25	306	93	168	140
5,10	100	30	25	41	24	45	0.37	0.34	-0.04	0.25	172	51	103	107
6	150	10	25	57	28	79	0.73	0.40	0.08	0.19	637	173	275	161

(1) Obtained from the test data. Input parameters in the analytical model

(2) Represent rotor temperatures at the bearing locations. Estimated from a constant temperature gradient (linear temperature drop) from the recorded rotor FE and DE temperatures (Tr_{FE} and Tr_{DE}).

Table 4 Complete free end bearing predicted dynamic force coefficients (whirl frequency synchronous with rotor speed)

Test Case #	T_{hs} [ºC]	Rotor speed [krpm]	Cooling flow rate (per bearing) [L/min]	$T_{Co}=T_e$ [ºC] (1)	T_{amb} [ºC] (1)	Rotor OD [ºC] (1)(2)	K_{xx} [MN/m]	K_{xy} [MN/m]	K_{yx} [MN/m]	K_{yy} [MN/m]	C_{xx} [Ns/m]	C_{xy} [Ns/m]	C_{yx} [Ns/m]	C_{yy} [Ns/m]
7	Off	10	175	25	23	33	0.53	0.42	0.03	0.23	702	218	349	242
7	Off	20	175	25	23	33	0.32	0.32	-0.02	0.23	258	86	153	154
7	Off	30	175	25	23	33	0.26	0.28	-0.05	0.23	147	43	90	116
4,8	65	10	175	30	29	56	0.49	0.37	0.03	0.20	621	198	307	218
4,8	65	20	175	32	29	63	0.29	0.28	-0.03	0.20	225	77	131	136
4,8	65	30	175	36	28	67	0.24	0.25	-0.05	0.20	129	39	77	104
5,9	100	10	175	28	22	65	0.49	0.35	0.03	0.19	603	193	293	207
5,9	100	20	175	33	23	74	0.29	0.27	-0.02	0.18	217	76	125	130
5,9	100	30	175	33	23	80	0.23	0.23	-0.05	0.19	124	39	74	99
6	150	10	175	37	26	98	0.45	0.30	0.02	0.16	519	173	252	182
4	65	10	125	31	29	57	0.50	0.36	0.03	0.19	600	189	288	194
4	65	20	125	34	29	63	0.29	0.27	-0.02	0.18	217	76	124	121
4	65	30	125	38	28	69	0.23	0.23	-0.04	0.18	122	40	73	91
5	100	10	125	31	22	67	0.51	0.33	0.04	0.17	570	177	263	171
5	100	20	125	35	23	75	0.29	0.25	-0.01	0.16	206	74	115	109
5	100	30	125	40	23	85	0.22	0.21	-0.03	0.16	114	40	68	81
6	150	10	125	42	27	103	0.48	0.27	0.03	0.13	473	150	211	135
4	65	10	75	34	28	60	0.50	0.35	0.03	0.18	591	185	281	188
4	65	20	75	38	28	66	0.29	0.26	-0.01	0.18	214	75	122	118
4	65	30	75	36	28	58	0.24	0.24	-0.04	0.19	128	41	77	97
5	100	10	75	34	22	70	0.51	0.32	0.03	0.16	561	174	257	166
5	100	20	75	40	23	80	0.29	0.24	-0.01	0.16	200	73	112	105
5	100	30	75	43	23	83	0.22	0.21	-0.03	0.16	114	40	68	81
6	150	10	75	48	27	106	0.48	0.27	0.03	0.13	466	148	208	133
4	65	10	25	38	28	59	0.51	0.35	0.03	0.18	594	186	283	189
4	65	20	25	37	29	53	0.30	0.28	-0.02	0.19	227	79	132	130
4	65	30	25	39	29	56	0.24	0.25	-0.04	0.19	128	41	78	97
5,10	100	10	25	40	23	66	0.51	0.33	0.03	0.17	574	178	265	172
5,10	100	20	25	38	23	57	0.30	0.27	-0.01	0.18	224	78	127	121
5,10	100	30	25	41	24	56	0.24	0.24	-0.04	0.19	128	42	77	94
6	150	10	25	57	28	110	0.48	0.27	0.03	0.13	473	150	211	135

(1) Obtained from the test data. Input parameters in the analytical model

(2) Represent rotor temperatures at the bearing locations. Estimated from a constant temperature gradient (linear temperature drop) from the recorded rotor FE and DE temperatures (Tr_{FE} and Tr_{DE}).

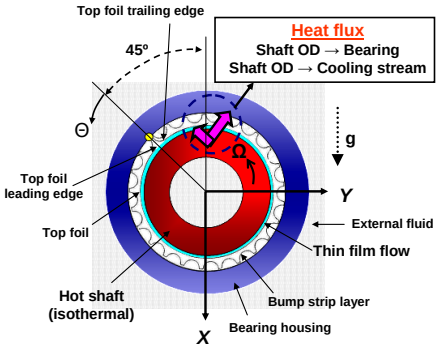

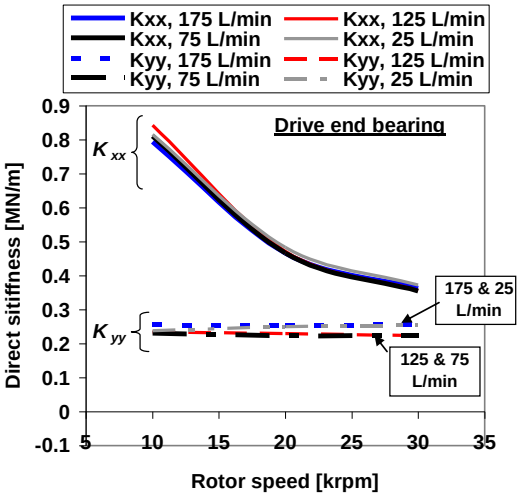

(a) Direct stiffness. Drive end bearing

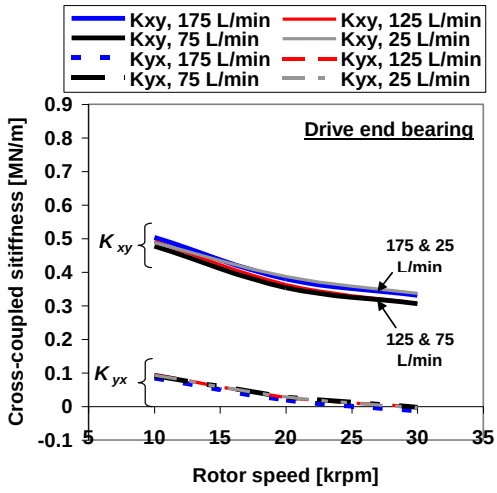

(b) Cross-coupled stiffness: Drive end bearing

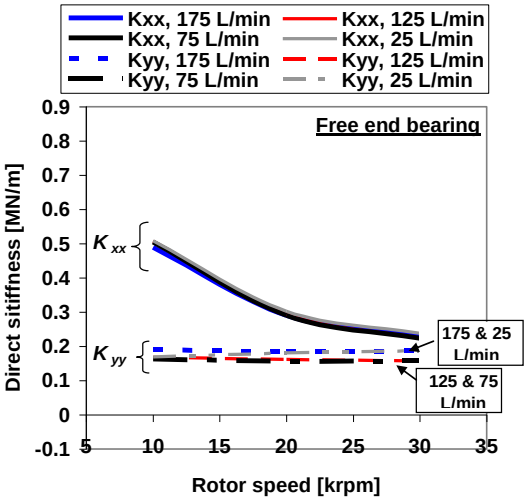

(c) Direct stiffness. Free end bearing

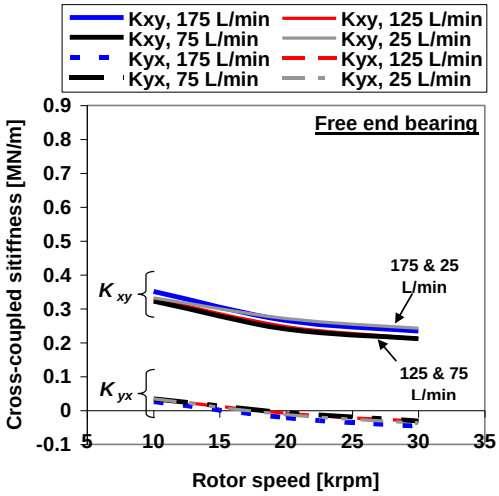

(d) Cross-coupled stiffness: Free end bearing

Fig. 43 Prediction: T_{hs}=100ºC. Drive end and free end foil bearing direct and cross-coupled stiffness versus rotor speed and increasing air cooling flow rates.

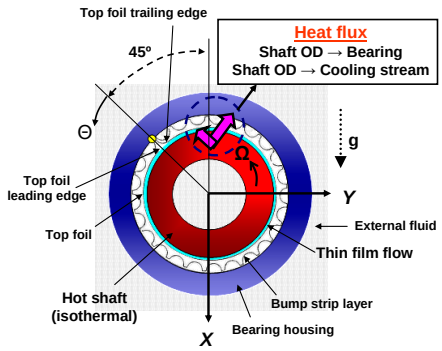

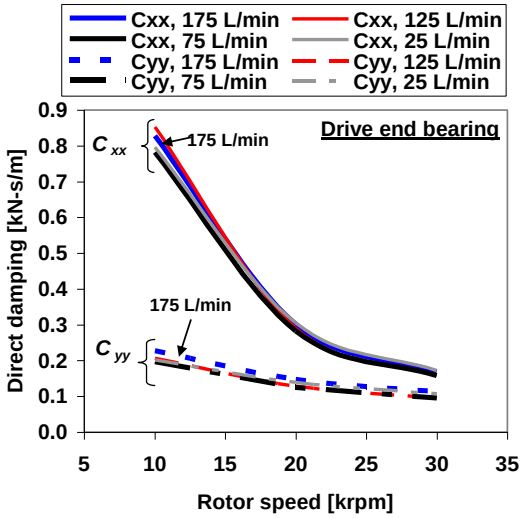

(a) Direct damping. Drive end bearing

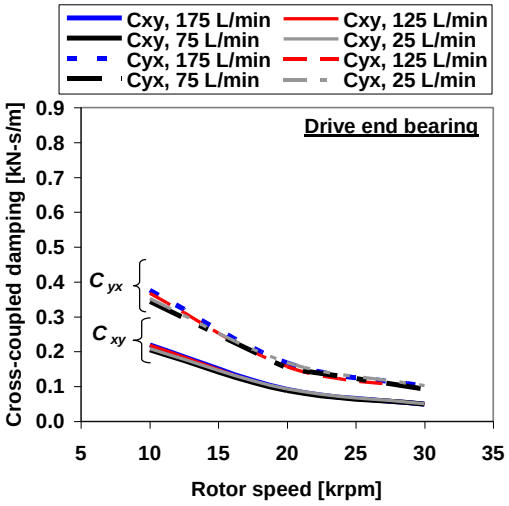

(b) Cross-coupled damping: Drive end bearing

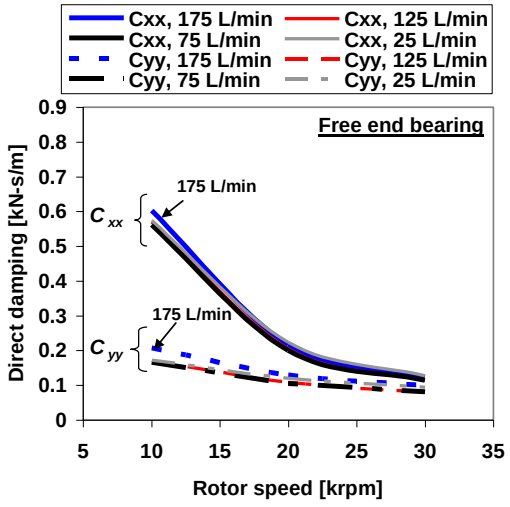

(c) Direct damping. Free end bearing

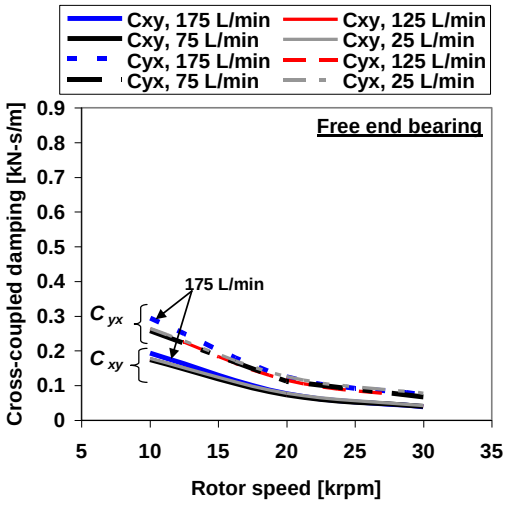

(d) Cross-coupled damping: Free end bearing

Fig. 44 Prediction: T_{hs}=100ºC. Drive end and free end foil bearing direct and cross-coupled damping coefficients versus rotor speed and increasing air cooling flow rates.

Figure 45 shows the 15 finite element structural model of the test rotor. The lateral stiffness of the flexible coupling is ~4 N/mm [14].

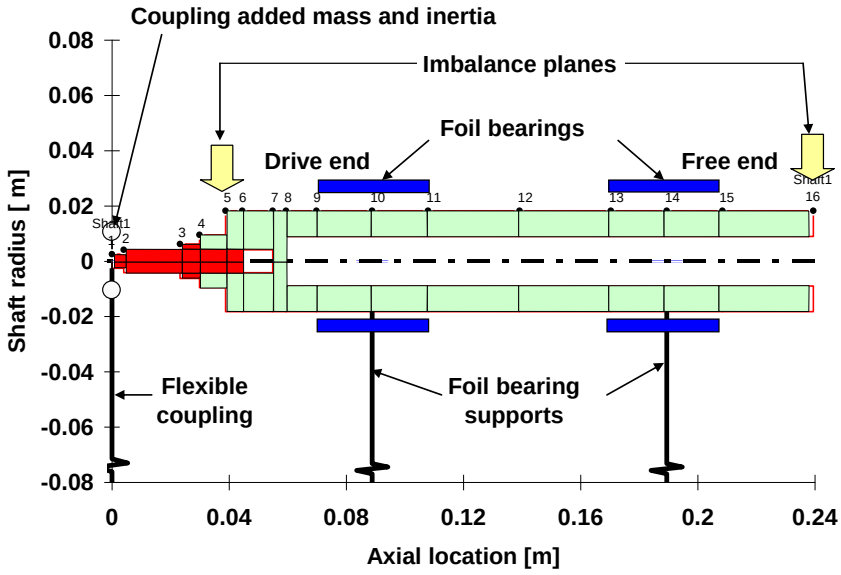

Fig. 45 Finite element model of test rotor supported on GFBs. Connecting rod and flexible coupling locate at drive end.

The predicted synchronous force coefficients of the bearings are incorporated into XLTRC^2® for prediction of the rotor imbalance response. The eigenvalue analysis of the rotor-GFB system renders the natural frequencies and modal damping ratios, depicted in Figs. 46 and 47. Figure 46 depicts the predicted damped natural frequencies of the test rotor-bearing system for test case #9 (T_{hs}=100°C). The figure also shows the four rigid body modes (forward conical and cylindrical modes and backward conical and cylindrical modes) and predicted forward mode critical speeds at 3.2 and 3.8 krpm and backward mode critical speeds at 4.3, 6.8, and 7.6 krpm. Note that the test results show

two distinctive critical speeds ~4 kprm and ~8 krpm as shown in Fig. 34. For the same test case, Fig. 47 depicts the predicted modal damping ratio versus rotor speed. The 3rd and 4th mode critical speeds are well-damped, damping ratio 0.65−0.89, while the 1st and 2nd mode shows a lower damping ratio ~0.1. The 2nd system natural mode renders a negative damping ratio for rotor speeds above ~12 krpm. This implies an unstable system. However, in the experiments, no rotordynamic instability ever occurred over for the entire speed range. Table 5 lists the predicted system critical speeds and damping ratios.

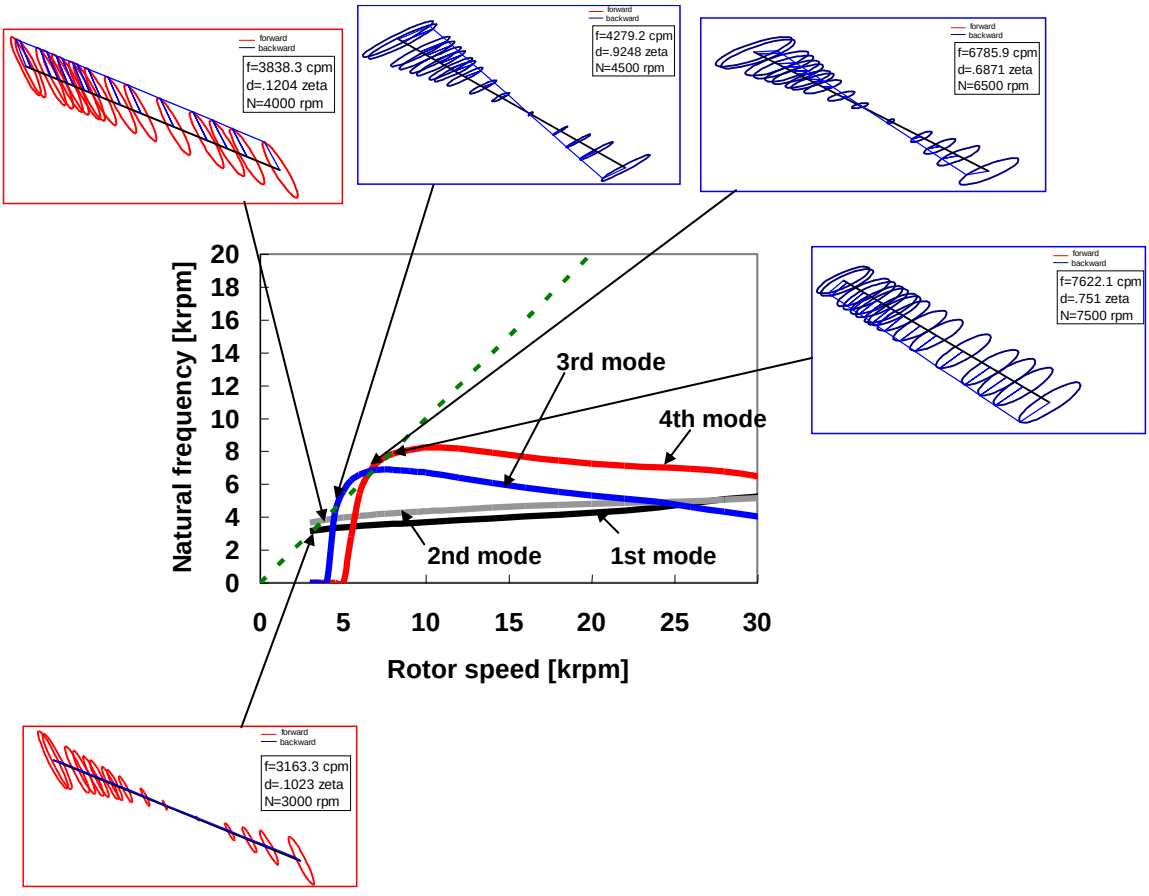

Fig. 46 Predicted damped natural frequency map of test rotor-GFB system. Mode shapes denoted. Test cases #5 and #9 (T_{hs}=100°C).

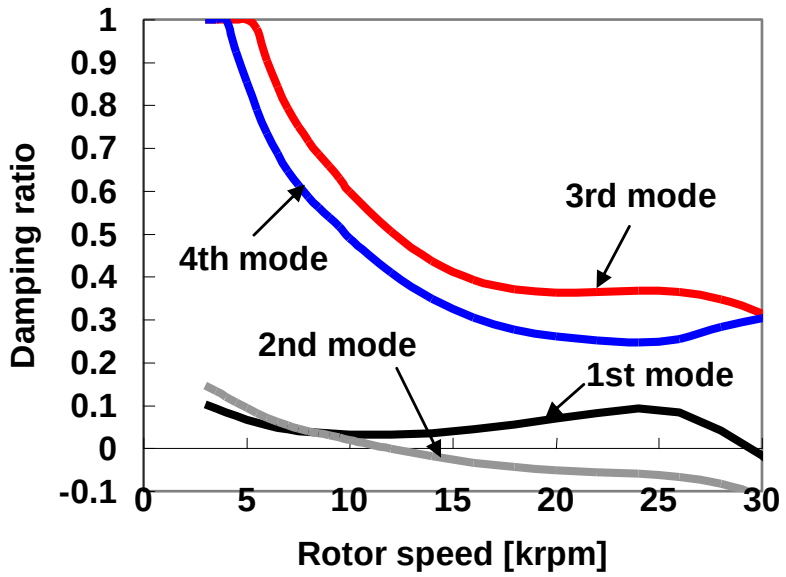

Fig. 47 Predicted damping ratio of test rotor-GFB system. Test cases #5 and #9 (T_{hs}=100°C).

Table 5 Predicted natural frequencies and damping ratios of rotor-GFB system for test cases #4,5, and 7−9

Test case #	Temperature [°C]			Cooling flow rate (per bearing) [L/min]	Predicted natural mode							
	T_{hs}	Rotor OD at 30 krpm			1st mode (Conical forward)		2nd mode (Cylindrical forward)		3rd mode (Conical backward)		4th mode (Cylindrical backward)	
		Drive end	Free end		N.F. (2) [krpm]	$\zeta^{(3)}$	N.F. (2) [krpm]	$\zeta^{(3)}$	N.F. (2) [krpm]	$\zeta^{(3)}$	N.F. (2) [krpm]	$\zeta^{(3)}$
7	Off	32 (33)(1)	33 (33)(1)	175	3.3	0.10	3.9	0.12	5.2 6.9	0.89 0.70	7.5	0.77
4,8	65	49 (53)(1)	71 (67)(1)	175	3.2	0.11	3.9	0.13	5.4 6.8	0.86 0.65	7.1	0.81
5,9	100	54 (61)(1)	87 (80)(1)	175	3.2	0.10	3.8	0.12	5.6 6.9	0.85 0.65	7.2	0.80

(1) The numbers in parentheses refer to the estimated rotor OD temperature at the bearing locations.

(2) N.F.= Natural frequency.

(3) ζ = Damping ratio.

Figure 48 presents the predicted and measured synchronous rotor responses for test cases #7 though #9. In the figure, the rotor motion measurements are along the horizontal planes near the rotor free end (FH) and drive end (DH). In the predictions, estimated imbalance masses are 0.01 gram·mm at the rotor drive end and 0.3 gram·mm at the rotor free end (see Fig. 45), with 180º out of phase[29]. The comparison between predicted and recorded rotor responses is less favorable at ~8 krpm; the experiments show a narrow peak at this speed, while the predicted rotor motion does not show a peak amplitude because of the large damping ratio (see Table 5). In addition, the predicted system critical speeds are well-damped, thereby rendering significantly lower rotor response amplitudes than those experimentally recorded. Note that large dynamic displacements near the system natural frequencies are typical of a mechanical system with dry-friction [48]. In FBs, Coulomb-type damping (dry friction) arises due to the relative motions between the bumps and the top foil, and between the bumps and the bearing cartridge ID, see Ref. [39].

[29] The actual mass imbalance distribution is unknown.

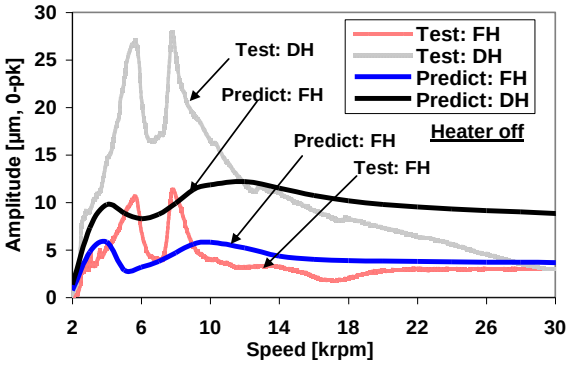

(a) Test case #7

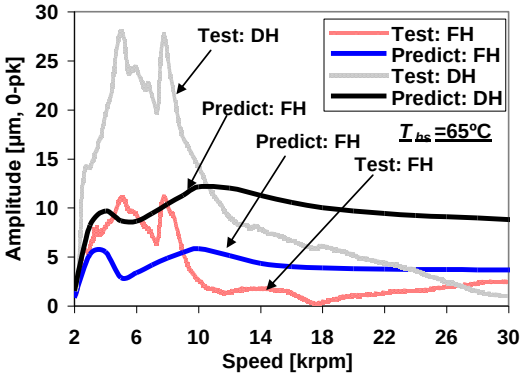

(b) Test case #8

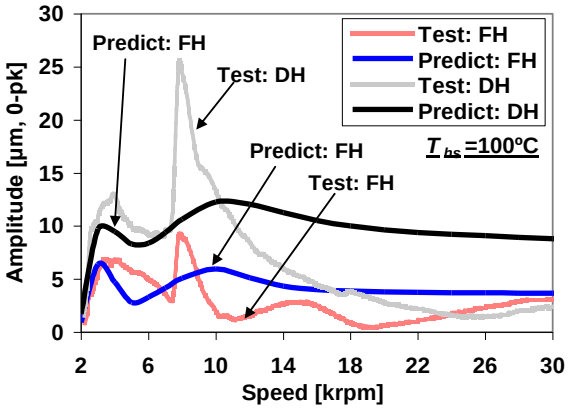

(c) Test case #9

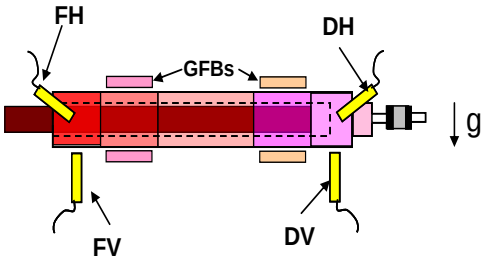

Imbalance Station #	Imbalance Amount gm*cm	Imbalance Phase deg
5	0.01	0
16	0.3	180

Fig. 48 Comparison of predicted and measured imbalance responses of test rotor supported on foil bearings. Estimated mass imbalance distribution noted.

CHAPTER VIII

CONCLUSIONS AND RECOMMENDATIONS

Successful implementation of gas foil bearings (GFBs) into high temperature rotating machinery rely on comprehensive and reliable performance measurements and accurate prediction models. An engineered thermal management in a hot rotor-GFB system is fundamental to avoid failure of a GFB thus increasing system reliability.

This dissertation presents measurements of temperatures in a laboratory rotor supported on gas foil bearings. The system operates at an elevated temperature (max. rotor OD temperature 120 ºC). An Inconel 718 hollow rotor (1.360 kg, 36.51 mm OD and 17.9 mm ID) is supported on two 1st generation GFBs. The rotor surface has a patented high temperature coating on its surface; the mating top foils have no surface coating. An electric cartridge heater inserted in the hollow rotor with a 1 mm radial gap warms the rotor unevenly. Thermocouples and non-contact infrared thermometers record the temperature of the bearing cartridges mid-plane and rotor surfaces, respectively. A forced air cooling stream (max. 420 L/min) is supplied axially on one side of the test bearings. The research focuses on evaluating the effectiveness of the cooling stream to reduce (control) the temperatures in the bearings and rotor.

When the rotor is stationary, the rotor and bearing temperatures steadily increase with cooling flow rate. At T_{hs}=100°C, for example, the free end rotor OD and FE bearing temperatures increase by ~20% (50°C→60°C) and ~200% (7°C→14°C), respectively, while decreasing cooling flow rate from 400 L/min to 0 L/min. When the shaft rotates,

temperature rises on the rotor and bearings are a strong function of shaft speed and the cooling flow rate into the bearings. The recorded temperatures on the bearings and rotor increase with rotor speed due to mechanical energy dissipation from viscous drag. The free end bearing temperature increases more than 200% (7°C→16°C) when the rotor speed increases from 0 to 30 krpm at 400 L/min of cooling flow rate and at T_{hs}=100°C.

The forced gas cooling stream plays a significant factor on the thermal management of the rotor-GFB system. As the cooling flow rate decreases, the gas flowing through a feed enclosure has a longer residence time, thus increasing its temperature. For example, as the cooling flow rate decreases from 400 L/min to 50 L/min at T_{hs}=100°C and 30 krpm, ($T_e - T_{amb}$) increases from 9°C to 18°C. The bearings sleeve temperature increases with the air temperature inside the feed enclosure. The rate of decrement in the recorded bearing temperature, calculated as the temperature rise per unit cooling flow rate, increases significantly as the strength of the cooling flow rate decreases. The temperature rises per unit cooling flow rate for the FE bearing and FE rotor temperatures increase by ~660% (~0.05°C/L/min→~0.35°C/L/min) and ~300% (~0.2°C/L/min→~0.8°C/L/min), respectively, when the cooling flow rate decreases from ~400 L/min to ~50 L/min at T_{hs}=100°C. Thus adequate thermal management using a cooling flow carries away heat from the foil bearings and controls the bearing temperatures. When the cooling air flow rates increases, the flow speed increases and there is not enough residence time for the passing air to remove heat more effectively.

Rotor speed-down tests for various rotor OD temperatures and strengths of cooling flow rate show an insignificant effect on the rotordynamic response of the test

system. Waterfall of rotor vibration show that there is no marked differences in the amplitude and frequency content of the rotor dynamic response while the rotor temperature and cooling flow increase.

Model predictions are benchmarked against the test data. The predicted bearing temperatures are in remarkable agreement with those measured. A rotor FE structural model and GFBs force coefficients from the TEHD model are used to predict the test system critical speeds and damping ratios for operation at increasing shaft temperatures. The predicted rotor responses agree reasonably with the measurements.

A thermal model for shaft temperature prediction along its axial length is necessary for more accurate estimation of the bearing performance characteristics. This is because the shaft surface temperature determines the film temperature and the gas viscosity and density, and the operating clearances which change due to thermal expansion of the components.

The quantitative assessment for the thermal management in a rotor-GFB system requires considerable empirical experience. Thermal runaway can easily occur when very low cooling flows are supplied. Cooling flow into GFBs diminishes the severity of thermal gradients and prevents hot-spots in the bearings, thereby extending their life, for example. The present work continues to extend the GFB knowledge database and provides guidance on system component integration for foil bearing application at high temperature. Most importantly, the present work provides to date the most complete measurements (rotordynamic response and temperature) on a rotor-gas foil bearing system operating hot.

REFERENCES

[1] Bruckner, R. J., 2004, "A Propulsion System Analysis of Oil Free Turbomachinery for Aviation Turbofan Engines," AIAA Paper No. 2004-4189.

[2] DellaCorte, C., and Valco, M. J., 2003, "Oil-Free Turbomachinery Technology for Regional Jet, Rotorcraft and Supersonic Business Jet Propulsion Engines," AIAA Paper No. ISABE-2003-1182.

[3] DellaCorte, C., Zaldana, A., Radil, K., 2003, "A System Approach to the Solid Lubrication of Foil Air Bearing for Oil-Free Turbomachinery," ASME J. Tribol., **126**(1), pp. 200−207.

[4] DellaCorte, C., and Pinkus, O., 2000, "Tribological Limitations in Gas Turbine Engines: A Workshop to Identify the Challenges and Set Future Directions," National Aeronautics and Space Administration, Report No. NASA/TM 2000-210059, Cleveland, OH.

[5] Heshmat, H., and Walton, J. F., 2000, "Oil-Free Turbocharger Demonstration Paves Way to Gas Turbine Engine Applications," ASME Paper No. 2000-GT-620.

[6] DellaCorte, C., and Edmonds, B. J., 2009, "NASA PS400: A New High Temperature Solid Lubricant Coating for High Temperature Wear Applications," National Aeronautics and Space Administration, Report No. NASA/TM—2009-215678, Cleveland, OH.

[7] DellaCorte, C., and Valco, M., 2000, "Load Capacity Estimation of Foil Air Journal Bearing for Oil-Free Turbomachinery Applications," STLE Tribol. Trans., **43**(4), pp. 795–801.

[8] Ku, C.-P. R., and Heshmat, H., 1993, "Compliant Foil Bearing Structural Stiffness Analysis−Part II: Experimental Investigation," ASME J. Tribol., **115**(3), pp. 364−369.

[9] Rubio, D., and San Andrés, L., 2006, "Bump-Type Foil Bearing Structural Stiffness: Experiments and Predictions," ASME J. Eng. Gas Turbines Power, **128**(3), pp. 653−660.

[10] Rubio, D., and San Andrés, L., 2007, "Structural Stiffness, Dry Friction Coefficient, and Equivalent Viscous Damping in a Bump-Type Foil Gas Bearing," ASME J. Eng. Gas Turbines Power, **129**(2), pp. 494−502.

[11] Valco, M. J., and DellaCorte, C., 2002, "Emerging Oil-Free Turbomachinery Technology for Military Propulsion and Power Applications," *Proceedings of the 23rd U.S. Army Science Conference*, Orlando, FL, Dec. 2−5.

[12] Dykas, B. D., 2006, "Factors Influencing the Performance of Foil Gas Thrust Bearings for Oil-Free Turbomachinery Applications," Ph.D. Dissertation, Case Western Reserve University, Cleveland, OH.

[13] Dykas, B. D., 2003, "Investigation of Thermal and Rotational Contributions to the Catastrophic Failure Mechanism of a Thin-Walled Journal Operating with Foil Air Bearings," MS Thesis, Case Western Reserve University, Cleveland, OH.

[14] San Andrés, L. Kim, T.H., and Ryu, K., 2009, "Thermohydrodynamic Analysis of Bump Type Gas Foil Bearings: A Model Anchored to Test Data," Final Project Report to NASA SSRW2-1.3 Oil Free Engine Technology Program.

[15] Blok, H. and van Rossum, J. J., 1953, “The Foil Bearing – A New Departure in Hydrodynamic Lubrication,” ASLE J. Lubr. Eng., **9**(6), pp. 316−320.

[16] Heshmat, H, 1994, “Advancements in the Performance of Aerodynamic Foil Journal Bearings High Speed and Load Capability,” ASME J. Tribol., **116**(2), pp. 284−295.

[17] Klaass, R. M., and DellaCorte, C., 2006, “The Quest for Oil-Free Gas Turbine Engines,” SAE Technical Papers, No. 2006-01-3055.

[18] Koepsel, W. F., 1977, “Gas Lubricated Foil Bearing Development for Advanced Turbomachines,” Technical report No. AFAPL-TR-76-114, AiResearch Manufacturing Company of Arizona, Phoenix, AR.

[19] Suriano, F. J., 1981, “Gas Foil Bearing Development Program,” Technical Report No. AFWAL-TR-81-2095, Garrett Turbine Engine Company, Phoenix, AR.

[20] Ruscitto, D., McCormick, J., and Gray, S., 1978, “Hydrodynamic Air Lubricated Compliant Surface Bearing for an Automobile Gas Turbine Engine I—Journal Bearing Performance,” National Aeronautics and Space Administration, Report No. NASA CR-135368.

[21] DellaCorte, C., 1998, “A New Foil Air Bearing Test Rig for Use to 700°C and 70,000 rpm,” STLE Tribol. Trans., **41**(3), pp. 335−340.

[22] Radil, K.C., and DellaCorte, C., 2010, “A Three-Dimensional Foil Bearing Performance Map Applied to Oil-Free Turbomachinery,” STLE Tribol. Trans., **53**(5), pp. 771−778.

[23] Radil, K.C., DellaCorte, C., and Zeszotek, M. 2007, “Thermal Management Techniques for Oil-Free Turbomachinery Systems,” STLE Tribol. Trans., **50**(3), pp. 319−327.

[24] Lee, D., Kim, D., and Sadashiva, R. P., 2011, “Transient Thermal Behavior of Preloaded Three-Pad Foil Bearings: Modeling and Experiments,” ASME J. Tribol., **133**(2), p. 021703.

[25] Lee, D., and Kim, D., 2010, “Thermohydrodynamic Analyses of Bump Air Foil Bearings with Detailed Thermal Model of Foil Structure and Rotor,” ASME J. Tribol., **132**(2), p. 021704.

[26] Kirschmann, A. E., and Agrawal . G. L., 1998, “High Temperature Foil Air Bearing Development for a Missile/UAV Engine Application,” *Proceedings of the 35th JANNAF Propulsion Meeting*, **1**, pp. 101−108, Tucson, AZ, Dec. 7−11.

[27] Walton, J. F., Heshmat, H., and Tomaszewki, M. J., 2004, “Testing of a Small Turbocharger/Turbojet Sized Simulator Rotor Supported on Foil Bearings,” ASME Paper No. GT2004-53647.

[28] Heshmat, H., Walton J. F., and Tomaszewski, M. J., 2005, "Demonstration of a Turbojet Engine Using an Air Foil Bearing," ASME Paper No. GT2005-6804.

[29] Larue, G. D., Kang, S. G., and Wick, W., 2006, “Turbocharger with Hydrodynamic Foil Bearings,” U.S. Patent No. 7,108,488 B2.

[30] Lubell, D., and Weissert, D., 2006, “Rotor and Bearing System for a Turbomachine,” U.S. Patent No. 7,112,036 B2.

[31] Lubell, D., DellaCorte, C., and Stanford, M.K., 2006, "Test Evolution and Oil-Free Engine Experience of a High Temperature Foil Air Bearing Coating," ASME Paper No. GT2006-90572.

[32] Lee, Y. B., Kim, C. H., Park, D. J., and Jo, J. H., 2008, "Medium Temperature Coating Material for High Speed Turbomachinery and Method of Coating Same," US Patent Application Publication No. US 2008/0057223 A1.

[33] DellaCorte, C., and Edmonds, B. J., 1999, "Self-Lubricating Composite Containing Chromium Oxide," U.S. Patent No. 5,866,518.

[34] Radil, K. C., and DellCorte, C., 2002, "The Effect of Journal Roughness and Foil Coatings on the Performance of Heavily Loaded Foil Air Bearings," STLE Tribol. Trans., **45**(2), pp. 199−204.

[35] OMEGA Engineering, 2010, "User's Guide: OS550A/OS550AM/OS550A," Industrial Infrared Thermometer/Transmitter, Stamford, CT, http://www.omega.com/pptst/OS550A.html (accessed Oct. 2011).

[36] Y. B. Lee; T. H. Kim; C. H. Kim; N. S. Lee, 2003, "Suppression of Subsynchronous Vibrations due to Aerodynamic Response to Surge in a Two-Stage Centrifugal Compressor with Air Foil Bearings," STLE Tribol. Trans., **46**(3), pp. 428−434.

[37] San Andrés, L. Kim, T.H., and Ryu, K., 2009, "Thermohydrodynamic Analysis of Bump Type Gas Foil Bearings: A Model Anchored to Test Data, Appendix M. Structural Load Capacity of KIST Foil Bearings," 7th Quarter Research Progress Report to NASA SSRW2-1.3 Oil Free Engine Technology Program, May 31.

[38] San Andrés, L., and Kim, T.H., 2008, "Forced Nonlinear Response of Gas Foil Bearing Supported Rotors," Tribol. Int., **41**(8), pp. 704−715.

[39] San Andrés, L., Ryu, K., and Kim, T.H., 2011, "Identification of Structural Stiffness and Energy Dissipation Parameters in a Second Generation Foil Bearing – Effect of Shaft Temperature," ASME J. Eng. Gas Turbines Power, **133**(3), p. 032501.

[40] Mott, R. L., 1999, *Machine Elements in Mechanical Design*, Third Edition, Prentice-Hall, Inc., Upper Saddle River, NJ, pp. 529−532.

[41] Heshmat, H., Tomaszewski, M., and Walton, J.F., 2006 "Small Gas Turbine Engine Operating with High Temperature Foil Bearings," ASME Paper No. GT2006-90791.

[42] Swain, R., and Preater, R., 1997, "Investigation of Windage Heating Effects on Rotating Components Using Pulsed ESPI," Opt. Laser. Eng., **26**, pp. 377−394.

[43] Millward, J. A. and Edwards, M. F., 1996, "Windage Heating of Air Passing Through Labyrinth Seals," ASME J. Turbomach., **118**(2), pp. 414−419.

[44] Bruckner, R. J., 2009, "Windage Power Loss in Gas Foil Bearings and the Rotor-Stator Clearance of High Speed Generators Operating in High Pressure Environments," ASME Paper No. GT2009-60118.

[45] San Andrés, L., and Kim, T.H., 2010, "Thermohydrodynamic Analysis of Bump Type Gas Foil Bearings: A Model Anchored to Test Data," ASME J. Eng. Gas Turbines Power, **132**(4), p. 042504.

[46] Kim, T.H. and San Andrés, L., 2010, "Thermohydrodynamic Model Predictions and Performance Measurements of Bump-Type Foil Bearing for Oil-Free Turboshaft Engines in Rotorcraft Propulsion Systems," ASME J. Tribol., **132**(1), p. 011701.

[47] San Andrés, L., and Kim, T.H., 2008, "Numerical Solution of Transport Equations for Gas Film Pressure and Temperature in a Foil Bearing," 2nd Quarter Research Progress Report to NASA SSRW2-1.3 Oil Free Engine Technology Program, Mar. 31.

[48] Ginsberg, J. H., 2001, *Mechanical and Structural Vibrations, Theory and Applications*, 1st edition, John Wiley & Sons, Inc., New York, pp. 135−139.

[49] Special Metals Corporation, 2007, "Inconel® Alloy 718," Publication No. SMC-045, Huntington, WV, http://www.specialmetals.com/products/inconelalloy718.php, (accessed Oct. 2011).

[50] Special Metals Corporation, 2004, "Inconel® Alloy X-750," Publication No. SMC-067, Huntington, WV, http://www.specialmetals.com/products/inconelalloyx750.php, (accessed Oct. 2011).

[51] Kipp, D. O., 2010, "AISI 4140 Steel, Oil Quenched, 315°C (600°F) Temper, 25 mm (1 in.) Round," Metal Material Data Sheets, MatWeb-Division of Automation Creation, Inc., Blacksburg, VA, http://www.matweb.com (accessed on Oct. 2011)

[52] ASM International, 1988, "AISI 4140, Oil-Hardening Cr-Mo Steel," Alloy Digest - Data on World Wide Metals and Alloys, Filing Code SA-18, Materials Park, OH, http://products.asminternational.org/datasheets/index.jsp (accessed Oct. 2011).

[53] Fox, R. W., McDonald, A. T., and Pritchard, P. J., 2004, *Introduction to Fluid Mechanics*, Sixth Edition, John Wiley & Sons, Inc., Hoboken, NJ, pp. 720−722.

[54] Hirs, G.G., 1973, "A Bulk-Flow Theory for Turbulence in Lubricant Films," ASME J. Lub. Tech., **95**(2), pp. 137−146.

[55] Zirkelback, N., and San Andrés, L., 1996, “Bulk-Flow Model for the Transition to Turbulent Regime in Annular Pressure Seals,” STLE Tribol. Trans., **39**(4), pp. 835−842.

[56] Yamada, Y., 1962, “Resistance of Flow through an Annulus with an Inner Rotating Cylinder,” Bull. JSME, **5**(18), pp. 302−310.

[57] Childs, D. W., and Kim, C-H., 1985, “Analysis and Testing for Rotordynamic Coefficients of Turbulent Annular Seals with Different, Directionally-Homogeneous Surface-Roughness Treatment for Rotor and Stator Elements,” ASME J. Tribol., **107**(3), pp. 296−305.

[58] Ha, T. W., Childs, D. W., 1992, “Friction-Factor Data for Flat-Plat Tests of Smooth and Honeycomb Surfaces,” ASME J. Tribol., **114**(4), pp. 722−730.

[59] Nelson, C. C. and Nguyen, D. T., 1987, "Comparison of Hirs' Equation With Moody's Equation for Determining Rotordynamic Coefficients of Annular Pressure Seals," ASME J. Tribol., **109**(1), pp. 144−148.

[60] Black, H. F., Allaire, P. E., and Barrett, L. E., 1981, “Inlet Flow Swirl in Short Turbulent Annular Seal Dynamics,” *Proceedings of the Ninth International Conference in Fluid Sealing*, BHRA Fluid Engineering, Leeuwenborst, The Netherlands, Apr. 1–3, pp. 141–152.

APPENDIX A

MATERIAL PROPERTIES OF INCONEL 718, INCONEL X-750, AND AISI 4140

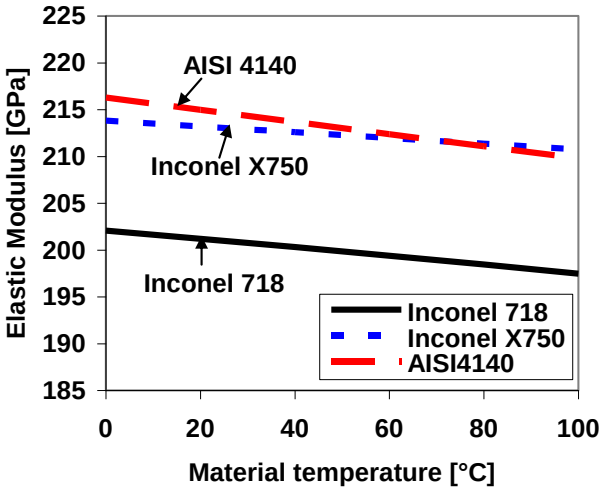

Fig. A.1 Elastic modulus versus material temperature for Inconel 718, Inconel X750, and AISI4140. Taken from [49−52].

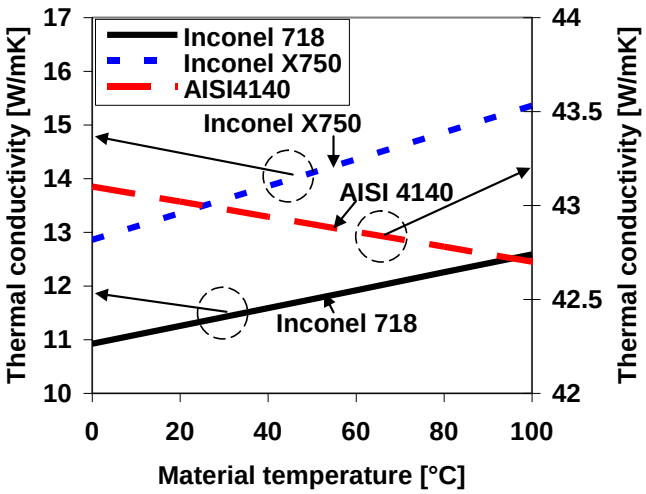

Fig. A.2 Thermal conductivity versus material temperature for Inconel 718, Inconel X750, and AISI4140. Taken from [49−52].

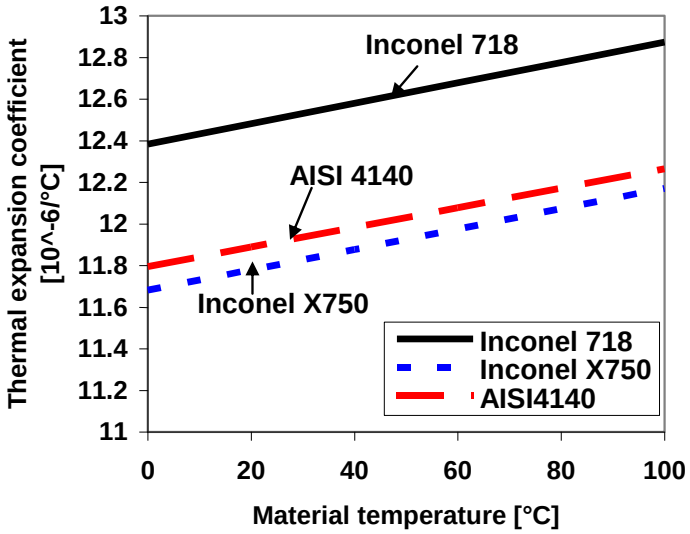

Fig. A.3 Thermal expansion coefficient versus material temperature for Inconel 718, Inconel X750, and AISI4140. Taken from [49−52].

Table A.1 Poisson's ratio, density, specific heat, and melting temperature of Inconel 718, Inconel X750, and AISI4140. Taken from [49−52]

	Inconel 718	Inconel X750	AISI 4140
Poisson's ratio [-]	0.284	0.29	0.3
Density [kg/m^3]	8220	8303	7833
Specific heat [J/kg-K]	473	440	473
Melting temperature [ºC]	1210	1393	1400

APPENDIX B

SPECIFICATIONS OF EQUIPMENT AND INSTRUMENTATION

Table B. 1 Specifications of major equipment and instrumentation for high temperature rotor-GFB test rig[30]

Item	Location in test rig	Specification	Vendor	Model #
High speed motor		9.5kW at 65krpm	KAES	MOO1C80905
Spindle drive	Motor controller	Power source for motor, input 380−480V, 3 phase, 50/60Hz	GMN	90-00124-8048-0000
Flexible Coupling		Rated torque 1.0 N-m, torsional stiffness 320 N-m/rad	R+W coupling technology	MK2/10/33
Water jet well pump	Water pump for motor cooling	¾ HP, 78 psi, 57L/min	Flotec	FP4022
Digital gas mass flow meter	Cooling flow rate into bearings	Max. 500L/min, accuracy ±1.5% of full scale	OMEGA	FMA1844, FMA178PW
Cartridge heater	T_h	Max. 1.6 kW with 240V	OMEGA	CSH-4101600/240
Heater controller	T_h	Programmable 1/8 DIN digital panel meter	OMEGA	CNi853
Thermocouple (K type)	T_1−T_{10}, T_e, T_{out}, T_{amb}	Up to 480°C, glass braid insulation	OMEGA	5SC-GG-K-30-36
Insulated thermocouple wire	T_1−T_{10}, T_e, T_{out}, T_{amb}	30m type K duplex insulated wire	OMEGA	PR-K-24-SLE-100
Thermocouple indicator	T_e, T_{out}, T_{amb}	Up to 1090°C, resolution 0.6°C	OMEGA	DP116-KF1
Benchtop thermometer	T_1− T_{10}	10-channel benchtop thermometer, dedicated thermocouple input with analog	OMEGA	MDSSi8A-TC
Infrared thermometer	Tr_{FE}, Tr_{DE}	Up to 1370°C, D/S Ratio 68:1, 5Vdc output, adjustable emissivity	OMEGA	OS552-V1-1

[30] Reference [14] fully lists the components of the test rig, including commercial designations and costs.

APPENDIX C

REPEATABILITY OF RECORDED TEMPERATURES:

TEST CASES #1 AND #3

Measurements for test cases #1 and #3 were repeated thrice (namely, tests 1, 2 and 3)[31]. Figures C.1 and C.2 depict the temperature rise of the free end rotor OD ($Tr_{FE} - T_{amb}$), free end bearing sleeve OD ($T_1 - T_{amb}$), drive end rotor OD ($Tr_{DE} - T_{amb}$), and air in the housing enclosure ($T_e - T_{amb}$) versus air cooling flow rate for test cases#1 and #3. The average variability is less than 5 °C for each test condition.

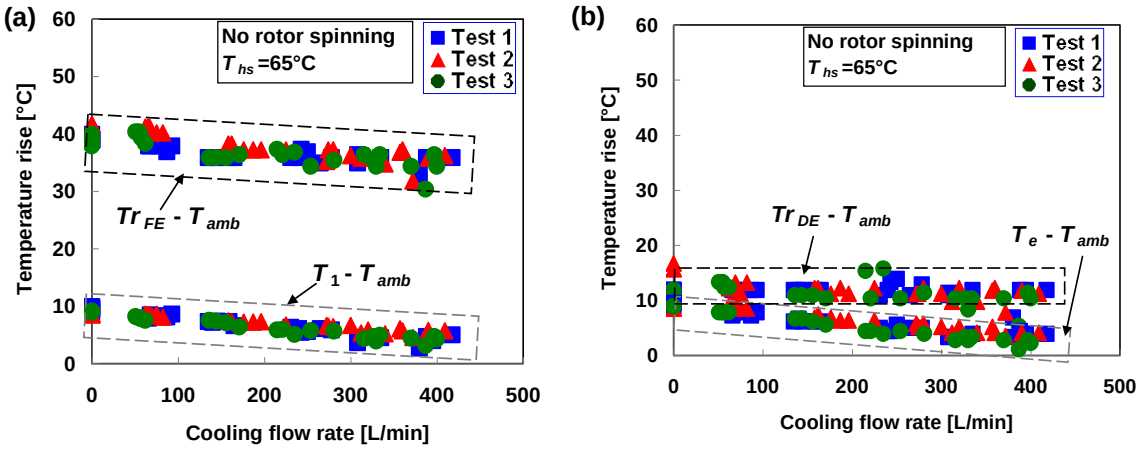

Fig. C.1 Test case #1. T_{hs}=65ºC. No rotor spinning: Recorded test system component temperature rises (T_i-T_{amb}; where $_{i}$ = (a) r_{FE} and 1, (b) r_{DE} and $_{e}$) versus cooling flow rate.

[31] In Figs. C.1 and C.2, temperatures for test 1 are taken from Figs. E.1 (shown later) and 17, respectively. The sets of tests 2 and 3 were conducted approximately seven months later after test 1.

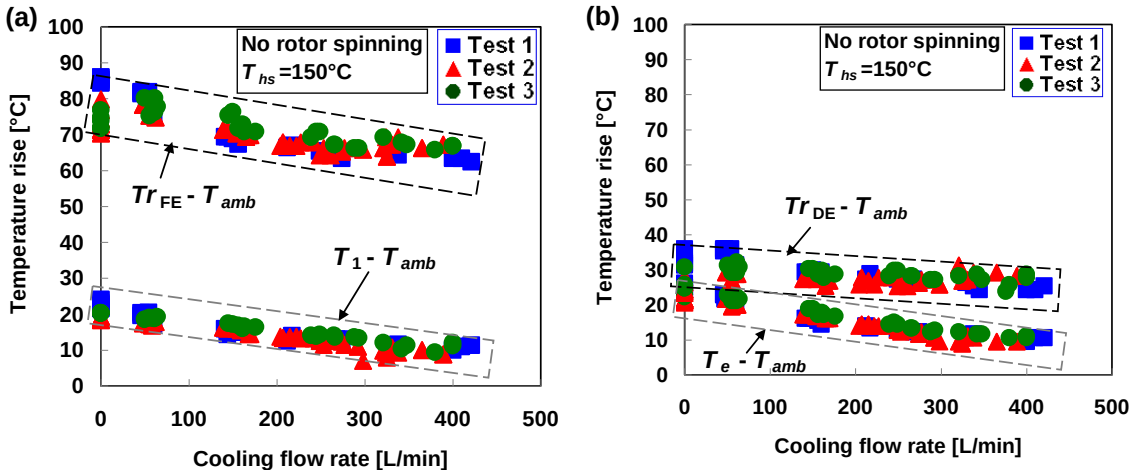

Fig. C.2 Test case #3. T_{hs}=150ºC. No rotor spinning: Recorded test system component temperature rises (T_i-T_{amb}; where $_{i}$ = (a) r_{FE} and 1, (b) r_{DE} and $_{e}$) versus cooling flow rate.

APPENDIX D

ELECTRIC POWER DELIVERED TO CARTRIDGE HEATER:

TEST CASE #3

Figure D.1 depicts the circuit diagram to measure the electric power delivered to the cartridge heater. Two multi-meters are connected in the heater controller circuit to measure voltage and current. The instruments displaying voltage and current digitally have uncertainties of 0.1V and 0.001A, respectively. While the heater set temperature T_{hs} is fixed at 150°C with a stationary shaft, measurements are conducted twice, namely tests 1 and 2. The test condition corresponds to test case #3. Note that the heater temperature is automatically controlled using a mechanical relay in a temperature controller.

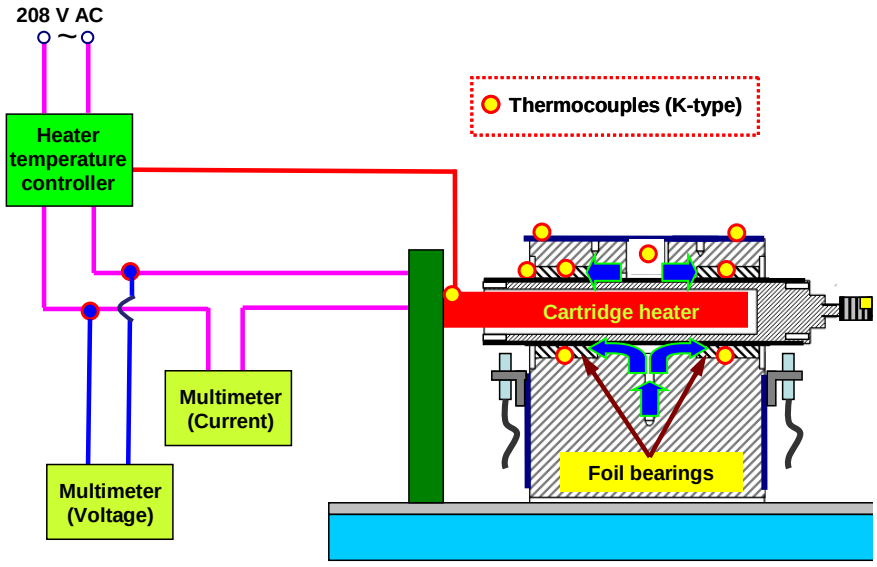

Fig. D.1 Schematic circuit diagram measuring voltage and current feeding the electrical heater.

Electric power, the rate at which electrical energy is transferred by an electric circuit, is calculated using Joule's law $P(t)=I(t)\cdot V(t)$, where $P(t)$ is the instantaneous power, $V(t)$ is the voltage drop across the heater, and $I(t)$ is the current through it.

Figure D.2 depicts the measured voltage and current of the heater circuit while decreasing the cooling flow rate. The recorded voltage remains nearly invariant for decreasing cooling flow strength (~205 V). As the cooling flow rate into the bearings decreases from ~400 L/min to ~150 L/min, the current decreases linearly from 5.64 A to 5.56 A to maintain the set heater temperature T_{hs}=150ºC. On the other hand, the current increases from 5.56 A to 5.64 A with decreasing cooling flow rate from ~150 to 0 L/min. The calculated electric power delivered to the heater follows a similar trend as with the recorded current, see Fig. D. 3.

Note that the heater does not only heats the rotor but also its surroundings; including the bearings and the enclosure. That is, the required power is also a function of the bounding solids and ambient conditions. As the cooling flow rate decreases, the air in the enclosure increases its temperature since it is not removed (quickly) by the cooling air stream. Something similar will happen with the bearing sleeves. Thus, the electric power increases at low flow rates.

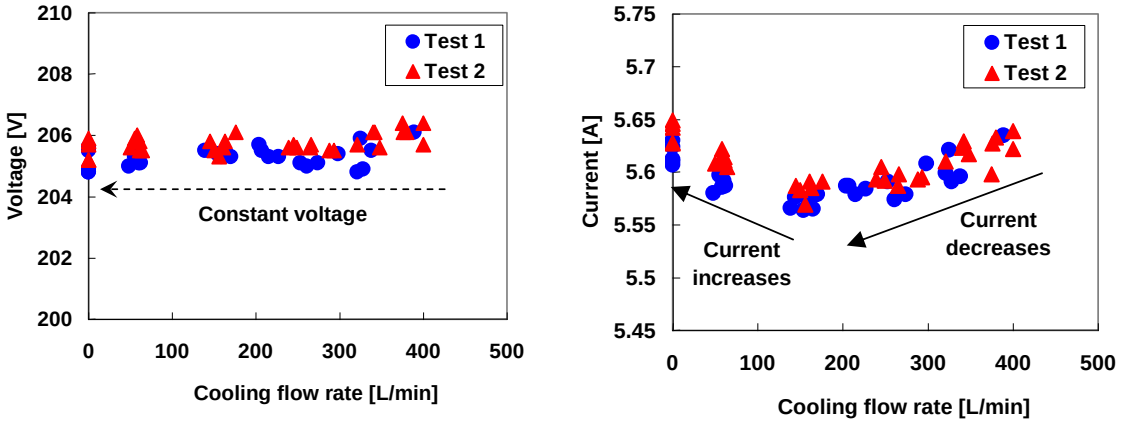

(a) Voltage

(b) Current

Fig. D.2 Test case #3. T_{hs}=150ºC. No rotor spinning: Recorded (a) voltage and (b) current of the heater circuit versus cooling flow rate.

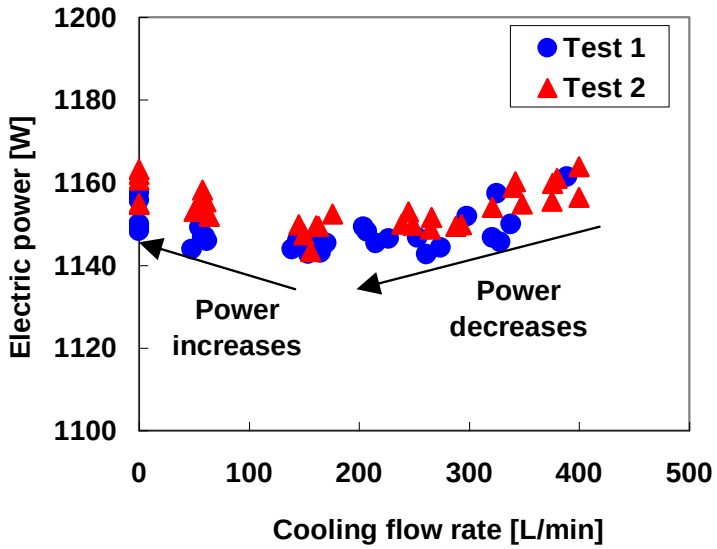

Fig. D.3 Test case #3. T_{hs}=150ºC. No rotor spinning: Measured electric power of the cartridge heater versus cooling flow rate.

APPENDIX E

TEMPERATURE RISES OF SYSTEM COMPONENTS VERSUS ELAPSED TIME: TEST CASES #1, #2, #4, AND #5

Figure E.1 through E.4 depict the temperature rises ($T_i - T_{amb}$ where $_{i\ =}$ $r_{FE,}$ $r_{DE,\ 1-10,\ in,\ e,\ out}$) of the test system components versus elapsed time for test cases#1,#2,#4, and #5.

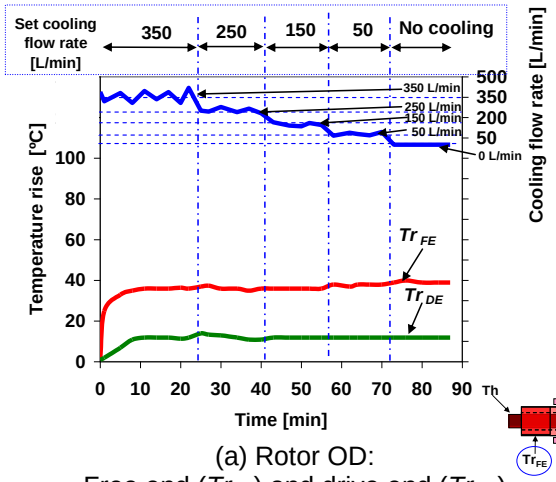

(a) Rotor OD:
Free end (Tr_{FE}) and drive end (Tr_{DE})

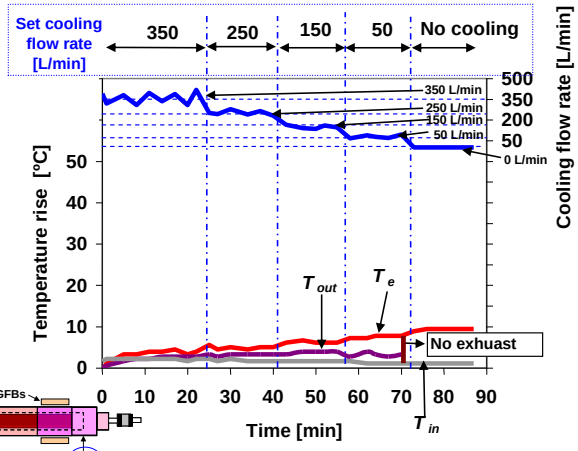

(b) Cooling air:
Upstream (T_{in}), enclosure (T_e), and exhaust (T_{out})

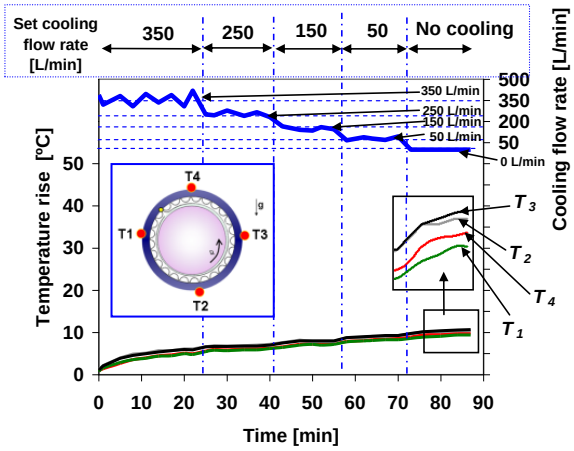

(c) FE bearing sleeve OD (T_1–T_4)

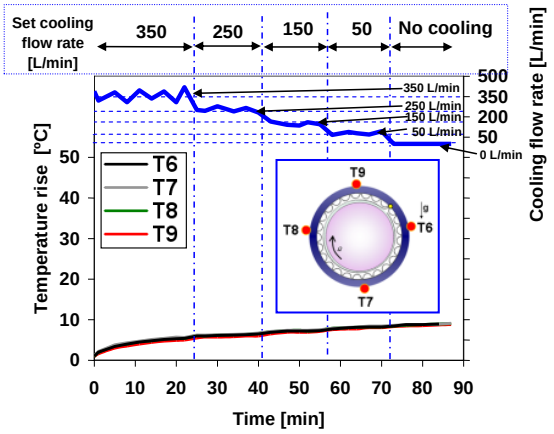

(d) DE bearing sleeve OD (T_6–T_9)

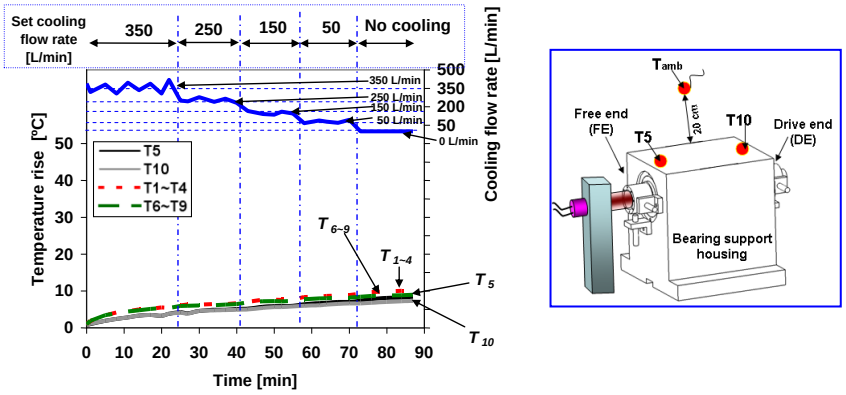

(e) Bearing housing surface (T_5 and T_{10}) and bearing mean temperature (FE: T_{1-4}, DE: T_{6-9})

Fig. E.1 Test case #1. Heater set temperature at 65ºC. No rotor spinning: Recorded test system components temperature rise $(T_i\text{-}T_{amb})_i$ = r_{FE}, r_{DE}, 1–10, *in*, *e*, *out* versus elapsed time. Axial cooling flow into bearings decreases from 420 to 0 L/min. Note different vertical scales.

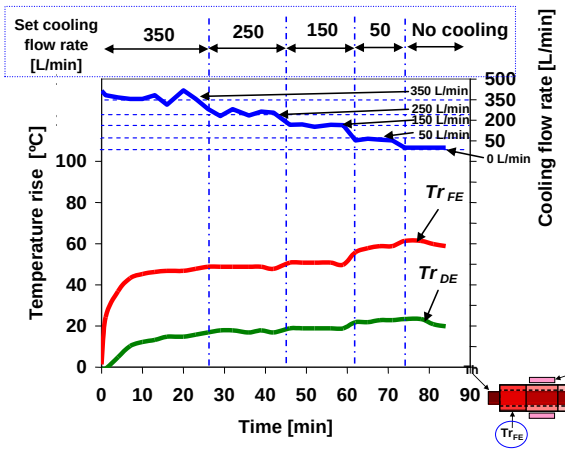

(a) Rotor OD:
Free end (Tr_{FE}) and drive end (Tr_{DE})

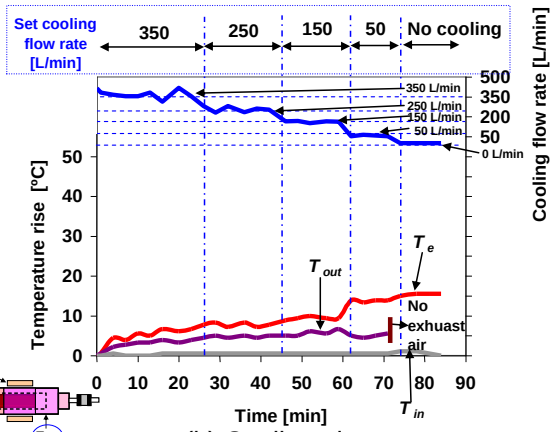

(b) Cooling air:
upstream (T_{in}), enclosure (T_e), and exhaust (T_{out})

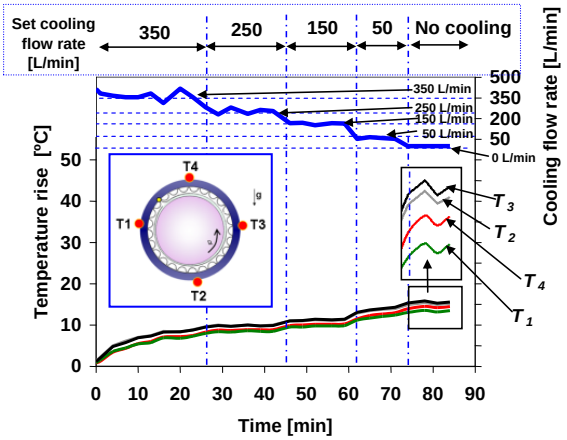

(c) FE bearing sleeve OD (T_1–T_4)

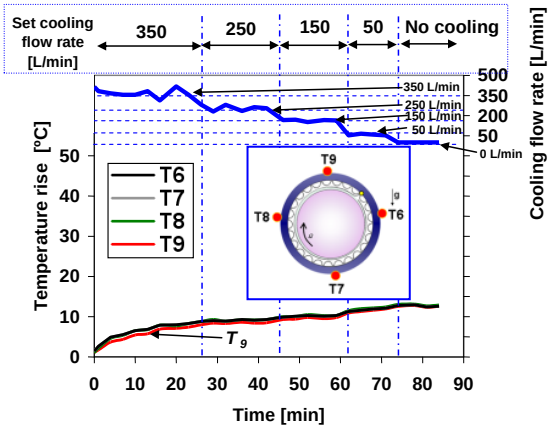

(d) DE bearing sleeve OD (T_6–T_9)

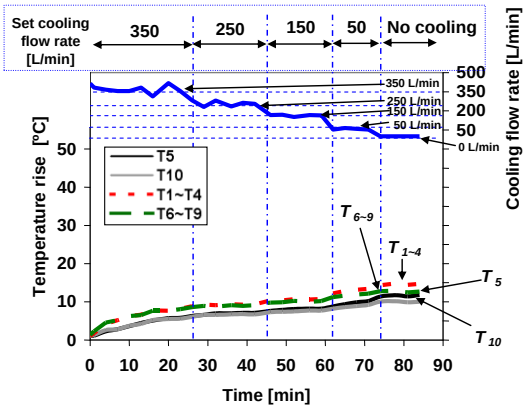

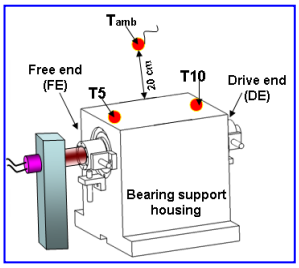

(e) Bearing housing surface (T_5 and T_{10}) and bearing mean temperature (FE: $T_{1–4}$, DE: $T_{6–9}$)

Fig. E.2 Test case #2. Heater set temperature at 100ºC. No rotor spinning: Recorded test system components temperature rise $(T_i\text{-}T_{amb})_i$ = r_{FE}, r_{DE}, 1–10, *in*, *e*, *out* versus elapsed time. Axial cooling flow into bearings decreases from 420 to 0 L/min. Note different vertical scales.

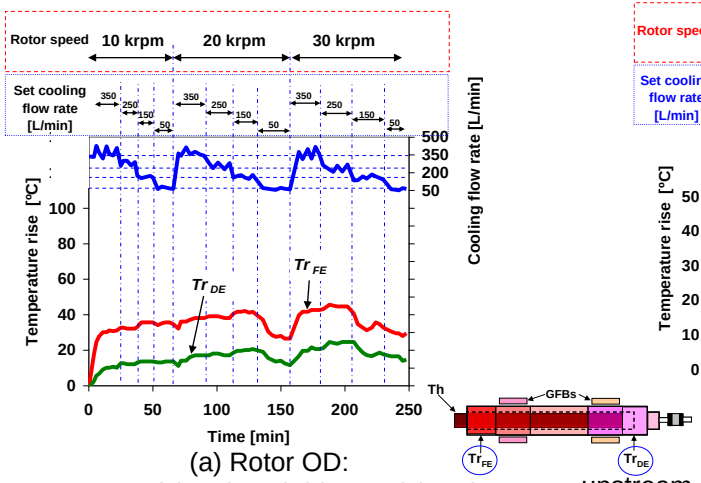

(a) Rotor OD: Free end (Tr_{FE}) and drive end (Tr_{DE})

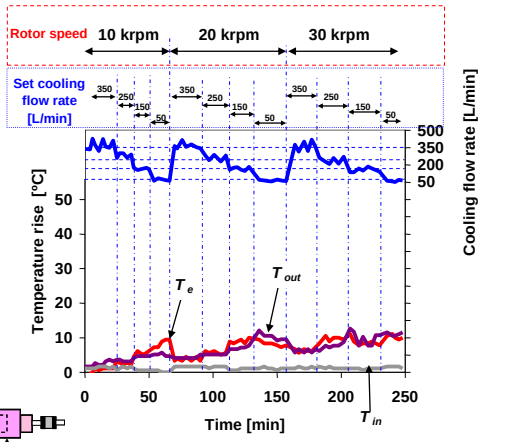

(b) Cooling air: upstream (T_{in}), enclosure (T_e), and exhaust (T_{out})

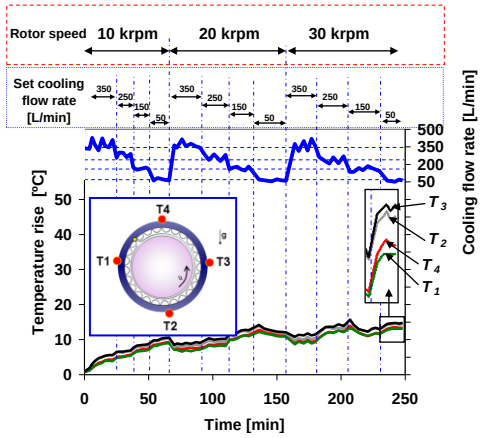

(c) FE bearing sleeve OD (T_1–T_4)

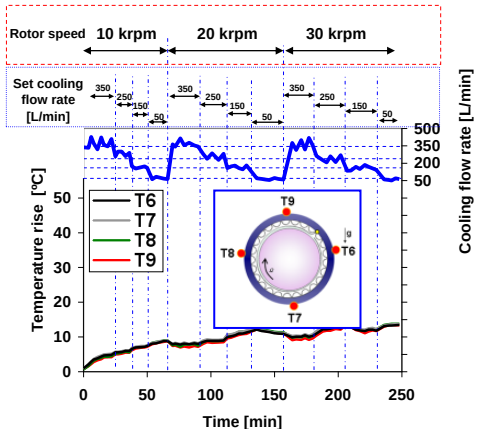

(d) DE bearing sleeve OD (T_6–T_9)

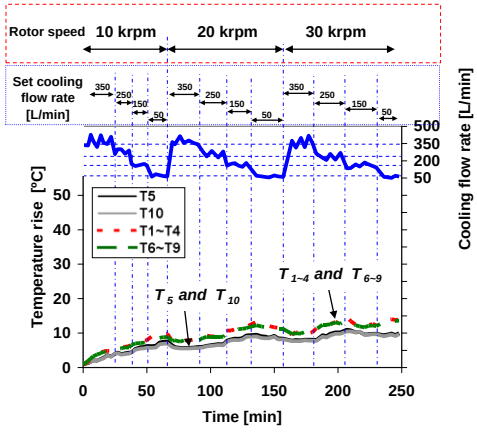

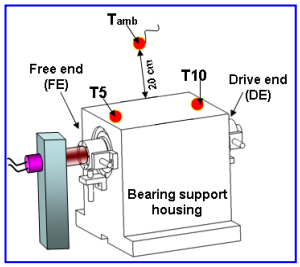

(e) Bearing housing surface (T_5 and T_{10}) and bearing mean temperature (FE: T_{1-4}, DE: T_{6-9})

Fig. E.3 Test case #4, Heater set temperature at 65ºC. Rotor speed of 10, 20, and 30 krpm: Recorded test system components temperature rise $(T_i\text{-}T_{amb})_i$ = r_{FE}, r_{DE}, 1–10, *in*, *e*, *out* versus elapsed time. Axial cooling flow into bearings decreases from 420 to 50 L/min. Note different vertical scales.

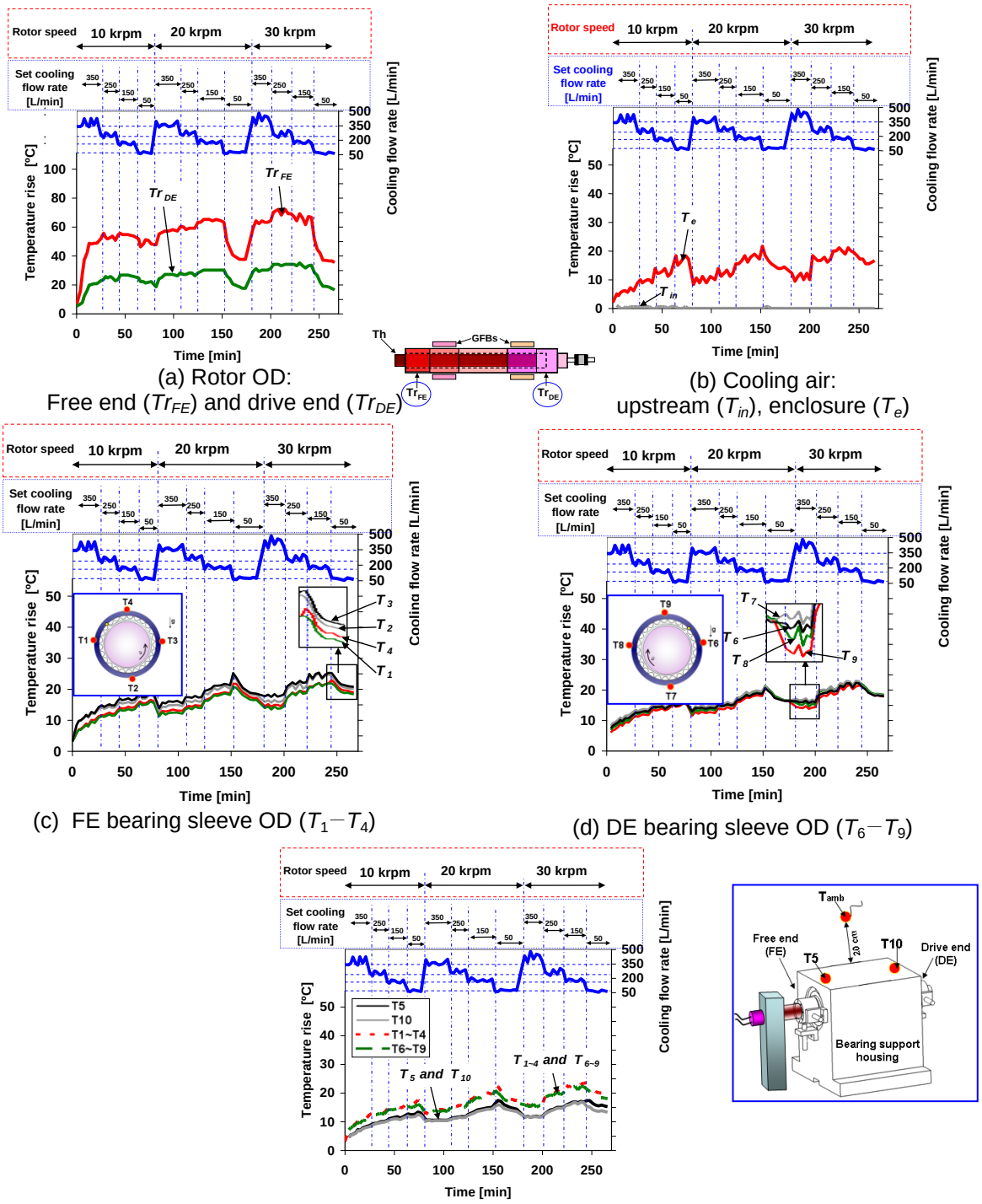

(a) Rotor OD: Free end (Tr_{FE}) and drive end (Tr_{DE})

(b) Cooling air: upstream (T_{in}), enclosure (T_e)

(c) FE bearing sleeve OD (T_1—T_4)

(d) DE bearing sleeve OD (T_6—T_9)

(e) Bearing housing surface (T_5 and T_{10}) and bearing mean temperature (FE: T_{1-4}, DE: T_{6-9})

Fig. E.4 Test case #5, Heater set temperature at 100ºC. Rotor speed of 10, 20, and 30 krpm: Recorded test system components temperature rise (T_i-T_{amb})$_i$ = r_{FE}, r_{DE}, 1–10, *in*, *e*, *out* versus elapsed time. Axial cooling flow into bearings decreases from 420 to 50 L/min. Note different vertical scales.

APPENDIX F

COMPLETE EXPERIMENTAL DATA

Table F.1 Complete recorded data of temperature rises for test case #1

Time [min]	Cooling flow rate [L/min]	Rotor Speed [krpm]	Tr_{FE} - T_{amb}	Tr_{DE} - T_{amb}	T_1 - T_{amb}	T_2 - T_{amb}	T_3 - T_{amb}	T_4 - T_{amb}	T_5 - T_{amb}	T_6 - T_{amb}	T_7 - T_{amb}	T_8 - T_{amb}	T_9 - T_{amb}	T_{10} - T_{amb}	T_e - T_{amb}	T_{out} - T_{amb}
1	320	0	25	2	1	2	2	2	1	2	2	2	2	1	1	1
5	380	0	33	7	3	3	4	4	2	3	4	4	3	2	3	2
8	308	0	35	11	4	4	5	5	2	3	4	4	4	2	3	2
11	395	0	36	12	4	4	5	5	3	4	5	5	4	3	4	2
14	335	0	36	12	4	4	6	5	3	4	5	5	5	3	4	3
17	388	0	36	12	5	4	6	6	3	5	5	5	5	3	4	3
20	308	0	36	11	5	5	6	6	3	5	5	6	5	3	3	3
22	418	0	36	12	5	5	6	6	4	5	5	6	5	4	4	3
25	250	0	37	14	6	5	7	7	4	5	6	6	6	4	6	3
27	243	0	37	13	6	6	7	7	4	6	6	6	6	4	4	3
30	278	0	36	13	6	6	7	7	5	6	6	6	6	5	5	3
34	240	0	36	12	6	6	7	7	5	6	6	6	6	5	4	3
37	265	0	35	11	6	6	7	7	5	6	6	6	6	5	5	3
40	231	0	36	11	6	6	7	7	5	6	7	7	6	5	5	3
43	165	0	36	12	7	6	8	7	5	6	7	7	7	5	6	3
47	140	0	36	12	7	7	8	8	6	7	7	7	7	5	7	4
50	135	0	36	12	7	7	8	8	6	7	7	7	7	6	6	4
52	159	0	36	12	7	7	8	8	6	7	7	7	7	6	6	4
55	145	0	36	12	7	7	8	8	6	7	7	7	7	6	6	4
58	66	0	38	12	8	8	9	9	6	7	8	8	8	6	7	3
62	87	0	37	12	8	8	9	9	7	8	8	8	8	6	7	4
64	78	0	38	12	8	8	9	9	7	8	8	8	8	6	8	3
67	68	0	38	12	8	8	9	9	7	8	8	8	8	6	8	3
70	93	0	38	12	9	8	9	9	7	8	8	8	8	7	8	3
73	0	0	39	12	9	9	10	10	7	8	8	9	8	7	9	16
76	0	0	40	12	9	9	10	10	8	8	9	9	9	7	9	15
80	0	0	39	12	10	9	10	10	8	8	9	9	9	7	9	16
84	0	0	39	12	10	9	10	11	8	9	9	9	9	7	9	16
87	0	0	39	12	10	9	10	11	8	9	9	9	9	7	9	14

Table F.2 Complete recorded data of temperature rises for test case #2

Time [min]	Cooling flow rate [L/min]	Rotor Speed [krpm]	Tr_{FE} - T_{amb}	Tr_{DE} - T_{amb}	T_1 - T_{amb}	T_2 - T_{amb}	T_3 - T_{amb}	T_4 - T_{amb}	T_5 - T_{amb}	T_6 - T_{amb}	T_7 - T_{amb}	T_8 - T_{amb}	T_9 - T_{amb}	T_{10} - T_{amb}	T_e - T_{amb}	T_{out} - T_{amb}
1	382	0	24	1	1	2	2	2	1	2	2	3	3	1	1	1
4	366	0	37	5	3	4	5	5	2	4	5	5	5	3	4	2
7	355	0	43	10	4	4	6	6	3	4	5	6	6	3	4	3
10	355	0	45	12	6	5	7	7	4	5	7	7	7	4	6	3
13	382	0	46	13	6	6	7	7	4	6	7	7	7	4	5	3
16	313	0	47	15	7	7	8	8	5	7	8	8	8	5	7	4
20	417	0	47	15	7	7	8	8	6	7	8	8	8	5	6	3
23	355	0	48	16	7	7	9	9	6	7	8	8	8	6	7	4
26	282	0	49	17	8	8	10	9	6	8	9	9	9	6	8	4
29	230	0	49	18	9	8	10	10	7	8	9	9	9	7	8	5
32	280	0	49	18	9	8	10	10	7	8	9	9	9	7	7	4
36	234	0	49	17	9	9	10	10	7	9	9	9	9	7	8	5
39	262	0	49	18	9	8	10	10	7	8	9	9	9	7	7	4
42	254	0	48	17	9	8	10	10	7	8	9	9	9	7	8	5
46	166	0	51	19	10	9	11	11	8	9	10	10	10	7	9	5
49	169	0	51	19	10	9	11	11	8	9	10	10	10	7	9	5
52	152	0	51	19	10	10	11	11	8	10	10	10	10	7	10	6
56	166	0	51	19	10	10	11	11	8	9	10	10	10	8	9	6
59	164	0	50	19	10	10	11	11	8	10	10	10	10	8	9	7
62	52	0	56	22	11	11	13	13	9	11	11	11	11	8	14	5
65	64	0	58	22	12	12	13	14	9	11	12	12	12	9	13	4
68	58	0	59	23	13	12	14	14	10	12	12	12	12	9	14	5
71	52	0	59	23	13	12	14	14	10	12	12	12	12	9	14	6
74	0	0	61	23	14	13	15	15	11	13	13	13	13	10	15	26
78	0	0	61	23	15	14	15	16	12	13	13	13	13	10	16	29
81	0	0	60	21	14	13	15	15	11	12	13	12	12	10	16	28
84	0	0	59	20	14	13	15	16	12	13	13	13	13	10	16	27

Table F.3 Complete recorded data of temperature rises for test case #3

Time [min]	Cooling flow rate [L/min]	Rotor Speed [krpm]	Tr_{FE} - T_{amb}	Tr_{DE} - T_{amb}	T_1 - T_{amb}	T_2 - T_{amb}	T_3 - T_{amb}	T_4 - T_{amb}	T_5 - T_{amb}	T_6 - T_{amb}	T_7 - T_{amb}	T_8 - T_{amb}	T_9 - T_{amb}	T_{10} - T_{amb}	T_e - T_{amb}	T_{out} - T_{amb}
1	381	0	8	6	4	3	3	4	4	4	4	4	4	4	1	1
2	412	0	44	10	4	4	6	5	3	5	6	6	6	4	6	2
5	336	0	56	18	7	7	9	8	4	7	8	8	8	4	8	4
8	400	0	60	21	8	8	10	10	5	8	9	9	9	5	8	4
11	345	0	63	24	9	9	11	11	7	9	11	10	10	6	11	6
14	400	0	63	24	10	9	12	11	7	9	11	10	10	7	9	6
17	329	0	65	26	11	11	13	13	8	11	12	12	12	8	11	6
20	410	0	63	24	11	10	12	12	8	11	12	12	12	8	11	6
23	338	0	64	25	12	11	13	13	9	11	13	12	12	8	12	7
26	421	0	62	25	11	11	13	13	9	11	12	12	12	9	11	6
29	212	0	66	27	13	12	14	14	9	12	14	13	13	9	14	7
32	268	0	65	27	13	12	14	14	10	12	13	13	13	9	12	7
35	249	0	65	27	13	13	14	14	10	12	14	13	13	10	13	7
38	217	0	67	29	14	13	15	15	11	13	14	14	14	10	13	8
41	274	0	63	26	13	13	14	14	10	12	13	13	13	10	12	7
44	144	0	69	29	14	14	16	16	11	14	15	14	14	10	16	8
47	160	0	69	29	15	14	16	16	11	14	15	14	14	11	14	8
51	150	0	69	30	16	15	17	17	12	15	16	15	15	12	16	9
58	156	0	67	29	15	15	17	17	12	14	15	15	15	12	16	8
61	141	0	69	29	16	15	17	17	12	15	16	15	15	12	16	8
64	60	0	75	31	17	17	19	19	13	16	17	17	17	12	21	6
67	52	0	80	34	19	18	20	21	14	17	18	18	18	13	22	8
70	46	0	82	36	20	19	21	22	15	18	19	18	18	14	23	9
73	47	0	82	36	20	19	22	22	16	18	19	18	18	14	22	9
76	54	0	82	36	20	19	21	22	16	18	19	19	19	14	22	8
81	46	0	81	35	20	19	22	22	16	18	19	18	18	14	23	9
84	0	0	86	36	21	20	23	24	18	19	20	19	19	15	24	47
88	0	0	85	34	22	20	23	24	17	19	19	19	19	15	24	47
92	0	0	85	32	22	21	23	24	18	19	20	19	19	15	24	48
97	0	0	84	31	23	21	24	25	19	20	20	20	20	16	25	42
101	0	0	84	31	23	21	24	25	19	20	20	20	20	16	25	47
105	0	0	85	32	24	22	25	26	20	21	21	21	21	17	26	45
108	0	0	86	32	24	22	25	26	20	21	21	21	21	17	26	46

Table F.4 Complete recorded data of temperature rises for test case #4

Time [min]	Cooling flow rate [L/min]	Rotor Speed [krpm]	Tr_{FE} - T_{amb}	Tr_{DE} - T_{amb}	T_1 - T_{amb}	T_2 - T_{amb}	T_3 - T_{amb}	T_4 - T_{amb}	T_5 - T_{amb}	T_6 - T_{amb}	T_7 - T_{amb}	T_8 - T_{amb}	T_9 - T_{amb}	T_{10} - T_{amb}	T_e - T_{amb}	T_{out} - T_{amb}
1	337	10	0	0	1	1	1	1	1	1	1	1	1	1	0	2
4	333	10	18	3	1	1	2	2	1	2	2	2	2	1	0	2
6	426	10	25	6	2	2	3	3	2	2	2	3	3	2	0	2
8	371	10	28	7	3	2	4	4	2	3	3	4	3	2	1	3
11	319	10	30	9	3	3	5	5	2	3	4	4	4	2	1	2
14	423	10	30	10	4	3	5	5	3	4	4	5	4	2	1	2
16	358	10	31	10	4	4	5	5	3	4	4	5	5	3	1	3
19	345	10	31	11	4	4	6	6	4	4	4	5	5	3	1	4
22	409	10	31	10	4	4	6	6	3	4	4	5	5	3	1	3
25	258	10	33	13	5	5	6	6	4	5	5	6	6	4	3	4
27	300	10	33	13	5	5	6	7	4	5	5	6	6	4	3	4
30	300	10	32	12	5	5	6	7	4	5	5	6	6	4	2	3
33	261	10	32	12	5	5	7	7	4	5	6	6	6	4	3	3
36	290	10	32	12	6	5	7	7	4	5	6	6	6	4	2	3
38	173	10	33	13	6	6	7	8	4	6	7	7	7	4	4	4
41	153	10	36	14	7	7	8	8	5	7	7	7	7	5	6	5
45	164	10	36	14	7	7	8	8	6	7	7	7	7	5	5	5
48	173	10	36	14	7	7	8	9	6	7	7	7	7	6	6	5
50	161	10	36	14	7	7	8	9	6	7	7	8	7	6	6	5
54	61	10	34	13	8	8	10	10	6	8	8	8	8	6	7	5
57	83	10	35	13	9	8	10	10	6	8	9	8	8	6	7	5
60	75	10	36	14	9	9	10	10	7	8	9	9	8	7	9	6
63	67	10	36	14	9	9	10	10	7	9	9	9	9	7	9	5
66	62	10	35	14	9	9	10	11	8	9	9	9	9	7	9	5
70	363	20	32	11	8	7	8	8	6	7	8	8	8	6	3	4
72	342	20	36	14	8	7	8	9	6	7	8	8	8	6	4	4
76	414	20	36	14	7	7	8	9	6	7	7	8	8	6	3	4
79	354	20	37	16	7	7	8	9	6	7	8	8	8	6	4	4
83	377	20	38	17	8	7	8	9	6	7	8	8	8	6	3	4
87	353	20	38	17	8	7	9	9	6	7	8	8	8	6	4	4
90	344	20	38	17	8	7	8	9	6	7	7	8	8	6	3	5
94	280	20	39	17	8	8	9	10	6	8	8	9	9	6	6	5
97	238	20	39	18	9	8	10	10	6	8	9	9	9	6	6	5
101	285	20	39	18	8	8	9	10	7	8	9	9	9	6	6	5
106	228	20	38	17	9	8	9	10	7	8	9	9	9	7	5	5
110	281	20	38	17	9	8	9	10	7	8	9	9	9	6	6	5
113	158	20	41	19	10	10	12	12	8	10	10	11	10	7	9	7

Table F.4 Continued

Time [min]	Cooling flow rate [L/min]	Rotor Speed [krpm]	Tr_{FE} - T_{amb}	Tr_{DE} - T_{amb}	T_1 - T_{amb}	T_2 - T_{amb}	T_3 - T_{amb}	T_4 - T_{amb}	T_5 - T_{amb}	T_6 - T_{amb}	T_7 - T_{amb}	T_8 - T_{amb}	T_9 - T_{amb}	T_{10} - T_{amb}	T_e - T_{amb}	T_{out} - T_{amb}
116	172	20	42	20	10	10	11	12	8	10	11	11	10	8	8	7
119	179	20	42	20	10	10	12	12	8	10	11	11	10	8	9	7
122	158	20	42	20	11	11	12	13	8	11	11	12	11	8	9	7
125	147	20	41	20	11	11	12	13	9	11	12	12	11	8	8	7
128	181	20	42	21	11	11	12	13	9	11	12	12	11	9	10	8
136	69	20	37	19	13	12	14	14	10	12	12	12	12	9	9	12
140	64	20	31	16	12	12	13	13	9	12	12	12	12	9	8	11
143	59	20	29	15	12	12	12	13	9	12	12	12	12	8	8	11
146	54	20	28	14	12	11	12	13	9	12	12	12	11	8	8	11
150	72	20	28	14	11	11	12	12	9	11	11	11	11	9	8	9
153	64	20	27	13	11	11	12	12	8	11	11	11	11	8	7	10
157	58	20	27	12	11	11	12	12	8	11	11	11	11	8	8	10
164	375	30	40	17	9	9	10	11	8	9	10	10	10	8	7	6
167	314	30	42	20	10	9	10	11	8	9	10	10	10	8	6	7
171	400	30	42	20	9	9	10	11	8	9	10	10	10	8	7	6
174	318	30	43	22	10	10	11	12	8	10	10	11	10	8	6	7
177	419	30	43	21	9	9	10	11	8	9	10	10	10	8	6	6
180	354	30	43	21	10	9	10	11	8	10	10	11	10	8	7	7
183	262	30	43	21	11	10	12	12	8	10	11	12	11	8	8	6
188	225	30	46	25	12	12	13	14	9	12	13	13	12	9	11	8
191	206	30	45	24	12	12	13	14	9	12	13	13	12	9	9	7
194	259	30	45	24	12	12	13	14	10	12	13	13	12	9	10	8
198	209	30	45	25	13	13	13	14	10	12	14	14	13	10	10	8
202	269	30	45	25	12	12	13	14	10	12	13	13	12	10	9	9
207	134	30	41	25	14	13	16	16	11	14	14	14	14	10	11	13
210	136	30	35	22	13	13	14	14	11	13	13	13	13	10	9	12
214	168	30	33	19	12	12	13	13	10	12	12	12	12	10	8	8
217	150	30	31	17	12	11	13	13	10	12	12	12	12	10	8	10
221	185	30	33	17	11	11	12	12	10	11	12	12	12	9	8	8
224	168	30	36	18	11	11	13	13	10	12	12	12	12	9	9	8
227	155	30	35	19	12	12	13	13	10	12	12	13	12	10	8	11
230	141	30	33	18	12	12	13	13	10	12	12	12	12	10	8	11
236	60	30	31	17	13	13	14	14	9	13	13	13	13	9	11	12
240	54	30	30	17	13	13	14	15	10	13	14	14	13	9	11	11
242	50	30	30	17	14	13	15	15	10	13	14	14	13	10	10	11
245	69	30	28	14	13	13	14	15	9	13	14	14	13	9	9	11
248	63	30	30	15	13	13	14	15	10	13	14	14	13	10	10	12

Table F.5 Complete recorded data of temperature rises for test case #5

Time [min]	Cooling flow rate [L/min]	Rotor Speed [krpm]	Tr_{FE} - T_{amb}	Tr_{DE} - T_{amb}	T_1 - T_{amb}	T_2 - T_{amb}	T_3 - T_{amb}	T_4 - T_{amb}	T_5 - T_{amb}	T_6 - T_{amb}	T_7 - T_{amb}	T_8 - T_{amb}	T_9 - T_{amb}	T_{10} - T_{amb}	T_e - T_{amb}
1	341	10	4	3	2	2	2	2	1	2	2	2	2	1	2
4	341	10	16	7	6	6	8	8	5	6	7	8	7	5	5
6	357	10	28	8	7	7	10	10	5	7	8	9	8	5	4
8	422	10	37	12	7	7	10	10	6	7	8	9	9	6	6
11	353	10	42	16	8	8	11	11	6	8	9	10	9	6	6
13	337	10	49	20	9	8	11	12	7	9	9	11	10	7	6
15	426	10	48	20	9	8	11	11	7	8	9	11	10	7	6
18	356	10	49	21	10	10	12	13	8	9	10	12	11	8	7
21	426	10	49	21	10	9	12	12	8	9	10	12	11	8	6
25	259	10	52	23	11	11	14	14	9	11	12	13	12	8	9
28	225	10	56	24	12	11	14	15	9	11	12	13	13	9	10
30	278	10	53	26	12	11	14	14	9	11	12	13	13	9	9
32	268	10	52	25	12	11	14	15	9	12	12	13	13	9	9
35	237	10	53	26	12	12	14	15	10	12	13	14	13	10	10
37	240	10	54	25	12	11	14	15	10	12	13	14	13	10	10
40	281	10	51	23	12	11	14	15	10	12	12	13	13	10	9
43	161	10	55	24	13	13	15	16	11	13	14	15	14	10	14
45	148	10	56	27	14	13	16	17	11	14	14	15	14	11	12
47	183	10	55	27	14	13	15	16	11	13	14	15	14	11	12
50	178	10	55	27	14	13	16	17	11	13	14	15	14	11	13
53	158	10	55	27	14	14	16	17	12	14	15	15	15	11	14
56	151	10	54	26	14	13	15	16	11	13	14	14	14	11	11
59	182	10	54	26	14	14	16	17	12	14	14	15	14	11	12
64	65	10	52	25	16	15	18	19	13	15	16	16	16	12	18
66	59	10	46	22	16	15	17	17	13	15	15	15	15	12	15
69	81	10	48	22	15	15	17	17	13	15	15	15	15	12	16
71	75	10	51	21	16	15	18	18	13	15	16	16	15	12	17
74	68	10	51	22	17	16	18	19	13	16	16	16	16	13	18
77	62	10	48	22	16	16	18	18	13	15	16	16	15	12	17
82	395	20	48	19	12	11	13	14	11	12	12	13	13	10	8
85	334	20	55	24	13	13	14	16	11	13	14	15	14	11	11
88	362	20	56	25	13	12	14	15	11	12	13	14	14	10	9
91	365	20	57	27	13	12	15	16	11	13	14	15	14	10	11
95	339	20	57	27	13	12	15	16	11	12	13	14	14	10	9
99	349	20	58	27	13	12	15	16	11	13	14	15	14	10	11
104	400	20	57	26	13	12	15	15	11	12	13	15	14	10	10
107	262	20	60	28	14	14	16	17	11	14	15	16	15	11	14

Table F.5 Continued

Time [min]	Cooling flow rate [L/min]	Rotor Speed [krpm]	Tr_{FE} - T_{amb}	Tr_{DE} - T_{amb}	T_1 - T_{amb}	T_2 - T_{amb}	T_3 - T_{amb}	T_4 - T_{amb}	T_5 - T_{amb}	T_6 - T_{amb}	T_7 - T_{amb}	T_8 - T_{amb}	T_9 - T_{amb}	T_{10} - T_{amb}	T_e - T_{amb}
110	251	20	60	27	15	14	16	17	11	14	15	15	15	11	11
113	296	20	58	27	14	14	16	17	12	14	15	16	15	11	12
116	255	20	59	28	15	14	16	18	12	14	15	16	15	12	13
119	276	20	59	28	15	14	16	17	12	14	15	16	15	11	11
122	289	20	59	26	15	14	16	17	12	14	15	16	15	12	12
125	160	20	63	28	17	16	19	20	13	16	17	18	17	12	16
128	207	20	63	29	17	16	18	20	13	16	17	18	17	13	16
131	186	20	65	30	17	17	19	20	14	17	18	18	18	13	17
134	164	20	65	30	18	18	20	21	14	18	19	19	18	14	18
137	176	20	65	30	18	18	20	21	14	17	19	19	18	14	16
140	186	20	64	30	19	18	20	21	15	18	19	20	19	14	18
144	165	20	65	30	19	19	21	22	15	18	20	20	19	14	19
149	193	20	64	30	19	18	20	21	15	18	19	20	19	14	17
152	64	20	63	30	22	21	24	25	16	21	21	21	21	15	22
155	60	20	50	26	22	20	23	24	17	20	20	20	20	16	18
158	84	20	45	24	20	19	21	22	17	19	19	19	19	16	17
161	75	20	41	21	19	18	20	20	16	18	18	17	17	15	16
168	71	20	38	19	17	17	18	19	15	17	17	17	17	14	14
171	80	20	38	18	17	16	18	19	15	17	17	17	16	14	14
174	73	20	38	18	17	17	18	19	14	16	17	17	16	14	14
182	435	30	59	29	15	14	16	18	12	14	16	17	16	12	12
185	367	30	64	31	15	14	16	18	12	14	15	17	16	12	9
188	481	30	62	29	14	13	16	18	12	14	15	17	16	12	11
191	400	30	64	30	15	14	17	18	12	15	16	17	17	12	12
194	452	30	63	30	15	14	16	18	12	14	15	16	16	12	10
197	440	30	63	30	15	14	16	18	12	14	15	17	16	12	12
200	377	30	64	31	15	14	17	18	12	14	15	17	16	12	10
203	261	30	70	34	17	17	20	21	13	17	19	20	18	13	18
208	229	30	72	34	19	19	21	22	14	18	20	20	19	14	17
211	291	30	68	33	18	18	20	22	14	18	20	20	19	14	17
215	241	30	72	34	20	20	22	23	15	19	21	21	20	15	18
218	303	30	69	34	19	19	20	22	15	18	20	20	19	15	16
221	283	30	69	34	19	19	21	22	15	19	20	21	20	15	17
224	164	30	67	34	21	21	25	25	16	21	22	22	21	16	20
227	192	30	64	33	21	21	23	23	16	20	22	22	21	16	20
230	186	30	69	35	21	22	25	25	17	21	23	23	22	16	21
233	167	30	66	33	22	22	25	25	17	22	23	23	22	17	20

Table F.5 Continued

Time [min]	Cooling flow rate [L/min]	Rotor Speed [krpm]	Tr_{FE} - T_{amb}	Tr_{DE} - T_{amb}	T_1 - T_{amb}	T_2 - T_{amb}	T_3 - T_{amb}	T_4 - T_{amb}	T_5 - T_{amb}	T_6 - T_{amb}	T_7 - T_{amb}	T_8 - T_{amb}	T_9 - T_{amb}	T_{10} - T_{amb}	T_e - T_{amb}
236	167	30	62	32	21	21	23	24	17	20	22	22	21	16	19
239	194	30	67	33	22	22	24	25	17	21	23	23	22	17	21
242	172	30	67	34	22	22	25	25	17	21	23	23	22	17	20
245	76	30	52	29	23	22	24	25	17	21	22	21	21	15	19
248	73	30	45	27	22	21	23	24	17	20	21	20	20	15	18
251	68	30	42	22	21	20	22	23	16	19	20	19	19	14	17
254	60	30	37	19	20	19	21	22	16	19	19	19	19	14	17
257	54	30	37	19	20	19	21	21	16	18	19	18	18	14	16
260	76	30	37	19	20	19	20	21	16	18	19	19	18	14	16
263	68	30	37	18	19	19	20	21	15	18	19	18	18	14	16
266	61	30	36	17	19	18	20	21	15	18	18	18	18	13	17

Table F.6 Complete recorded data of temperature rises for test case #6

Time [min]	Cooling flow rate [L/min]	Rotor Speed [krpm]	Tr_{FE} - T_{amb}	Tr_{DE} - T_{amb}	T_1 - T_{amb}	T_2 - T_{amb}	T_3 - T_{amb}	T_4 - T_{amb}	T_5 - T_{amb}	T_6 - T_{amb}	T_7 - T_{amb}	T_8 - T_{amb}	T_9 - T_{amb}	T_{10} - T_{amb}	T_e - T_{amb}	T_{out} - T_{amb}
1	371	10	1	1	1	1	1	1	1	1	1	1	1	1	1	2
5	342	10	14	5	2	1	2	2	2	2	1	2	2	2	0	2
8	350	10	36	9	3	3	5	5	2	3	4	5	5	3	4	2
11	290	10	69	19	6	7	10	11	4	7	9	10	9	4	7	5
14	384	10	77	29	9	9	13	13	6	9	11	13	11	6	9	6
16	335	10	82	32	11	10	15	16	7	11	12	14	13	7	11	7
19	295	10	85	35	12	11	16	17	9	12	13	14	13	8	9	8
22	367	10	81	33	12	12	16	17	9	12	13	15	14	9	11	8
25	323	10	83	35	13	13	17	18	10	13	14	16	15	10	12	8
28	389	10	81	34	14	13	17	17	11	13	14	16	15	10	11	8
31	339	10	82	33	14	13	17	18	10	14	15	17	16	10	12	8
34	287	10	86	36	15	14	18	19	11	14	15	17	16	11	11	9
38	358	10	81	34	14	13	17	18	11	14	15	17	16	11	12	9
41	305	10	84	35	15	14	18	19	12	15	16	17	16	11	12	9
44	380	10	81	34	15	13	18	18	12	14	15	17	16	11	11	9
47	247	10	87	35	16	15	20	21	12	16	17	18	17	11	15	9
50	245	10	89	36	17	16	20	21	13	16	17	18	17	12	13	10
53	300	10	85	34	16	15	19	20	13	16	17	18	17	12	13	10
56	238	10	88	36	17	16	20	22	13	17	18	19	18	13	16	11
58	209	10	90	37	18	17	21	23	14	17	18	19	18	13	16	10
61	270	10	85	35	18	16	20	22	14	17	18	19	18	13	14	10
64	237	10	87	35	18	17	21	22	14	17	18	19	19	13	16	11
67	210	10	90	37	19	18	21	23	14	18	19	20	19	13	15	11
70	263	10	85	35	18	17	21	22	14	17	18	19	19	13	15	10
74	229	10	88	37	19	17	21	23	14	18	19	20	19	14	16	10
77	216	10	88	37	19	18	22	23	15	18	19	20	19	14	14	11
80	252	10	86	35	18	17	21	22	14	18	19	20	19	14	16	10
83	143	10	92	39	21	19	23	25	15	20	21	21	21	14	22	13
87	153	10	92	39	21	20	23	25	16	20	20	21	20	15	19	12
90	163	10	89	39	21	20	23	25	16	20	21	21	20	14	19	13
93	150	10	89	39	21	20	23	25	16	20	21	21	21	15	21	13
96	142	10	90	39	22	20	24	26	16	21	21	21	21	15	18	14
99	168	10	88	38	21	20	23	25	17	20	21	22	21	15	20	13
103	150	10	89	39	22	20	24	26	17	21	22	22	21	15	21	14
107	139	10	90	39	23	21	24	26	17	21	22	22	21	15	18	14
111	161	10	89	38	22	20	24	26	17	21	21	22	21	15	20	14
114	151	10	89	38	22	21	24	26	17	21	22	22	22	15	21	13

Table F.6 Continued

Time [min]	Cooling flow rate [L/min]	Rotor Speed [krpm]	Tr_{FE} - T_{amb}	Tr_{DE} - T_{amb}	T_1 - T_{amb}	T_2 - T_{amb}	T_3 - T_{amb}	T_4 - T_{amb}	T_5 - T_{amb}	T_6 - T_{amb}	T_7 - T_{amb}	T_8 - T_{amb}	T_9 - T_{amb}	T_{10} - T_{amb}	T_e - T_{amb}	T_{out} - T_{amb}
117	68	10	88	38	24	23	27	28	17	22	24	23	23	16	24	11
120	91	10	92	39	25	24	27	29	18	23	24	24	24	16	27	14
123	83	10	94	40	26	24	28	29	19	24	25	25	24	17	28	13
127	67	10	87	37	26	25	29	30	19	24	25	25	24	17	27	13
130	87	10	87	37	26	25	28	29	19	24	25	25	24	17	25	15
133	85	10	92	39	27	25	29	30	20	25	26	26	25	18	28	14
136	80	10	92	40	27	26	29	31	20	25	26	26	25	18	29	15

APPENDIX G

RECORDED COOLING FLOW RATE VERSUS SUPPLY AIR PRESSURE: TEST CASES #1−#6

Figure G.1 depicts the air cooling flow rate versus the supply air pressure. Recall Fig. 11 for a layout of the flow path of the forced cooling air and measurement locations (i.e., mass flow meter and pressure gauge 2 in Fig. 11). The uncertainties of the flowmeter and pressure gauge are ±7.5 L/min and ±1 psig, respectively. Cooling flow rates increase linearly with supplied pressure. The cooling flow rate and pressure do not change with increasing rotor speeds and heater set temperatures.

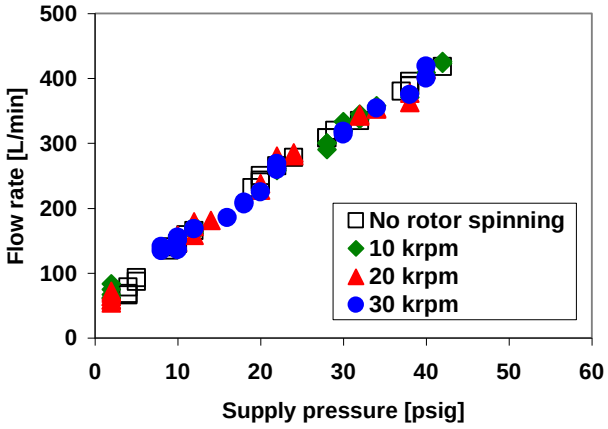

(a) Test cases 1 and 1: T_{hs}=65°C

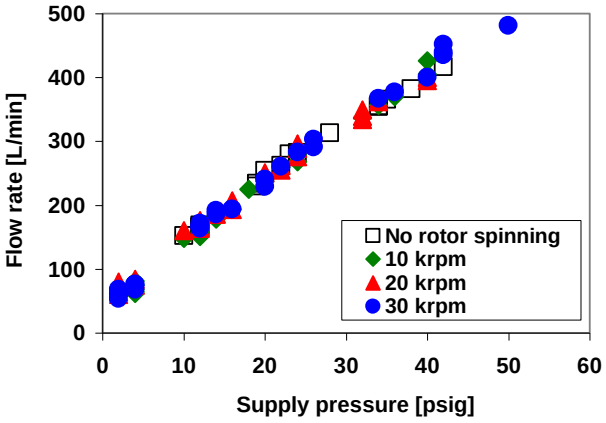

(b) Test cases 2 and 5: T_{hs}=100°C

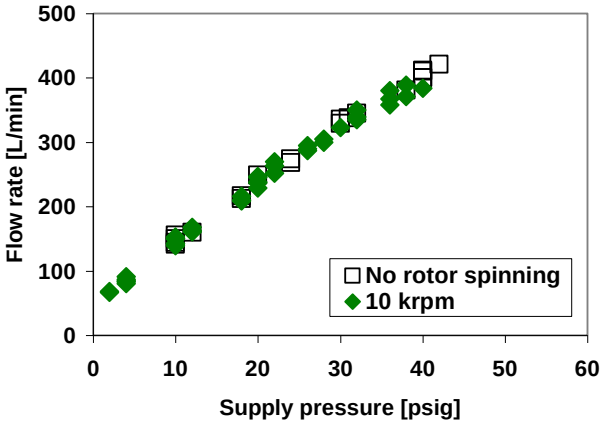

(c) Test cases 3 and 6: T_{hs}=150°C

Fig. G.1 Test cases #1−#6: recorded cooling flow rate versus supply air pressure.

APPENDIX H

TEMPERATURE RISE OF BEARING SLEEVE VERSUS TEMPERATURE RISE OF AIR INSIDE HOUSING ENCLOSURE: TEST CASES #1AND #4, #3 AND #6

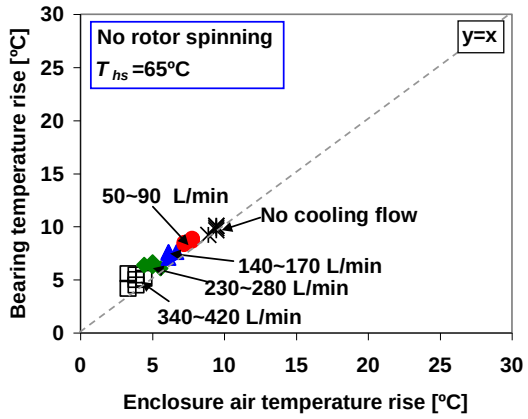

(a) No rotor spinning

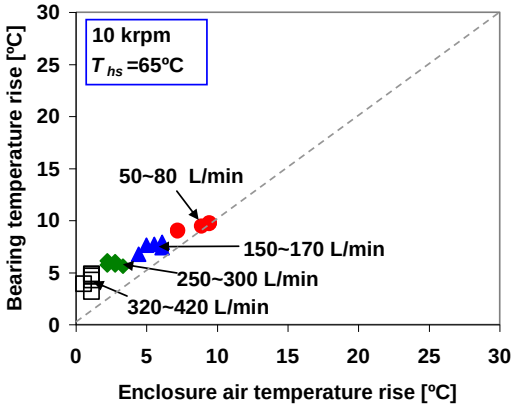

(a) 10 krpm

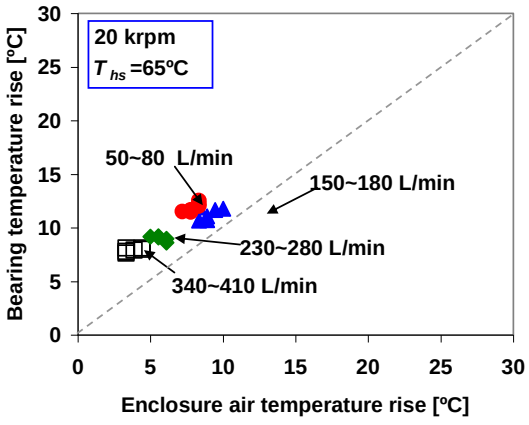

(a) 20 krpm

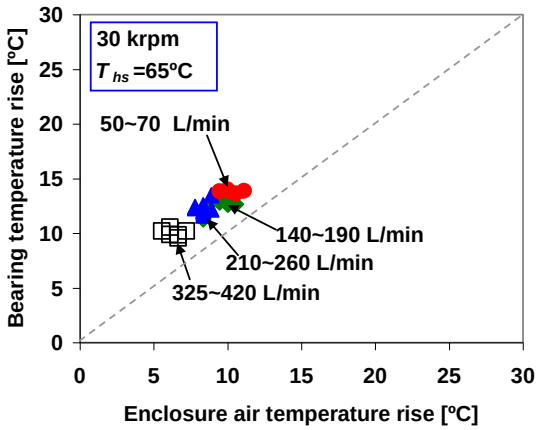

(c) 30 krpm

Fig. H.1 Test cases #1 and #4. T_{hs}=65ºC: <u>Free end bearing</u> temperature rise (T_{1-4}-T_{amb}) versus air temperature rise in the feed enclosure (T_e-T_{amb}). Arithmetic mean of (T_1, T_2, T_3, and T_4) shown.

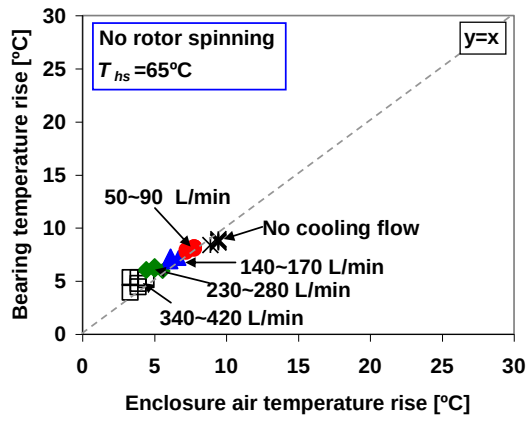

(a) No rotor spinning

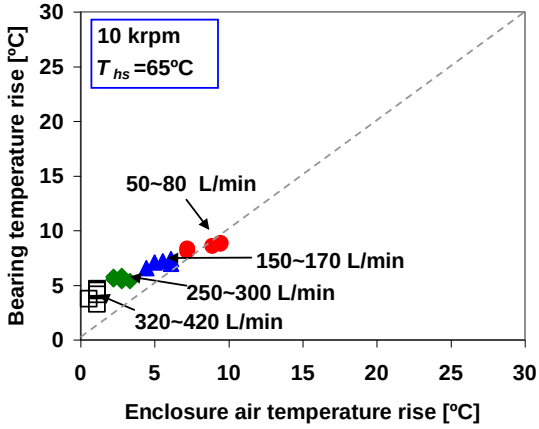

(b) 10 krpm

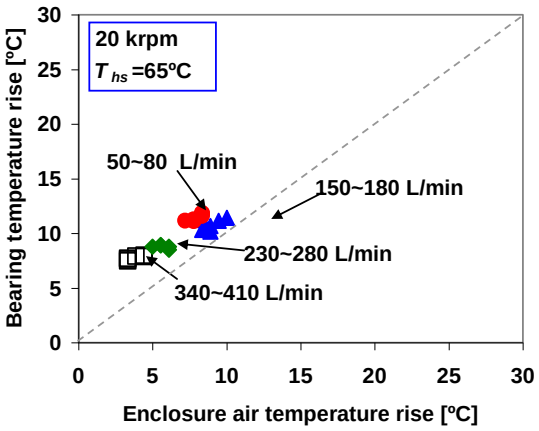

(c) 20 krpm

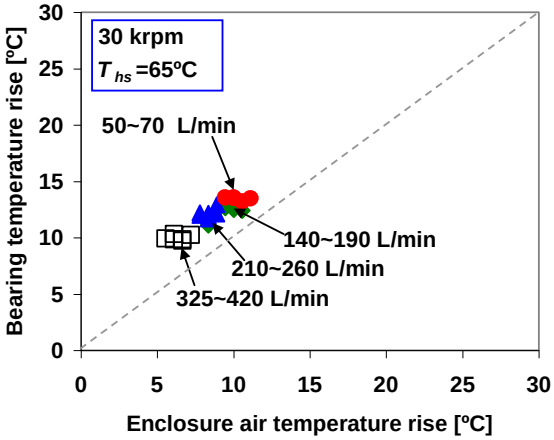

(d) 30 krpm

Fig. H.2 Test cases #1 and #4. T_{hs}=65ºC: <u>Drive end bearing</u> temperature rise (T_{6-9}-T_{amb}) versus air temperature rise in the feed enclosure (T_e-T_{amb}). Arithmetic mean of (T_6, T_7, T_8, and T_9) shown.

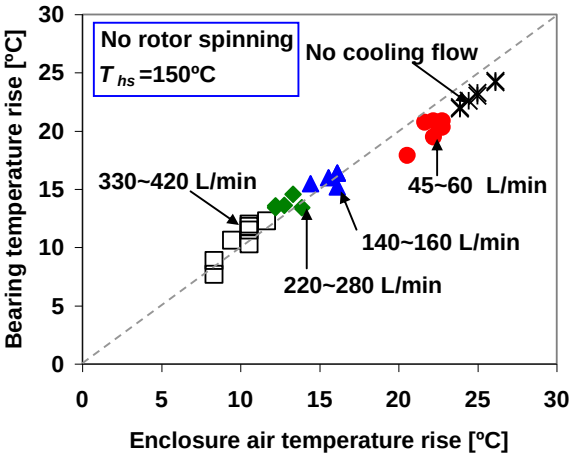

(a) No rotor spinning

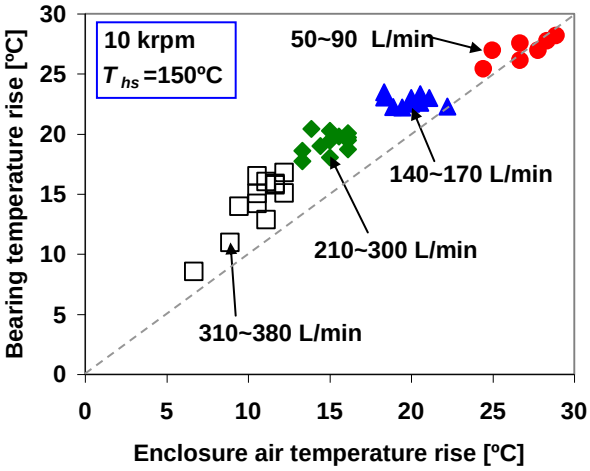

(a) 10 krpm

Fig. H.3 Test cases #3 and #6. T_{hs}=150ºC: <u>Free end bearing</u> temperature rise (T_{1-4}-T_{amb}) versus air temperature rise in the feed enclosure (T_e-T_{amb}). Arithmetic mean of (T_1, T_2, T_3, and T_4) shown.

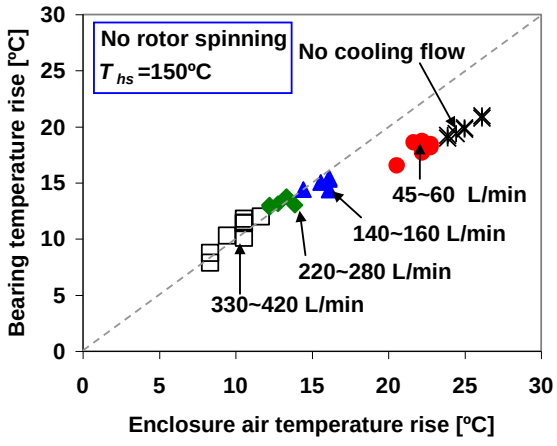

(a) No rotor spinning

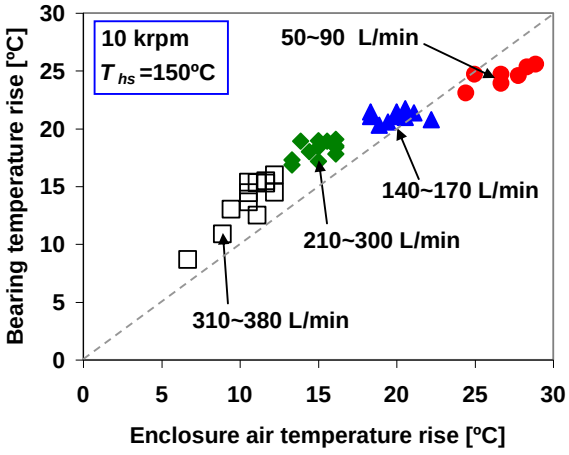

(a) 10 krpm

Fig. H.4 Test cases #3 and #6. T_{hs}=150ºC: <u>Drive end bearing</u> temperature rise (T_{6-9}-T_{amb}) versus air temperature rise in the feed enclosure (T_e-T_{amb}). Arithmetic mean of (T_6, T_7, T_8, and T_9) shown.

APPENDIX I

PREDICTION OF AXIAL AND CIRCUMFERENTIAL FLOW CONDITIONS FOR THE INNER AND OUTER COOLING STREAMS

Upon entering a foil bearing, the cooling gas stream splits into two streams; one flowing axially through the thin film gas region (inner stream) and the other flowing through the region underneath the top foil and the ID of the bearing sleeve (outer stream). The outer stream removes heat from the back surface of the top foil. Along the bearing axial length, the outer stream temperature increases as it removes heat, while its pressure decreases to ambient condition. This outer flow is eminently axial; hence, it is not disturbed by the rotating shaft. An outer stream with large flow rate takes away effectively most of the heat from the back of the top foil, with little heat conduction into the bearing cartridge [46]. Within the thin gas film, mechanical energy from viscous shear drag and heat convected from the shaft are removed and convected into the top foil. Note that the gas film thickness is very small compared to the rotor OD and bearing axial length. In this region, the hydrodynamic gas film pressure is generated while its temperature varies.

The rotor and bearing thermal expansion and centrifugal growth due to rotor spinning determine the actual bearing clearance c_{+}. Note that thermal expansion of the shaft and the bearing leads to a significant reduction in the operating clearance (see Appendix M). Presently, the rotor centrifugal growth, a function of rotor speed and material properties, is less than 1 μm at the top rotor speed of 30 krpm.

For concentric rotor operation, Fig. I.1 depicts a schematic view of a gas foil bearing with axially fed flow as in the current test rig. Forced cooling air flows through the mid-section of the bearing support housing, and then enters the test bearings. The flow is confined to the annular regions between the rotor OD and top foil ID, and between the top foil OD and bearing sleeve ID. For simplicity, the radial gaps for the outer and inner cooling flow streams equal the bump height h_B and uniform bearing clearance c_+ along the bearing axial length, respectively. Note that the outer gas flow through the outer gap region behind the top foil is only axial, not greatly restricted by the bump foils.

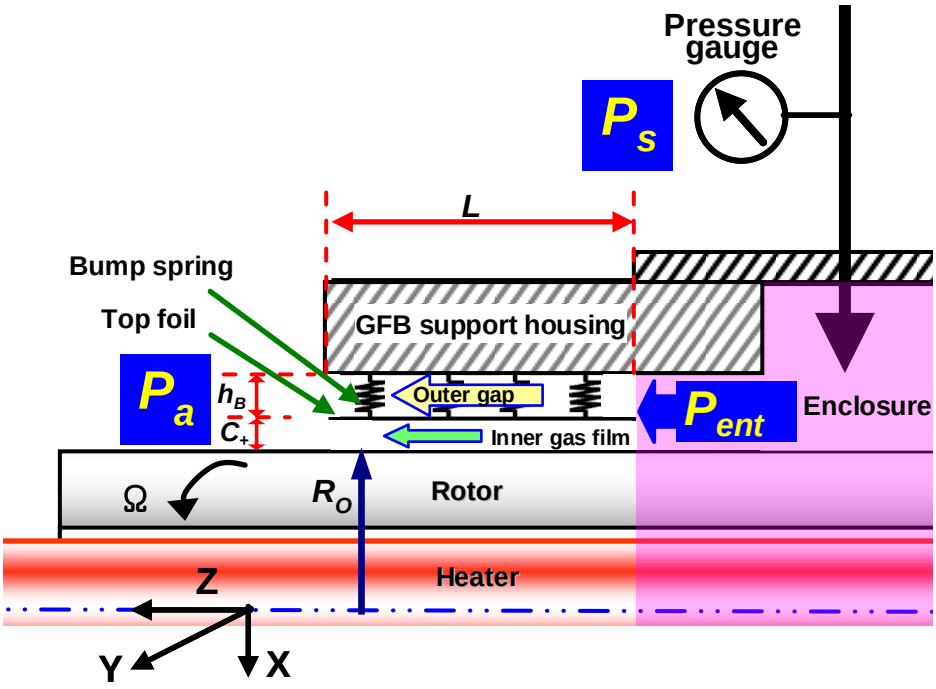

Fig. I.1 Schematic view (not to scale) of axial flows induced by forced cooling flow in the test foil bearing system.

The present analysis regards the fluid as an ideal gas and neglects energy transport considerations for simplicity[32]. At the bearing exist plane ($z=L$), the air pressure equals ambient pressure P_a and no pressure recovery effect is assumed. The density of a perfect gas is $\rho = \frac{P}{Z_c R_c T}$[33], while air viscosity is $\mu = \frac{1.458\times10^{-6} T^{\frac{3}{2}}}{110.4+T}$ [53]. For test case #6 (the highest operating temperature condition T_{hs}=150°C), air viscosity increases by 8% relative to its ambient condition value.

The continuity and momentum equations for the bulk flows in the outer gap is

$$\frac{\partial(\rho \cdot h_B \cdot W_{outer})}{\partial z} + \frac{\partial(\rho \cdot h_B)}{\partial t} = 0$$
$$-h_B \frac{\partial P}{\partial z} = -\tau_{zy}\Big|_0^{h_B} + \frac{\partial(\rho \cdot h_B \cdot W_{outer})}{\partial t} + \frac{\partial(\rho \cdot h_B \cdot W_{outer}{}^2)}{\partial z} \quad \text{(I.1)}$$

, while for the inner gap

$$\frac{\partial(\rho \cdot c_+ \cdot U)}{\partial x} + \frac{\partial(\rho \cdot c_+ \cdot W_{inner})}{\partial z} + \frac{\partial(\rho \cdot c_+)}{\partial t} = 0$$
$$-c_+ \frac{\partial P}{\partial x} = -\tau_{xy}\Big|_0^{c_+} + \frac{\partial(\rho \cdot c_+ \cdot U)}{\partial t} + \frac{\partial(\rho \cdot c_+ \cdot U^2)}{\partial x} + \frac{\partial(\rho \cdot c_+ \cdot U \cdot W_{inner})}{\partial z} \quad \text{(I.2)}$$
$$-c_+ \frac{\partial P}{\partial z} = -\tau_{zy}\Big|_0^{c_+} + \frac{\partial(\rho \cdot c_+ \cdot W_{inner})}{\partial t} + \frac{\partial(\rho \cdot c_+ \cdot U \cdot W_{inner})}{\partial x} + \frac{\partial(\rho \cdot c_+ \cdot W_{inner}{}^2)}{\partial z}$$

Above U is the circumferential bulk-flow velocity in the inner gap, and W_{outer} and W_{inner} are the axial bulk-flow velocities in the outer and inner gaps, respectively; x is the

[32] In practice, the rotor surface temperature is much higher than the temperatures of the top foil and the bearing housing, see Figs. 17−19 and Appendix E.

[33] Z_c (=1) is the compressibility factor, R_c (=287 J/kg-K) is the ideal gas constant, and T is temperature in degrees Kelvin.

circumferential coordinate along the bearing circumferential length, and z is the axial coordinate system spanning the bearing length.

For steady-state operating conditions ($\partial/\partial t = 0$) and assuming $\partial U/\partial x = 0$, substitution of the wall shear stress differences, $\tau_{yz}\Big|_0^{h_B} = -\dfrac{\mu(k_{z_{outer}} \cdot W_{outer})}{h_B}$ and $\tau_{yz}\Big|_0^{c_+} = -\dfrac{\mu(k_{z_{inner}} \cdot W_{inner})}{c_+}$ into Eqs. (I.1) and (I.2), and neglecting fluid inertia effects obtain

$$-h_B \frac{dP}{dz} = \frac{\mu(k_{z_{outer}} \cdot W_{outer})}{h_B} \text{ for the outer stream} \tag{I.3}$$

$$-c_+ \frac{dP}{dz} = \frac{\mu(k_{z_{inner}} \cdot W_{inner})}{c_+} \text{ for the inner stream} \tag{I.4}$$

where $k_{z_{outer}}$ and $k_{z_{inner}}$ are shear flow parameters depending on the flow Reynolds number and friction factors based on Hirs' formula [54]. Presently, $k_{z_i} = 12$ if Reynolds number ≤ 1000, otherwise $k_{z_i} = f_{z_i} \mathrm{Re}_{a_i}$ [55]. For a turbulent flow condition, the friction factor is calculated using Hir's formulation [54],

$$f_{z_i} = n \cdot \mathrm{Re}_{a_i}{}^{m} \text{ ; } i\text{=inner or outer} \tag{I.5}$$

where n=0.066 and m=-0.25 for smooth surfaces[34]. Note that, for smooth surfaces, Hirs' and Moody's friction factors are nearly identical for most Reynolds numbers [59]. The

[34] For smooth surfaces, Yamada [56], Childs and Kim [57], and Ha and Childs [58] report the values to be (n=0.079, m=-0.25), (n=0.0674, m=-0.217), and (n=0.0586, m=-0.217), respectively.

axial flow Reynolds numbers are defined as $\mathrm{Re}_{a_{outer}} = \dot{m}_{outer} / [\mu \cdot \pi \cdot 2(R_O + c_+)]$ for the outer stream and $\mathrm{Re}_{a_{inner}} = \dot{m}_{inner} / (\mu \cdot \pi \cdot 2R_O)$ for the inner stream.

Since $W_{outer} = \dot{M}_{outer} / (\rho h_B)$ and $W_{inner} = \dot{M}_{inner} / (\rho c_+)$, Eqs (I.3) and (I.4) become

$$\frac{d}{dz}\left(\frac{\rho \cdot {h_B}^3}{k_{z_{outer}} \cdot \mu} \frac{dP}{dz}\right) = \frac{d}{dz}(-\dot{M}_{outer}) = 0 \text{ for the outer stream} \tag{I.6}$$

$$\frac{d}{dz}\left(\frac{\rho \cdot {c_+}^3}{k_{z_{inner}} \cdot \mu} \frac{dP}{dz}\right) = \frac{d}{dz}(-\dot{M}_{inner}) = 0 \text{ for the inner stream} \tag{I.7}$$

Above, $\dot{M}_{outer}$ is the mass flow rate per circumferential length through the outer gap, and $\dot{M}_{inner}$ is the mass flow rate per circumferential length through the bearing clearance (i.e., inner gas film). Integrating equations (I.6) and (I.7) across the bearing axial length (L), and using the ideal gas law leads to

$$\dot{M}_{outer} = \frac{{h_B}^3}{2 k_{z_{outer}} \mu R_c T L} ({P_{ent}}^2 - {P_a}^2) \text{ for the outer stream} \tag{I.8}$$

$$\dot{M}_{inner} = \frac{{c_+}^3}{2 k_{z_{inner}} \mu R_c T L} ({P_{ent}}^2 - {P_a}^2) \text{ for the inner stream} \tag{I.9}$$

Then, the axial mass flow rates over the bearing circumference are

$$\dot{m}_{outer} = \dot{M}_{outer} \cdot \pi \cdot [2(R_O + c_+)] \text{ for the outer stream} \tag{I.10}$$

$$\dot{m}_{inner} = \dot{M}_{inner} \cdot \pi \cdot 2R_O \text{ for the inner stream} \tag{I.11}$$

Therefore, the overall cooling flow rate ($\dot{m}_{overall} = \dot{m}_{outer} + \dot{m}_{inner}$) into a bearing equals

$$\dot{m}_{overall} = \frac{(P_{ent}{}^2 - P_a{}^2)\cdot\pi}{\mu\cdot R_c\cdot T\cdot L}\cdot\left(\frac{h_B{}^3\cdot(R_O + c_+)}{k_{z_{outer}}} + \frac{c_+{}^3\cdot R_O}{k_{z_{inner}}}\right) \tag{I.12}$$

From Eq. (I.12), the entrance pressure P_{ent} is

$$P_{ent}{}^2 = \frac{\dot{m}_{overall}\cdot\mu\cdot R_c\cdot T\cdot L}{\left[\frac{h_B{}^3\cdot(R_O + c_+)}{k_{z_{outer}}} + \frac{c_+{}^3\cdot R_O}{k_{z_{inner}}}\right]\cdot\pi} + P_a{}^2 \tag{I.13}$$

Combination of equations (I.5) and (I.13) allows estimation of the entrance pressure P_{ent}. Since $\mathrm{Re}_{a_{outer}} = \frac{\dot{m}_{outer}}{\mu\cdot\pi\cdot 2(R_O + c_+)} = \frac{\dot{m}_{overall} - \dot{m}_{inner}}{\mu\cdot\pi\cdot 2(R_O + c_+)}$, the procedure to solve Eq. (I.13) is iterative. Recall the overall cooling flow rate ($\dot{m}_{overall} = Q\cdot\rho$) is recorded using the flow meter as shown in Fig. 11. Hence, the current calculation uses the recorded flow rate of the cooling stream and measured bearing sleeve temperatures[35].

The calculated shear factor for the bearing inner thin film region $k_{z_{inner}}$ is 12 for every test case since the axial flow Reynolds number for the inner stream is below 25, see Fig. I.6 (a) later.

For test case #5, Fig. I.2 depicts the shear factor ($k_{z_{outer}}$) for the outer stream versus cooling flow rate. $k_{z_{outer}}$ =12 at cooling flow rate<115 L/min (per bearing) and $k_{z_{outer}}$ =12−20 at cooling flow rates between 115 L/min and 250 L/min (per bearing). For the outer cooling flow, transition from laminar flow to turbulent flow occurs when the cooling flow rate into the test bearings is larger than ~115 L/min (per bearing). The shear factor does not change with rotor speed.

[35] For simplicity, the gas film temperature is taken as equal to the recorded bearing sleeve temperatures.

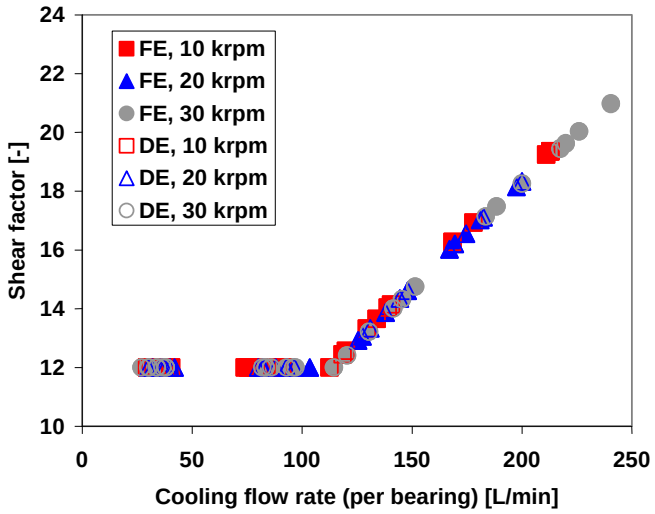

Fig. I.2 Test cases #5. Heater set temperature T_{hs} = 100ºC. Rotor speed of 10, 20, and 30 krpm: Shear factor of outer gap flow versus cooling flow rate. FE: Free end bearing, DE: Drive end bearing.

Figure I.3 depicts the calculated bearing entrance pressure P_{ent} versus cooling flow rate. The entrance pressures for the free end and drive end bearings are nearly identical. The entrance pressure steadily increases with cooling flow rate. P_{ent} for cooling flow rate above 115 L/min (per bearing) increases more rapidly than that for cooling flow rate below 115 L/min. This is because the shear factor at cooling flow rate above 115 L/min (per bearing) increases with cooling flow rate from 12 up to 20. Note that, at the largest cooling flow rate ~250 L/min (per bearing), P_{ent} is just ~4% higher than the ambient pressure P_a. This implies that the air inside the rig housing enclosure (mid-section) is not stagnant but flows quickly towards the bearing exit plane because of the very little flow resistance through the test FBs.

P_{ent}/P_s, omitted for brevity, ranges 0.9−0.3 and drops significantly with cooling flow rate. That is, the recorded gauge pressure P_s (see Fig. 11, pressure gauge 2) is much higher than the actual pressure (P_{ent}) inside the bearing housing enclosure (i.e., upstream bearing region). Note that the gauge pressure is recorded about 1 m away from the rig housing (long hose line)[36].

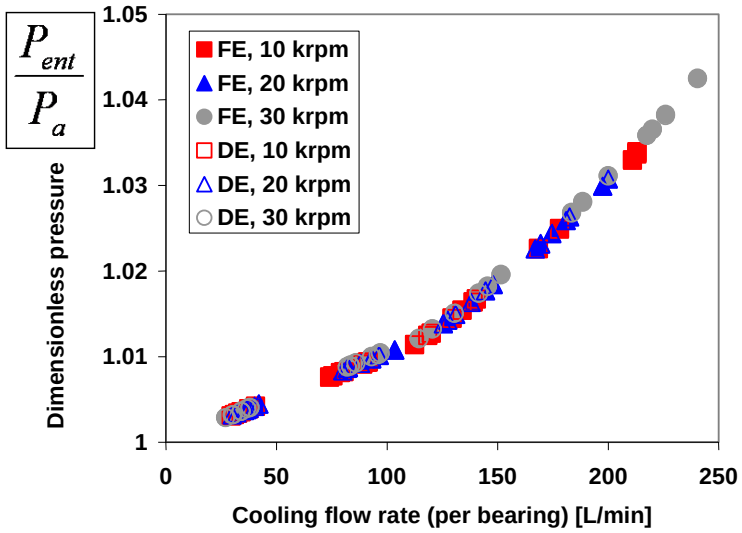

Fig. I.3 Test cases #5. Heater set temperature T_{hs} = 100ºC. Rotor speed of 10, 20, and 30 krpm: Dimensionless pressure (entrance pressure P_{ent} over ambient pressure P_a) versus cooling flow rate. FE: Free end bearing, DE: Drive end bearing.

Through the outer gap underneath the top foil, the axial distribution of the gas pressure from the bearing entrance toward the bearing exit equals:

[36] Recent independent tests conducted by another student confirm the assertion. The static pressure in the rig enclosure cannot be distinguished from ambient pressure. Presently, a static pressure gauge located in the enclosure hardly records a change, a few tenths of a bar for a supply pressure of 4 bar.

$$P_{outer}(z) = \frac{\sqrt{P_{ent}^{\,2} - \dfrac{2 \cdot k_{z_{outer}} \cdot \mu \cdot R_c \cdot T \cdot L \cdot z \cdot \dot{m}_{outer}}{h_B^{\,3} \cdot \pi \cdot [2(R_O + c_+)]}}}{P_a} \quad \text{for the outer stream} \tag{I.14}$$

Figure I.4 depicts the calculated pressure field (P/P_a) between the top foil OD and the bearing sleeve ID. As the cooling flow rate increases, the pressure along the bearing axial length decreases rapidly from the bearing entrance P_{ent} toward the bearing exit P_{exit}=P_a.

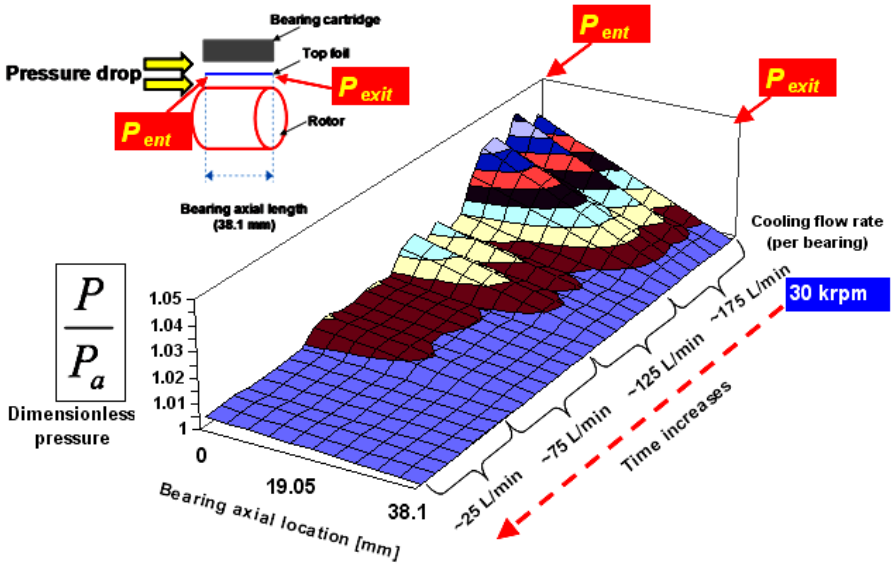

Fig. I.4 Test case #5. Heater set temperature T_{hs} = 100 ºC. Rotor speed of 30 krpm. Free end bearing: Dimensionless axial pressure distribution within outer gap versus cooling flow rate. $P_{exit} = P_a$.

Figure I.5 shows the mass flow rate through the outer gap over mass flow rate through inner gap, i.e., $\frac{\dot{m}_{inner}}{\dot{m}_{outer}}$. The figure also depicts $\left(\frac{c_+}{h_B}\right)^3$ since $\frac{\dot{m}_{inner}}{\dot{m}_{outer}} \propto \left(\frac{c_+}{h_B}\right)^3$, see

Eqs. (I.8) through (I.11). For cooling flow rates < 115 L/min (per bearing), $\frac{\dot{m}_{inner}}{\dot{m}_{outer}} \approx \left(\frac{c_+}{h_B}\right)^3$ since $k_{z_{inner}} = k_{z_{outer}}$=12 when both flows are laminar. On the other hand, for cooling flow rates above 115 L/min (per bearing), $\frac{\dot{m}_{inner}}{\dot{m}_{outer}} > \left(\frac{c_+}{h_B}\right)^3$ since the shear $k_{z_{inner}}$ = $12 < k_{z_{outer}}$ (see Fig. I.2). Note that less than just 10% of the overall cooling mass flows through the inner thin film region.

Figure I.6 shows the calculated axial flow Reynolds numbers for the outer and inner streams ($\mathrm{Re}_{a_{outer}}$ and $\mathrm{Re}_{a_{inner}}$) versus cooling flow rate. $\mathrm{Re}_{a_{outer}}$ and $\mathrm{Re}_{a_{inner}}$ range 200−2,000 and 1−23, respectively. The results indicate that laminar flow prevails in the inner film gap. For the outer gap, flow is laminar for cooling flow rates < 115 L/min. Presently, $\mathrm{Re}_{a_{outer}}$ increases linearly with cooling flow rate while $\mathrm{Re}_{a_{inner}}$ increases nearly exponentially with cooling flow rate. This is because, for the present calculation, the inner and outer gap flows are determined by c_+ (decreasing with rotor speed and increasing with cooling flow rate) and h_B (constant regardless of the operating condition), respectively. $\mathrm{Re}_{a_{inner}}$ for the drive end bearing is slightly higher than that for the free end bearing because the operating clearance c_+ is larger than that of the free end bearing.

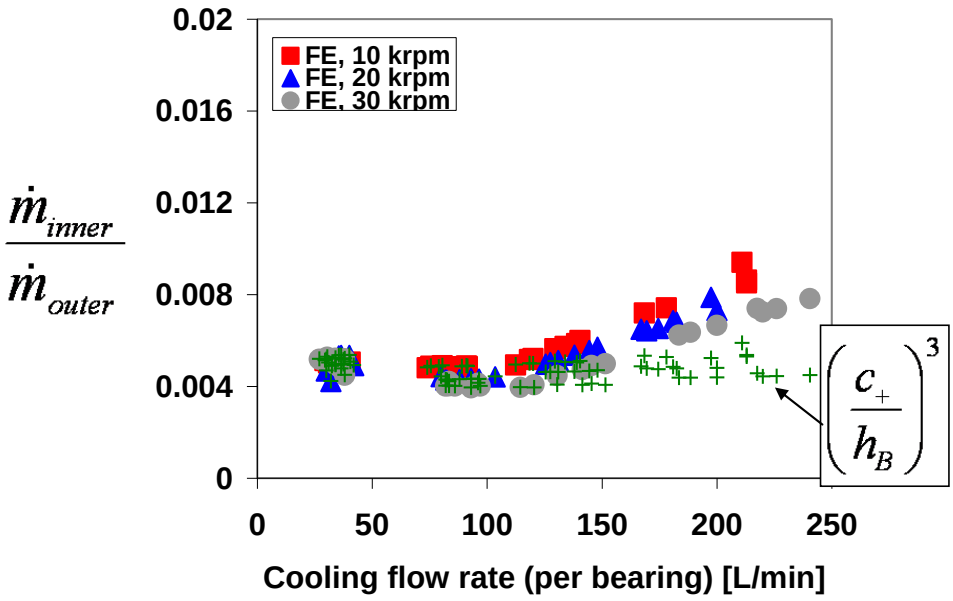

(a) Free end bearing

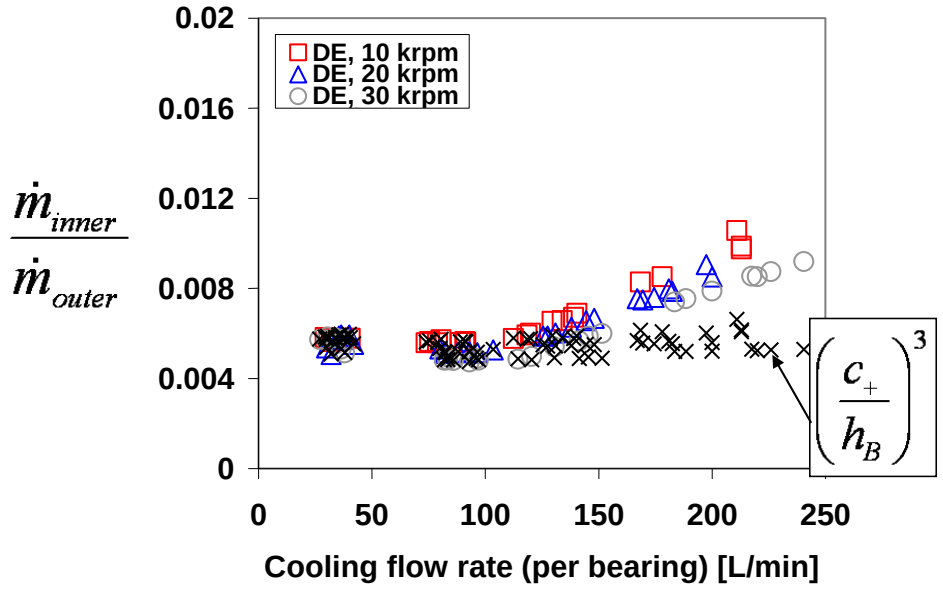

(b) Drive end bearing

Fig. I.5 Test cases #5. Heater set temperature T_{hs} = 100 ºC. Rotor speed of 10, 20, and 30 krpm: Mass flow rate though outer gap over mass flow rate through inner gap versus cooling flow rate. $(c_+/h_B)^3$ also shown. FE: Free end bearing, DE: Drive end bearing.

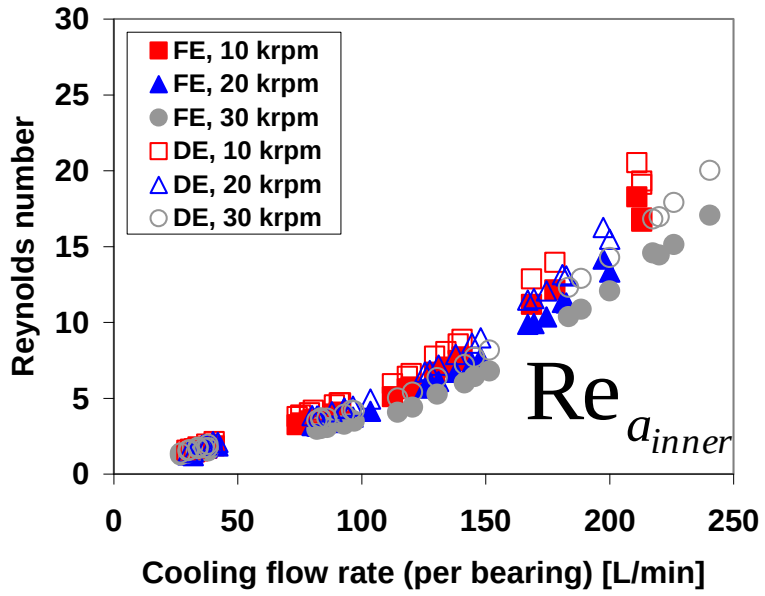

(a) Inner thin film region

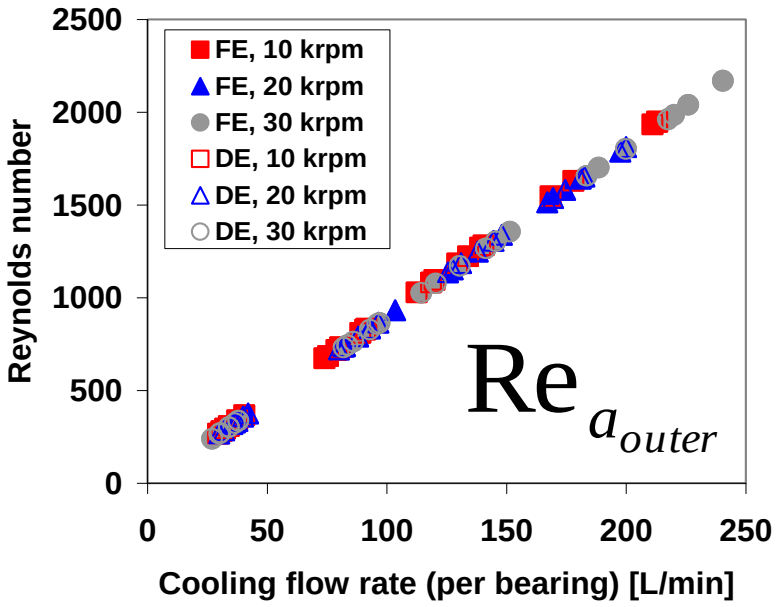

(b) Outer gap region

Fig. I.6 Test cases #5. Heater set temperature T_{hs} = 100ºC. Rotor speed of 10, 20, and 30 krpm: Axial flow Reynolds numbers of (a) inner and (b) outer cooling streams versus cooling flow rate. Note different vertical scale.

In a centered journal bearing, the circumferential flow Reynolds number is $\mathrm{Re}_c = \frac{\rho}{\mu} R_O \Omega c_+$, where R_O is the rotor radius, Ω is the rotor speed, c_+ is a operating radial clearance, and ρ and μ are the gas density and viscosity, respectively. Figure I.7 depicts the predicted circumferential flow Reynolds number $\mathrm{Re}_{c_{exist}}$ in the thin film region at the bearing exit plane[37]. $\mathrm{Re}_{c_{exist}}$ at 10, 20, and 30 krpm are ~100, ~200, ~300, respectively. $\mathrm{Re}_{c_{exist}}$ decreases as the operating temperature increases since c_+ decreases with T_{hs}.

In the inner gap flow region, and for all test cases, i.e., $\mathrm{Re}_c >> \mathrm{Re}_{a_{inner}}$, compare Figs. I.6 (a) and I.7. Therefore, the forced axial cooling flow rate does not alter significantly the development of the circumferential velocity, see Fig. I.8 later.

[37] The circumferential flow Reynolds number at the entrance plane is similar with the circumferential flow Reynolds number at the exit plane, i.e., for all test cases, $\frac{\mathrm{Re}_{C_{exit}}}{\mathrm{Re}_{C_{ent}}} \approx 0.96 \sim 0.99$, where $\mathrm{Re}_{C_{ent}} = \frac{\rho_{ent}}{\mu} R\Omega c_+$.

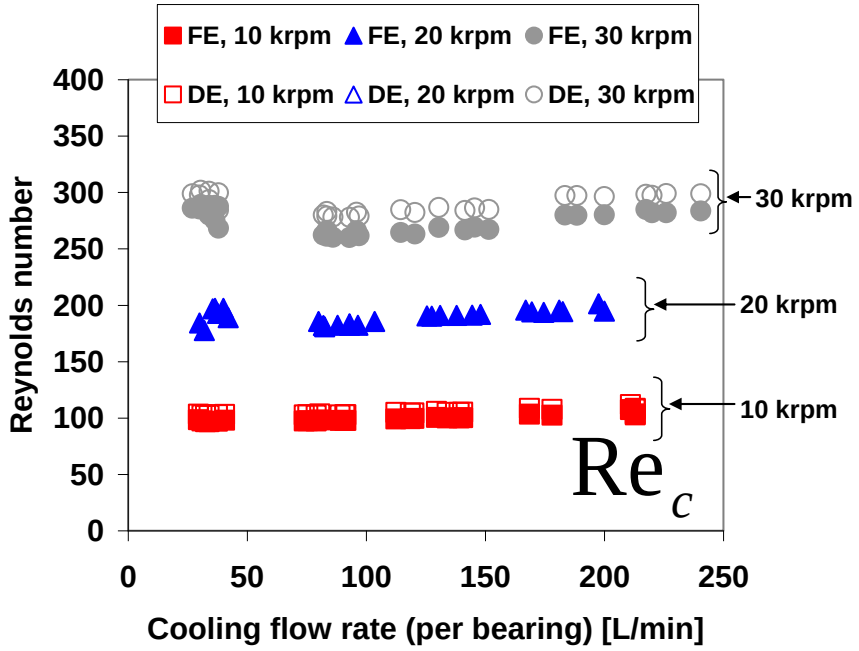

Fig. I.7 Test cases #5. Heater set temperature T_{hs} = 100ºC. Rotor speed of 10, 20, and 30 krpm: Circumferential flow Reynolds number for thin film gas region at the bearing exit plane (P=P_a) versus cooling flow rate. FE: Free end bearing, DE: Drive end bearing.

In the inner gap flow region (i.e., the thin film), the entrance circumferential velocity is

$$U_{ent} = U(x,0) = \alpha \Omega R_O \tag{I.15}$$

where α is an inlet flow pre-swirl factor, Ω is rotor angular velocity, and R_O is the rotor radius. The current analysis assumes α = 0, i.e., negligible fluid rotation at the bearing entrance plane since the cooling flow is imposed directly into the bearing entrance. The evolution of the gas circumferential velocity (u_c) along the axial direction is[38] [60]

[38] This equation is valid for centered journal operation.

$$u_c = \frac{\Omega R_O}{2}(1-e^{-\sigma z}) + U_{ent}e^{-\sigma z} \tag{I.16}$$

where $\sigma = \dfrac{k_{z_{inner}}}{\dfrac{\dot{m}_{inner}}{2R_O\pi \cdot \mu}} \dfrac{L}{c_+}$ is a parameter relating drag friction to fluid inertia effects. Note that u_c = 0 at the inlet plance and $u_c \to \dfrac{\Omega R_O}{2}$ as $z \to L$ (exit plane). For test case #5 (T_{hs}=100°C), Fig. I.8 depicts the dimensionless circumferential gas velocity $\dfrac{u_c}{\Omega R_O}$ versus dimensionless bearing axial length while increasing the cooling flow rate for rotor speeds of 10−30 krpm. The results are shown over 20% of the bearing axial length, i.e., from z=0 to z=0.2L. As the cooling flow rate into the bearings increases, the axial location where $u_c = \dfrac{\Omega R_O}{2}$ shifts toward the bearing exit plane. That is, the gas film circumferential flow velocity decreases with an increasing cooling flow rate. For the present test configuration, $u_c / \Omega R_O$ reaches ½ within 5% of the bearing axial length since $P_{ent} \approx (1 \sim 1.05) \times P_a$, recall Fig. I.3.

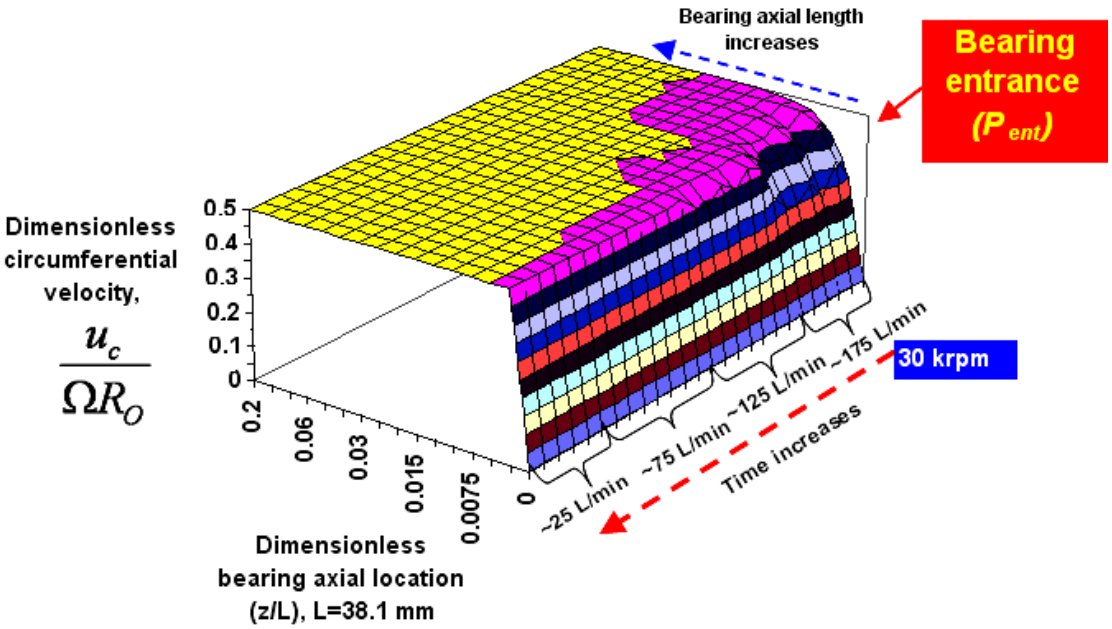

Fig. I.8 Test case #5. Heater set temperature T_{hs} = 100 ºC. Rotor speed of 30 krpm. Free end bearing: Dimensionless circumferential mean flow velocity versus dimensionless bearing axial length within bearing inner thin film region.

APPENDIX J

ROTORDYNAMIC RESPONSE DURING START-UP:

COLD ROTOR CONDITION. TEST CASE #7

For test case #4, Fig. J.1 depicts waterfall plots of vertical and horizontal motion recorded at the rotor drive and free ends for operation from rest to 30 krpm. The forced cooling flow rate into the bearings is ~350 L/min. The ramp rate for rotor acceleration is 16.7 Hz/s. Note that the temperatures of the rotor and bearings are close to ambient temperature, i.e., cold rotor and bearings. Recall that the tests demand enough time to reach steady state thermal conditions. No subsynchronous rotor motions are recorded. The rotor responses along the rotor drive end are mainly synchronous. On the other hand, the 2X rotor whirl motions are dominant at the rotor free end.

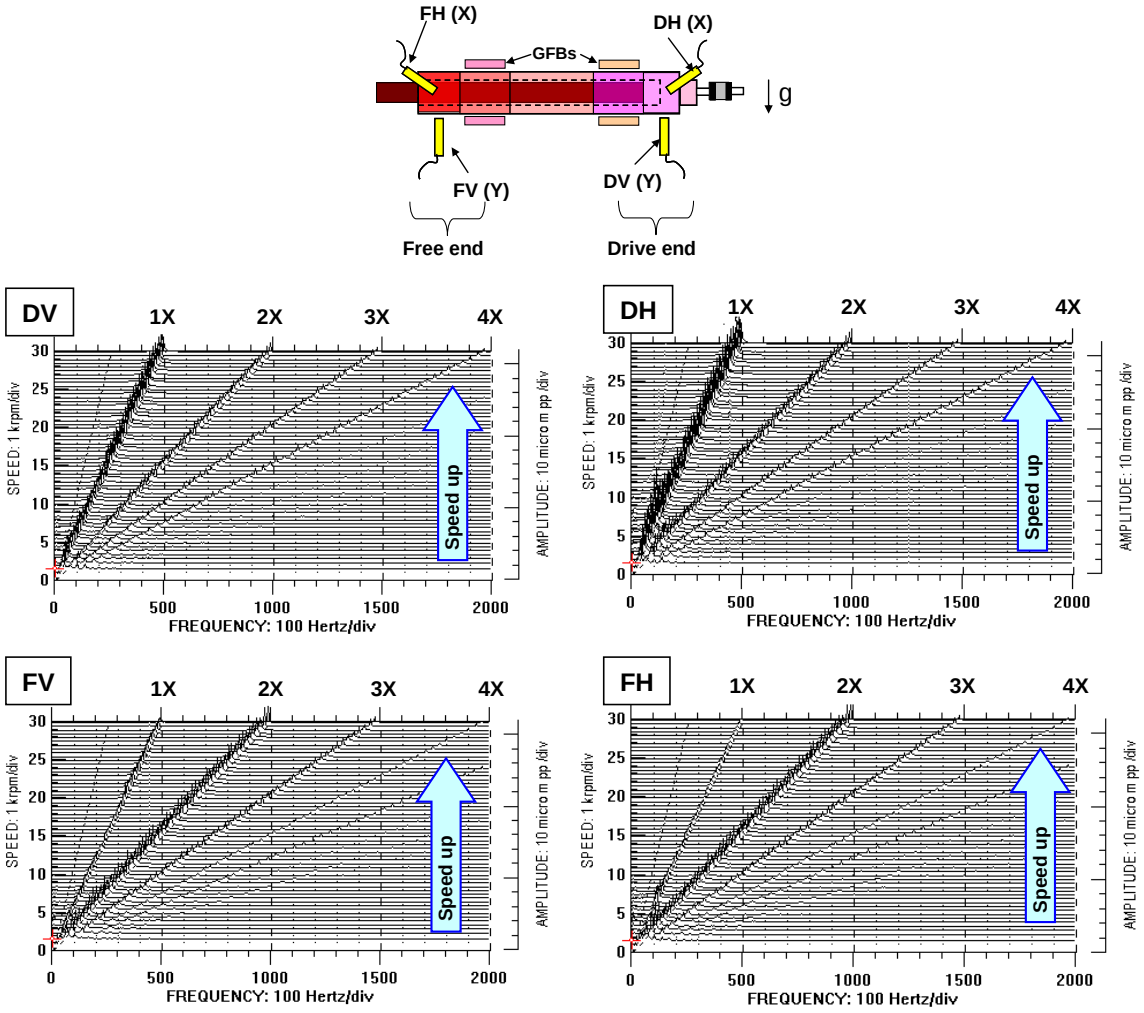

Fig. J.1 Test case #7: Waterfalls of rotor motion during accelerating from rest to 30 krpm. Heater off, set cooling flow rate 350 L/min, acceleration= 16.7 Hz/s. Rotor drive end, vertical (DV) and horizontal (DH) planes and rotor free end, vertical (FV) and horizontal (FH) planes.

Figure J.2 shows synchronous speed (1X) and 2X response amplitude of rotor motions during the start up process from rest to 30 krpm. Slow roll compensation is at 4 krpm. The rotor motion amplitude peaks at ~7 krpm. The rotor response amplitudes at the system critical speed region are damped well. The 2X rotor response amplitudes are

almost constant above the system critical speed. The measured rotor response does not show any evidence of nonlinearity in the rotor-bearing system[39].

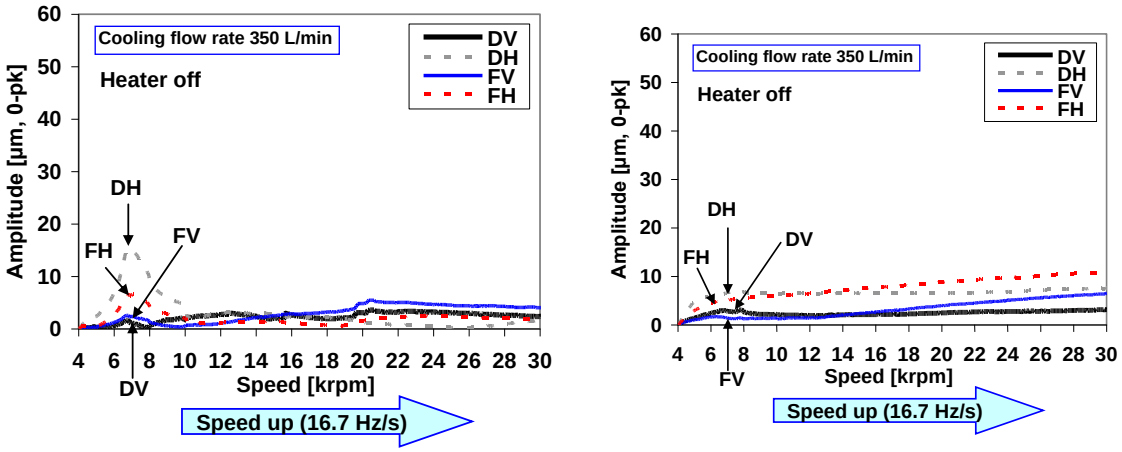

(a) Synchronous (1X) rotor motion

(b) 2X rotor motion

Fig. J.2 Test case #7: Amplitude of rotor synchronous response versus rotor speed. Speed up from rest to 30 krpm with ramp rate of 16.7 Hz/s Slow roll compensation 4100 rpm.

Figure J.3 depicts a phase difference of 180 deg while traversing the speeds with largest response amplitudes. Figure J.4 shows the ratio of amplitudes between the rotor responses at the drive and free ends.

[39] Reference [46] shows the nonlinear rotor dynamic response characterized as a sudden drop in rotor motion amplitudes at rotor speed just above the system critical speed due to large rotor imbalances.

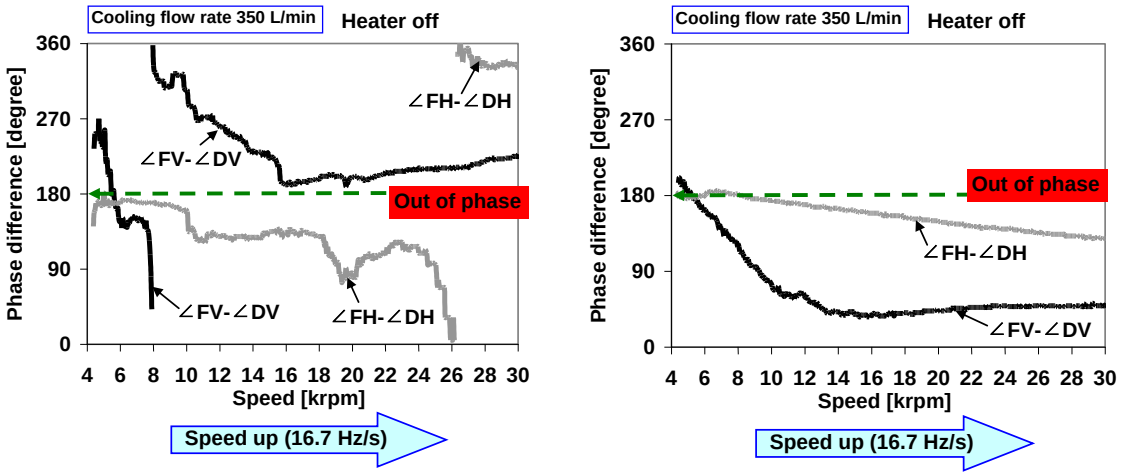

(a) Synchronous (1X) rotor motion (b) 2X rotor motion

Fig. J.3 Test case #7: Phase differences of recorded imbalance response. T_{hs} = 65ºC. Speed up from rest to 30 krpm with ramp rate of 16.7 Hz/s Cooling flow rate 350 L/min.

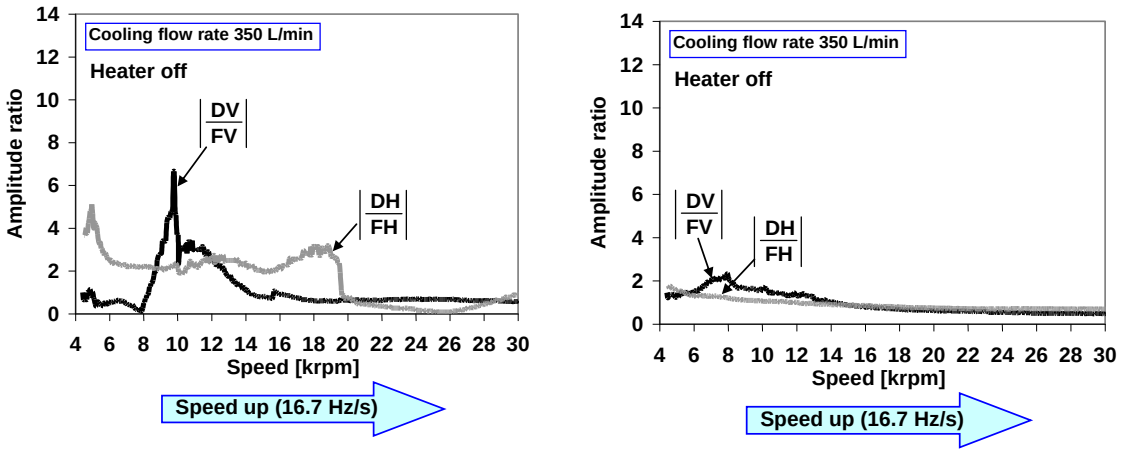

(a) Synchronous (1X) rotor motion (b) 2X rotor motion

Fig. J.4 Test case #7: Amplitude ratio of recorded imbalance response. T_{hs} = 65ºC. Cooling flow rate 350 L/min.

APPENDIX K

NATURAL FREQUENCIES OF TEST ROTOR-BEARING SYSTEM

A miniature accelerometer (PCB352C23, sensitivity 5.11 mV/g) measures the natural frequency of the test rotor-bearing system. The accelerometer is affixed on (a) the flexible coupling, or (b) connecting rod, or (c) rotor drive end, or (d) rotor free end, refer the insets in Fig. G.1.

Figure K.1 depicts the FFT of the recorded accelerations. A thin steel rod impacts the indicated location in the inset figure for each measurement. The flexure mode of the thin connecting rod and coupling (namely, a *dog tail wagging* mode, 1.50 kHz=90 krpm) exists beyond the present operating speed (up to 30 krpm) and is lower than the first bending natural frequency (3.74 kHz=224 krpm) of the test rotor.

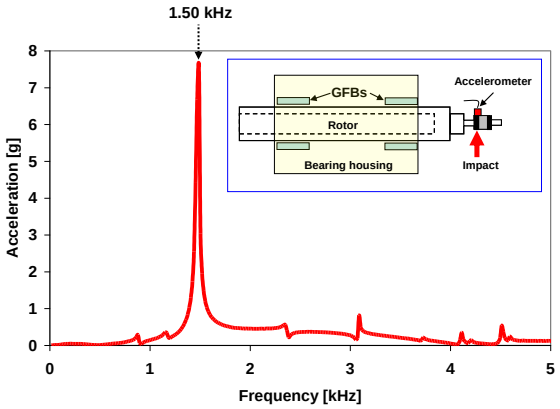

(a) Impact and sensor location: flexible coupling

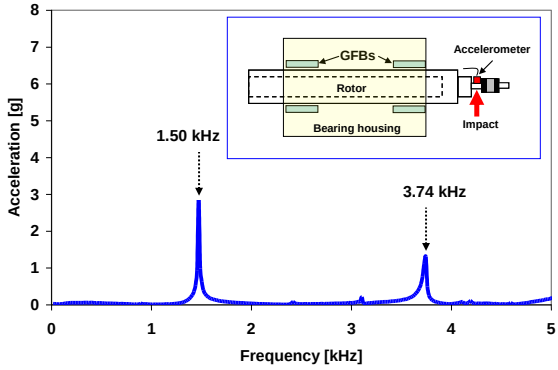

(b) Impact and sensor location: connecting rod

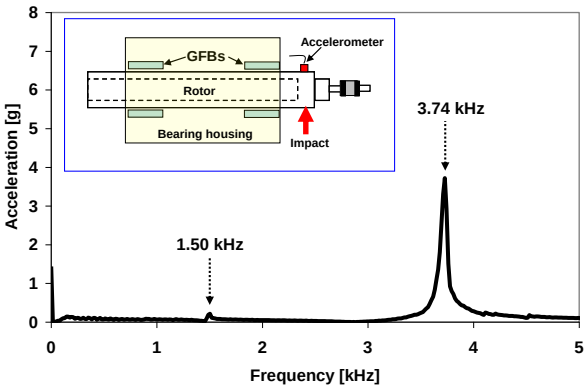

(c) Impact and sensor location: rotor drive end

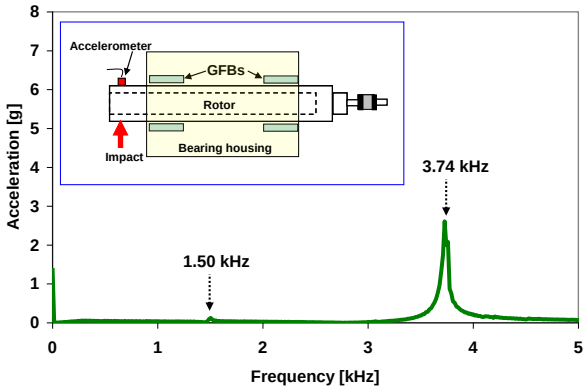

(d) Impact and sensor location: rotor free end

Fig. K.1 Acceleration spectra at (a) flexible coupling, (b) connecting rod, (c) rotor drive and (d) free ends. Uncertainty in frequency 16 Hz. No shaft rotation. Ambient temperature 22ºC.

APPENDIX L

ROTOR WHIRL ORBITS: TEST CASES #7 AND #9

Figures L.1 through L.4 show rotor whirl orbits for test cases #7 (heater off) and #9 (T_{hs}=100ºC). There is no major difference in rotor response amplitude and phase angles while increasing the rotor OD temperature.

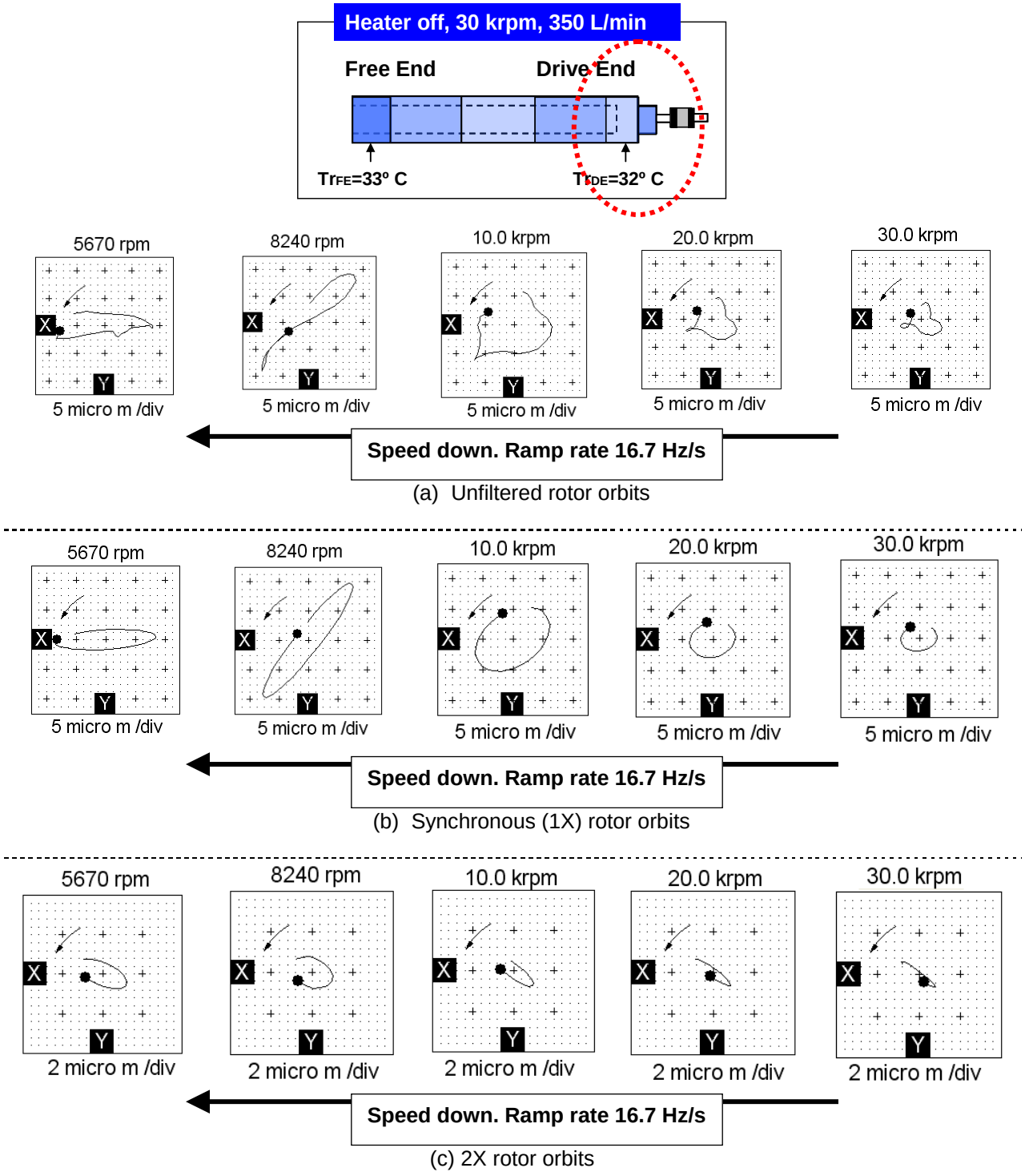

Fig. L.1 Test case #7. Drive end rotor orbits. Heater off. Speed down from 30 krpm to rest with ramp rate of 16.7 Hz/s. Cooling flow rate ~350 L/min. No slow roll compensation. Note different scale.

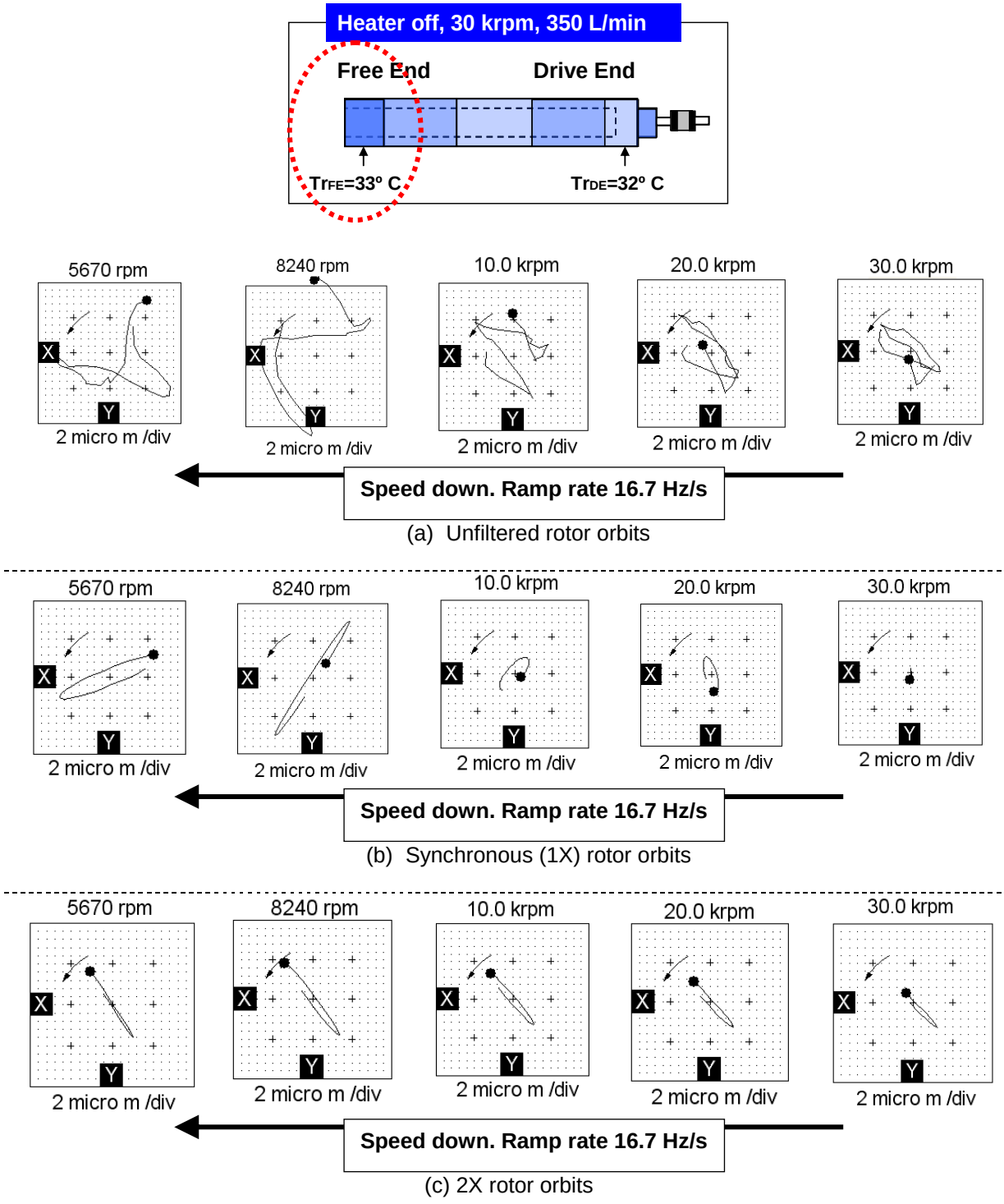

Fig. L.2 Test case #7. Free end rotor orbits. Heater off. Speed down from 30 krpm to rest with ramp rate of 16.7 Hz/s. Cooling flow rate ~350 L/min. No slow roll compensation.

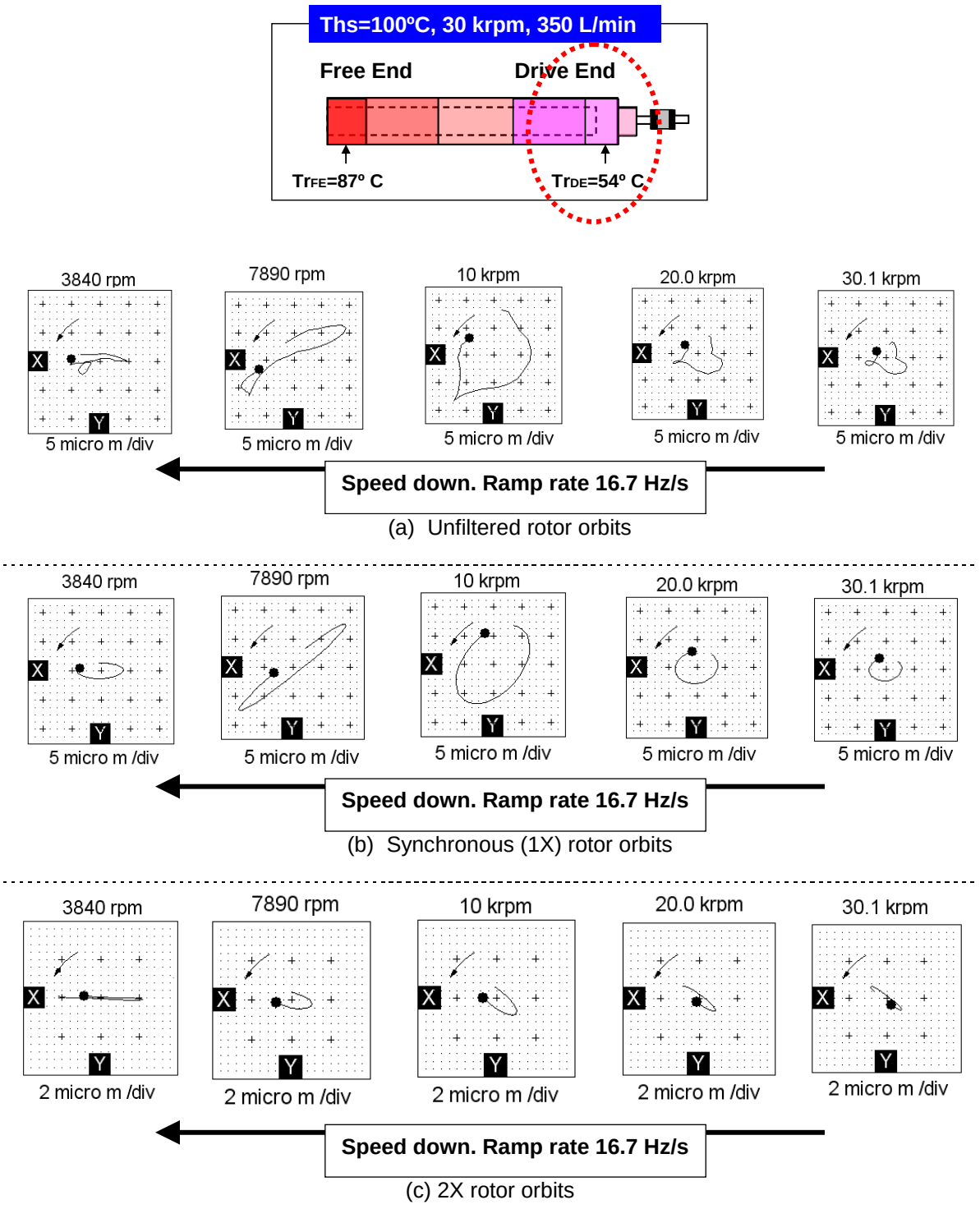

Fig. L.3 Test case #9. Drive end rotor orbits. T_{hs}=100ºC. Speed down from 30 krpm to rest with ramp rate of 16.7 Hz/s. Cooling flow rate ~350 L/min. No slow roll compensation. Note different scale.

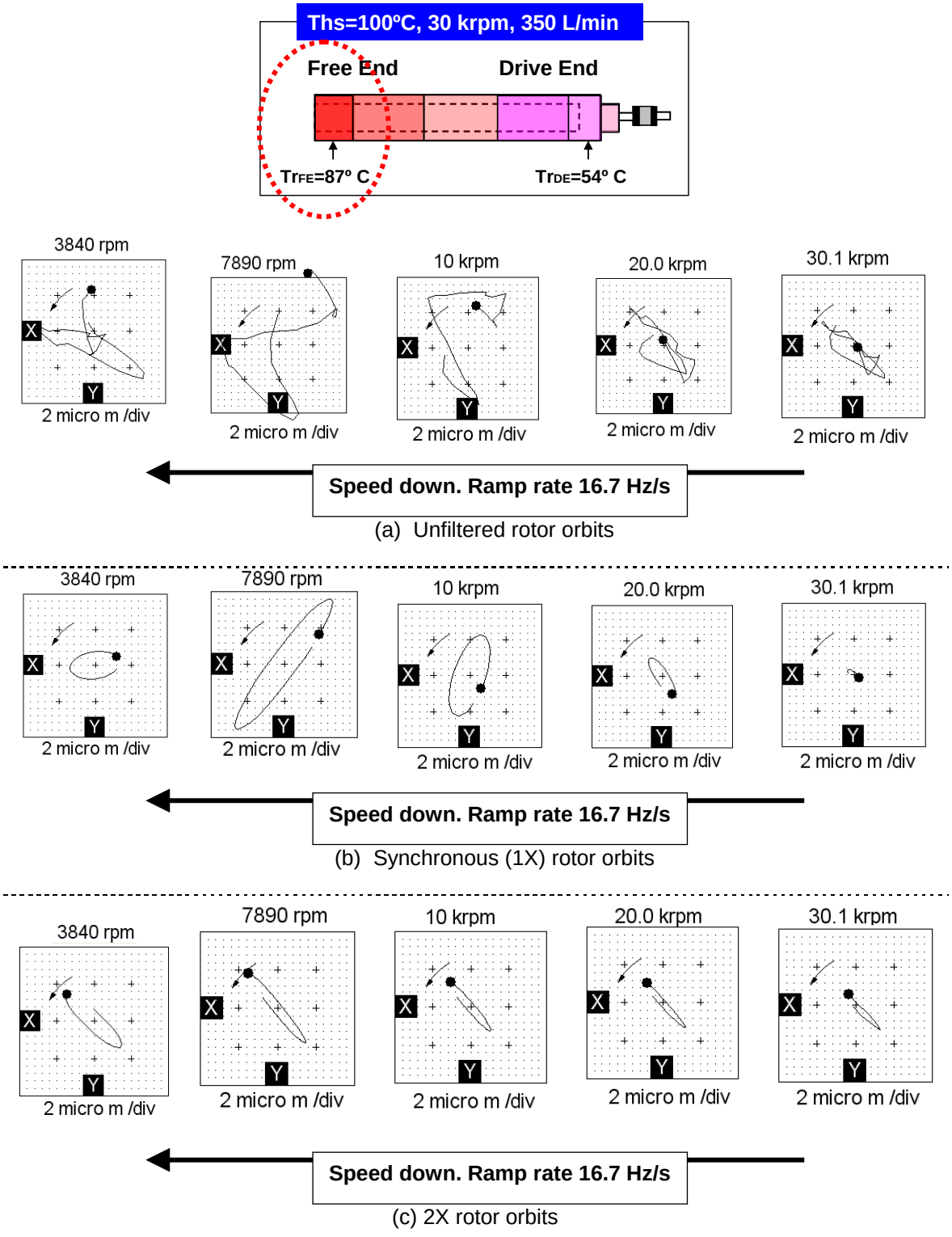

Fig. L.4 Test case #9. Free end rotor orbits. T_{hs}=100ºC. Speed down from 30 krpm to rest with ramp rate of 16.7 Hz/s. Cooling flow rate ~350 L/min. No slow roll compensation.

APPENDIX M

COMPLETE INPUT DATA FOR PREDICTION OF FOIL BEARING PERFORMANCE AND PREDICTED TEMPERATURES AND STATIC LOAD PARAMETERS

Table M.1 Complete input parameters for GFB prediction

Parameters		Value	Unit
Cooling stream gas condition	Flow rate	See Tables M.2 and M.3	L/min
	Temperature (=T_e)	See Tables M.2 and M.3	°C
Operating condition	Ambient pressure	1.013	bar
	Ambient temperature (=T_{amb})	See Tables M.2 and M.3	°C
	(Constant) Shaft temperature: (Material: Inconel 718)	See Tables M.2 and M.3	°C
Thermal mixing condition	Thermal mixing parameter	0.65 (4)	-
Bump geometry (Material: Inconel X-750)	Bump foil thickness	1.20×10^{-4}	mm
	Bump pitch	4.35×10^{-3}	mm
	Bump half length	1.25×10^{-3}	mm
	Bump height	5×10^{-4}	mm
	Friction coefficient, μ_f (1)	0.2	-
	Structural loss factor, γ (2)	0.2	-
	Number of Bumps	26	-
Top foil geometry and properties (Material: Inconel X-750)	Foil Arc Diameter (= Rotor outer diameter)	3.65×10^{-2}	mm
	Foil Arc Length	355	degree
	Top foil width (=Axial length)	3.81×10^{-2}	mm
	Foil thickness	1.20×10^{-4}	mm
	Stiffening factor(3) (circumferential direction)	4	-
Nominal radial clearance		1×10^{-4}	mm

(1) Assumed as $\mu_f \approx \gamma$. In general, the experimentally identified friction coefficient has the same magnitude as the loss factor [10,39].
(2) Estimated from the area enclosed by the mechanical hysteresis loop in the static load versus FB deflection curves at room temperature (Fig. 14).
(3) Empirical parameter. A measure of the anisotropic elastic properties in a top foil.
(4) The thermal mixing ratio depends on the bearing configuration and applied cooling method.

Table M. 2 Drive end GFB: Predicted bearing static parameters

Test Case #	T_{hs} [ºC]	Rotor speed [krpm]	Cooling flow rate (per bearing) [L/min]	Cooling flow Temp -erature T_{Co} $=T_e$ [ºC](1)	T_{amb} [ºC] (1)	Rotor OD [ºC] (1)(2)	Shaft centri -fugal growth [µm] (3)	Net Shaft -bearing thermal expan -sion [µm] (3)	Axially averaged gas film temp- erature [ºC]	Peak gas film temp- erature [ºC]	Axially averaged bearing sleeve ID temp- erature [ºC]	Peak bearing sleeve ID temp- erature. [ºC]	Eccent -ricity [µm]	Attitude angle [º]	Mini- mum film Thick -ness [µm]	Drag torque [N -mm]
7	Off	10	175	25	23	33	0.08	1.72	28.8	31.6	25.6	26.9	91	25	10	0.72
7	Off	20	175	25	23	33	0.34	1.59	28.6	33.2	25.5	27.6	83	32	18	1.07
7	Off	30	175	25	23	33	0.76	1.49	28.4	34.4	25.4	28.2	76	38	25	1.35
4,8	65	10	175	30	29	43	0.08	0.62	37.1	40.5	32.8	34.4	88	25	11	0.73
4,8	65	20	175	32	29	50	0.34	1.00	40.5	46.3	34.5	37.3	79	34	19	1.08
4,8	65	30	175	36	28	53	0.76	1.19	41.7	48.9	34.9	38.4	71	39	27	1.38
5,9	100	10	175	28	22	49	0.08	4.55	37.5	42.3	28.2	31.4	94	24	11	0.73
5,9	100	20	175	33	23	55	0.34	5.36	41.1	48.1	31.2	34.4	86	32	19	1.07
5,9	100	30	175	33	23	61	0.76	5.49	42.5	51.1	31.9	35.9	79	38	26	1.36
6	150	10	175	37	26	70	0.08	7.83	51.6	58.5	37.9	41.1	97	24	11	0.73
4	65	10	125	31	29	45	0.08	0.53	40.2	44.4	37.7	41.0	90	25	11	0.73
4	65	20	125	34	29	50	0.34	0.51	43.0	49.3	39.8	44.8	81	33	20	1.08
4	65	30	125	38	28	57	0.76	0.46	46.3	54.4	42.3	48.6	73	39	27	1.38
5	100	10	125	31	22	51	0.08	12.35	42.0	47.7	36.4	40.5	103	23	10	0.70
5	100	20	125	35	23	56	0.34	13.58	44.9	53.1	38.6	44.6	95	31	18	1.06
5	100	30	125	40	23	64	0.76	15.68	48.9	58.7	41.5	48.5	89	35	25	1.35
6	150	10	125	42	27	72	0.08	19.72	58.6	66.8	49.4	55.2	110	22	10	0.71
4	65	10	75	34	28	46	0.08	0.63	41.2	45.5	38.3	41.7	90	25	11	0.73
4	65	20	75	38	28	53	0.34	0.69	45.3	52.0	41.5	46.7	81	34	20	1.08
4	65	30	75	36	28	49	0.76	0.43	41.8	49.1	38.7	44.4	73	39	26	1.37
5	100	10	75	34	22	54	0.08	13.75	44.3	50.4	38.0	42.4	103	23	10	0.72
5	100	20	75	40	23	60	0.34	15.66	48.2	57.0	41.0	47.2	97	30	18	1.06
5	100	30	75	43	23	64	0.76	15.97	49.6	59.4	42.1	49.1	90	36	25	1.35
6	150	10	75	48	27	75	0.08	20.92	61.2	69.5	51.3	57.2	110	23	11	0.73
4	65	10	25	38	28	46	0.08	0.66	41.3	45.4	38.4	41.5	90	25	11	0.73
4	65	20	25	37	29	44	0.34	0.50	39.8	45.2	37.5	41.6	81	33	19	1.08
4	65	30	25	39	29	47	0.76	0.58	41.8	48.9	39.0	44.5	74	39	26	1.38
5,10	100	10	25	40	23	50	0.08	12.26	42.4	47.6	36.9	40.5	102	23	10	0.73
5,10	100	20	25	38	23	45	0.34	9.70	38.8	45.1	34.4	39.0	91	31	18	1.06
5,10	100	30	25	41	24	45	0.76	9.64	39.6	47.2	35.3	40.8	84	36	25	1.35
6	150	10	25	57	28	79	0.08	22.23	64.0	72.4	53.4	59.3	111	23	11	0.75

(1) Obtained from the test data. Input parameters in the analytical model

(2) Represent rotor temperatures at the bearing locations. Estimated from a constant temperature gradient (linear temperature drop) from the recorded rotor FE and DE temperatures (Tr_{FE} and Tr_{DE}).

(3) Operating radial clearance = nominal clearance – shaft centrifugal growth – net shaft-bearing thermal expansion).

Table M.3 Free end GFB: Predicted bearing static parameters

Test Case #	T_{hs} [ºC]	Rotor speed [krpm]	Cooling flow rate (per bearing) [L/min]	Cooling flow Temp -erature $T_{Co}=T_e$ [ºC](1)	T_{amb} [ºC] (1)	Rotor OD [ºC] (1)(2)	Shaft centri -fugal growth [µm] (3)	Net Shaft -bearing thermal expan -sion [µm] (3)	Axially averaged gas film temp- erature [ºC]	Peak gas film temp- erature [ºC]	Axially averaged bearing sleeve ID temp- erature [ºC]	Peak bearing sleeve ID temp- erature [ºC]	Eccent -ricity [µm]	Attitude angle [º]	Mini- mum film Thick -ness [µm]	Drag torque [N -mm]
7	Off	10	175	25	23	33	0.08	1.70	28.8	31.3	25.6	26.8	89	27	12	0.66
7	Off	20	175	25	23	33	0.34	1.58	28.5	32.4	25.5	27.2	80	36	22	0.98
7	Off	30	175	25	23	33	0.76	1.48	28.3	33.2	25.4	27.6	72	41	29	1.25
4,8	65	10	175	30	29	56	0.08	4.55	44.1	49.1	35.8	38.1	92	27	13	0.67
4,8	65	20	175	32	29	63	0.34	5.03	46.6	53.1	37.0	40.0	82	36	23	0.98
4,8	65	30	175	36	28	67	0.76	5.14	47.3	54.5	37.1	40.5	74	41	31	1.26
5,9	100	10	175	28	22	65	0.08	7.36	47.0	54.0	33.6	36.7	94	27	13	0.67
5,9	100	20	175	33	23	74	0.34	7.85	50.2	58.5	35.4	39.3	85	35	23	0.98
5,9	100	30	175	33	23	80	0.76	7.39	50.7	59.7	35.7	39.9	76	41	31	1.26
6	150	10	175	37	26	98	0.08	12.90	67.9	78.7	45.5	50.6	99	27	14	0.67
4	65	10	125	31	29	57	0.08	11.96	48.0	53.9	42.7	47.0	99	26	13	0.67
4	65	20	125	34	29	63	0.34	12.76	49.9	57.2	44.0	49.3	90	34	22	0.98
4	65	30	125	38	28	69	0.76	13.64	51.5	59.8	45.0	51.0	83	40	30	1.24
5	100	10	125	31	22	67	0.08	19.23	53.3	61.7	44.5	50.5	107	25	12	0.66
5	100	20	125	35	23	75	0.34	19.92	55.9	65.8	46.5	53.6	98	33	22	0.98
5	100	30	125	40	23	85	0.76	20.87	58.7	69.2	48.4	56.0	90	38	30	1.24
6	150	10	125	42	27	103	0.08	32.19	79.5	92.7	64.0	73.3	119	24	13	0.67
4	65	10	75	34	28	60	0.08	13.44	49.9	56.0	43.8	48.3	101	26	13	0.66
4	65	20	75	38	28	66	0.34	14.53	52.2	59.9	45.5	51.0	92	34	22	0.98
4	65	30	75	36	28	58	0.76	10.38	45.7	52.9	40.9	46.1	80	40	30	1.25
5	100	10	75	34	22	70	0.08	20.64	55.7	64.3	46.1	52.2	108	25	12	0.67
5	100	20	75	40	23	80	0.34	22.23	59.7	70.2	49.1	56.6	100	33	22	0.98
5	100	30	75	43	23	83	0.76	20.94	59.0	69.4	48.7	56.2	90	38	30	1.24
6	150	10	75	48	27	106	0.08	33.41	82.2	95.4	65.9	75.2	121	24	13	0.67
4	65	10	25	38	28	59	0.08	13.26	49.6	55.3	43.6	47.7	101	26	13	0.67
4	65	20	25	37	29	53	0.34	9.50	44.8	50.6	40.5	44.8	87	35	22	0.98
4	65	30	25	39	29	56	0.76	10.04	46.0	52.8	41.4	46.3	79	40	30	1.25
5,10	100	10	25	40	23	66	0.08	18.67	53.0	60.4	44.3	49.6	106	25	12	0.66
5,10	100	20	25	38	23	57	0.34	13.78	45.8	52.8	39.4	44.5	92	34	22	0.97
5,10	100	30	25	41	24	56	0.76	12.81	45.3	52.9	39.4	44.8	83	39	30	1.24
6	150	10	25	57	28	110	0.08	34.89	85.5	98.8	68.2	77.5	119	24	13	0.67

(1) Obtained from the test data. Input parameters in the analytical model

(2) Represent rotor temperatures at the bearing locations. Estimated from a constant temperature gradient (linear temperature drop) from the recorded rotor FE and DE temperatures (Tr_{FE} and Tr_{DE}).

(3) Operating radial clearance = nominal clearance – shaft centrifugal growth – net shaft-bearing thermal expansion.

APPENDIX N

PREDICTED TEMPERATURE FIELDS: TEST CASE #5. 10 KRPM

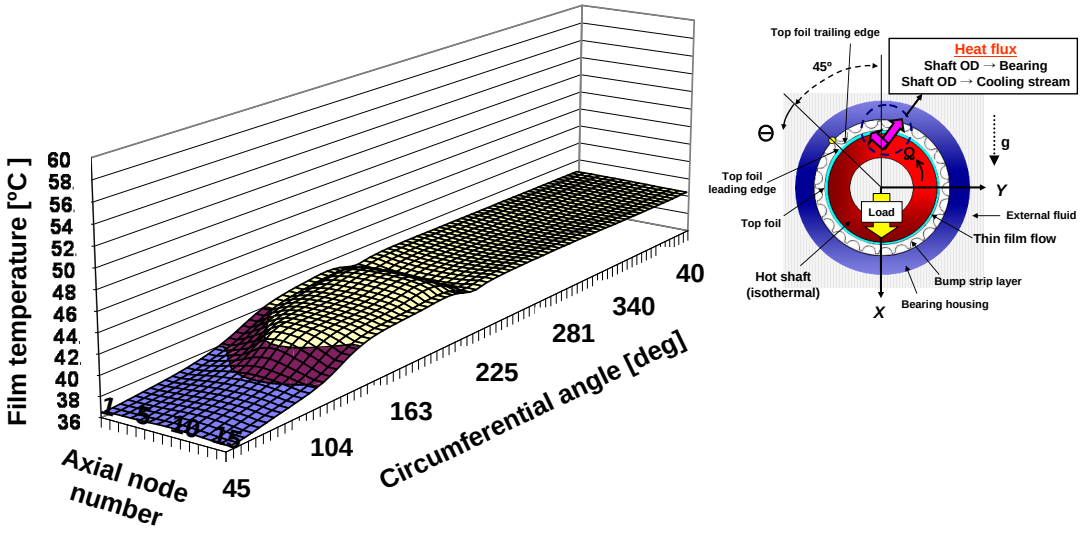

(a) Drive end bearing

(Cooling stream inlet temperature= 28ºC, uniform rotor OD temperature= 49ºC, T_a= 22ºC)

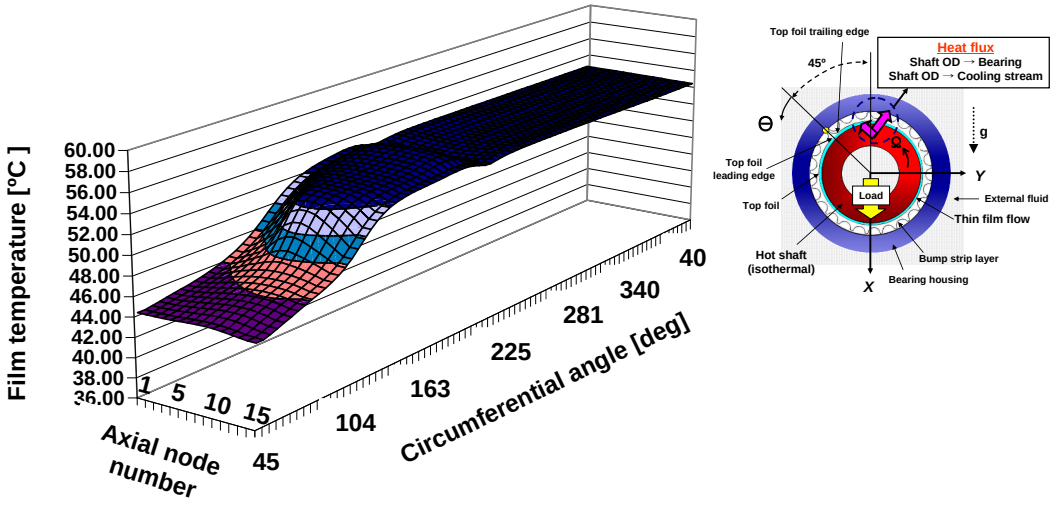

(b) Free end bearing

(Cooling stream inlet temperature= 28ºC, uniform rotor OD temperature= 65ºC, T_a= 22ºC)

Fig. N.1 Prediction: Test case #5. Thin film temperature fields in GFBs. T_{hs}=100ºC, rotor speed at 10 krpm. Cooling flow rate per each bearing 175 L/min. Thermal mixing coefficient λ=0.65.

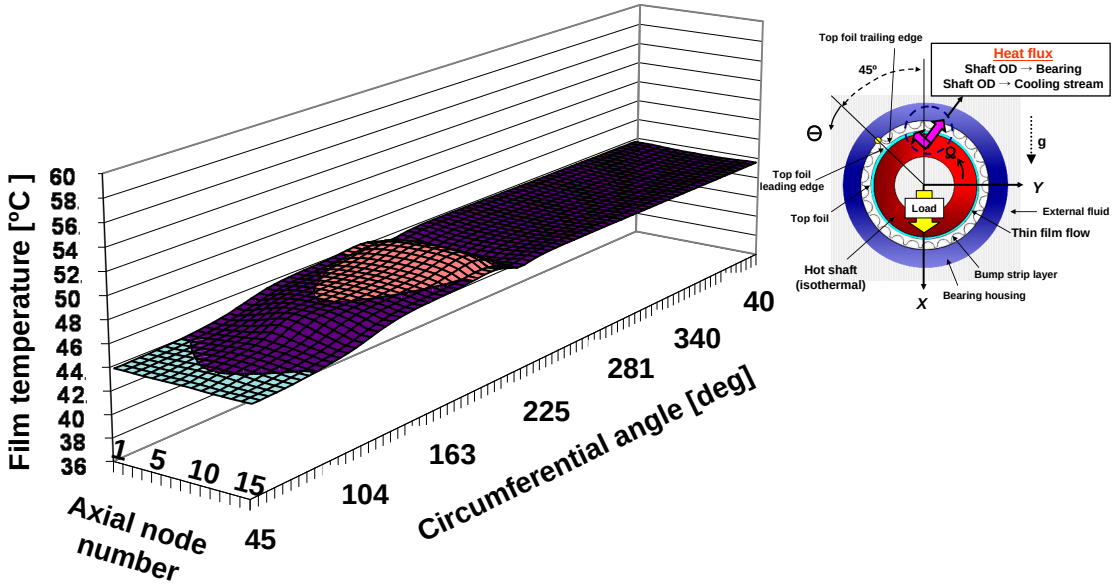

(a) Drive end bearing

(Cooling stream inlet temperature= 40ºC, uniform rotor OD temperature= 50ºC, T_a= 23ºC)

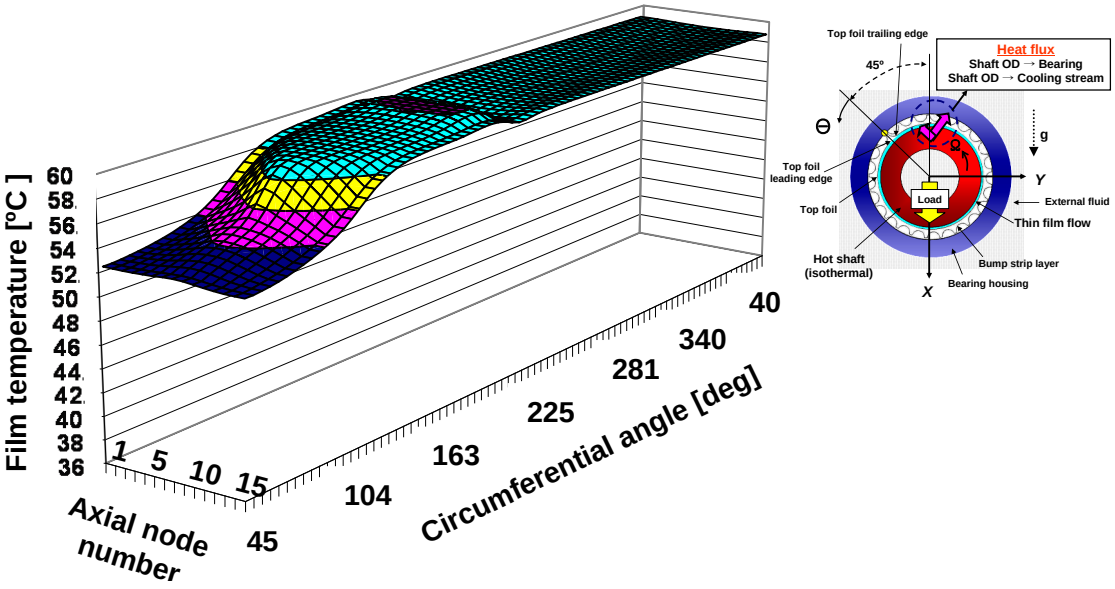

(b) Free end bearing

(Cooling stream inlet temperature= 40ºC, uniform rotor OD temperature= 66ºC, T_a= 23ºC)

Fig. N.2 Prediction: Test case #5. Thin film temperature fields in GFBs. T_{hs}=100ºC, rotor speed at 10 krpm. Cooling flow rate per each bearing 25 L/min. Thermal mixing coefficient λ=0.65.

APPENDIX O

PREDICTED STIFFNESS AND DAMPING COEFFICIENTS:

TEST CASES #4 AND #6

Figures O.1 through O.3 depict the predicted force coefficients calculated at synchronous frequency for test cases #4 and #6.

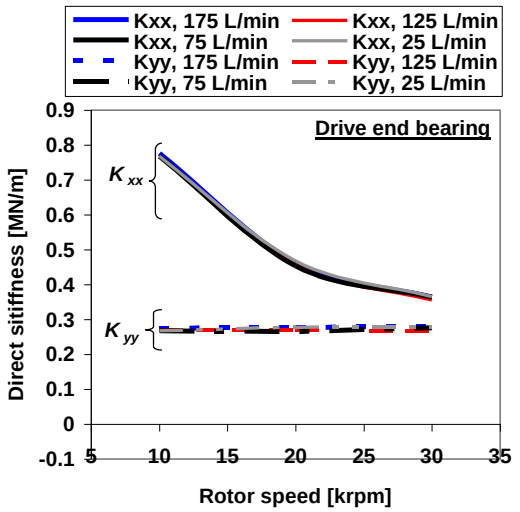

(a) Direct stiffness. Drive end bearing

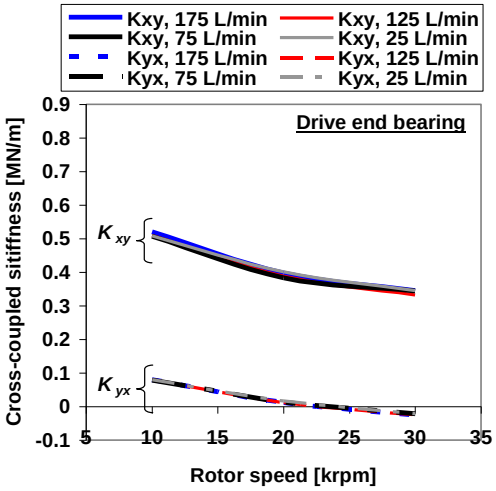

(b) Cross-coupled stiffness: Drive end bearing

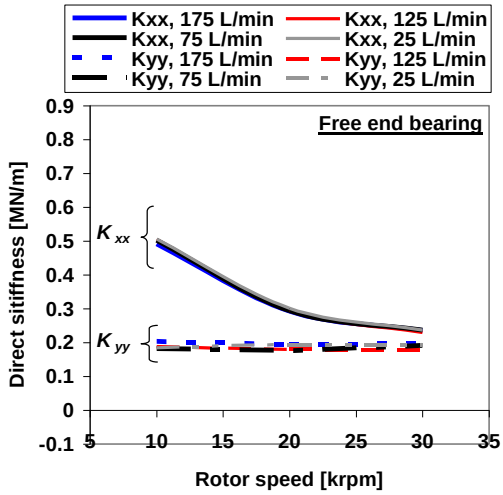

(c) Direct stiffness. Free end bearing

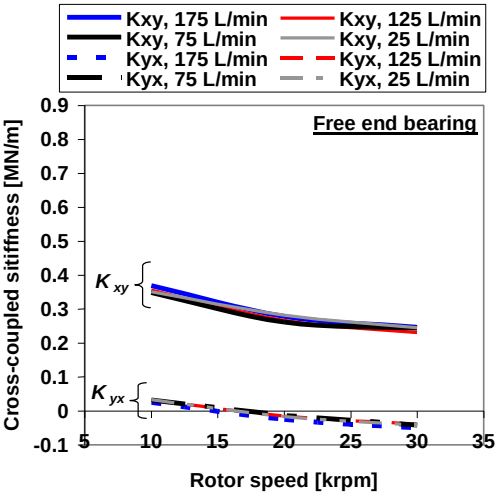

(d) Cross-coupled stiffness: Free end bearing

Fig. O.1 Prediction: Test case #4. T_{hs}=65ºC. Drive end and free end foil bearing direct and cross-coupled stiffness versus rotor speed and increasing air cooling flow rates.

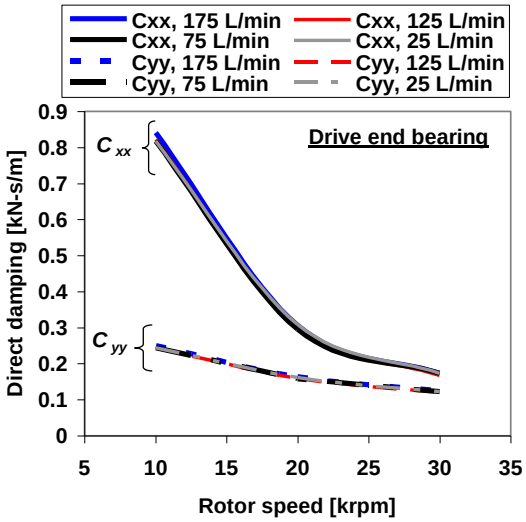

(a) Direct damping. Drive end bearing

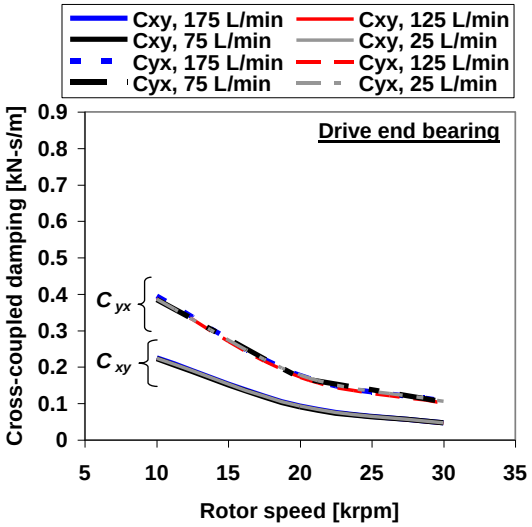

(b) Cross-coupled damping: Drive end bearing

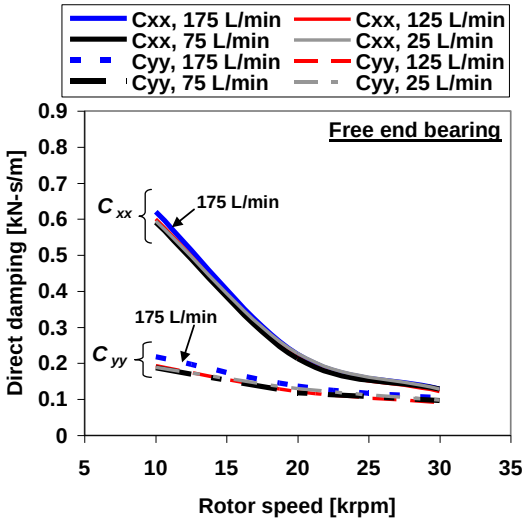

(c) Direct damping. Free end bearing

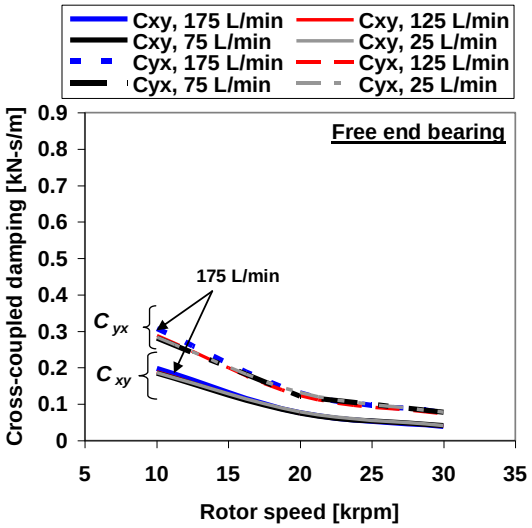

(d) Cross-coupled damping: Free end bearing

Fig. O.2 Prediction: Test case #4. T_{hs}=65ºC Drive end and free end foil bearing direct and cross-coupled damping coefficients versus rotor speed and increasing air cooling flow rates.

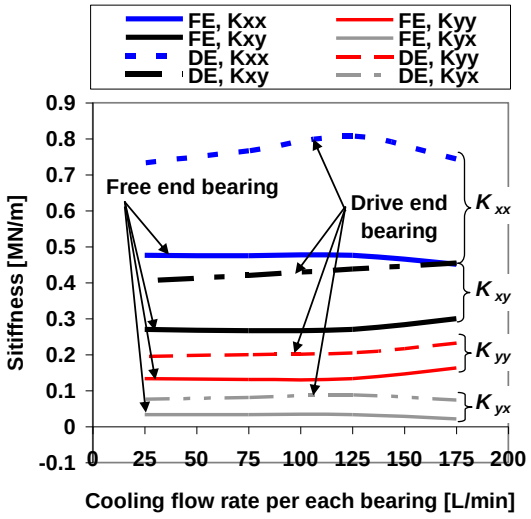

(a) Direct and cross-coupled stiffness

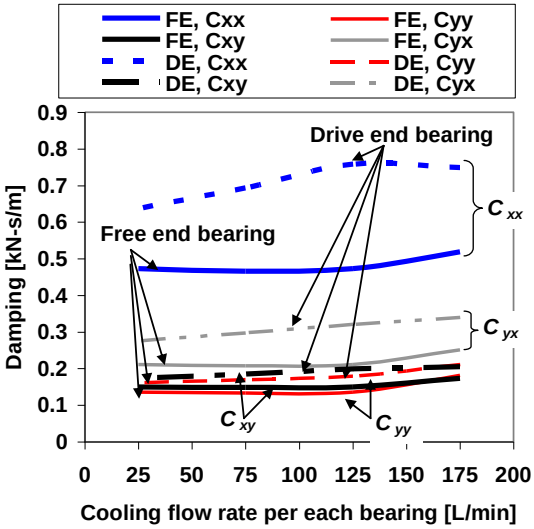

(b) Direct and cross-coupled damping

Fig. O.3 Prediction: Test case #6. T_{hs}=150ºC. Drive end and free end foil bearing force coefficients versus air cooling flow rates for rotor speed = 10 krpm.

VITA

Keun Ryu is a Senior Development Engineer in the Basic Development Team within Global Commercial Diesel Product Development at BorgWarner Turbo Systems in Asheville, NC. He received B.S. (2003) and M.S. (2005) degrees (Mechanical Engineering) from Hanyang University in Seoul, Korea as well as M.S (2007) and Ph.D (2011) degrees (Mechanical Engineering) from Texas A&M University. He worked for two years (2003−2004) as a Graduated Studying Fellow at the Korea Institute of Science and Technology (KIST). He joined the Turbomachinery Laboratory at Texas A&M University in 2005 and worked for five years (2005−2010) as a Graduate Research Assistant. Presently, at BorgWarner Turbo Systems, he focuses on the development of bearing and sealing system components with emphasis on oil-free bearing technology.

Keun Ryu has presented and published more than twenty technical papers and reports on gas bearings and rotordynamics. He also holds several patents for foil bearings and a micro gas turbine system. Since 2007, he has served the ASME Turbo Expo conference as a reviewer and technical session organizer/chair/co-chair. Presently, he is an invited technical paper reviewer for ASME Journal of Tribology, Elsevier Tribology International, and STLE Tribology Transactions.

Keun Ryu may be reached at BorgWarner Turbo Systems, 1849 Brevard Road, Arden, NC 28704. His email is keun.ryu@gmail.com.